



A Study on the Impact of Space Weather Events on the Ionosphere over the Antarctic Station Bharti and the Indian Sub-Continent

Thesis submitted to
Cochin University of Science and Technology

In partial fulfillment of the requirements
for the award of

Doctor of Philosophy
in
Physics

UNDER THE FACULTY OF SCIENCES

by
Shreedevi P R

Space Physics Laboratory
Vikram Sarabhai Space Centre
Indian Space Research Organisation
Thiruvananthapuram
INDIA

June 2017

Dedicated to

Those special women who gave me a part of their life...

Geetha, Jamuna Mam, Radhamani and Vasuma

Acknowledgments

First and foremost, I would like to express my sincere thanks to Dr. Raj Kumar Choudhary for being a great mentor throughout the last five years of my PhD course. I am deeply indebted to him for all the knowledge and experience that I gained from him which helped me grow as a researcher as well as a person. It was solely because of his support that I could travel to Antarctica, study the polar ionosphere and watch beautiful auroras, all of which have been the most memorable events in my life. I express my heartfelt gratitude to him for encouraging my research, helping me think rationally, questioning my ideas and even hearing my problems. I owe my deepest gratitude to him as without his support this doctoral study would not have been possible.

My sincere thanks goes to Dr. Anil Bhardwaj for being my supervisor, who set high standards for work and inspired me to meet those standards. The several useful discussions we had shaped my ideas and the freedom to pursue my ideas instilled confidence in me. I thank you sir, for the invaluable guidance and the motivation to bring out the best in me.

The last two years of my PhD life became the most productive years of my life also because of the presence of Smitha mam. I am at loss of words to describe the support and affection I received from her. I thank you whole heartedly mam, for teaching me and inspiring me to do better every day. I express my sincere gratitude to her for being there for me whenever I needed support in my career as well as personal life.

My sincere thanks to Dr. Yiqun Yu and Dr. Misa Cowee for their guidance and encouragement throughout the time I worked at the Los Alamos National Lab (LANL), USA as well as here at SPL. I gratefully acknowledge them for providing me an opportunity to be a part of the 4th Los Alamos Space weather Summer School. I thank Dr. Yiqun Yu for introducing me to modeling. This work would not have been possible without her encouragement and support.

My sincere thanks to Dr. Radhika Ramachandran, Director, SPL for facilitating the course of the present work and the valuable suggestions, as Academic committee chairman during my tenure as research fellow. I also extend my gratitude to the former director of SPL, Dr. K. Krishna Moorthy for the constant encouragement and guidance.

Thanks are due to the Academic committee and the doctoral committee of SPL for their feedback and guidance which helped me grow as a scientist as well as a person. I would like to thank Dr. Radhika Ramachandran, Dr. K. Rajeev, Dr. Geetha Ramkumar, Dr. C. Suresh Raju, Dr. Tarun Kumar Pant, Dr. Rajkumar Choudhary, Dr. K. Kishore Kumar, Dr. Suresh Babu, Dr. S. V. Sunil Kumar, Dr. Siji Kumar, Dr. D. Bala Subrahmanyam, Dr. Kiran Kumar, Dr. Siddharth, Dr. Satheesh, Dr. G. Manju, Dr. Sandhya and Dr. Vipin and the Central Level Monitoring Committee (CLMC) for their feedback and criticism especially during the annual reviews which helped in the successful completion of the thesis work.

It is my pleasure to thank the doctoral committee members from CUSAT, Dr. B. Pradeep, Dr. C. A. Babu, Dr. K. Mohan Kumar, Dr. Godfrey Loius, Dr. Kurian Sajan, Dr. Santhosh Raghavan and Head of physics department for their feedback and encouragement.

I would like to thank Dr. Sneha Yadav, Dr. C. Vineeth, Dr. Sandhya, Dr. Vipin Kumar Yadav, Dr. Mukunda Gogoi, Dr. Prashant Hegde, Dr. M. Mossarraf Hossain, M. B. Dhanya, Dr. Uma Das, Dr. Nizy Mathew, M. Mridula, Venkata Subrahmanyam, Santhosh Muralidharan, Girach Imaran Asator, Sobhan, Santhosh Kumar Pandey and Dr. Swain for their support and encouragement.

I would like to acknowledge the financial assistance provided by the Indian Space Research Organization through the research fellowship. Thanks are due to the staff at the VSSC Library for the reprographic facility and assistance, which was much needed during the course of this thesis. Sincere thanks to Mr. Jayakumar, Mr. Harikrishna Kishore, Mrs. Suseela and Mrs. Sisira, Mrs. Salini, Mrs. Shiji, Mr. Vijayan-administrative staff of SPL for their help, cheerful assistance and logistic support during my tenure at SPL. I express my sincere gratitude to the members of the Atmospheric Technology Division (ATD), Mr. S. V. Mohan Kumar, Mrs. P. Sreelatha, Mr. P. Pradeep Kumar, Dr. M. Ahmed, Mr. T. P. Das, Mr. Shajahan, Ms. Neha, Mr. Vajja, Mr. Manikantan Nair, Mr. Uttam S Purthy, Mr. Nazeer, Ms. P. T. Lali, Ms. Rosmi, Mr. G. Ashok Kumar, Mr. Pramod, Mr. Satheesh, Mr. Anumod, Mr. Ajeesh, Ms. Mabel, Ms. Shanthi, Mr. Samdas and Mr. Vijayan for providing the necessary support.

I acknowledge my batchmates Ashok Kumar Gupta, Lakshmi N. B and Ajesh for their encouragement and help. I thank all the student members of the research group at SPL Mulsin, Jayachandran, Aneesh, Vrinda, Sneha, Freddy, Maria, Lavanya, Ashwathy, Govind, Nalini, Roshny, Edwin and Koushik for their friendship, help and company.

I would like to thank a special group of people Ambili, Aryasree, Sneha Yadav, Nithin Mohan, Simi and Abhishek for their friendship and care. The time I spent with them have been undoubtedly the best moments of my life here at Trivandrum. My special thanks to Sneha Yadav for her encouragement and friendship. Her invaluable guidance and support helped me a lot in giving shape to my thesis. Special thanks to my dear friends Jethin, Karthika, Rajesh, Athul, Krishnaraj, Madhavi, Poornima and Kiran for their love and support.

All my love to Geetha and Radhakrishna for giving me a wonderful life. Any amount of thanks would be less to express my gratitude for the love and trust you have in me. I am also indebted to my dear sisters Lovelue and Tipu for their friendship, love and care throughout my life. Special thanks goes to my loving nephews, Ayush and Abhiram for adding so much more happiness to our lives. I could easily forget my worries in the times I spent with Ayush. If not for his cheerful conversations and happy smiles, my time at Trivandrum would have been difficult. I would like to thank my brothers, Prasanth and Charan for their love and support.

Sincere thanks to Mr. Sasidhara Kurup for his encouragement and support.

I owe my deepest gratitude to my soulmate, Prasanth for the last 12 years of companionship which undoubtedly helped me grow into the best version of me. I thank him for his love and friendship which added so much beauty to my life. I am greatly indebted to you, Prasanth for inspiring me to bring out the best in me, each and every day. This thesis is dedicated to you too.

Contents

Preface	i
Publications and Conference presentations	iii
List of Acronyms	vii
List of Figures	viii
List of Tables	xi
1 Introduction	1
1.1 The Earth's Atmosphere	1
1.2 The Earth's Ionosphere	3
1.3 Ionospheric conductivity and currents	6
1.4 Ionospheric current systems at different latitudes	10
1.5 The Sq (Solar quiet) Current system	12
1.6 Electric fields in the Polar ionosphere	15
1.7 Electric fields in the Low and Mid latitude ionosphere	16
1.8 Dissipation of solarwind energy in the Earth's M-I system	19
1.8.1 Solarwind-Magnetosphere-Ionosphere (SWMI) coupling	19
1.8.2 Geomagnetic storms	21
1.8.3 Ionospheric storms	23
1.8.3.1 Changes in global circulation and composition	23
1.8.3.2 Travelling Atmospheric disturbances (TADs)	24
1.8.3.3 Storm time electric fields	25
1.9 Objective of the thesis	29
1.10 Outline of the thesis	30
2 Experimental Techniques	33
2.1 Introduction	33
2.2 Global Positioning System (GPS)	34
2.2.1 GPS Errors	36
2.2.2 Satellite based errors	37
2.2.3 Receiver based errors	38
2.2.4 Atmospheric errors	38
2.2.4.1 Tropospheric effects on GPS signals	40
2.2.4.2 Ionospheric effects on GPS signals	41
2.3 The InSWIM network	44
2.4 Ionosonde	47
2.4.1 Digisonde Portable sounder (DPS-4D)	50
2.4.1.1 Ionospheric data derived from Ionograms	52

2.4.1.2	Derived products from Drift measurements	52
2.4.1.3	Electron density Inversion Algorithm	53
2.5	Magnetometer	54
2.5.1	Proton precession magnetometer (PPM)	55
2.5.2	Flux gate magnetometer (FGM)	56
2.6	Summary	58
3	Quiet time variation of the Total Electron Content (TEC)	59
3.1	Introduction	59
3.2	Database	62
3.3	Variations in the TEC at the polar station, Bharti	63
3.3.1	Diurnal variations	64
3.3.2	Seasonal variations	67
3.3.3	Solar activity dependence	69
3.4	Variations in the TEC at the mid latitude station, Hanle	70
3.4.1	Diurnal variations	71
3.4.2	Seasonal variations	72
3.4.3	Solar activity dependence	74
3.5	Variations in the TEC at the dip equatorial station, Trivandrum	75
3.5.1	Diurnal variations	75
3.5.2	Seasonal variations	76
3.5.3	Solar activity dependence	78
3.6	Latitudinal variations in the TEC	78
3.7	Comparison with the IRI 2012 model	80
3.8	Conclusions	84
4	Impact of space weather events on the southern polar ionosphere	87
4.1	Introduction	87
4.2	Database	91
4.3	The impact of St.Patrick's day storms of 2013 and 2015 on the ionosphere over Bharti	92
4.3.1	Geomagnetic conditions	92
4.3.2	Response of the polar ionosphere on 17 March 2013 and 17 March 2015	94
4.3.3	Salient points of the observations on the two days:	95
4.3.4	Plausible reasons for the differences in the enhancement of the TEC on the two days	97
4.3.4.1	DMSP–SSUSI Observations on 17 March 2013	97
4.3.4.2	DMSP–SSUSI Observations on 17 March 2015	99
4.3.4.3	DMSP ion drift measurements on 17 March 2013, and 17 March 2015	102
4.3.4.4	Variations in magnetopause on 17 March 2013 and 17 March 2015	104
4.3.5	Summary of Discussion	105
4.4	Morphology of the TEC over Bharti during geomagnetic disturbances	106
4.4.1	Storm onset time : How does it impact TEC variations at Bharti	107
4.4.1.1	Onset of storm in the morning sector	108

4.4.1.2	Onset of storm in the afternoon sector	109
4.4.1.3	Onset of the storm in the nighttime sector	109
4.4.2	Storm impact : Positive and Negative Ionospheric storms	110
4.4.2.1	Negative ionospheric storms	111
4.4.2.2	Positive ionospheric storms	112
4.4.3	Salient features of the stormtime variation of TEC at Bharti	112
4.5	Conclusions	113
5	High-mid-low latitude coupling	115
5.1	Introduction	115
5.2	Database	118
5.3	Role of electrodynamic coupling: How the low latitude ionospheric system responded to the intense geomagnetic storm of 17 March 2013	120
5.3.1	Geomagnetic conditions on 17 March 2013	121
5.3.2	F-region over the dip equator	122
5.3.3	Redistribution of plasma in the ionosphere over the Indian region	123
5.3.4	Synthesis of observations	125
5.3.5	The Indian low latitude ionospheric region during a typical CEJ event	126
5.3.6	Polar ionosphere on 17 March 2013	130
5.3.7	Plausible reasons for a positive ionospheric storm in the Indian sector on 17 March 2013	133
5.3.8	Salient features	136
5.4	Role of neutral dynamical coupling: How the low latitude ionosphere responded to the intense geomagnetic storm of 28 June 2013	136
5.4.1	Geomagnetic conditions between 27-29 June 2013	137
5.4.2	Ionospheric Response on 28 and 29 June 2013	139
5.4.3	Digisonde observations on 28 and 29 June 2013	141
5.4.4	The role of composition disturbances	143
5.4.5	Possible reasons for the ionospheric storm during 28-29 June 2013	143
5.4.6	Salient features	147
5.5	Relative contribution of stormtime electric fields and composition disturbances in redistribution of plasma	147
5.5.1	Geomagnetic conditions during 18-21 February 2014	148
5.5.2	Latitudinal variation of TEC	150
5.5.3	Digisonde measurements over the dip equator	152
5.5.4	What led to the evolution of ionospheric storm during 18-21 February 2014?	153
5.5.5	Salient features	157
5.6	Conclusions	158
6	Influence of ionospheric conductivity on the magnetospheric dynamics	159
6.1	Introduction	159
6.2	Description of the Model	162
6.3	Simulation results	164
6.3.1	Type 1: The realistic conductance model	165
6.3.2	Type 2: Uniform conductance model	168
6.4	How the ionospheric conductivity influences the magnetospheric dynamics?	171
6.5	Conclusion	175

7 Summary and Future Scope	177
7.1 Summary	177
7.2 Scope for future studies	181
Appendix A Publications	183
References	233

Preface

The study of the space environment around the Earth and the Sun is given much emphasis in the current scenario due to its implications for satellite and ground based technology. The Earth's ionosphere due to its variabilities, that are, necessarily related to the Sun, significantly affects the radio waves that pass through it. The influence on radio wave propagation further worsens when ionospheric behaviour undergoes large deviations during space weather events, like geomagnetic storms, that are caused by magnetic disturbances originating on the Sun. Though the quiet time variations and the anomalies of the ionosphere are known upto a great extent, little is known regarding the erratic behaviour of the ionosphere during the active phase of the Sun. One of the biggest problems in achieving a comprehensive understanding of the ionospheric variabilities during space weather events is the lack of simultaneous measurements from different geographical locations. Day to day variations in the background zonal electric field and neutral thermospheric winds further complicate the scenario. As an attempt towards gaining a better understanding of the latitudinal evolution of ionospheric storms, the response of the ionosphere over the Antarctic region and the Indian region to space weather events has been studied in this doctoral work. Study of the ionosphere over the Indian region becomes suitable to achieve this objective as the Indian region extends from the magnetic equator to the anomaly crest and beyond the Sq focus region in the northern hemisphere. The high latitude component was included by having measurements from the Indian research station, Bharti located in Antarctica which also lies along the same longitude as the Indian region.

The important results obtained from the present doctoral study are organized into seven chapters. The first chapter provides an introduction to the existing information about the behaviour of the Earth's ionosphere and the magnetosphere. The experimental techniques and details of the instrumentation used in data collection are provided in the second chapter. Understanding the quiet time variations of the ionosphere over Bharti and the Indian region is a prerequisite to understand the disturbed time variations therein. Hence, the quiet time behaviour of the ionosphere over Bharti and two stations in the Indian region that represent the mid latitude region (Hanle) and dip equatorial region (Trivandrum) is discussed in the third chapter. The fourth chapter examines the response of the ionosphere over Bharti to space weather events, in order to provide a comprehensive understanding of the behaviour of plasma thereat and the processes that modulate it. Various aspects of coupling between the high, mid, low and equatorial ionosphere are investigated in the fifth chapter. The sixth chapter investigates the role of ionosphere in controlling the magnetospheric behaviour during geomagnetic storms by using the SWMF (Space Weather Modeling Framework) which is a unified self-consistent model that allows for a comprehensive investigation of the processes happening in the global magnetosphere, inner magnetosphere and the ionosphere. A summary of this doctoral work and the future scope is provided in the seventh chapter.

Publications:

1. **Shreedevi P. R.**, Yiqun Yu; Vania Jordanova, Influence of ionospheric conductivity on the magnetospheric dynamics, (2014) Los Alamos Space Weather Summer School Research Reports, LANL, 2014, LA-UR 15-20136.
2. **Shreedevi P. R.**, S. V. Thampi, D. Chakrabarty, R. K. Choudhary, T. K. Pant, A. Bhardwaj, and S. Mukherjee (2016), On the latitudinal changes in ionospheric electrodynamics and composition based on observations over the 76-77°E meridian from both hemispheres during a geomagnetic storm, *J. Geophys. Res. Space Physics*, 121, doi:10.1002/2015JA021841.
3. Thampi, S. V., **P. R. Shreedevi**, R. K. Choudhary, T. K. Pant, D. Chakrabarty, S. Sunda, S. Mukherjee, and A. Bhardwaj (2016), Direct observational evidence for disturbance dynamo on the daytime low-latitude ionosphere: A case study based on the 28 June 2013 space weather event, *J. Geophys. Res. Space Physics*, 121, doi:10.1002/2016JA023037.
4. Guha, A., Saha K., De, B. K., Subrahmanyam, K. V., **P. R. Shreedevi**, (2016), Space weather effects on lower ionosphere : First investigation from Bharati station during 34th scientific expedition to Antarctica, *Adv. Space Res.*, Volume 59, Issue 8, Pages 2007-2018, doi:10.1016/j.asr.2017.02.004.
5. Unnikrishnan, K., H. Sreekumar, R. K. Choudhary, V. M. Ashna, K. M. Ambili, **P. R. Shreedevi** and P. B. Rao (2016), A study on the evolution of plasma bubbles using the single station-multisatellite and multistation-single satellite techniques, *J. Geophys. Res. Space Physics*, 122, doi:10.1002/2016JA023502.
6. **Shreedevi P. R.** and R. K. Choudhary, A study on the impact of storm-time fast fluctuating IMF Bz on the distribution of plasma over low latitude ionosphere. [Under review, *J. Geophys. Res. Space Physics*]
7. Sneha Yadav, T. K. Pant, R. K. Choudhary, C. Vineeth, S. Sunda, K. Kishore Kumar, **Shreedevi P. R.** and S. Mukherjee, Impact of sudden stratospheric warming of 2009 on the equatorial and low-latitude ionosphere of the Indian longitudes: A case study. [Under review, *J. Geophys. Res. Space Physics*]
8. **Shreedevi P. R.**, Smitha V. Thampi, R. K. Choudhary, Ryan M. Mcgranaghan, Tarun Kumar Pant and Anil Bhardwaj, Response of the southern polar ionosphere to the St. Patrick's day storms of 2013 and 2015. [In revision, *J. Geophys. Res. Space Physics*]
9. **Shreedevi P. R.**, R. K. Choudhary, A morphological study of the variation of Total Electron Content (TEC) of the ionosphere over the dynamically variable polar station, Bharti. [In revision, *J. Geophys. Res. Space Physics*]

Conference presentations:

1. **Shreedevi P. R.**, Yiqun Yu, Vania Jordanova (2014), Ionospheric control of the magnetosphere: Conductance, 4th Los Alamos Space Weather Summer School, 2 June-25 July 2014.

2. **Shreedevi P. R.** and R. K. Choudhary (2015), On the distribution of plasma over the low-mid latitude region during the intense geomagnetic storm of 17 March, 2013, Indian Geophysical Union, NCAOR, Goa, 3-5 November 2015.
3. **Shreedevi P. R.**, S. V. Thampi, D. Chakrabarty, R. K. Choudhary, T. K. Pant, A. Bhardwaj, and S. Mukherjee (2015), On the variation of Total Electron Content (TEC) over the equatorial, mid and high latitudes during a long duration positive ionospheric storm, URSI-RCRS, JNU, Delhi, November 2015
4. **Shreedevi P. R.** and R. K. Choudhary (2015), A study on the impact of fast fluctuating IMF Bz on the distribution of plasma over low and mid latitude region, URSI-RCRS, JNU, Delhi, November 2015
5. **Shreedevi P. R.**, S. V. Thampi, D. Chakrabarty, R. K. Choudhary, T. K. Pant, A. Bhardwaj, and S. Mukherjee (2015), On the relative contributions of prompt penetration electric field and disturbance dynamo electric field in modulating the ionospheric dynamics over the Equatorial, Mid and High Latitudes during a geomagnetic storm, NSS College, Chenganassery, December 2015.
6. **Shreedevi P. R.**, R. K. Choudhary (2016), A morphological study on the variation of Total Electron Content (TEC) over the southern polar ionosphere, NSSS, SPL, Trivandrum, February 2016.
7. **Shreedevi P. R.**, Smitha V. Thampi, R. K. Choudhary, T. K. Pant and Anil Bhardwaj (2016), On the variation of TEC over the northern hemisphere low-mid latitude and southern polar ionosphere during a long duration positive ionospheric storm (Poster), NSSS, SPL, Trivandrum, February 2016.
8. **Shreedevi P. R.**, R. K. Choudhary (2016), On the distribution of plasma over low and mid latitude region during the intense geomagnetic storm of March 17, 2013 (Poster), NSSS, SPL, Trivandrum, February 2016.

Acronyms

- AAI** Airport Authority of India.
ACE Advanced Composition Explorer.
AE Auroral Electrojet.
AEJ Auroral Electrojet.
AL Auroral Lower.
AMIE Assimilative Mapping of Ionospheric Electrodynamics.
ARTIST Automatic Real-Time Ionogram Scaler with True height.
BATS-R-US Block-Adaptive Tree Solar-Wind Roe Upwind Scheme.
C/A Coarse Acquisition.
CEJ Counter Electrojet.
CGM Corrected Geomagnetic Coordinates.
CHAMP Challenging Minisatellite Payload.
CME Coronal Mass Ejection.
COSMIC Constellation Observing System for Meteorology, Ionosphere, and Climate.
CPCP Cross Polar Cap Potential.
CRABEX Coherent Radio Beacon Experiment.
DCART Digisonde Commanding and Acquisition Remote terminal.
DD Disturbance Dynamo.
DDEF Disturbance Dynamo Electric field.
DMSP Defence Meteorological Satellite Program.
DOP Dilution Of Precision.
DPS Digisonde Portable Sounder.
Dst Disturbance Storm Time.
EEJ Equatorial Electrojet.
EEJ Eastward Electrojet.
EIA Equatorial Ionization Anomaly.
EPCP Expanding/Contracting Polar Cap.
EUV Extreme Ultraviolet.
F10.7 10.7-cm radio flux.
FACs Field aligned currents.
FAST Fast Auroral Snapshot Explorer.
FGM Flux Gate magnetometer.
foF2 F-region peak frequency.

FUV Far Ultraviolet.

GAGAN GPS Aided Geo Augmented Navigation.

GITM Global Ionosphere Thermosphere Model.

GLONASS Global Navigation Satellite System.

GPS Global Positioning System.

GRBR GNU Radio Beacon Receiver.

GUVI Global Ultraviolet Imager.

HF High Frequency.

hmF2 F-region peak height.

I-T Ionosphere-Thermosphere.

IDM Ion Drift Meter.

IEF Interplanetary Electric Field.

IGRF International Geomagnetic Reference Field.

IMF Interplanetary Magnetic Field.

InSWIM Indian Network for Space Weather Impact Monitoring.

IPP Ionospheric Pierce Point.

IRI International Reference Ionosphere.

IRNSS Indian Regional Navigation Satellite System.

ISR Incoherent Scatter Radar.

ISRO Indian Space Research organization.

IST Indian Standard Time.

JPL Jet Propulsion Laboratory.

LBHL Lyman-Birge-Hopfield Long.

LBHS Lyman-Birge-Hopfield Short.

LEOS Low Earth Orbiting satellite.

M-I Magnetosphere-Ionosphere.

MHD MagnetoHydroDynamic.

MIT Magnetosphere-Ionosphere-Thermosphere.

MLT Magnetic Local Time.

MSIS-86 Mass Spectrometer Incoherent Scatter radar.

MUF Maximum Usable Frequency.

NAVSTAR Navigational System Tracking and Range.

NmF2 F-region peak density.

NPS Nadir-looking Photometers.

NRLMSIS-00 United States Naval Research Laboratory Mass Spectrometer and Incoherent Scatter Radar.

P Precision.

PBL Plasmaspheric Boundary Layer.

PC Polar Cap.

PCE Polar Cap Enhancements.

POLAN POLynomial ANalysis.

PPEF Prompt Penetration Electric field.

PPM Proton Precession Magnetometer.

-
- PRE** Pre Reversal Enhancement.
PRN Pseudo Random Noise.
- R1 FACs** Region 1 Field aligned currents.
R2 FACs Region 2 Field aligned currents.
RAM Ring current Atmosphere interactions Model.
RAM-SCB Ring current Atmosphere interactions Model-Self Consistent B.
RBSP Radiation Belt Storm Probes.
RPA Retarding Potential Analyser.
- SAPS** Subauroral Polarisation Streams.
SBF Septentrio Binary Format.
SEDs Storm Enhanced Densities.
SIS Scanning Imaging Spectrograph.
Sq Solar quiet.
SSC Storm Sudden Commencement.
SSUSI Special Sensor Ultraviolet Spectral Imager.
STEC Slant Total electron content.
SuperDARN Super Dual Auroral Radar Network.
SWMF Space Weather Modelling Framework.
SWMI Solar Wind-Magnetosphere-Ionosphere.
Sym-H Symmetric Geomagnetic Disturbance.
- TADs** Travelling Atmospheric Disturbances.
TEC Total Electron Content.
TIE-GCM Thermosphere-Ionosphere- Electrodynamic General Circulation Model.
TIMED Thermosphere-Ionosphere-Mesosphere Energetic Dynamics.
TOI Tongue Of Ionization.
TOPEX Ocean Topography Experiment.
- UHF** Ultra High Frequency.
UMLCAR University of Massachusetts Lowell centre for Atmospheric Research.
UT Universal time.
UTC Universal Time Coordinate.
UV Ultraviolet.
- VTEC** Vertical Total Electron Content.
- WEJ** Westward Electrojet.

List of Figures

1.1	Vertical temperature profile of the atmosphere	2
1.2	Structure of ionosphere	4
1.3	Locations of the polar cap and auroral oval in the Northern hemisphere	6
1.4	Conductivity profile of the ionosphere	9
1.5	Average global Sq current system	13
1.6	High latitude Sq system	14
1.7	Electric fields and plasma convection in the polar ionosphere	15
1.8	Electric fields in the low and mid latitude ionosphere	17
1.9	Operational principle of the solar wind dynamo	20
1.10	Different phases of a geomagnetic storm	22
2.1	Schematic representation of GPS segments	34
2.2	Position determination in GPS using Triangulation	36
2.3	Schematic representation of GPS signal propagation through the Earth's atmosphere	39
2.4	Location of InSWIM stations	45
2.5	Sample ionogram	49
2.6	Six dimensional ionogram	52
2.7	Working principle of Proton Precession Magnetometer (PPM)	55
2.8	Basic circuit of a Flux Gate Magnetometer (FGM)	57
3.1	The approximate location of Bharti station with respect to the plasma convection, the quiet time auroral oval	64
3.2	Diurnal variation of TEC at Bharti on quiet days	65
3.3	Solar zenith angle variation at Bharti	66
3.4	Seasonal variation of TEC at Bharti during the years 2013-2016	68
3.5	Variation of F10.7 cm radio flux and mean TEC at Bharti during 2013-2016	70
3.6	Diurnal variation of TEC at Hanle on quiet days	71
3.7	Seasonal variation of TEC at Hanle during the years 2014-2016	72
3.8	Variation of the F10.7 cm flux and mean TEC at Hanle during 2014-2016	74
3.9	Diurnal variation of TEC at Trivandrum on a typical quiet day in summer, winter and equinoctial period, respectively	76
3.10	Seasonal variation of TEC at Trivandrum during the years 2014-2016	77
3.11	Variation of the F10.7 cm flux and mean TEC at Trivandrum during 2014-2016	78

3.12	Variation of TEC at Bharti, Hanle and Trivandrum during the March equinox, September equinox, Northern summer and Northern winter months of the year 2015	79
3.13	TEC at Bharti during the years 2014-2016 derived from GPS observations and IRI model	81
3.14	TEC at Hanle during the years 2014-2016 derived from GPS observation-sand IRI model	82
3.15	TEC at Trivandrum during the years 2014-2016 derived from GPS obser-vationsand IRI model	83
4.1	Geomagnetic conditions during 16-18 March 2013 and 16-18 March 2015	93
4.2	Temporal variation of TEC and σ_ϕ index on 17 March 2013	95
4.3	Temporal variation of TEC and σ_ϕ index on 17 March 2015	96
4.4	Auroral emissions over the southern high latitudes during 17 March 2013	98
4.5	Temporal variation of the H and Z component of the magnetic field at Bharti on 17 March 2013	99
4.6	Auroral emissions over the high latitudes in the southern hemisphere during 17 March 2015	100
4.7	Temporal variation of the H and Z component of the magnetic field at Bharti on 17 March 2015	101
4.8	Cross-track velocity and ion density obtained from DMSP F-17 observa-tions on 17 March 2013	102
4.9	Cross-track velocity and ion density obtained from DMSP F-17 observa-tions on 17 March 2015	103
4.10	Temporal variation in the magnetopause along with the IMF B_z during 16-18 March 2013 and 16-18 March 2015	105
4.11	Temporal variation of Sym-H, AE index and TEC on 01–03 Oct 2013 . .	108
4.12	Temporal variation of Sym-H, AE index and TEC during 11-13 April 2014	109
4.13	Temporal variation of Sym-H, AE index and TEC during 09–11 April 2015	110
5.1	Geomagnetic conditions on 17 March 2013	121
5.2	Digisonde measurements from Trivandrum on 17 March 2013	123
5.3	Temporal variation of TEC on 17 March 2013 at different locations in the Indian region	124
5.4	Geomagnetic conditions on 10 February 2013	127
5.5	Digisonde measurements from Trivandrum on 10 February 2013	128
5.6	TEC variations at different locations in the Indian region on 10 February 2013	130
5.7	Temporal variation of TEC at Bharti on 17 March 2013	131
5.8	O/N_2 changes on 14 March 2013 and 17 March 2013	132
5.9	Simulated electron density and meridional winds on 17 March 2013 using GITM	134
5.10	Geomagnetic conditions during 27-29 June 2013	137
5.11	Temporal variation of EEJ during 28-29 June 2013	138
5.12	TEC variations at GPS stations on 28 and 29 June 2013	139
5.13	The Latitudinal variation in TEC as observed by the radio beacon	140
5.14	Digisonde observations from Trivandrum during 28-29 June 2013	141
5.15	O/N_2 changes on 28 and 29 June 2013	142
5.16	Simulated electron density on 29 June 2013 using GITM model	145

5.17	Geomagnetic conditions during February 18-21, 2014.	148
5.18	Temporal variation of EEJ during 18-21 February 2014	149
5.19	Temporal variation of TEC over Bharti during 18-21 February 2014 . . .	150
5.20	Temporal variation of TEC over Hanle, Ahmedabad and Trivandrum during 18-21 February 2014	151
5.21	Digisonde observations from Trivandrum during 18-21 February 2014 . .	152
5.22	O/N_2 changes during 18-21 February 2014	154
6.1	The Space Weather Modeling Framework model	163
6.2	Geomagnetic conditions on 17 March 2013	164
6.3	Results of Type 1 simulation using the realistic conductance model) . . .	166
6.4	Ring current energy density simulated using the realistic conductance model	167
6.5	Results of Type 2 simulation using the uniform conductance model . . .	169
6.6	Ring current energy density simulated using the uniform conductance model	170
6.7	Cross Polar Cap Potential (CPCP) in the southern hemisphere on 17 March 2013 obtained from the Type 1 and Type 2 simulations	172
6.8	Comparison of simulated Dst index with observations	174
6.9	Comparison of B_z simulated using the Type 1 and Type 2 models with satellite measurements	175

List of Tables

1.1	Characteristics of the different regions of the ionosphere	4
2.1	Error budget in GPS	37
2.2	The hardware specifications of Septentrio's PolaRxS GPS receiver	46
2.3	The specifications of DPS-4D Ionosonde system at Trivandrum	51
2.4	Specifications of PPM at Trivandrum	56
2.5	Specifications of Bartington Mag-03 Three axis FGM at Trivandrum	58
3.1	Geographic and Geomagnetic Coordinates at Bharti, Hanle and Trivandrum	62
4.1	Geophysical conditions during the St.Patrick's day storms of 2013 and 2015	90
4.2	TEC response at Bharti to the 24 geomagnetic storm events that occurred during 2013-2015.	107
5.1	Details of the locations of different stations and instruments thereat used in the present study.	118

Chapter 1

Introduction

Though the idea of the existence of an electrically conducting layer in the upper atmosphere was first suggested by Stewart in 1882, systematic studies of the ionosphere started only in the beginning of the nineteenth century. The Trans-Atlantic radio experiment by Marconi in 1901, prompted Kennelly and Heaviside to suggest the presence of the “Kennelly-Heaviside layer” above 80 km in the atmosphere. This layer was thought to contain free charges that could reflect radio waves. Two decades later, in 1924, the presence of this layer was confirmed by the experiments done by Appleton and Barnett, and Breit and Tuve. Later, in 1933, Watson-Watt gave the name “Ionosphere” to this conducting region of the atmosphere. Since its discovery, the ionosphere has been of great interest to physicists as it not only provided scope for study of plasma physics under natural conditions, but also led to the beginning of a new era of radio communication. Later, work by Chapman, describing the relationship between the Sun and the ionosphere impelled studies of the ionosphere in new directions. Since then, both experimental and modeling work on the different aspects of the ionosphere has been pursued. The most important among these studies are the interaction of the ionospheric system with the Sun. The activities on the Sun are known to directly affect the physical structure and chemical composition of the ionospheric system. Though the quiet time variations and the anomalies of the ionosphere are known upto a great extent, little is known regarding the erratic behaviour of the ionosphere during the active phase of the Sun. In this regard, the present work is an attempt towards understanding the variabilities in the ionosphere during the active phase of the Sun. A study of the disturbed ionosphere assumes significance, also because it has serious implications for satellite navigation and communication.

1.1 The Earth’s Atmosphere

Among the planets of the solar system, the Earth is the only one which sustains life and has an “atmosphere” composed of N_2 (78%), O_2 (21%) and 1% of minor gases which includes green house gases like water vapour, CO_2 , methane (CH_4), nitrous oxide (N_2O) etc, that surrounds the surface of the Earth. The Sun is the ultimate source of energy

for almost all the physical processes in the Earth's atmosphere. Since the intensity of solar irradiation varies with latitude and altitude, the composition of the atmosphere and the physical processes therein also differs. Based on the latitudinal variations, the atmosphere within $\pm 30^\circ$ latitude is classified as "low latitude", between $\pm 30^\circ$ to $\pm 60^\circ$ as "mid latitude" and beyond $\pm 60^\circ$ latitude is known as the "high latitude" respectively. Similarly, based on the altitudinal variations, the atmosphere below the altitude of 15 km is termed as "lower" atmosphere, between 15-90 km as "middle" and above 90 km as the "upper" atmosphere respectively.

The solar radiation reaching the Earth's atmosphere is absorbed by its constituents. The resulting changes in the chemical composition as well as the physical properties of the atmosphere gives rise to the temperature structure of the atmosphere shown in Figure 1.1. Based on the vertical temperature profile, the atmosphere is classified into four distinct layers namely, the "troposphere" ($\sim 0-15$ km), "stratosphere" ($\sim 15-50$ km), "mesosphere" ($\sim 50-90$ km) and the "thermosphere" (above 90 km). The transition region between the individual layers are not well defined and are known to vary with latitude [*Goody and Walker, 1972*].

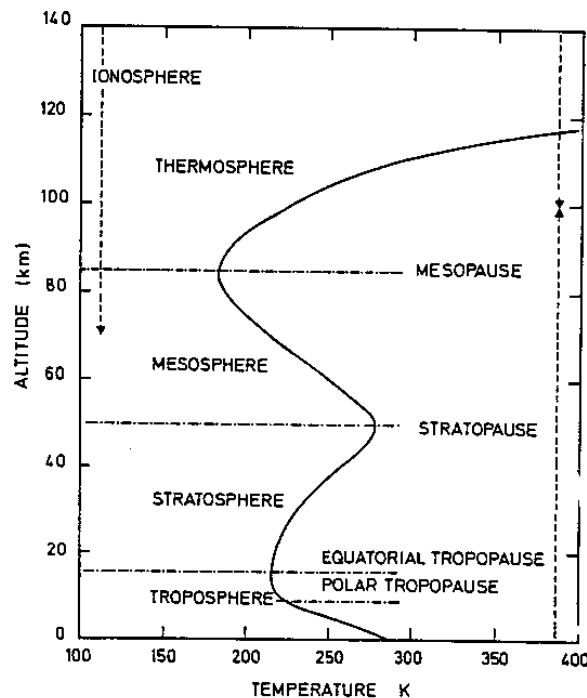


Figure 1.1: Vertical temperature profile of the atmosphere [After, *Brasseur and Solomon, 2005*].

The troposphere is the lowest region of the atmosphere and is known to extend from the surface of the Earth to an altitude of 16 km at the equator and 8 km at the poles respectively. Absorption of the solar radiation during daytime leads to heating up of the surface of the Earth. Consequently, the air close to the surface warms up and rises while the cooler air from higher altitudes descend. As a result, the temperature of

the troposphere is highest near the surface and decreases with height. However, the temperature is observed to increase after a particular altitude. The region where this reversal in temperature takes place is the upper boundary of the troposphere and is called the tropopause. Due to the inversion of temperature at these heights, the vertical mixing reduces and a stratified layer known as the stratosphere is formed. The air temperature in the stratosphere is seen to increase mainly due to the absorption of solar Ultraviolet (UV) rays by ozone. However, there is little ozone at altitudes above ~ 50 km in the atmosphere and hence, the temperature starts to decrease once again above these altitudes. The altitude where this inversion of temperature takes place is known as the stratopause. The new layer formed above the stratopause is known as the mesosphere.

The mesosphere is the coldest region of the atmosphere with a temperature of 180 K (at ~ 87 km) at tropics and 140 K (~ 85 km) at the poles. As described earlier, it is the absorption of ozone by solar radiation that leads to heating up of the atmosphere above the tropopause. Since there is very low concentration of ozone at mesospheric altitudes, the temperature remains low. In addition, the presence of CO_2 molecule at these heights also leads to radiative cooling [Andrews *et al.*, 1987; Rodger *et al.*, 1992; Lopez-Puertas *et al.*, 1992]. Above the mesosphere lies the thermosphere which is the hottest region of the atmosphere. The temperature in this region continues to increase and above ~ 400 km it is almost isothermal. Since the density is very low and the collisions are minimal, the absorption of solar radiation by fewer atoms/molecules give rise to the large increase in temperature in this region.

Although the neutral species are the dominant constituents, the atmosphere, has a significant concentration of ionized species also. This ionized region of the atmosphere known as the “Ionosphere”, becomes important due to the various interesting phenomena that it exhibits including the creation of the beautiful aurora. In addition to facilitating long distance radio communication, it also poses serious concerns to satellite navigation and communication. The origin of the ionosphere and its various features are described in the forthcoming sections.

1.2 The Earth’s Ionosphere

The Sun is the primary source of energy for all the planets in the solar system. The solar radiations reaching the Earth’s atmosphere ionize the neutral atoms/molecules and create free charges i.e., ions and electrons. The intensity of the ionizing radiation, atmospheric density, composition and ionization cross-sections of the neutral species determine the rate of production of plasma in the ionosphere [Chapman, 1931a, b]. The plasma produced in this way is subjected to physical, chemical and dynamical processes which leads to the formation of different regions (D (~ 60 -90 km), E (~ 90 -120 km) and F region (~ 150 -600 km)) in the ionosphere [Rishbeth and Garriott, 1969]. A schematic representation of the different regions of the ionosphere and the radiations contributing

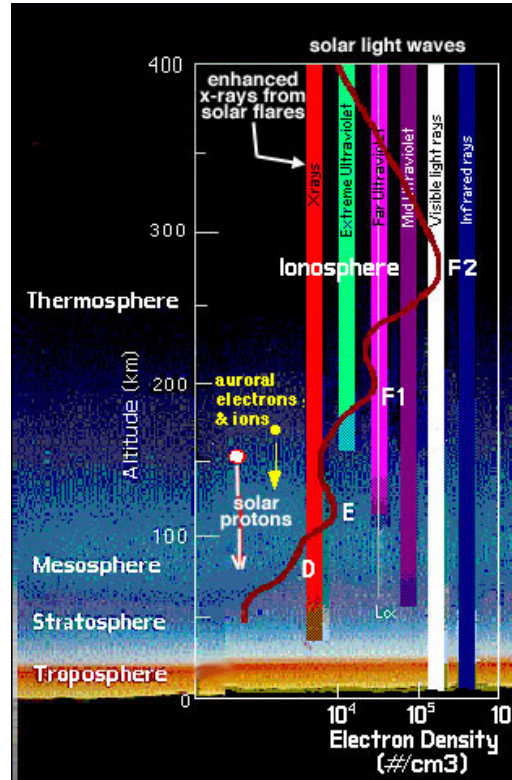


Figure 1.2: Structure of the Earth's ionosphere: The different regions of the ionosphere and the sources that contribute to the formation of the different regions of the ionosphere are indicated. Courtesy :[http : //www.windows2universe.org/earth/Atmosphere/layers_activity_print.html](http://www.windows2universe.org/earth/Atmosphere/layers_activity_print.html)

to their formation is shown in Figure 1.2. The major sources of ionization in the Earth's atmosphere are the solar Extreme Ultraviolet (EUV) and the X-ray radiation. The ionizing radiation, chemical species, and electron concentration in the D, E and F region of the ionosphere are listed in Table 1.1.

Table 1.1: Characteristics of the different regions of the ionosphere

	D-region (50–90 km)	E-region (90–150 km)	F-region (150–600 km)
Ionizing radiations	Ly α : 1216 Å X rays: 1–10 Å Cosmic rays	EUV : 911–1027 Å Ly β :1026 Å X rays : 10–170 Å	EUV : 170-911 Å
Chemical species	NO,NO ⁺ ,O ₂ ⁺ ,O,O ₃ , CO ₂ , H ₂ O and alkali metals	NO ⁺ , O ₂ ⁺ , trace metal atoms like Fe, Mg, Na	O ⁺ ,N ₂ ⁺ , N ₂ , O ₂ , O ₂ ⁺
Electron concentration	10 ² –10 ⁴ cm ⁻³	10 ⁵ cm ⁻³	10 ⁶ cm ⁻³

Essentially, the radiations in the range 140 Å – 796 Å produce the F-layer of the ionosphere. The major contribution to the F-region comes from the wavelengths in the range 500 – 600 Å that get absorbed heavily at about 170 km [Rishbeth and Garriott,

1969]. Other major emissions which attain unit optical depth above 150 km are He I (584 Å), He II (304 Å) and O V (630 Å). The E-region is formed by the absorption of both X rays in the wavelength range 8 – 140 Å and the UV radiation in the wavelength range 796 – 1027 Å. The production processes in the E-region are fairly complex as secondary ionization is produced by photoelectron impact also. The D-region is formed by the absorption of radiation in the 1027 – 1340 Å wavelength range. The major species (NO), present at D-region altitudes is ionized by the strongest line Lyman- α (1216 Å) radiation. In addition, galactic cosmic rays are also known to give rise to very small amounts of ionization in the D-region of the ionosphere [Rishbeth and Garriott, 1969].

The ionospheric plasma produced by photoproduction is also subjected to loss processes and diffusion along magnetic field lines. As a result, the F-region of the ionosphere splits into F_1 and F_2 regions during the daytime. However, at nighttime, the F_1 region disappears along with the E and D regions as the loss processes dominate in the absence of photoionization. The F_2 layer sustains at nighttime as the major ion species in the F_2 layer (which is O^+) has a longer lifetimes [Rishbeth and Garriott, 1969]. The presence of an additional layer known as the F_3 layer between 500-700 km is also found in the equatorial and low latitude ionosphere [Balan *et al.*, 1997a]. An additional feature present only in the electron density profile at the high latitudes is the secondary peaks that appear during events of auroral particle precipitation [Brekke, 2013].

An important source of ionization in the high latitude ionosphere, in addition to photoionization, is particle precipitation [Rishbeth and Garriott, 1969; Heikkila and Winningham, 1971]. But the characteristics of the electric field, currents and particles that precipitate into the high latitude ionosphere differs in the polar cap, auroral oval and the subauroral regions. This is because the magnetic field lines originating from these regions map to different regions of the magnetosphere. The polar cap as shown in Figure 1.3, is a circular area surrounding the magnetic pole with a typical diameter of about 30° . The magnetic field lines emanating from the polar cap are open and extend high up into the magnetosphere and connect with the Interplanetary Magnetic Field (IMF) as well. Hence this is the region of the polar ionosphere which is continuously in contact with the magnetospheric lobe population at quiet times as well. The auroral oval is the region surrounding the polar cap which is connected to the tail plasma sheet through the closed magnetic field lines. The subauroral regions lie equatorward of the auroral oval and is connected to the trapped particle population in the magnetosphere. Accordingly, the polar cap, auroral oval and the subauroral oval are all connected to different regions of the magnetosphere and so the associated particle populations in the magnetosphere, electric fields and currents in these regions differ [Newell and Meng, 1992; Prölss, 2004].

A notable feature in Figure 1.3 is the rotation of the polar cap, auroral oval and the subauroral regions around the geographic pole, because of which, a station lying in the

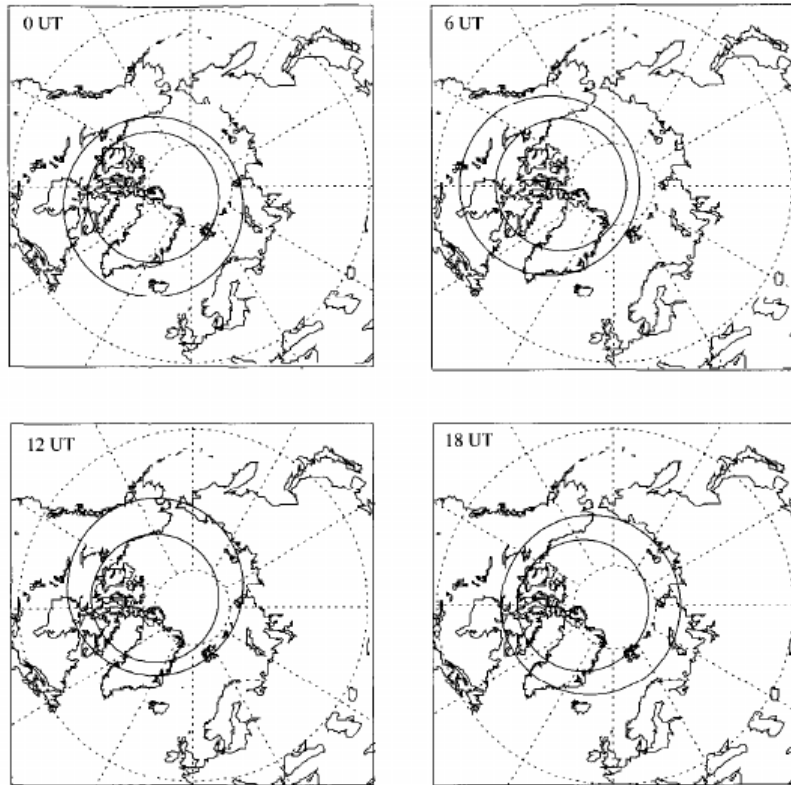


Figure 1.3: Location of the polar cap and auroral oval in the Northern hemisphere at selected times on a magnetically quiet day. [After, *Prölss*, 2004].

polar cap at nighttime may shift its position into the auroral oval during a different local time. As the polar atmosphere traverses through different regions dominated by photoionization, particle precipitation, ionospheric convection etc, fascinating phenomena exclusive to the high latitudes like the aurora, joule heating are created. The Earth's magnetic field plays a key role not only at the high latitudes, but also in the low latitude regions. This arises from the strong interaction of the magnetic field with the charged particles resulting in the generation of ionospheric conductivity and currents.

1.3 Ionospheric conductivity and currents

The Earth's ionosphere is partially ionized plasma embedded in the neutral atmosphere. In reality, the neutrals are much greater in number than the charged particles. Therefore, collisions with neutrals greatly influence the motion of charged particles. Hence, in addition to the electric and magnetic forces, a frictional force is also experienced by the ionized species due to collisions with coexisting neutral atoms/molecules in the atmosphere. This frictional force is proportional to the collision frequency and relative velocity of the charged particles with the neutrals. The movement of plasma in the ionosphere is therefore governed by the electrodynamic forces, diffusion along the magnetic field and collision with neutral species [*Kelley*, 1989]. Therefore, the equation

of motion for ions and electrons can be expressed as,

$$n_i m_i \frac{dv_i}{dt} = n_i e (E + v_i \times B) - n_i m_i v_{in} (v_i - u_n) \quad (1.1)$$

$$n_e m_e \frac{dv_e}{dt} = -n_e e (E + v_e \times B) - n_e m_e v_{en} (v_e - u_n) \quad (1.2)$$

where,

$n_e = n_i$ is the number density,

E is the electric field measured in the Earth-fixed reference frame,

B is the magnetic field,

v_i and v_e are the ion and electron velocity respectively, and

m_i and m_e are the masses of ion and electrons respectively.

The ion and electron velocity obtained by solving the above equation is,

$$v_i = u_n + \frac{e}{m_i v_{in}} (E + V_i \times B) \quad (1.3)$$

$$v_e = u_n - \frac{e}{m_e v_{en}} (E + V_e \times B) \quad (1.4)$$

The ion and electron velocity in a reference frame moving with the neutral wind is given by,

$$v'_i = v_i - u_n = \frac{1}{1 + k_i^2} \left[\left(\frac{k_i}{B} \right) E' + \left(\frac{k_i}{B} \right)^2 E' \times B + \left(\frac{k_i}{B} \right)^3 (E' \cdot B) B \right] \quad (1.5)$$

$$v'_e = v_e - u_n = \frac{1}{1 + k_e^2} \left[- \left(\frac{k_e}{B} \right) E' + \left(\frac{k_e}{B} \right)^2 E' \times B - \left(\frac{k_e}{B} \right)^3 (E' \cdot B) B \right] \quad (1.6)$$

where the electric field measured in the frame of reference moving with the neutral wind is given by,

$$E' = E + u_n \times B, \quad (1.7)$$

$$k_{e/i} = \frac{\Omega_{e/i}}{v_{en/in}} \quad \text{is the electron/ion mobility coefficient, and} \quad (1.8)$$

$$\Omega_{e/i} = \frac{eB}{m_{e/i}} \quad \text{is the gyrofrequency of electrons/ions.} \quad (1.9)$$

If the electric field E' is assumed to be perpendicular to the magnetic field B , then the ion velocity becomes,

$$v_i = \frac{k_i}{1 + k_i^2} \frac{E'}{B} + \frac{k_i^2}{1 + k_i^2} \frac{E' \times B}{B^2} \quad (1.10)$$

and the electron velocity becomes,

$$v_e = \frac{k_e}{1 + k_e^2} \frac{E'}{B} + \frac{k_e^2}{1 + k_e^2} \frac{E' \times B}{B^2} \quad (1.11)$$

As indicated in the above equations, the ion and electron velocities are determined primarily by the ratio of collision frequency to gyro frequency (i.e., $k = \Omega/v$). The electron and ion collision frequencies are much larger than their respective gyro frequencies in the lower ionosphere i.e., below 70 km (D-region). Hence, frequent collisions deter the gyration of ions and electrons around magnetic field. Also, the ionization density itself is low in the D-region of the ionosphere. As a result, no reasonable current exists at these altitudes. However, in the upper ionosphere, above 250 km (F_2 region), the gyrofrequency of electrons and ions are larger than their respective collision frequencies. Hence, the motion of the ions and electrons are controlled by the magnetic field and the only current that can be substantial is the parallel or field aligned current.

At about 70 km to 130 km i.e., in the E-region of the ionosphere, the ion-neutral collision frequency is larger than the gyrofrequency of ions whereas the electron-neutral collision frequency is much lower than the gyrofrequency of electrons. Consequently, the electrons gyrate around the magnetic field and the ions are held back by collisions with neutrals. Thus the differential motion between ions and electrons give rise to a current. The ion current, known as the Pederson current, is along the direction of the electric field (E). If the electric field is orthogonal to the magnetic field, then the charges also experience $E \times B$ drift. But since the ion motion is heavily retarded by collisions, only the electrons drift in $E \times B$ direction. Hence, a hall current flows in the $-B \times E$ direction. In this way, substantial currents are generated in the E-region of the ionosphere due to the dynamo action of neutral winds. It is for this reason that the E-region is also referred to as the “dynamo region”.

The current density (j) at a given height in the ionosphere is given by:

$$j = n_e \cdot e \cdot (v_e - v_i) \quad (1.12)$$

Substituting for v_e and v_i from eq.(1.10) and eq.(1.11) gives,

$$j = n_e \cdot e \left[\left(\frac{k_e}{1 + k_e^2} + \frac{k_i}{1 + k_i^2} \right) \frac{E'_\perp}{B} - \left(\frac{k_e^2}{1 + k_e^2} - \frac{k_i^2}{1 + k_i^2} \right) \frac{E' \times B}{B^2} + (k_e + k_i) \frac{E'_\parallel}{B} \right] \quad (1.13)$$

where,

$$E = E_\perp + E_\parallel,$$

E_\perp is the component of electric field parallel to B, and

E_\parallel is the component of electric field perpendicular to B.

The above equation can be expressed as,

$$j = \sigma_P E'_\perp - \sigma_H \frac{E' \times B}{B} + \sigma_o E'_\parallel \quad (1.14)$$

where,

$$\sigma_P = \frac{n_e \cdot e}{B} \left(\frac{k_e}{1 + k_e^2} + \frac{k_i}{1 + k_i^2} \right) \quad \text{is the Pederson conductivity,} \quad (1.15)$$

$$\sigma_H = \frac{n_e \cdot e}{B} \left(\frac{k_e}{1 + k_e^2} - \frac{k_i}{1 + k_i^2} \right) \quad \text{is the Hall conductivity, and} \quad (1.16)$$

$$\sigma_o = \frac{n_e e \cdot e}{B} (k_e + k_i) \quad \text{is the Parallel conductivity.} \quad (1.17)$$

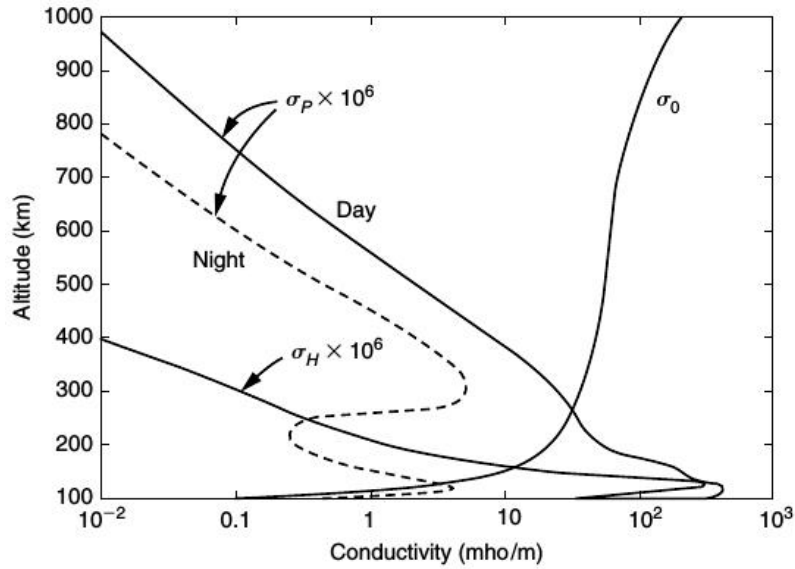


Figure 1.4: Conductivity as a function of altitude for the midlatitude daytime ionosphere [After, *Kelley, 1989*]

The altitudinal profiles of conductivity in the ionosphere is shown in Figure 1.4. As one can see, the parallel conductivity is found to increase with increasing altitude. The high parallel conductivity along magnetic field lines supports the transmission of electric fields to long distances. Accordingly, the stormtime electric fields of solar wind and magnetospheric origin are known to get transmitted to the polar, low and equatorial latitudes along magnetic field lines [*Kikuchi et al., 1978; Kikuchi, 1986*]. The quiet time electric fields from lower latitudes also get mapped along the magnetic field lines to equatorial latitudes [*Farley et al., 1986*]. However, the Pederson conductivity becomes important around 140 km and is determined by the altitude where collision frequency becomes equal to the gyrofrequency. The Hall conductivity which is closely related to the peak in the ionization [*Brekke and Hall, 1988*], dominates around 110 km i.e., in

the E region of the ionosphere and gives rise to significant currents and electric fields. It is clear from the above discussion that the ionospheric currents are produced due to the interaction of the tidal winds with the ionospheric plasma embedded in the Earth's magnetic field. Since the magnetic field over the high, mid and low latitudes have different orientations, the current systems over these latitudes have innate differences. In what follows, the ionospheric current systems at different latitudes have been described.

1.4 Ionospheric current systems at different latitudes

The height integrated current density in the ionosphere is given by,

$$J = \Sigma_P E_{\perp} - \Sigma_H E_{\perp} \times B + \Sigma_{\parallel} (E \cdot \hat{B}) \cdot \hat{B} = J_{\parallel} + J_{\perp} \quad (1.18)$$

where,

J_{\perp} is the height-integrated current density perpendicular to B,
 J_{\parallel} is the height-integrated current density along the magnetic field, and
 $\Sigma_P, \Sigma_H, \Sigma_{\parallel}$ are the height integrated pederson, hall and parallel conductivities respectively.

In an Earth-fixed cartesian coordinate system (x,y,z) where z points vertically downward in the direction of magnetic field, x points in northward direction and y points in the eastward direction, the above equation can be expressed as,

$$\begin{pmatrix} J_x \\ J_y \\ J_z \end{pmatrix} = \begin{pmatrix} \Sigma_P & 0 & 0 \\ 0 & \Sigma_H & 0 \\ 0 & 0 & \Sigma_{\parallel} \end{pmatrix} \begin{pmatrix} E_x \\ E_y \\ E_z \end{pmatrix} \quad (1.19)$$

The magnetic field in this coordinate system is given by,

$$\mathbf{B} = B(\cos I \hat{x} + \sin I \hat{z}) \quad (1.20)$$

where I is the angle of inclination.

The current density is then given by,

$$\begin{pmatrix} J_x \\ J_y \\ J_z \end{pmatrix} = \begin{pmatrix} \Sigma_P \sin^2 I + \Sigma_{\parallel} \cos^2 I & -\Sigma_H \sin I & (\Sigma_{\parallel} - \Sigma_P) \sin I \cos I \\ \Sigma_H \sin I & \Sigma_P & -\Sigma_H \cos I \\ (\Sigma_{\parallel} - \Sigma_P) \sin I \cos I & \Sigma_H \exp I & \Sigma_P \cos^2 I + \Sigma_{\parallel} \sin^2 I \end{pmatrix} \begin{pmatrix} E_x \\ E_y \\ E_z \end{pmatrix} \quad (1.21)$$

The magnetic field is almost vertical at high latitudes and $I \approx 90^\circ$. Therefore,

$$\begin{pmatrix} J_x \\ J_y \\ J_z \end{pmatrix} = \begin{pmatrix} \Sigma_P & -\Sigma_H & 0 \\ \Sigma_H & \Sigma_P & 0 \\ 0 & 0 & \Sigma_{\parallel} \end{pmatrix} \begin{pmatrix} E_x \\ E_y \\ E_z \end{pmatrix} \quad (1.22)$$

At the high latitudes, the currents in the north-south direction are very weak as compared to the currents in the east-west direction [*Coroniti and Kennel, 1972*], hence

$$J_x = \Sigma_P E_x - \Sigma_H E_y = 0 \quad (1.23)$$

which gives,

$$E_x = \frac{\Sigma_H}{\Sigma_P} E_y \quad (1.24)$$

Substituting this in

$$J_y = \Sigma_P E_y + \Sigma_H E_x \quad (1.25)$$

we get,

$$J_y = \left(\Sigma_P + \frac{\Sigma_H^2}{\Sigma_P} \right) E_y = \Sigma_A E_y \quad (1.26)$$

where Σ_A is the auroral electrojet conductance.

This auroral electrojet Σ_A conductance gives rise to the Auroral Electrojet (AEJ) currents. The AEJs are two current sheets that flow at E region altitudes in the auroral oval region [*Baumjohann, 1983; Boström, 1964*]. There is a dawn-side current sheet that flows from noon towards midnight in the westward direction and is known as the auroral Westward Electrojet (WEJ). The magnetic field induced by the westward electrojet currents go upto 500-1000 nT and results in a decrease in the magnetic field at the surface. On the other hand, the dusk-side current that flows from noon to midnight in the eastward direction (known as auroral Eastward Electrojet (EEJ)) leads to an increase in the magnetic field. The total current in both the auroral EEJ and WEJ is of the order of 1 MA [*Baumjohann, 1983*]. The disturbances produced by the auroral EEJ are usually of lesser magnitude than the auroral WEJ.

On the other hand, at the equatorial regions, the angle of inclination is zero ($I = 0$) and magnetic field is in the horizontal direction. Therefore the conductivity becomes,

$$\begin{pmatrix} J_x \\ J_y \\ J_z \end{pmatrix} = \begin{pmatrix} \Sigma_{\parallel} & 0 & 0 \\ 0 & \Sigma_P & -\Sigma_H \\ 0 & \Sigma_H & \Sigma_P \end{pmatrix} \begin{pmatrix} E_x \\ E_y \\ E_z \end{pmatrix} \quad (1.27)$$

The hall conductivity is negligible above and below the E-region of the ionosphere. Hence, vertical currents can be neglected at the equator i.e., $J_z = 0$.

$$E_z = -\frac{\Sigma_H}{\Sigma_P} E_y \quad (1.28)$$

The zonal current is given by,

$$J_y = \Sigma_P E_y - \Sigma_H E_z \quad (1.29)$$

Substituting for E_z in the above equation gives,

$$J_y = \left(\Sigma_P + \frac{\Sigma_H^2}{\Sigma_P} \right) E_y = \Sigma_C E_y \quad \text{is the Equatorial Electrojet current.} \quad (1.30)$$

and

$$\Sigma_C = \Sigma_P + \frac{\Sigma_H^2}{\Sigma_P} \quad \text{is the cowling conductance.} \quad (1.31)$$

The enhanced conductivity Σ_C gives rise to an intense band of currents flowing within $\pm 3^\circ$ latitude on the either side of the dip equator [*Bartels and Johnston*, 1940a, b; *Egedal*, 1947, 1948; *Chapman*, 1948]. These currents, known as the Equatorial Electrojet (EEJ) has a typical noontime current density of the order of 10^{-5} A/m^2 . The AEJ and the EEJ are outcomes of the restrictions $J_x = 0$ and $J_z = 0$, enforced on the flow of current in the ionosphere. In other words, the two current systems, AEJ and EEJ are a result of the anisotropic conductivity resulting from the presence of the geomagnetic field. In the case of the equator, the electric fields that are created to oppose the build up of vertical polarization electric field, forces the currents to flow in the zonal direction and gives rise to the EEJ. On the other hand, the polarisation electric fields created in the north-south direction in the auroral oval forces the currents to flow in the east-west direction and gives rise to the AEJ. These overhead currents produced as a result of the spatial variations of ionospheric conductivities induce fluctuations in the magnetic field measured at the ground [*Egedal*, 1947, 1948; *Chapman*, 1918, 1919, 1948, 1951; *Chapman and Rajarao*, 1965; *Onwumechili*, 1997, 1998]. The systematic study of such magnetic field observations from ground based magnetic observatories brought to light the existence of the global Solar quiet (Sq) current system.

1.5 The Sq (Solar quiet) Current system

Ground-based magnetic field measurements for more than 10 decades now have been used to construct patterns of electrical current in the entire ionosphere that is referred to as the Sq current system. The average Sq current system as observed from the magnetic equator at selected local times is presented in Figure 1.5. These patterns which represent the low and mid latitude current systems were derived using magnetic field measurements from 35 stations located below 60° magnetic latitude [*Matsushita*, 1967]. The most prominent daytime feature is an anticlockwise vortex in the northern hemisphere and a clockwise vortex in the southern hemisphere with maximum/minimum intensities observed at about $+30^\circ\text{N}$ and -30°S latitude respectively.

Since the Sq currents are driven by the dynamo action of the winds that are induced by solar heating, they are strongest during the noontime (12:00 LT) and weakest around the midnight. Over the midlatitudes, the currents poleward of the Sq focus flow

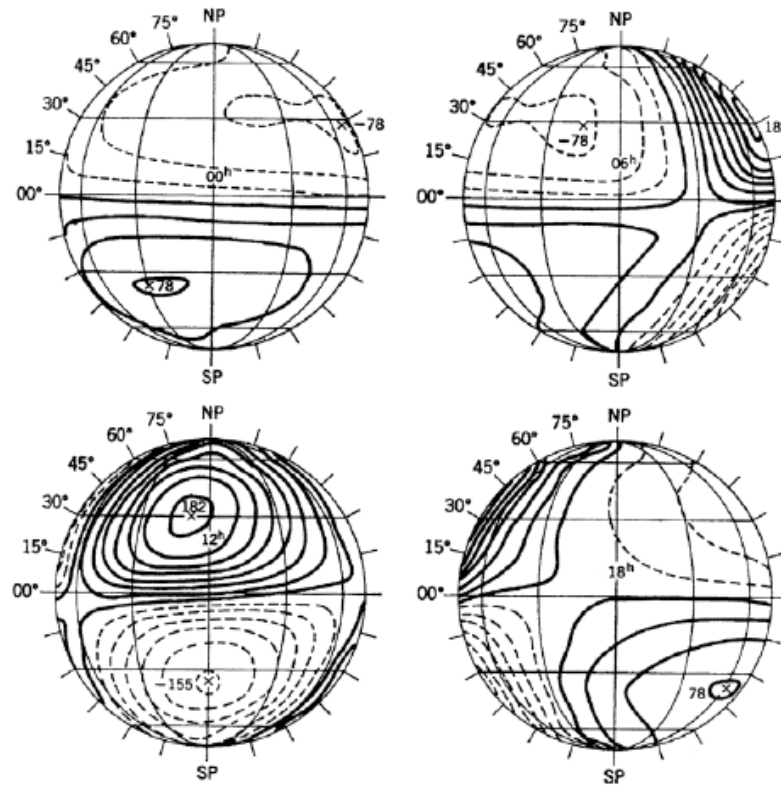


Figure 1.5: Average mean Sq (solar quiet) current systems viewed from the dip equator at the 00:00, 06:00, 12:00, and 18:00 LT meridians. [After, *Matsushita*, 1967]

westward, and the currents equatorward of the Sq focus flow eastward during daytime. However, at latitudes near the dip equator, the two antisymmetric vortices are closer and act to intensify each other. Consequently, the EEJ which is an intense band of current flowing in a narrow belt of $\pm 3^\circ$ latitude is formed. At nighttime, however, the situation is different as the currents are seen to reverse their direction.

Similarly, a Solar quiet polar current system (S_q^p) shown in Figure 1.6, was derived using magnetic field measurements from 13 stations located above 60° N magnetic latitude. Panel (a) and (b) of Figure 1.6 which represents the conditions during summer/winter solstice shows a two-cell convection pattern. The convection flow is in the anticlockwise direction in the dayside and in the clockwise direction in the nightside with a cross-polar cap current flowing across the noon-midnight meridian. The intensity of the current is twice as higher during the summer solstice as compared to the winter solstice primarily because of low ionospheric conductivities in the winter due to absence of ionization. Several experimental and theoretical studies using satellite measurements [e.g., *Burke*, 1984], radar observations [e.g., *Evans et al.*, 1980; *Foster et al.*, 1981; *Foster*, 1983; *Evans et al.*, 1983; *Maynard*, 1974] and models [*Heppner and Maynard*, 1987a; *Heelis et al.*, 1982] have shown similar two cell current patterns in the high latitude ionosphere.

It is believed that the polar cap current systems are formed by the interaction of the polar ionosphere with the IMF and magnetospheric processes rather than by winds

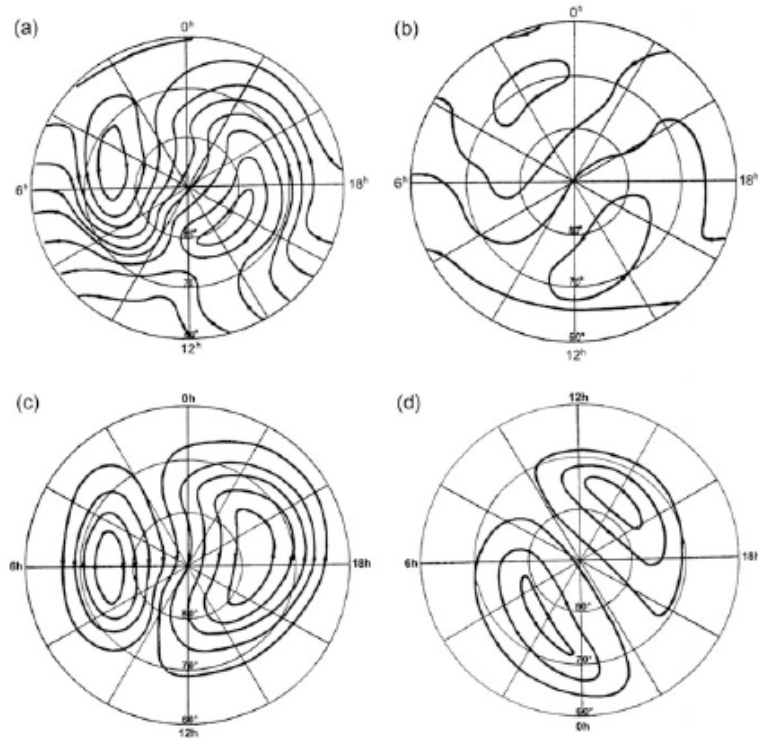


Figure 1.6: Panels (a) and (b) represent the current systems on quiet days in the northern high latitude region during summer and winter solstices respectively. Panels (c) and (d) represents the current systems of additional geomagnetic variation in the northern polar cap, the S_q^p field during the summer and winter solstice conditions. [After, Nagata and Kokubun, 1962; Brekke, 2013]

induced by solar heating like in the case of low and mid latitudes [Brekke, 2013]. The polar cap current systems derived by removing the mid latitude contribution is shown in panel (c) and (d) of Figure 1.6. The polar cap currents system exhibits a typical two cell pattern (the reasons for which is described in the later sections). Evidently, the strength and magnitude of the currents in the polar regions depends on season. It is found that the currents are weaker in the winter polar cap as compared to the summer solstice owing to seasonal changes in ionospheric conductivity and the tilt angle [Beaujardiére *et al.*, 1991].

In any case, the currents generated in the ionosphere are not divergence free if there are conductivity changes in the ionosphere. This gives rise to charge density which, in turn, creates an electric field. This electric field opposes the source of charge separation and forces the divergence to zero. Thus, electric fields are quickly set up in the ionosphere within a time scale of 10^{-6} s [Kelley, 1989]. A brief discussion of the electric fields in the polar, mid, low and equatorial latitudes are presented in the subsequent sections.

1.6 Electric fields in the Polar ionosphere

A schematic diagram of the electric field distribution over the northern polar ionosphere is shown in the left panel of Fig 1.7. As indicated in Fig 1.7, the electric field in the polar cap region is directed from dawn-to-dusk and has a strength of 5 mV/m during typical quiet conditions [Heppner, 1973, and references therein]. This electric field, when combined with the high conductivities, creates strong currents in the polar ionosphere.

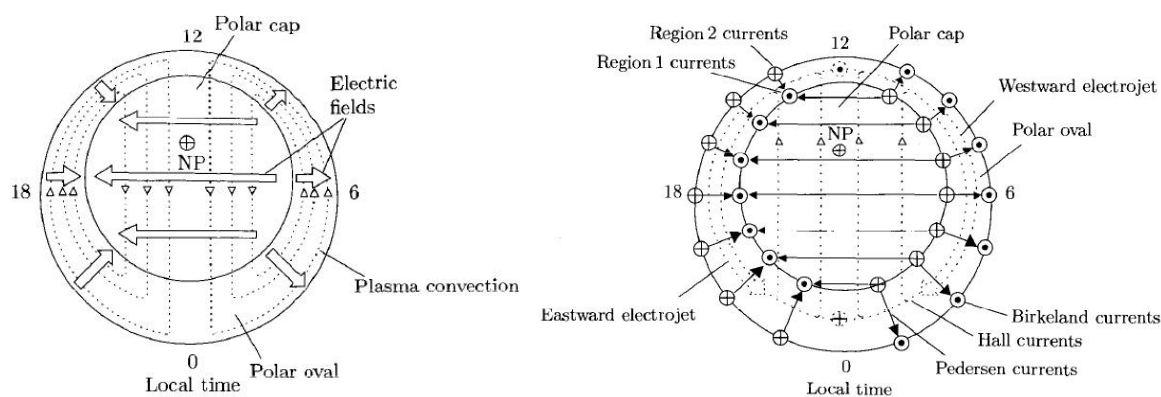


Figure 1.7: Schematic representation of the electric fields and currents in the polar ionosphere is shown in the left and right panels, respectively. NP denotes the north geomagnetic pole. [After, Prölss, 2004]

As the electric field is orthogonal to the magnetic field, the plasma in the F-region experiences an ambipolar $E \times B$ drift. Since this plasma drift is a large scale feature, it is usually referred to as convection [Lyons, 1992; Prölss, 2004]. The plasma convects in the antisunward direction in the polar cap and in the sunward direction in the auroral oval [Knudsen, 1974; Heelis *et al.*, 1982]. The convection velocity depends on the electric field strength which amounts to about 200 m/s in the polar cap and 600 m/s in the auroral oval during quiet times [Roble *et al.*, 1982; Prölss, 2004]. The current, however flows in a direction opposite to that of plasma convection, since the ions drift slower than the electrons. The Hall currents thus trace a two cell pattern with the currents flowing clockwise in the dusk cell and anticlockwise in the dawn cell as indicated by dotted lines in the left panel of Fig 1.7. The integrated intensity of the Hall current amounts to 0.1-1 MA with westward flowing currents (auroral westward electrojet) in the dawn sector and eastward flowing currents (auroral eastward electrojet) in the dusk sector [Richmond and Thayer, 2000]. In the midnight region, where the direction of plasma convection reverses, complex fields and drifts are observed [Harang, 1946; Maynard, 1974; Erickson *et al.*, 1991; Marghitu *et al.*, 2009]. This region was found by Harang while studying the magnetic field perturbations in the polar cap region. Harang [1946] found that a

boundary exists between the positive and negative fluctuations in the magnetic field in the nightside. This region is now known as the Harang discontinuity.

The other important currents in the polar ionosphere are the Birkeland currents (Region 1 Field aligned currents (R1 FACs) and Region 2 Field aligned currents (R2 FACs)) and the Pederson currents. The R1 FACs and R2 FACs have their origin in the Earth's magnetosphere [Eastman *et al.*, 1976; Sato and Iijima, 1979; Schield *et al.*, 1969; Vasylunas, 1984]. These currents flow into the ionosphere at the poleward and equatorward edge of the auroral oval and achieve closure through the Pederson currents flowing in the ionosphere [Baumjohann, 1983]. As illustrated in the right panel of Fig 1.7, the Pederson currents flow in the radial direction in the auroral oval and is connected to the R1 FACs and R2 FACs. The electric field points equatorward in the dawnside of the auroral oval and poleward in the duskward of the auroral oval respectively. The strength of the electric field in the auroral oval during magnetically quiet conditions is found to be about 30 mV/m while that in the subauroral region is less than 5mV/m. The intensity of the Pederson and Birkeland currents both combined amounts to $\simeq 1\text{-}3$ M.A in each half of the auroral oval [Cowley, 2000].

From the above discussions, it is clear that the plasma convection and the electric field distribution in the polar ionosphere are closely coupled to the electric fields and currents in the magnetosphere. The low and equatorial regions are however not affected by the magnetospheric electric fields during quiet times [Vasylunas, 1972; Southwood, 1977]. A description of the quiet time electric field distribution in the mid, low and equatorial ionosphere is presented in the next section.

1.7 Electric fields in the Low and Mid latitude ionosphere

As described in the earlier sections, the origin of the electric fields in the mid and low latitude ionosphere is from the divergence of the electric currents produced by the tidal motions of the neutral atmosphere in the highly conducting ionosphere [Kelley, 1989]. The magnitude of the electric field over a particular station can be deduced from the measurement of the vertical drifts therein as it is the perpendicular electric field that produces a drift of plasma through $E_{\perp} = -V_i \times B$. Calculations show that a primary electric field of 0.5 mV/m in the ionosphere can produce a vertical polarization field of around 10 mV/m with a 400 m/s ($B \sim 0.25$ Gauss) westward drift of electrons. Rocket experiments have shown the largest electric field measured in the ionosphere to be of the order of 9 mV/m corresponding to a drift of 360 m/s. The maximum nighttime zonal drift and maximum vertical electric field (downward) measured over the magnetic equator are about 150 m/s and 4.5 mV/m, respectively.

The seasonally averaged quiettime drifts and electric fields measured using the In-

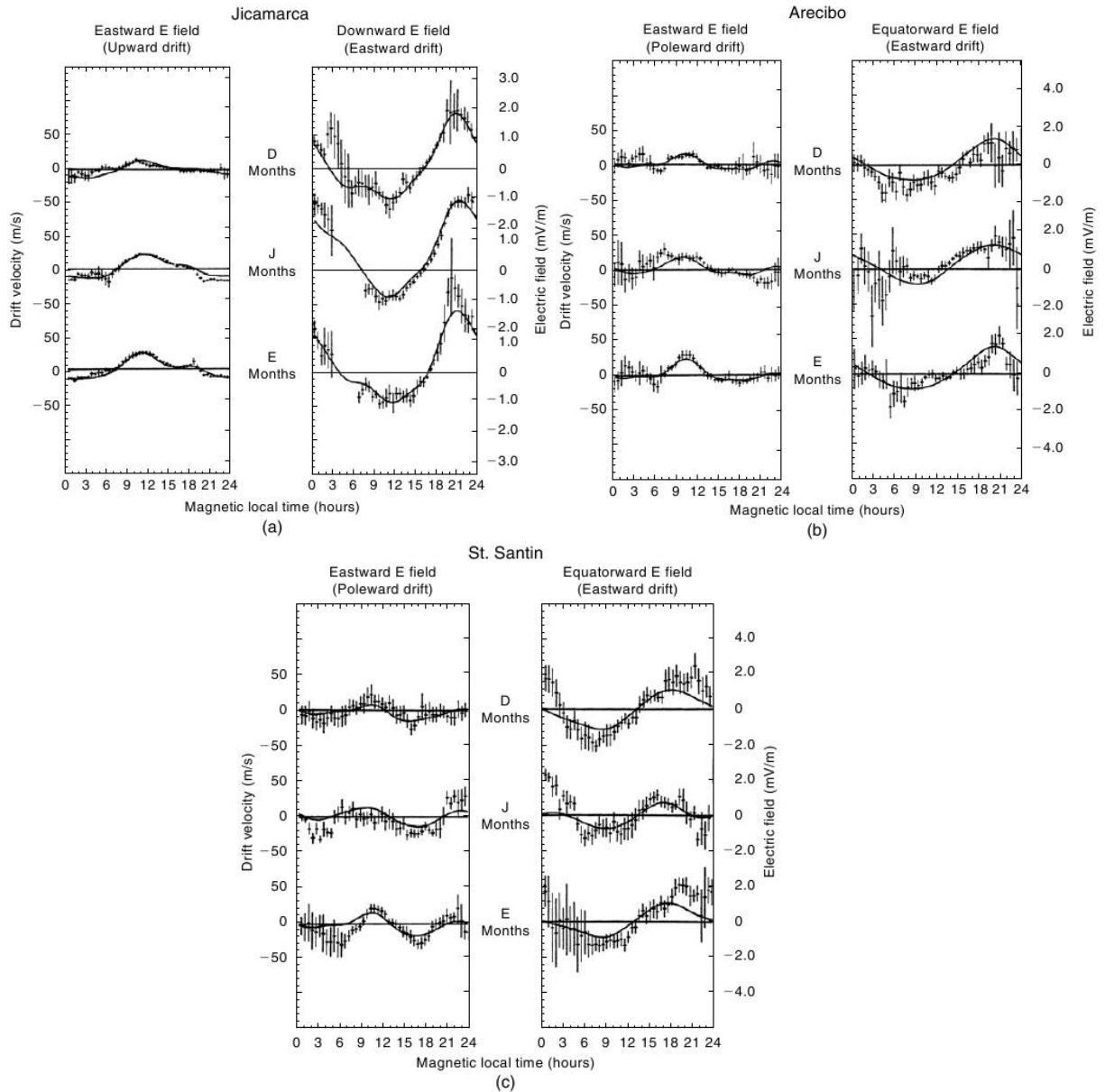


Figure 1.8: Panels (a), (b), (c) show the electric fields and vertical drifts at Jicamarca (dip equator), Arcibo (low latitude) and St. Santin (mid latitude), respectively. [After, Kelley, 1989]

coherent Scatter Radar (ISR) data from three northern hemisphere stations are shown along with model drifts in Figure 1.8. The three stations, Jicamarca, Arcibo and St. Santin represent the dip equator, low latitude and mid latitude stations respectively. The D, J and E months refer to the winter, summer and the equinox period in the northern hemisphere, respectively. The strength of the electric field is shown in the Y-axis. In each panel, the left side corresponds to the zonal eastward electric field component and the right side corresponds to the meridional component. The notable features of the ionospheric plasma drift near the F-region peak are (1) over the magnetic equator, the drifts are upward and westward during daytime and downward and eastward during

nighttime and (2) over the low and mid latitudes, the drifts are poleward and westward during daytime, equatorward and eastward during nighttime. Accordingly, the electric fields are eastward during the day and westward during the night over dip equator. The meridional component of electric field is in the poleward direction during daytime over the low and mid latitudes.

The daytime eastward electric field over the magnetic equator, creates an upward $E \times B$ plasma drift during the day. Just after sunset, the strong electric field over the off-equatorial latitudes maps to the F-region altitudes at the equatorial plane leading to the intensification of the electric field therein. The enhanced electric field at the equatorial latitudes, when combined with the perpendicular magnetic field uplifts the plasma to much higher altitudes. As a result, the plasma from the equatorial region starts to diffuse along the magnetic field lines to the low latitudes in what is known as the fountain effect [*Hanson and Moffett, 1966*]. Consequently, the electron density of the F-region peak at the dip equator becomes lower than that observed at the low latitudes. This phenomena, also known as the Equatorial Ionization Anomaly (EIA) plays an important role in the redistribution of the plasma density over the equatorial and low latitude ionosphere [*Rastogi, 1959; Anderson, 1973a; Walker, 1981; Tulasiram et al., 2009*]. Experimental and theoretical studies of the quiet time features of the EIA provides an overall understanding of the solar cycle, seasonal and longitudinal dependencies of the fountain effect [*Hanson and Moffett, 1966; Bramley and Peart, 1965a; Anderson, 1973b; Martyn, 1947; Rush and Richmond, 1973; Huang and Cheng, 1996; Liu et al., 2007*] whereas its behaviour during the magnetically disturbed times still needs clarity [*Fejer and Emmert, 2003; Balan et al., 2013; Horvath and Lovell, 2014; Shreedevi et al., 2016; Smitha et al., 2016*].

During magnetically disturbed times, the high latitude currents and electric fields strengthen and during this process, not only local but global changes are observed in the Ionosphere-Thermosphere (I-T) system [*Prölss, 1995*]. The behaviour of the ionospheric system at all latitudes is determined primarily by the spatial and temporal changes in electric fields, currents, intensity of particle precipitation and associated phenomena prevalent during stormtime [*Richmond and Lu, 2000*]. The plasma distribution over the mid, low and equatorial ionosphere deviates significantly due to the direct penetration of the electric field of magnetospheric origin as well as the gradual changes initiated at the polar regions [*Shreedevi et al., 2016*]. The absorption and dissipation of solar wind energy into the magnetosphere and the related changes in the Earth's I-T system during disturbed periods is discussed in detail in the subsequent sections.

1.8 Dissipation of solarwind energy in the Earth's M-I system

The Sun continuously emits energy into space in the form of electromagnetic radiation and energetic particles. The charged atoms and sub-atomic particles, embedded in the Sun's magnetic field, flow out radially in what is called as the solar wind. The solar wind flows into the interplanetary space and forms a part of the interplanetary medium. The Earth is hence immersed in the magnetic field of the Sun and continuously interacts with the hot magnetized supersonic collisionless plasma that the solar magnetic field contains. Occasionally, during the active phase of the Sun, charged particles of high energy and high velocity, are expelled from the Sun's atmosphere into the space along with the solar magnetic field. The interaction of these with the geomagnetic field leads to the transfer of energy and momentum into the Earth's magnetosphere and thereby into the terrestrial atmosphere [Kivelson and Russell, 1995; Prölss, 1995, 2004]. It is estimated that a potential difference of the order of 30,000 Volts can be generated across the Earth's magnetosphere depending on the direction of the Sun's magnetic field and the solar wind velocity [Kelley, 1989]. Only a fraction of this energy gets transferred into the Earth's atmosphere during the Solar Wind-Magnetosphere-Ionosphere (SWMI) interaction, which itself can be of serious implications for Earth's space weather. In the following, a brief description of the SWMI coupling processes is presented.

1.8.1 Solarwind-Magnetosphere-Ionosphere (SWMI) coupling

The transfer of solar wind energy and momentum into the Earth's atmosphere is basically controlled by the IMF [Dungey, 1961; Gonzalez *et al.*, 1989; Rostoker and Falthammar, 1967]. Reconnection of geomagnetic field with the IMF is possible when the IMF is southward in direction. When this happens, the kinetic energy of the solar wind particles is converted into electrical energy in what is similar to the action of a dynamo. In the case of a solar wind dynamo, the conducting plasma in the solar wind flows across the geomagnetic field and induces the convection electric field [Prölss, 2004]. A schematic illustration of the operation of the solar wind dynamo is presented in Fig 1.9. As the solar wind particles enter the Earth's magnetosphere, the protons are deflected towards the dawn side and the electrons are deflected towards the dusk side. Since, the ionosphere is a conducting medium, the charges flow into the ionosphere and complete the electrical circuit. The ions flow along the magnetic field lines into the polar cap ionosphere in the dawn side causing a downward current into the ionosphere. The electrons in the dusk side flow into the polar cap and create an upward current. These currents (J_b) known as the R1 FACs [Iijima and Potemra, 1978], achieve closure through the Pederson currents flowing across the polar cap as illustrated in Fig 1.7. The polarisation electric field created due to the ensuing charge separation is called the

magnetosphere from the convection electric field. Meanwhile, the presence of the excess charges give rise to a current directed into the ionosphere in the duskside region and away from the ionosphere in the dawnside region. These currents correspond to the R2 FACs shown in Fig 1.7. The associated electric field when mapped along the magnetic field lines will reach the subauroral latitudes and will be in the poleward direction at ionospheric altitudes [Yeh *et al.*, 1991; Foster and Burch, 2002]. This poleward electric field when combined with the vertical magnetic field acts to transports the plasma from subauroral latitudes towards the noontime region [Yeh *et al.*, 1991; Foster, 1993, 2008; Foster and Burch, 2002]. Hence it is known as the Subauroral Polarisation Streams (SAPS) electric field.

To summarise, when the IMF is southward in direction, strong electric fields and Field aligned currents (FACs) are generated in the magnetosphere. The FACs appear in two pairs (R1 FACs and R2 FACs), one pair extending from the noon through the dusk sector to the midnight sector and the other pair extending from the noon through the dawn sector to the midnight sector. Region 1 current sheet is located on the high poleward boundary of the auroral zone and the region 2 current sheet is flows into the equatorward boundary of the auroral zone. These magnetospheric current systems achieve closure through the Pederson currents in the auroral ionosphere. The FACs flowing into the polar ionosphere gives rise to several interesting phenomena including the creation of the aurora and heating of the thermosphere. Basically, the energization of the polar ionosphere begins with the dayside reconnection of magnetic field lines and continues throughout what is known as the “Geomagnetic Storm ”. The impact of geomagnetic storms on the Earth’s upper atmosphere is discussed in the subsequent sections.

1.8.2 Geomagnetic storms

A geomagnetic storm can be defined as the time interval during which a sufficiently intense and long-lasting interplanetary convection electric field leads, through a substantial energization in the Magnetosphere-Ionosphere (M-I) system, to an intensified ring current sufficiently strong to exceed some key threshold for quantifying the storm time index [Gonzalez *et al.*, 1994]. The primary cause of geomagnetic storms at the Earth is the generation of the strong convection electric field (dawn-to-dusk) as a result of the solarwind-magnetosphere interaction. The most important and inevitable feature of geomagnetic storms is the large fluctuations in the geomagnetic field [Chapman and Bartels, 1940].

A typical geomagnetic storm has three phases namely, the Storm Sudden Commencement (SSC), the main phase and the recovery phase. The variation of magnetic field at the dip equatorial station, Trivandrum on a storm day, is shown in Figure 1.10 along with its various phases. The beginning of a geomagnetic storm is usually marked by

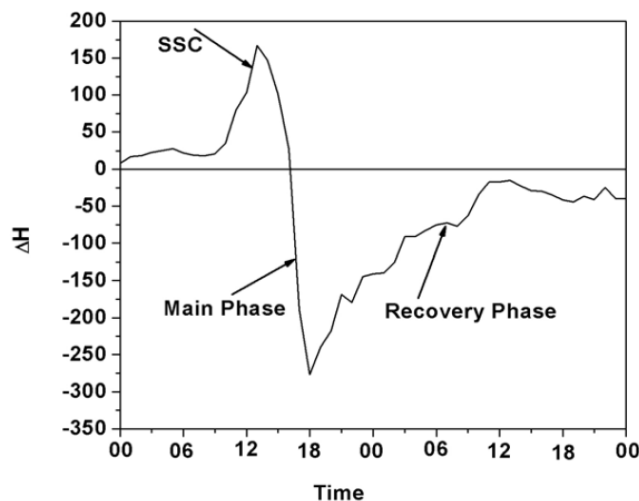


Figure 1.10: The variation of geomagnetic field during a typical storm.

the sudden increase in the horizontal component of geomagnetic field as indicated in Figure 1.10. The sudden compression of the dayside magnetopause by the fast moving solar wind results in an enhancement of the horizontal component of geomagnetic field [Kivelson and Russell, 1995]. This enhancement known as the SSC lasts for a very short while (~ 1 -6 minutes). The main phase of the storm follows the SSC and is marked by a decrease in the H component of magnetic field. Such a decrease in the H component of magnetic field is a result of the development of the ring current. The ring current which is in the westward direction produces a magnetic field that is directed opposite to the Earth's magnetic field [Ebihara and Miyoshi, 2010]. This leads to the reduction of the horizontal component of magnetic field over the surface as indicated in Figure 1.10. The time of maximum depression in the H component corresponds to the maximum intensity of the ring current indicating significant energy transfer during that time [Dessler and Parker, 1959; Schopke, 1966]. Hence the most important characteristic of a geomagnetic storm is the decrease in the horizontal intensity of magnetic field [Chapman and Bartels, 1940]. Later, as the reconnection ceases, the ring current starts to degrade. Hence a recovery of magnetic field strength is seen during what is known as the recovery phase.

The intensity of a geomagnetic storm can be considered to be an indication to the level of disturbance of other geospace phenomena. A useful index in quantifying the intensity of geomagnetic storm is the Disturbance Storm Time (Dst). Based on the Dst index, the storms can be classified as weak (-30 nT), moderate (-50 nT), intense (-100 nT), severe (-200 nT) and super storms (-300 nT) [Gonzalez and Tsurutani, 1987]. Depending on the intensity of the storm, the effects of the geomagnetic storm as observed in the Earth's I-T system lasts for hours to days [Prölss, 1995]. As a result, the global structure and the dynamics of the ionospheric system is greatly modified by the geomagnetic storms. A description of these effects known as ionospheric storms is presented in the following section.

1.8.3 Ionospheric storms

A hierarchy of processes are triggered in the ionosphere-thermosphere system during geomagnetic storms resulting in either an increase or decrease in the electron density of the ionosphere. Such global perturbation of the ionosphere caused by the dissipation of the solar wind energy is known as “Ionospheric storms” [Prölss, 2004]. Ionospheric storms were first discovered by Hafstad and Tuve in 1929. The generation of ionospheric storms is associated with various fascinating phenomena like for e.g., auroral particle precipitation, joule heating, prompt penetration of electric fields etc., all occurring under magnetically disturbed conditions [Rishbeth and Garriott, 1969; Ratcliffe, 1972; Rees, 1989; Kelley, 1989; Hargreaves, 1992]. Despite several years of efforts, understanding the various aspects of these processes has been a challenging task and that is why even today ionospheric storms remain a topic of interest. As described in earlier sections, during magnetically disturbed times, a large amount of energy is dissipated into the ionosphere-thermosphere system. One of the consequences of the excess energy input is the heating up and expansion of the high latitude atmosphere. In the events that follow, the thermosphere expands, its composition gets altered, Travelling Atmospheric Disturbances (TADs) are generated and ionospheric plasma gets redistributed [Prölss, 1995]. The ionospheric plasma over the mid and low latitudes is also modified by the stormtime electric fields originated through SWMI coupling or storm induced thermospheric circulation [Blanc and Richmond, 1980; Buonsanto, 1999; Prölss, 1995]. These processes result in either an increase or decrease in the ionospheric electron density and are known as positive/negative ionospheric storms [Rishbeth and Garriott, 1969; Buonsanto, 1999; Prölss, 2004]. In the following sections, the stormtime changes in the global circulation and electric field that give rise to ionospheric storms are discussed.

1.8.3.1 Changes in global circulation and composition

During geomagnetic storms, energy in the form of particle precipitation and currents arrive at the polar upper atmosphere and cause significant heating [Richmond and Lu, 2000; Fuller-Rowell et al., 2002]. Enhanced joule heating of the polar atmosphere during storms leads to upwelling of air which is rich in molecular species (like N_2 and O_2). Hence, a composition bulge is established at the high latitudes with an increase in molecular mass at the higher altitudes [Prölss, 1980; Prölss et al., 1988; Prölss, 1991]. Since the loss rates are directly proportional to the density of molecular species, the increase in molecular mass leads to an increase in loss rates. This means that recombination is enhanced at F-region altitudes as a result of which there will be a decrease in the electron density (Negative ionospheric storm) [Buonsanto, 1999; Prölss, 1995].

The strong horizontal winds set up by joule heating flow equatorward in both the hemispheres [Field et al., 1992; Richmond and Lu, 2000]. Since the magnetic field lines are inclined at the mid latitudes, the strong equatorward winds push the ionization up to

higher altitudes along the magnetic field lines [Prölss, 1978, 1993a]. As recombination is less at higher altitudes, this also gives rise to an increase in the electron density (positive ionospheric storm). These storm induced meridional winds are strong enough to reverse the usual daytime poleward winds blowing from the summer to winter hemisphere [Fuller-Rowell *et al.*, 1994, 1996, 2002; Field *et al.*, 1998]. Accordingly, the global circulation cell is disturbed and composition changes are transported.

The storm induced equatorward meridional winds which carry the composition bulge converges at some latitude depending on the background winds. Such converging air downwells, usually, at the mid or low latitudes depending on the strength of the background winds. During daytime, as they blow in the opposite direction, downwelling happens at a point where the background poleward winds are balanced by the storm induced equatorward. But, at night, they move in the same direction and hence downwelling happens farther at lower latitudes. The downwelling brings in atomic rich air to lower regions of the ionosphere resulting in a decrease of mean molecular mass therein. The decrease in molecular mass leads to a decrease in loss rates and thereby an increase in the electron density (positive ionospheric storm) [Buonsanto, 1999]. Thus, the composition changes are not only limited to the polar regions and are observed even at the mid and low latitudes [Fuller-Rowell *et al.*, 1994].

1.8.3.2 Travelling Atmospheric disturbances (TADs)

Observations have shown that the generation of positive ionospheric storm at the mid latitudes can happen through the raising of the F-layer either by storm induced meridional winds or TADs [Prölss, 1978, 1993a, 1995]. The TADs are wave-like structures formed by the superposition of a broad spectrum of gravity waves generated as a result of the impulsive heating of the polar atmosphere during magnetic disturbances [Richmond and Matsushita, 1975; Millward *et al.*, 1993; Fuller-Rowell *et al.*, 1994; Prölss, 2004]. These are known to propagate equatorward with high velocity (700 m/s) from their source region and while doing so they also carry the equatorward winds of moderate velocity (150 m/s). They are known to uplift the plasma to higher altitudes as they propagate equatorward [Prölss, 1978; Roble *et al.*, 1978; Prölss, 1993a, b]. Changes in the F-region peak height (hmF2) and F-region peak density (NmF2) over the mid and low latitudes during geomagnetic storms give clear signatures for the presence of TADs [Prölss, 1995]. Since the TADs uplift the plasma to altitudes where recombination is low, it leads to an increase in the plasma density (positive ionospheric storm) during daytime. At nighttime, since the background ionization density is already low, one may not find a significant enhancement in plasma density. However, TAD associated changes are usually shortlived and are observable irrespective of the local time as they propagate all over the globe from their source region. Although, several studies involving experiments and calculations have substantiated the role of TADs in giving rise to ionospheric storms

over the mid and low latitudes [Evans, 1970a; Roble et al., 1978; Buonsanto et al., 1990], the direct verification of the TAD hypothesis is still lacking due to limited observations. Nevertheless, it has been hard to delineate the contribution of TADs from that of storm induced meridional winds in causing ionospheric disturbances at mid latitudes. The role of TADs in modulating the electric field distribution is not known too.

1.8.3.3 Storm time electric fields

While the ionospheric response to the changes in global circulation induced by joule heating and associated phenomena occur gradually, the immediate changes in the ionosphere observed during geomagnetic storms are primarily caused by the action of stormtime electric fields [Sastri et al., 1995; Fejer and Scherliess, 1995; Maynard et al., 1998]. It is fairly known that during magnetically quiet times, the convection electric field does not penetrate into the low and equatorial latitudes as it is shielded by the electric fields associated with the ring current [Vasyliunas, 1972]. However, during stormtime, the enhanced convection electric field penetrates instantaneously to the low and equatorial latitudes because the shielding electric field associated with the ring current takes at least 30 minutes to build up. The Earth's ionosphere acts as a waveguide and transmits the polar electric field as TM_o mode waves to the low and equatorial latitudes [Araki, 1977; Kikuchi et al., 1978; Kikuchi and Araki, 1979]. This electric field, known as the undershielding electric or Prompt Penetration Electric field (PPEF) is in the eastward direction during daytime [Nishida et al., 1966; Gonzales et al., 1983; Kikuchi et al., 1978, 1996] and when combined with the daytime ionospheric electric field leads to enhanced vertical drifts. As a result, at the low latitudes, a positive ionospheric storm occurs due to the action of PPEF which is eastward during daytime [Maruyama et al., 2004] and a negative ionospheric storm which appears as the PPEF has a westward polarity during nighttime [Abdu et al., 2005]. The occurrence of positive/negative ionospheric storm caused by the action of the PPEF also depends on the background conditions in the ionosphere [Shreedevi et al., 2016]. The upliftment of plasma to higher altitudes may or may not enhance the fountain effect depending on the strength of the convection electric field and the vertical drift it causes [Sastri et al., 2003].

As the geomagnetic storm progresses, enhanced magnetospheric convection brings more plasma into the nightside region of the magnetosphere leading to the generation of a strong ring current [Ebihara and Miyoshi, 2010]. As a result, the shielding electric field associated with the ring current strengthens. This westward (dusk-to-dawn) electric field penetrates into the subauroral latitudes and shields the low and equatorial latitudes from the prompt penetration of convection electric field [Kelley et al., 1979; Fejer et al., 1979]. However, when the IMF becomes northward, the convection electric field weakens. Under such conditions, this shielding electric field associated with the ring current itself

gets transmitted to the low and equatorial latitudes. This is known as the overshielding condition because the ring current associated westward electric field overshields the convection electric field in this case [Wolf, 1983]. The overshielding electric field is westward in direction during daytime and leads to a Counter Electrojet (CEJ) condition at the equatorial latitudes [Kelley et al., 1979; Huang et al., 2005]. The westward electric field acts opposite to the daytime ionospheric electric field which is in the eastward direction and may lead to a lowering of the F-region of the ionosphere. Consequently, the fountain effect is known to weaken resulting in a depletion in electron density over the low latitudes [Abdu et al., 1991]. In this case, a positive ionospheric storm appears if the F-region is not pushed to altitudes low enough for loss processes to become dominant [Shreedevi et al., 2016]. In contrast, a negative ionospheric storm appears over the dip equator if the overshielding electric field is strong enough to drive the F-region to very low altitudes [Shreedevi et al., 2016]. In any case, under the action of the PPEF or overshielding electric field, the EIA and hence the plasma distribution over the low latitudes gets significantly modulated [Abdu et al., 1991; Sastri et al., 2003]. The EIA is known to respond to the changes in the zonal electric field within about 1-2 hours [Stolle et al., 2008].

There is also a delayed disturbance dynamo effect observed at the low and equatorial latitudes during geomagnetic storms. The Disturbance Dynamo (DD) is driven by the storm induced winds in the polar upper atmosphere [Blanc and Richmond, 1980]. When the storm induced equatorward meridional winds reach the mid latitudes, they are deflected westwards due to the action of the coriolis force. An equatorward Pederson current is generated as the wind induced westward zonal flow combines with the magnetic field in the downward direction. In order to balance this current flow, an electric field is generated in the poleward direction. Consequently, an eastward Hall current and a poleward Pederson current arises in the ionosphere at the mid latitudes. The Hall current generated by this mechanism is located at around 45° magnetic latitude in a wide strip of 20° and are interrupted at the dawn and dusk terminators. These currents achieve closure by flowing through the highly conducting ionosphere in the adjacent latitudes and is followed by the formation of two separate current vortices namely, an equatorial vortex via low latitudes and a polar vortex via the high latitudes. Thus an anti-Sq current system is formed with a westward electric field at the equatorial latitudes [Blanc and Richmond, 1980; Richmond and Roble, 1997]. Studies have shown that, a few hours are required for the disturbance winds and Disturbance Dynamo Electric field (DDEF) to set up, after the SSC [Blanc and Richmond, 1980; Fejer, 1997; Sastri, 1988]. Once set up, they can persist for many hours [Huang, 2013; Fuller-Rowell et al., 1994]. Short lived DD effects over the nighttime equatorial F-region with a time delay of 4 hours or even less have also been shown by Kakad et al. [2011].

Over low latitudes, the DD effects are seen prominently in the zonal and vertical

drifts during afternoon and nighttime [Fejer and Emmert, 2003] and not during the morning-noon hours. In one of the recent studies by Tulasiram *et al.* [2015], the duskside enhancement of equatorial electric field was shown to be in response to the eastward PPEF despite the existence of background westward disturbance dynamo electric field DDEF. Many times, it is seen that although DD currents develop in the daytime, the resulting dynamo electric fields are shorted out by the large E-region conductivities [Huang, 2013]. However, model simulations have shown that DD tends to reduce the daytime upward drifts [Maruyama *et al.*, 2005]. Hence the effect of the daytime westward DDEF on the ionosphere is a reduction in electron density [Tsurutani *et al.*, 2004], while because of the eastward nature of DDEF during nighttime, there might be an increase in electron density at nighttime depending on the prevailing conditions [Fuller-Rowell *et al.*, 2002]. The electric fields originated through the dynamo action of the disturbance winds cause long lasting effects on the ionosphere over low and equatorial latitudes Fejer *et al.* [2005]. It is to be noted that the intensity of the DD electric field is highly dependent on the conditions in the high latitude ionosphere [Huang, 2013; Fejer *et al.*, 2005].

It is the large changes in the high latitude ionosphere brought about by the impact of geomagnetic storms that determines the global structure of the I-T system. The intense electric fields in the polar ionosphere cause enhanced plasma convection which allows for the exchange of energy and momentum among the neutral and ionized species of the polar upper atmosphere. This leads to electrodynamic heating of the polar atmosphere which in turn causes thermospheric expansion and large vertical flows [Yeh and Foster, 1990; Moffett *et al.*, 1992; Smith, 1998a]. Consequently, there will be an increase in the mean molecular mass of the thermosphere and an increase in the loss rates and by that means a negative ionospheric storm [Prölss, 1995]. This depletion in electron density is further amplified by the strong electric fields as they affect the ion reaction rates at high temperature (the reaction rate constants vary as the fourth power of electric field strength) [St-Maurice and Torr, 1978; Rodger *et al.*, 1992]. However, when a geomagnetic storm is in progress, significant amounts of ionization may also be found in the polar cap region even during the winter time [Foster, 2008; Prölss, 1995].

The positive ionospheric storms observed over the high latitudes are also caused by stormtime electric fields. As described in the previous sections, plasma convection in the high latitude ionosphere follows the two cell convection pattern with sunward directed plasma flow in the auroral regions which reach the noontime cusp and flow across the polar cap towards the nightside region in antisunward direction. When the IMF is southward, i.e., when dayside reconnection happens, more closed field lines are converted to open ones causing polar cap to expand and the auroral oval to shift equatorward to the then subauroral latitudes causing the expansion of the convection cell [Lyons, 1992; Kivelson and Russell, 1995]. During this time the equatorward edge of the auroral oval will be at much lower latitudes farther beyond the composition disturbance zone. The

high density ionospheric plasma at these latitudes are carried towards the noontime cusp and into the polar cap under the action of enhanced stormtime electric fields. Such a channel of high density plasma convecting in the sunward direction towards the noon sector is called as Tongue Of Ionization (TOI) [Foster, 1993, 2008]. The extension of the convection electric field to mid latitudes and the formation of the polar TOI has been substantiated through several experimental and theoretical studies [Prölss, 1995; Foster, 2008; Thomas *et al.*, 2013].

The energy received at the high latitudes in the form of electric field, currents and energetic particle precipitation, during stormtime play a very important role in determining the global structure of not only the I-T system, but also the magnetospheric configuration too [Ridley *et al.*, 2004; Lotko, 2007; Amm *et al.*, 2008; Yu *et al.*, 2015, and references therein]. The closing of the R1 FACs through the high latitude ionosphere enables the occurrence of magnetospheric convection and the penetration of convection electric field into the ionosphere [Kivelson and Russell, 1995]. Similarly, the presence of the conducting ionosphere diminishes the build up of ring current density in the inner magnetosphere by allowing the R2 FACs to flow into the ionosphere, and the penetration of the undershielding electric field into the mid latitudes [Ebihara and Miyoshi, 2010]. Many experimental and theoretical studies in the past have described the influence of the magnetosphere in controlling the ionospheric electrodynamics [Ebihara and Miyoshi, 2010; Lotko, 2007; Akasofu and Chapman, 1964, and references therein]. However, only a very few studies in the past have attempted to quantify the role of ionospheric conductivity in regulating the behaviour of the magnetosphere during stormtime. Understanding the role of ionospheric conductivity in controlling the stormtime magnetospheric phenomena is one of the objectives of the present thesis (Chapter 6). The role played by ionospheric conductivity is of importance to the global ionosphere too as it restricts the magnetospheric convection to the high latitudes only and shields the mid and low latitude ionosphere from the direct impact of solar wind energy.

In general, the occurrence of positive/negative ionospheric storms over the low latitudes is attributed to either the PPEF or the DDEF [Shreedevi *et al.*, 2016; Smitha *et al.*, 2016]. A number of studies using observations, models and case studies describe the effects of disturbance electric fields on the mid and low latitude ionosphere in detail [Mannucci *et al.*, 2005; Rishbeth *et al.*, 1987; Mendillo, 2006; Abdu *et al.*, 2005; Sastri *et al.*, 2003]. Similarly, a large number of studies have also documented the role of neutral winds and composition disturbances in generating positive/negative ionospheric storm over the high and mid latitudes [Immel *et al.*, 2001; Prölss, 1976; Rishbeth *et al.*, 1987; Roble *et al.*, 1977; Burns *et al.*, 1995]. In most of these studies, the effects of PPEF on the low latitude ionospheric system is inferred using IMF B_z or IEF $_y$ data, which has clear signatures in ground magnetic field data [Kelley *et al.*, 1979; Fejer *et al.*, 1979; Huang *et al.*, 2005; Simi *et al.*, 2012; Shreedevi *et al.*, 2016]. On the contrary,

the identification of DD electric field is mostly based on inferences from the ionospheric observations and modeling [*Sastri*, 1988; *Fejer et al.*, 2008; *Huang*, 2013]. As a result, the evidences for DD electric fields over the low latitude region are sparse, especially during daytime. *Sastri* [1988] have even shown that some geomagnetic storms do not generate detectable patterns of equatorial DD electric fields for the entire day. Apart from this, it is always difficult to delineate the DD effects from the compositional disturbances based on ionospheric observations (like Global Positioning System (GPS) based diurnal variation of Total Electron Content (TEC)) alone. Similarly, the relative contributions of stormtime electric fields (PPEF and DDEF) and composition changes in causing the positive/negative ionospheric storms is not clear. In the Chapter 5 of this doctoral thesis, an attempt has been made to understand the relative role of stormtime electrodynamic forcing over chemistry (composition changes) in the latitudinal evolution of ionospheric storms.

1.9 Objective of the thesis

As described in the previous sections, the action of both, the storm time electric fields and neutral winds cause redistribution of plasma and associated irregularities in the high, mid and low latitude ionosphere during geomagnetic storms. It is the solar wind-magnetosphere coupling that primarily generates the strong dawn-to-dusk electric fields which initiates the disturbance at the polar ionosphere. The electrodynamic coupling of the high-to-low latitude ionosphere facilitates the instantaneous penetration of the dawn-to-dusk electric field to the lower latitudes. Also, the impact of the energetic particles of solar wind origin that directly enter the polar atmosphere gives rise to enhanced conductivities which combined with strong electric fields give rise to substantial electric currents and strong joule heating of the atmosphere. This inturn modulates the global thermospheric circulation and gives rise to the disturbance dynamo which also affects the low latitude ionospheric system. Such large departures in the electrodynamic and neutral dynamics of the I-T system during magnetically disturbed periods cause irregularities in plasma behaviour thereby affecting the Earth's space weather. The study of the space weather events therefore demands much attention in the current scenario.

Despite the continued efforts for decades, a comprehensive understanding of the behaviour of the I-T system during quiet as well as disturbed times is far from complete mainly due to the lack of simultaneous coordinated observations from the equatorial, low and polar regions. For eg., little is known regarding the variabilities of the southern polar ionosphere while most of the knowledge of the stormtime behaviour of the polar ionosphere comes from studies done using measurements from the northern hemisphere. This is because a large data set of ionospheric parameters from the northern polar regions are available while the southern polar region is difficult to access. Notwithstanding the

fact that the southern polar region is least explored compared to its northern counterpart, the degree of response of the polar regions of the Earth to the space weather events like geomagnetic storms, may differ even if the driving mechanisms are the same. This could be partly due to its dependence on factors like the season, time of day etc., or the offset between the geographic and geomagnetic poles which is large in the southern hemisphere. Consequently, the polar regions may exhibit different behaviour during space weather events which also affects the equatorial, low and mid latitudes that are electro-dynamically and neutral dynamically coupled to the polar regions. To mention, a few of the least explored aspects in this direction are, the quiet and disturbed time behaviour of the southern polar ionosphere, its role in controlling the magnetospheric dynamics, and the relative contributions of the stormtime electric fields and composition changes in altering the plasma distribution over the mid and low and equatorial regions. In this doctoral thesis, an attempt is made to address the aforementioned aspects with the help of simultaneous space and ground based observations from equatorial, low, mid and the polar region lying in the 76-78°E meridian.

1.10 Outline of the thesis

The entire work carried out in this thesis has been organized into seven chapters, the brief description of which is presented below:

The first chapter provides an introduction to the already existing information about the quiet and disturbed time behaviour of the Earth's magnetosphere and the ionosphere. The contributions from various experimental and theoretical studies in understanding the impact of geomagnetic storms on the geospace has also been described. The data necessary for this study has been collected from various instruments. The experimental techniques and details of the instrumentation is provided in Chapter 2.

Understanding the quiet time variations of the ionosphere over the high mid, low and equatorial latitudes is a prerequisite to understanding the disturbed time variations therein. Hence, Chapter 3 describes the quiet time variations in integrated electron density over the high latitude Bharti, mid latitude station, Hanle and the dip equatorial station Trivandrum all lying in the 76-78°E meridian. The diurnal, seasonal and solar activity dependence of integrated electron density over these three stations have been studied in detail and compared with the predictions from the International Reference Ionosphere (IRI) model.

The fourth chapter focusses on understanding the behaviour of the southern polar ionosphere during geomagnetic storms. The St.Patrick's day storms of 2013 and 2015 provided a unique opportunity to understand how the polar ionosphere responds to geomagnetic disturbances of different intensities occurring at the same time, same season, and similar conditions on the Sun and the Earth. The morphology of stormtime TEC variation over Bharti has also been investigated to obtain a comprehensive understanding

of the behaviour of plasma over the southern polar station and the processes that modulate it.

Various aspects of the coupling between the high-mid-low and equatorial latitudes is investigated in the fifth chapter. Three case studies have been presented to understand the electrodynamical and neutral dynamical coupling of the high, mid and low latitude ionosphere during geomagnetic storms. The relative contributions of the disturbance electric fields (PPEF and DDEF) and the composition disturbances in altering the ionospheric system also has been studied in this chapter to get an overall understanding of the evolution of positive/negative ionospheric storms over the high, mid and low latitudes during magnetically disturbed periods.

The sixth chapter examines the influence of ionospheric conductivity on the magnetospheric dynamics. A case study of the St.Patrick's day storm of 2013 was performed using the Space Weather Modelling Framework (SWMF) which is an unified self-consistent model that allows for a comprehensive investigation of the processes happening in the global magnetosphere, inner magnetosphere and the ionosphere during a geomagnetic storm event. This work highlights the role of global conductance patterns in modulating the dynamic M-I system. A summary of the major scientific outcomes and the future scope of the present doctoral thesis work is presented in the seventh chapter.

Chapter 2

Experimental Techniques

2.1 Introduction

In the last chapter we discussed how the Earth's space weather is controlled by the highly complex solar driven Magnetosphere-Ionosphere (M-I) system. The stormtime energy input gives rise to several phenomena of importance to both the neutral as well as ionized component of the atmosphere and significantly modifies almost all the ionospheric parameters. Examining the ionospheric parameters thus becomes essential in understanding the complex phenomena involved in modifying the structure of the ionosphere during geomagnetic storms. This calls for the measurement of various ionospheric parameters using multiple techniques from several vantage points.

One such important parameter is the Total Electron Content (TEC) of the ionosphere which is the number of electrons in a column of unit cross-section along the satellite ray path. The ionospheric contribution to TEC mainly comes from the F_2 -region of the ionosphere. The F_2 -region has the maximum electron density and is mainly controlled by transport processes [*Rishbeth and Garriott, 1969*]. Therefore, any changes in the transport processes or chemical composition (induced by geomagnetic storms) are expected to get reflected promptly in the ionospheric TEC [*Klobuchar, 1996*]. Another advantage of using TEC to assess the behaviour of plasma in the near-Earth environment is that the radio signals (Ultra High Frequency (UHF)) employed in calculation of TEC do not undergo severe degradation during disturbed times as they are trans-ionospheric in nature [*Mendillo, 2006*]. Hence, regional and global chains of GPS receivers can provide high resolution spatial and temporal data using which the distribution of plasma in the ionosphere during the quiet as well as disturbed times can be studied.

Another important parameter that is of great use in ionospheric research is electron density derived from the digisonde measurements. The digisonde which is a digitized version of the ionosonde employs radio signals (High Frequency (HF)) to probe the ionosphere. The NmF2, hmF2 and several other parameters that can be used to define the ionospheric structure is obtained using the digisonde along with drift measurements. These digisonde observations when combined with the GPS TEC observations, gives

a clear picture of the behaviour of the bottomside as well as the topside ionosphere. Information about the E-region currents and the stormtime electric fields which plays an important role in altering the plasma distribution are inferred from the magnetic field measurements obtained using ground based magnetometers. Ground based magnetometers provide data of high temporal resolution using which various aspects of the behaviour of the ionosphere during quiet as well as disturbed times can be studied. Data from the aforementioned instruments have been used for studying the impact of geomagnetic storms on the ionosphere over the Indian Antarctic station, Bharti and the Indian subcontinent. The details of the instruments are described in the following sections.

2.2 Global Positioning System (GPS)

Development of satellite systems that enabled three dimensional position determination was one of the important achievements of the early 1960's. At present, there are several constellations of satellites like the NAVSTAR GPS (USA), GLONASS (Russia), GALILEO (Europe), NAVIC (India) and COMPASS (China) that provide positioning service. The fully operational GPS established by the USA is a system of satellites placed at an altitude of 20200 km in such a way as to provide maximum coverage over the entire globe. The space segment, the control segment and the user segment shown in Figure 2.1 are the three important components of the GPS.

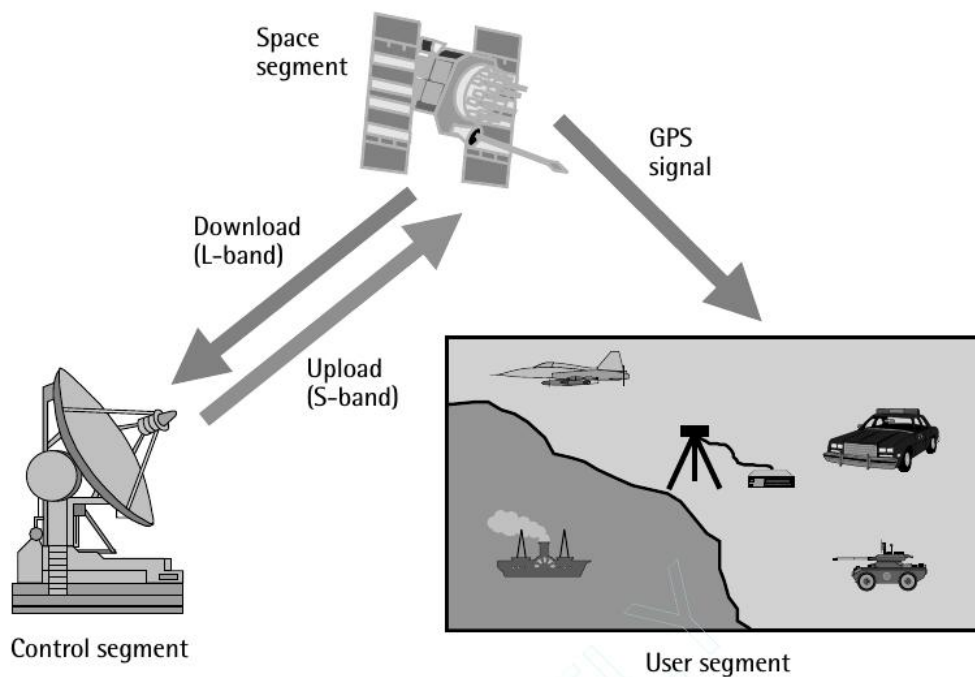


Figure 2.1: Schematic representation of GPS segments [After, *El-Rabbany*, 2002]

The GPS constellation is a part of the space segment that consists of 32 satellites. Four each of these satellites are placed in 6 orbital planes inclined at 55° . These satellites

take 12 hours to complete one nearly circular orbit around the Earth. The atomic clocks placed in each satellite generate the fundamental radio frequency which after modulation is transmitted to the receiver on the Earth along with two digital codes and a navigation message. The navigation message includes the current position of the satellite and the correction to time along with other information determined by the control segment. The control segment, which is a wide network of GPS tracking stations, has been functioning with an objective to track satellite locations, predict future positions, determine the satellite almanac, health of the satellite and atomic clocks etc. These information are periodically uploaded through an S-band link to the GPS satellites from where it is transmitted to the user segment. The user segment comprises of both the civilian and military users who with the help of a GPS receiver and antenna can receive the signals.

All GPS satellites transmit microwave radio signals that has two carrier frequencies namely, L1 (1575.42 MHz) and L2 (1227.60 MHz) signals. These signals are modulated by a navigation message and two digital codes known as the Precision (P) code and the Coarse Acquisition (C/A) code. At present, the C/A code which has a chipping rate of 1.023 Mbps is modulated only onto the L1 signal. This being the principal civilian ranging signal is always available to users all over the world, free of cost. However, the C/A code is less precise than the P code which is a long code that is 10 times faster than the C/A code. The P code which has a chipping rate of 10.23 Mbps is modulated onto both the L1 and L2 frequencies. The P code and the C/A code are commonly known as the Pseudo Random Noise (PRN) codes as they are random binary sequences. Different satellites use different PRN codes for modulation to have minimum cross correlation. It is also easy to identify the satellite that transmits a particular code as each satellite is assigned a unique PRN number.

The receiver generates an exact replica of the signal when the satellite transmits a signal. A comparison of the signal transmitted by the GPS satellite with the replica generated by the receiver gives the time taken for the signal to travel from the satellite to the receiver. The distance from the satellite to the receiver, also known as range, is then calculated using,

$$\text{Range} = \text{speed of light} \times \text{travel time of the signal } (\Delta t)$$

The range measured in this way can be considered as the radius of a sphere with the satellite as its center. The position of the receiver should lie anywhere on the surface of this sphere. If range measurements are available from atleast three satellites tracked simultaneously, the position of the receiver would lie at the point where the three spheres (with radii given by corresponding ranges) intersect as depicted in Figure 2.2. In panel (a) of Figure 2.2 is shown an ideal case in which all the three spheres intersect at a single point. Such a configuration is possible only when all the three satellites lie at the vertex

of an equilateral triangle. The real situation depicted in panel (b) of Figure 2.2 shows at least two probable positions for the receiver. This is known as Dilution Of Precision (DOP). Estimation of position using more number of satellites can solve this problem of DOP. The various other GPS errors that can degrade the performance of the GPS receivers are described in the following section.

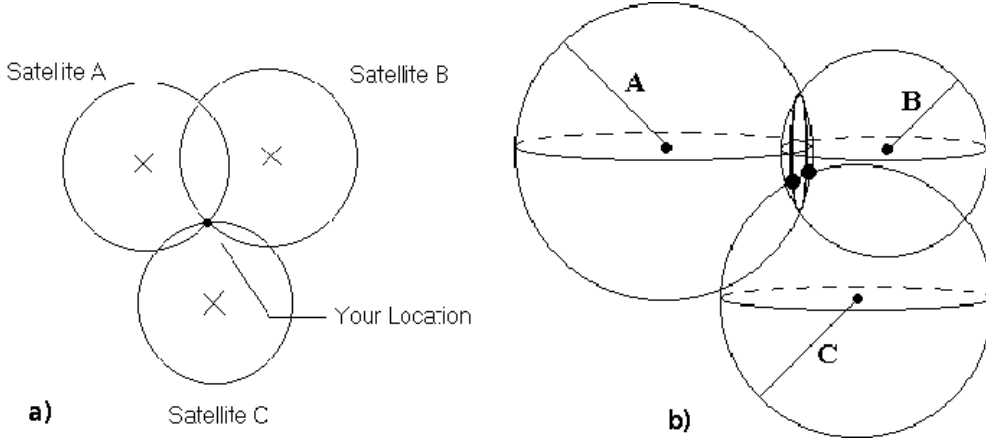


Figure 2.2: Position determination in GPS using Triangulation.

2.2.1 GPS Errors

In any case the satellite clock and the receiver clock have to be in synchronization for the estimated range to be true. But, in reality, in addition to synchronization errors in the satellite and receiver clocks, the true range is offset by contributions from various factors including the delay introduced by the atmosphere. The measured range therefore remains different from the true range due to the GPS errors. For this reason the measured range is called as the pseudorange and is given by,

$$PR = \rho + d\rho + c\varepsilon^{sc} + cdT + io + trop + \varepsilon_{PR} \quad (2.1)$$

Similarly, the carrier phase range (ϕ_{cr}) obtained from phase measurements is given by,

$$\phi_{cr} = \rho + d\rho + c\varepsilon^{sc} + cdT + io + trop + \varepsilon_{\phi} + \lambda N \quad (2.2)$$

where,

- ρ = geometric (or true) range
- ε^{sc} = satellite clock error
- dT = receiver clock error
- $d\rho$ = orbit errors
- λ = carrier wavelength
- c = velocity of light in vacuum

N = carrier-phase integer ambiguity (in number of cycles)
 $trop$ = troposphere error
 io = ionosphere errors
 $\varepsilon_\phi, \varepsilon_{PR}$ = receiver noise and multipath contributions to carrier-phase and pseudorange respectively.

The GPS errors mentioned above can be classified into three categories namely, (a) satellite based errors, (b) receiver based errors, and (c) the atmospheric errors. The different aspects of the GPS system that can give rise to the range error, listed in Table 2.1, is described briefly in the following subsections.

Table 2.1: Error budget in GPS. [After, *El-Rabbany*, 2002]

Source	Error (m)
Satellite Clock Error	0.3 – 4
Satellite Ephemeris Error	1 – 6
Multipath	3 – 10
Receiver Noise	0.5 – 5
Tropospheric Error	2.5 – 30
Ionospheric Error	5 – 45

2.2.2 Satellite based errors

An error in pseudorange usually results as the atomic clocks onboard the GPS satellites drift from the GPS time. The GPS time is calculated statistically from a set of readings of time measured by clocks placed onboard the GPS satellite and at various control stations. The GPS system time that was coincident with the Universal Time Coordinate (UTC) on 0000 hours of 6 January 1980, is not corrected for leap seconds. Hence, at present, the GPS time is ahead of the UTC by ~ 14 seconds. The stability of the atomic clock over a period of one day is about 1 to 2 parts in 10^{13} from which the satellite clock error is estimated to be about 8.64 to 17.28 ns. This results in a 0.3 – 4 m error in position [*Kaplan and Hegarty*, 2006]. The clock errors and the correction parameters are uploaded to the GPS satellite by the master control station. These parameters are transmitted to the user as part of the navigation message.

The navigation message includes the satellite ephemeris also, which is the position of the satellite as a function of time. The ground control station calculates the orbital elements of the satellite for each one hour period by overlapping the previous 4 hour GPS observations. The predictions of the future position of the satellite done in this way will generally not be accurate. Hence, an ephemeris error of about 1-6 m gets introduced in the predicted position of the satellite which is transmitted as a part of the navigation message [*Warren and Raquet*, 2002].

2.2.3 Receiver based errors

The GPS signal that arrives at the antenna might be a direct line of sight signal or a reflected signal depending on where the antenna is placed. The reflected signal will usually be a weak and delayed signal as compared to the direct signal. The estimated position in such a case can be erroneous if the signals that arrive at the antenna after reflection from nearby structures or the ground, interfere with the direct signal and cause signal distortion. This type of error, called the multipath error amounts to about 3 – 10 m and affects both the pseudorange and carrier-phase measurements [Kaplan and Hegarty, 2006]. An easy option to remove multipath effects is to place the GPS antenna in locations free of reflectors. Placing the antenna closer to the ground also helps in reducing the transit time of the reflected signals and by that means the multipath errors. Usage of choke ring antenna to attenuate the reflected signals also reduces the multipath errors.

The limitations in the receiver electronics can also give rise to random noise that can affect the range and carrier-phase measurements. The receiver noise depends on the strength of the signal, the quality of the GPS antenna, cable, receiver and its electronics. The effects of interference and the thermal noise jitter are the main contributors to the range error that arises from receiver noise. Because the C/A code has a smaller rms bandwidth, its contribution to receiver noise will be slightly higher than that by the P code. The receiver noise, on average, is known to introduce an error of the order of 0.6 m in position.

2.2.4 Atmospheric errors

As microwaves pass through different regions of the atmosphere, they are subjected to refraction, scattering and attenuation. The velocity with which the electromagnetic wave travels in a medium is given by,

$$v = \frac{c}{n} \quad (2.3)$$

where

v = velocity of the electromagnetic wave in the medium,

c = speed of light, and

n = refractive index of the medium.

This means that the velocity of an electromagnetic wave depends on the refractive index of the atmosphere. The refractive index of the atmosphere is inturn a function of temperature, pressure and humidity. Since these quantities increase with decreasing altitude, the refractive index of the medium also increases with decrease in altitude. As a result, the velocity of microwaves decrease as they enter into the atmosphere and they bend towards the Earth due to refraction. The decrease in velocity and the bending

of the microwave signal, both gives rise to delay which translates as range error. A schematic illustration of signal propagation through the Earth's atmosphere is presented in Figure 2.3. Once the signal is transmitted from the satellite, it reaches the outermost region which represents vacuum. Here the signal does not undergo any changes as there is virtually no atmosphere.

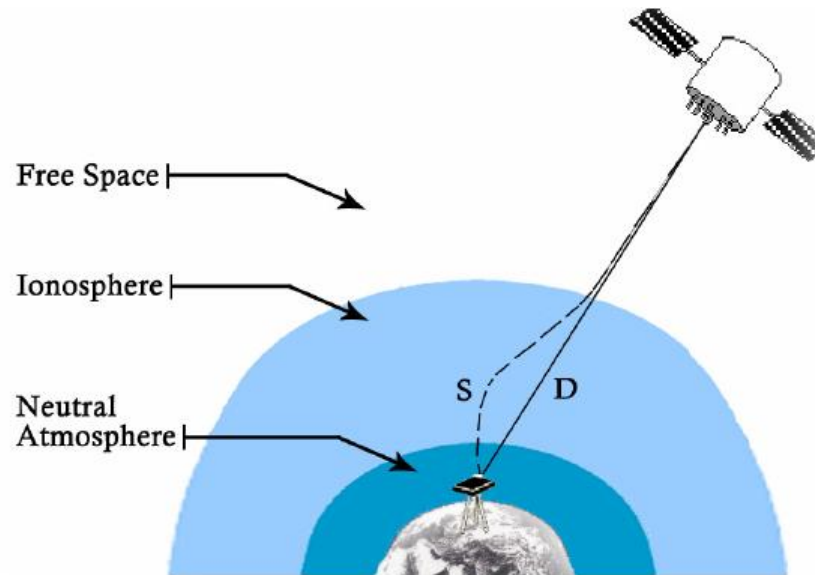


Figure 2.3: Schematic representation of GPS signal propagation through the Earth's atmosphere. [After, Saha, 2008]

If we neglect horizontal variabilities and assume that the atmosphere is made up of concentric layers each of refractive index n_i and thickness ds , then, the transit time of the signal from the satellite to the receiver can be calculated using,

$$\Delta t = \frac{1}{c} \int_s n \cdot ds \quad (2.4)$$

The measured range will be,

$$R = c \times \Delta t \quad (2.5)$$

In other words, the refraction effects of the intervening atmosphere gives rise to an error ΔR in range given by the difference of the measured range (R) and the true range (D).

$$\Delta R = R - D \quad (2.6)$$

which can be expressed as,

$$\Delta R = c \times \Delta t - D \quad (2.7)$$

Substituting for $c \times \Delta t$ from eq. (2.4) gives,

$$\Delta R = \int_s n \cdot ds - D \quad (2.8)$$

The Earth's atmosphere can thus be the largest source of error in the GPS signals. The electromagnetic waves which pass through the Earth's atmosphere interact with both the neutral as well as ionized components of the atmosphere resulting in a change in direction and speed of the signals. For this reason, the GPS signals are chosen appropriately from the L-band of the microwave frequency which is least affected by atmospheric refraction, scattering and attenuation. Even so, the GPS signals are still affected to some extent by the changes introduced in propagation speed and path of the signal due to the intervening Earth's atmosphere. The higher the frequency of the electromagnetic waves, the lesser the effects. Hence, a proper knowledge of the variation of refractive index along the satellite ray path is essential in increasing the accuracy of position determined using GPS signals. Since both the neutral and ionized component of the Earth's atmosphere affect the signal propagation in their own way, it is convenient to describe them separately. A brief description of the effects of the neutral atmosphere and the ionosphere on GPS signals is presented in the following sections.

2.2.4.1 Tropospheric effects on GPS signals

Since 98% of the neutral atmosphere is contained in the troposphere, the contribution of the neutral atmosphere to the range error is known as the tropospheric delay [Misra and Enge, 2001; Barry and Chorley, 1998]. Both the GPS PRN code as well as the carrier phase gets delayed uniformly as the radio signals pass through the troposphere. The tropospheric delay will be maximum when the satellite is at the horizon as the signal has to travel a longer distance through the atmosphere whereas it will be minimum when the satellite is overhead. The error in positioning introduced by the tropospheric delay corresponds to about 2.3 m when the satellite is overhead, about 9.3 m for a satellite elevation angle of 15° and about 20-28 m for satellite elevation angles of 15° [Ramjee and Ruggieri, 2005; Brunner et al., 1999; Leick, 1995].

As described in Chapter 1, the troposphere is the region of the atmosphere extending from the surface of the Earth to ~ 15 km. Gases like CO_2 , O_3 and water vapour also form a minor part of the tropospheric composition. Among these, water vapour is a polar molecule which has a permanent electric dipole moment. Hence, water vapour aligns itself in the direction of the applied electromagnetic field. Water vapour unlike the non polar molecules (CO_2 , O_3) does not mix well in the atmosphere and forms the wet component of the troposphere. The non-polar molecules which obey the hydrostatic equations are well mixed in the troposphere and form the dry part of the troposphere. These dry and wet parts contribute to 90% and 10% of the total tropospheric delay respectively. The dry part of the tropospheric delay can be predicted accurately using mathematical models whereas the wet part is hard to predict using models. In any case,

the tropospheric delay is less than the delay caused by the ionosphere in the GPS signals.

2.2.4.2 Ionospheric effects on GPS signals

The Earth's ionosphere is an ionized medium consisting of free charges that can significantly affect the propagation of radio waves [Ratcliffe, 1962]. At lower frequencies (below 30 MHz), the ionosphere acts as a mirror and reflects the radio waves back into the ionosphere enabling long-distance radio communication. Even though the radio waves with higher frequencies pass through the ionosphere, they are affected by it. The phase velocity of the radio signal increases in the presence of the electron density. As a result, a particular phase of the carrier arrives at the receiver on the surface of the Earth earlier. On the other hand, the group velocity decreases in the presence of the electrons and ions in the ionosphere. Hence, a group delay is experienced whose magnitude will be equal and opposite in sign to that of the phase advance [Ratcliffe, 1962]. The propagation speed of the radio signals as they pass through the ionosphere is necessarily determined by the electron density of the ionosphere. It is the carrier frequency that decides the magnitude of the group delay or the phase advance. The greater the carrier frequency, the lower is the delay/advance in group/phase of the GPS signal [Klobuchar, 1996].

For phase propagation, the refractive index of the ionosphere is given by,

$$n_p = 1 + \frac{c_2}{f^2} + \frac{c_3}{f^3} + \frac{c_4}{f^4} \dots \quad (2.9)$$

where

c_2 , c_3 and c_4 are coefficients that depend on the electron density

The refractive index of the ionosphere for group propagation (n_g) is given by,

$$n_g = n_p + f \frac{dn_p}{df} \quad (2.10)$$

On substituting eq. (2.9) in eq. (2.10) and neglecting the higher order terms, the group delay is written as,

$$n_p = 1 + \frac{c_2}{f^2} \quad n_g = 1 - \frac{c_2}{f^2} \quad (2.11)$$

Here $c_2 = -40.3 n_e Hz^2$, and

n_e is the electron density.

Therefore,

$$n_p = 1 - \frac{40.3}{f^2} \quad n_g = 1 + \frac{40.3}{f^2} \quad (2.12)$$

The phase velocity and the group velocity is then given by,

$$v_p = \frac{c}{1 - \frac{40.3}{f^2}} \quad v_g = \frac{c}{1 + \frac{40.3}{f^2}} \quad (2.13)$$

As the refractive index of the ionosphere depends on the frequency of the propagating radio wave, the ionosphere acts as a dispersive medium. The radio waves having lower frequencies undergo severe refraction as compared to the waves with higher frequencies [Kaplan and Hegarty, 2006]. It is not only the refractive effects, but also the change in propagation speed that contribute to the ionospheric delay. Infact, for a satellite elevation greater than 5° , the ionospheric delay caused by bending of the path of the GPS signal is negligible whereas, the delay caused by the change in its propagation speed can be significant [El-Rabbany, 2002]. As the speed of the carrier phase increases in the ionosphere, the estimated range will be lower than the true range if obtained by the carrier phase. Otherwise, the estimated range will be higher than the true range if estimated using the PRN codes (C/A code or P code) as group velocity decreases in the ionosphere.

The error in true range caused by the ionospheric delay is estimated as,

$$\Delta R_{iono} = -\frac{40.3}{f^2} \int N_e dl = -\frac{40.3}{f^2} \text{TEC} \quad (2.14)$$

where,

$$\int N_e(l) dl = \text{the Total Electron Content (TEC) along the path of the signal} \quad (2.15)$$

Hence, the ionospheric delay is proportional to the TEC of the ionosphere which is defined as the integrated electron density in a vertical column of unit cross-sectional area along the satellite ray path [Petrie et al., 2011]. The TEC is measured in TEC units given by,

$$1 \text{ TECu} = 10^{16} \text{el/m}^2 \quad (2.16)$$

From the above discussion, it is clear that the group delay/phase advance of the GPS signals as they travel through the ionosphere gives rise to pseudorange errors that can be estimated by multiplying the ionospheric delay with the speed of light. It is known that the error in range measurements introduced by the ionosphere alone can vary between 1 meter to more than 100 meters [Klobuchar, 1996]. It is difficult to predict the ionospheric delay using models as it depends on the TEC of the ionosphere which exhibits high variabilities depending on the solar cycle, geographic location, season and time of the day. However, the contribution of the ionospheric delay to range errors can be completely removed by making use of the dispersive property of the ionosphere [Klobuchar, 1996; Mendillo, 2006]. Since the ionosphere is a dispersive medium, the ionospheric delay experienced by the L2 signal will be higher than that experienced by the L1 signal and

so the pseudorange measurements obtained from the slightly different L1 and L2 carrier frequencies will be different. Combining these pseudorange measurements estimated using both L1 and L2 frequencies, the TEC of the ionosphere can be expressed as,

$$TEC = \frac{1}{40.3} \left[\frac{f_1^2 f_2^2}{f_1^2 - f_2^2} \right] [PR_1 - PR_2] \quad (2.17)$$

Similarly, in terms of the carrier phase measurements estimated using L1 and L2 frequencies, TEC can be expressed as,

$$TEC = -\frac{1}{40.3} \left[\frac{f_1^2 f_2^2}{f_1^2 - f_2^2} \right] [\phi_1 - \phi_2] \quad (2.18)$$

where f_1 and f_2 are the L1 and L2 frequencies transmitted by the GPS satellite respectively.

Thus, the ionospheric delay can be calculated by substituting for TEC in eq. (2.14), using which the error in the position due to the ionospheric effects can be completely removed. The TEC measured in this way has also been used extensively to study the ionospheric variabilities during quiet as well as disturbed times [Mendillo, 2006, and references therein]. The Slant Total electron content (STEC) obtained using the differential code and carrier phase measurements are both used in ionospheric studies. The TEC obtained from the carrier phase measurements are relatively noise free as compared to the TEC derived from PRN code measurements. Similarly, the TEC obtained from the PRN code measurements is free of ambiguity whereas the TEC obtained from the carrier phase measurements is ambiguous. In such cases, to minimize the pseudorange noise, a technique called carrier phase smoothing is used in which the GPS pseudorange data is smoothed using carrier phase measurements [Hansen *et al.*, 2000; Tariku, 2015]. The accuracy of the TEC can be improved by linearly combining both the code pseudorange and the carrier phase measurements for the same satellite pass [Klobuchar, 1996].

Since the GPS satellites are visible only for a few hours per pass, the STEC is derived from several GPS satellites having different elevation angles at different times. The STEC estimated in this way depends on the angle of elevation of the satellite and hence on the geometry of the ray path. To allow for comparison of the TEC obtained for satellite ray paths with different elevation angles, the STEC is usually projected to the Vertical Total Electron Content (VTEC) which is a parameter independent of satellite elevation angle. This is done by dividing the STEC with the secant of elevation angle at the Ionospheric Pierce Point (IPP) [Smith *et al.*, 2008]. The IPP is that altitude where GPS receiver line-of-sight intersects the centroid of the mass of the ionosphere. The IPP is calculated by assuming that the whole concentration of electrons lie in a thin layer at an altitude of 350 km at equator. The VTEC is then given by,

$$\text{VTEC} = \text{STEC}(\cos\chi') \quad (2.19)$$

where

$$\chi' = \arcsin\left[\frac{R_e}{R_e + h_m}\sin\chi\right] \text{ is the zenith angle at a the height corresponding to IPP.} \quad (2.20)$$

χ is the zenith angle at the receiver position,

R_e is the radius of the Earth, and

h_m is the height of IPP.

From the above discussion, it is clear that the GPS can be used to get the integrated electron density along the satellite and receiver path (TEC) using which the behaviour of plasma in the ionosphere at any point can be studied. Since atleast four GPS satellites are visible at all times from any point on the globe, having a network of GPS receivers over different locations can provide information about the temporal and spatial variation of TEC over a wide geographical location. In the present study, TEC measurements from the Indian Network for Space Weather Impact Monitoring (InSWIM) and GPS Aided Geo Augmented Navigation (GAGAN) network of GPS stations have been used to study the plasma distribution over the Indian region during quiet as well as disturbed times (Chapter 3 and Chapter 5). In addition, a GPS receiver installed at the Indian Antarctic research station, Bharti, gives information of TEC variations at the southern polar station (Chapter 3 and Chapter 4). It is worth mentioning here that the southern polar station, Bharti, shares the same longitude as the Indian sector. Hence when combined with the measurements from the GPS stations across India, the latitudinal evolution of geomagnetic storms along the Indian longitude extending from the southern polar region to the dip equator can be investigated. The details of the GPS receiver stations in the Indian sector from where TEC measurements were obtained for the present thesis is provided in the following section.

2.3 The InSWIM network

The InSWIM network of GPS stations was established with an objective to study the physical processes responsible for the distribution of plasma over the high, mid, low and equatorial latitudes during different space weather conditions.

The Indian region is highly suitable for such a study as it extends latitudinally from the magnetic equator to the northern anomaly crest, the Sq focus region and beyond, and hence covers the mid, low and equatorial latitudes. For a comprehensive study of the impact of geomagnetic storms over the Indian region, in addition to the TEC measurements, measurements of the electron density profiles, magnetic field variations and thermospheric variations are all imperative. The ultimate goal of the InSWIM

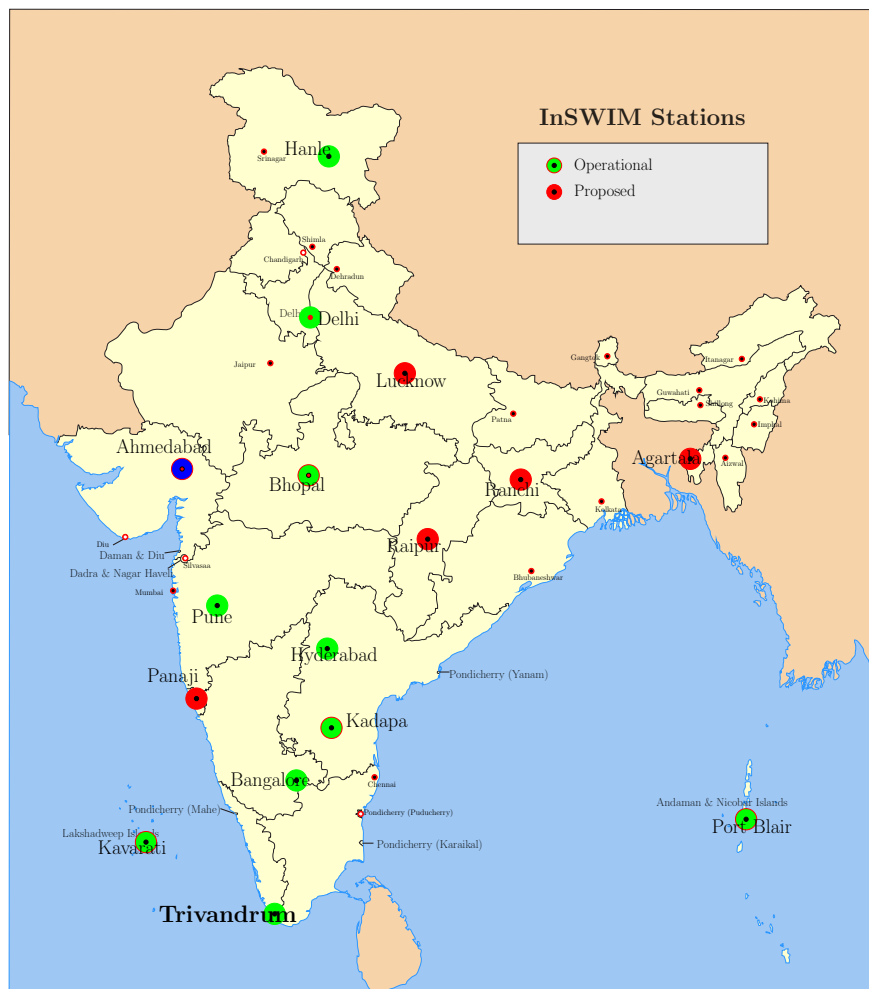


Figure 2.4: Location of InSWIM stations. The GPS receivers at locations marked using green are currently operational while those shown in red are the proposed GPS stations.

project is to have such a comprehensive set of high resolution spatial and temporal data of several ionospheric parameters using which the space weather impact over the entire Indian region could be modeled.

The InSWIM network is currently operational with 7 dual frequency GPS receivers functioning at different locations as shown in Figure 2.4. The Septentrio PolaRxS GPS receivers installed at these locations are multi-frequency multi-constellation receivers which provides continuous measurements of TEC and scintillation indices (S4 index, Spectral slope and SI indices). The hardware specifications of the PolaRxS receiver compatible with Septentrio's SSRC3 Software Packages is provided in Table 2.2. For all frequency bands and satellite constellations, 50-Hz phase and amplitude samples are generated by the Septentrio PolaRxS GPS receiver. A RxLogger graphical interface is provided using which the 50-Hz phase and amplitude samples can be obtained on a computer. The raw data stored in the Septentrio Binary Format (SBF) format contains 50-Hz raw correlation and phase data. The raw data can be converted into ASCII files (ISMR format) by using the `sbf2ismr` program which is a command line tool provided

by the RxLogger. The unprocessed 50-Hz raw correlations and phase data can also be stored into an ASCII file using the `sfb2ismr` program. The GPS TEC measurements are recorded at every 15 seconds based on the L2-P and L1-P pseudorange measurements. The phase scintillation (σ_ϕ) indices are the standard deviation of the detrended carrier phase averaged over intervals of 1, 3, 10, 30 and 60 seconds. A 6th order Butterworth high-pass filter is used phase detrending. Options are available for the user to select the cutoff frequency of the detrending filter which takes 4 minutes to converge after the initial satellite acquisition. The TEC and scintillation indices computed for all visible satellites can also be viewed in real time using the RxLogger.

Table 2.2: The hardware specifications of Septentrio’s PolaRxS GPS receiver.

Power consumption	:	Nominal operation: 6.5W typical
	:	During initial OCXO warm-up: up to 10W.
Size	:	284 x 140 x 37 mm (length including connectors)
Temperature Range	:	-40 to +60 °C (operational)
	:	-55 to +85 °C (storage)
Ingress Protection	:	IP65
Shock	:	MIL-STD-810F, 516.5
Vibration	:	MIL-STD-810F, 514.5

In addition to GPS receivers, the InSWIM network also includes the Low Earth Orbiting satellite (LEOS) radio receiver which were already operational as a part of SPL’s Coherent Radio Beacon Experiment (CRABEX). At some of the InSWIM stations, other instruments like ionosonde and magnetometer are also continuously operational. Longitudinal coverage of these stations varies from 76°E to 92°E, and the geographic latitudinal coverage varies from 8°N to 32°E. The GPS receivers located at all InSWIM stations are capable of receiving signals from the Navigational System Tracking and Range (NAVSTAR) GPS, Global Navigation Satellite System (GLONASS), GALILEO systems. The InSWIM network also tracks the Indian Regional Navigation Satellite System (IRNSS) signals which provides scope for developing ionospheric models that would help for regional navigation.

Some of the GPS TEC data used in the present thesis was obtained from the GAGAN network of GPS stations. The GAGAN network was established by the Indian Space Research organization (ISRO) in collaboration with the Airport Authority of India (AAI). The STEC data obtained from both these stations, has been converted to VTEC using the technique described in the previous section. In addition to the TEC derived from GPS measurements at InSWIM stations, the electron density profiles obtained from ionosonde measurements have been used to study the redistribution of plasma over the dip equatorial region, Trivandrum. A brief description of the working of the ionosonde is described in the forthcoming section.

2.4 Ionosonde

An ionosonde is a type of radar which uses a wide range of operating frequencies to obtain echoes from different regions of the ionosphere. It works on the principle of specular reflection of the radio waves from plasma in the ionosphere by virtue of its inherent frequency, given by,

$$f_p^2 = \frac{N_e e^2}{4\pi\epsilon_0 m} = kN_e \quad (2.21)$$

where, e is charge of an electron, m is mass of an electron, ϵ_0 is the permittivity of free space, and N_e stands for electron density per m^3 .

The plasma frequency thus depends on the electron density of the ionosphere. When the frequency of the radio waves transmitted vertically using an ionosonde matches with the plasma frequency of the ionosphere, then total internal reflection takes place. Essentially, the propagation of an electromagnetic wave in the ionosphere is affected by the ionosphere which is an ionized medium. It is the refractive index of the ionosphere that decides the extent to which the electromagnetic wave gets affected. In a collisionless and magnetic field free plasma, the refractive index (μ) of the ionosphere [Davies, 1989; Chen, 1987] is given by ,

$$\mu^2(h) = 1 - \frac{kN_e}{f^2} = 1 - \frac{f_p^2}{f^2} \quad (2.22)$$

where $kN_e = f_p^2$ is the plasma frequency, and f is the transmitting frequency in Hz.

An obvious connection between the refractive index of the ionosphere, plasma frequency, frequency of the transmitted wave and the electron density in the ionosphere is evident from the above equations. It is clear that, the refractive index (μ) becomes zero and then negative if the plasma frequency is equal to or greater than the frequency of the transmitted wave ($f_p^2 \geq f^2$). Since, the the group velocity of the transmitting wave is proportional to the refractive index which inturn falls with increasing plasma frequency, the group velocity of the wave decreases as f approaches f_p . At a particular height corresponding to $\mu = 0$, the propagation velocity finally reverses. In other words, an electromagnetic wave can penetrate through the ionized medium only if μ is positive (or $f > f_p$). Hence, the refractive index of the ionosphere and by that means the propagation characteristics of the electromagnetic wave in the ionosphere are determined by the plasma frequency of the ionosphere.

But the presence of a magnetic field brings about significant changes in the behavior of the ionospheric plasma and the refractive index (μ). The refractive index of the ionosphere given by the Appleton-Hartee equation is,

$$\mu = 1 - \frac{X}{(1 \pm Y_L)} \quad (2.23)$$

where,

$$X = \frac{\omega_N^2}{\omega^2} \quad \text{and} \quad Y_L \quad \text{are magnetoionic parameters.} \quad (2.24)$$

If the angle between magnetic field and the direction of wave normal is θ ,

$$Y_L = Y \cos\theta \quad \text{and} \quad Y_T = Y \sin\theta \quad (2.25)$$

If $\theta = 0$ i.e., the wave normal lies in the direction of the magnetic field, then

$$Y_L = Y = \frac{\omega_H}{\omega} \quad \text{and} \quad Y_T = 0 \quad (2.26)$$

where,

$\omega_N^2 = \frac{Ne^2}{m\epsilon_0}$ is the plasma frequency,

$\omega_H = \frac{Be}{m}$ is the gyro frequency,

N is the concentration of free electrons,

m and e are the electron mass and charge,

ϵ_0 is the permittivity of free space,

B is the Earth's magnetic flux density,

f is the radio wave frequency, and

ω is the angular frequency.

The refractive index of the ionosphere has two values depending on the angle between the direction of the wave normal and the magnetic field. Hence, the ionosphere acts as a doubly refracting medium in the presence of the magnetic field. Therefore as a plane polarized wave passes through the ionosphere, it splits into the "ordinary (o)" and the "extraordinary (e)" waves. Both the ordinary and the extraordinary waves have different phase velocities and are circularly polarized in the opposite sense. These waves get reflected from the ionosphere for the following set of conditions.

(1) The reflection of the ordinary wave occurs at a height where $X = 1$.

(2) The extraordinary wave gets reflected at a height where

$$X = 1 - Y \quad \text{if} \quad Y < 1 (f > f_H) \quad \text{and} \quad (2.27)$$

$$X = 1 + Y \quad \text{if} \quad Y > 1 (f < f_H) \quad (2.28)$$

where f_H is the gyro frequency.

An ionosonde, which works using the principle of reflection of radio waves by the ionosphere, transmits sweep frequencies from 1 MHz to as high as 30 MHz vertically up

into the ionosphere. When the transmitted frequency matches with the plasma frequency of the medium, the radio waves are reflected back into the medium. The altitude at which reflection occurs is estimated by measuring the transit time of the signals between the transmission and the reception. The electron density at a particular altitude in the ionosphere is derived from the frequency of the radio wave that gets reflected from that particular altitude. The signals travelling through the ionosphere, in reality have a velocity much lesser than the velocity of light. But, the height is calculated by assuming that the signals travel with the velocity of light. Hence, the estimated height is called the virtual height. The corresponding frequency where reflection occurs is called as the critical frequency. An ionogram which is a pictorial representation of the frequency of the reflected signals (in the x-axis) as a function of height (in the y-axis) is shown in Figure 2.5. Since both the o-wave and the e-wave gets reflected under different set of conditions, they appear as two separate traces in the ionogram as seen in Figure 2.5. Sometimes, in the ionograms obtained at high latitudes, a third type of trace known as the “z-trace” is also visible. The z-trace appears as a result of the reflection of the waves that have been propagated along the magnetic field. These waves undergo reflection at the height, $f_0 - \frac{1}{2}f_H$.

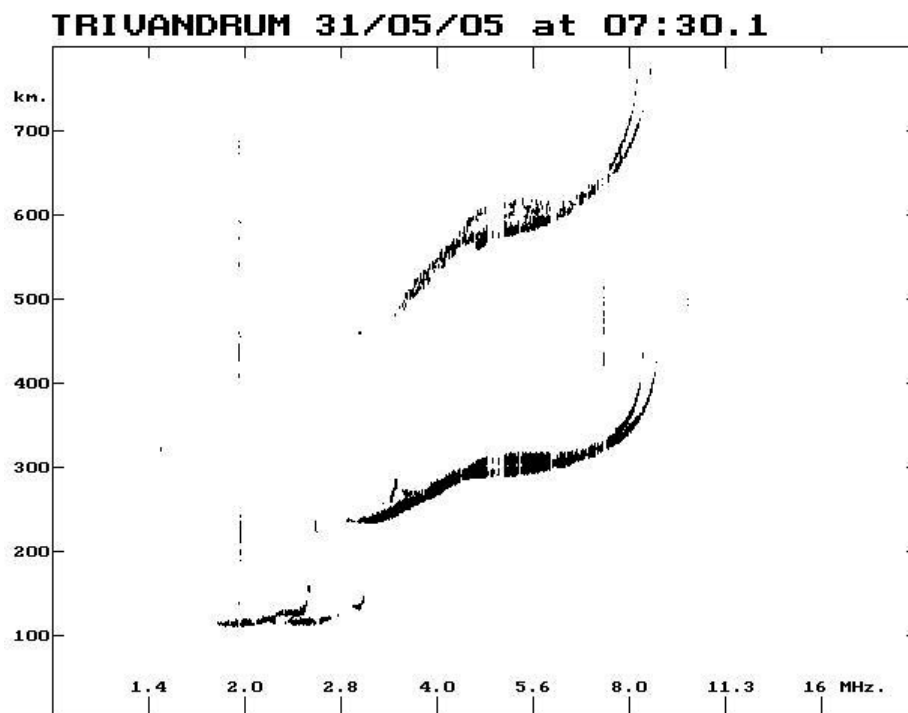


Figure 2.5: Sample ionogram from KEL IPS-42 Ionosonde.

The virtual height-frequency trace obtained from the ionosonde can be inverted to obtain the electron density profile of the ionosphere in what is known as the true-height analysis. The Automatic Real-Time Ionogram Scaler with True height (ARTIST) [Tang and Reinish, 1988] and the POLynomial ANALYSIS (POLAN) [Titheridge, 1985] are two such programs used to derive the electron density real height profile from the

digisonde and the ionosonde, respectively. In the Chapter 5 of the present thesis, digisonde measurements from Trivandrum have been used for studying the response of the equatorial ionosphere to geomagnetic storms. A Digisonde Portable sounder (DPS-4D), developed by University of Massachusetts Lowell centre for Atmospheric Research (UMLCAR), has been used to monitor the ionosphere over the dip equatorial station, Trivandrum. A description of the digisonde DPS-4D is presented in the following section.

2.4.1 Digisonde Portable sounder (DPS-4D)

DPS-4D is the new generation Digisonde Portable Sounder (DPS) capable of estimating the electron density profile of the ionosphere upto 1000 km above the Earth's surface. The digisonde works on the principle of reflection of radio waves from the ionosphere and provides (a) frequency (b) phase (c) amplitude (d) Doppler shift and Spread (e) angle of arrival and (f) wave polarization. The vertical transmission of circularly polarized radio signals and the reception of the echoes from the ionosphere are done using two antenna systems each. A transmitting antenna is a crossed delta antenna of approximately 30.5 meters height which transmits circularly polarized radio signals in the frequency range 2 to 15 MHz. The receiver antenna system is an array of four crossed loop antennas, among which one is placed at the centroid and three at the vertex of an equilateral triangle. Each crossed loop antenna is of height 1.5 m and occupies an area of 1.2×1.2 square meter. Two loop antennas are placed orthogonal to each other with one loop facing magnetic north-south and the other loop facing magnetic east-west. In order to receive lefthanded/righthanded circularly polarized signals from overhead, a polarization switch which combines the signals from each of the two loops is mounted under the crossed loop antenna. The system specifications of the DPS-4D is given in Table 2.3.

The transmitted signal, after reflection from the ionosphere is received by the four antennas. The received signal is processed to obtain a set of four doppler spectra for each sampled range bin using which three types of a measurement modes and corresponding data products are obtained. Ionograms (includes vertical and oblique incidence), drift measurements (to detect multiple echoes and the velocity of their source) and Passive RF sensing mode are the three types of measurement modes from which data products can be derived as SAO and GRM or DFT files. The SAO and GRM are ionogram files while DFT is an ionosonde drift file. In the drift mode, all four spectra are analyzed seperately to derive the skymap and bulk drift velocity of the plasma. However, in the ionogram mode, only one echo is recorded per range bin by reducing four Doppler spectra to one echo status (amplitude, Doppler shift, angle arrival). The software component used in the digisonde for reduction of collected raw data to data products is the Digisonde Commanding and Acquisition Remote terminal (DCART). It also provides the control platform to send commands and acquire telemetry data and user interface for manual and autonomous operations. A typical ionogram obtained from the digisonde has the

Table 2.3: The specifications of DPS-4D Ionosonde system at Trivandrum (Digisonde-4D Technical Manual).

Antenna	
Receiver Antenna Type	: Active Crossed loops Turnstile antennas (1.5m diameter);4 antennas in 60 m triangle with central antenna
Transmitter Antenna Type	: Turnstile Delta or Rhombic (2 orthogonal radiating elements) 30 m
Quad Receiver	
Frequency Range	: 0.5–30 MHz (all modes of operation)
Bandwidth	: 34 kHz @ 3 dB (for 5 km range resolution)
Dynamic Range	: > 90 dB instantaneous : >140 dB total operating range including gain control
RF Output	
Frequency Scan	: 0.5 - 30 MHz, start, stop and step size selectable to 1 kHz
Pulse Repetition Rate	: 100 and 200 pps
Pulse Width	: 533 μ s (16 chips of 33 μ s) waveform with 30 kHz signal bandwidth
Peak Pulse Power	: 2 channels @ 150 W each
Transmitter Type	: Dual RF MOSFET Amplifiers for polarized transmission using turnstile transmit antenna
Signal Processing	
No. of Range Bins	: Selectable: 256 or 512
Height Range	: 0-1200 km (0 km used for self calibration)
Height Resolution	: 2.5 km sample spacing : 500 m using differential phase technique
Doppler Processing	: 4 to 128 integrations can provide up to 21 dB signal processing gain
Doppler Range	: \pm 3 Hz to \pm 50 Hz
Doppler Resolution	: 0.0125 to 12.5 Hz
Amplitude Resolution	: < 0.01 dB

transmitting frequency as the abscissa, virtual reflection height as the ordinate, signal amplitude as the dot size, and echo status (polarization, Doppler shift and angle of arrival), all mapped into 12 available distinct colors as shown in Figure 2.6. The wave polarizations are shown in green or neutral colours for extraordinary and red scale for ordinary. The angle of arrival is shown by different colors such as warm for South and cold for North. The Doppler shift is indicated by the color shades. For manual processing and viewing of ionograms, the softwares used are SAO Explorer and Drift Explorer. A brief description of the derived products is presented in the following.

Trivandrum, TM308 2010.03.06 (065) 16:00:11

STATION NAME, URSI CODE YYYY.MM.DD (DDD) TIME (UT)

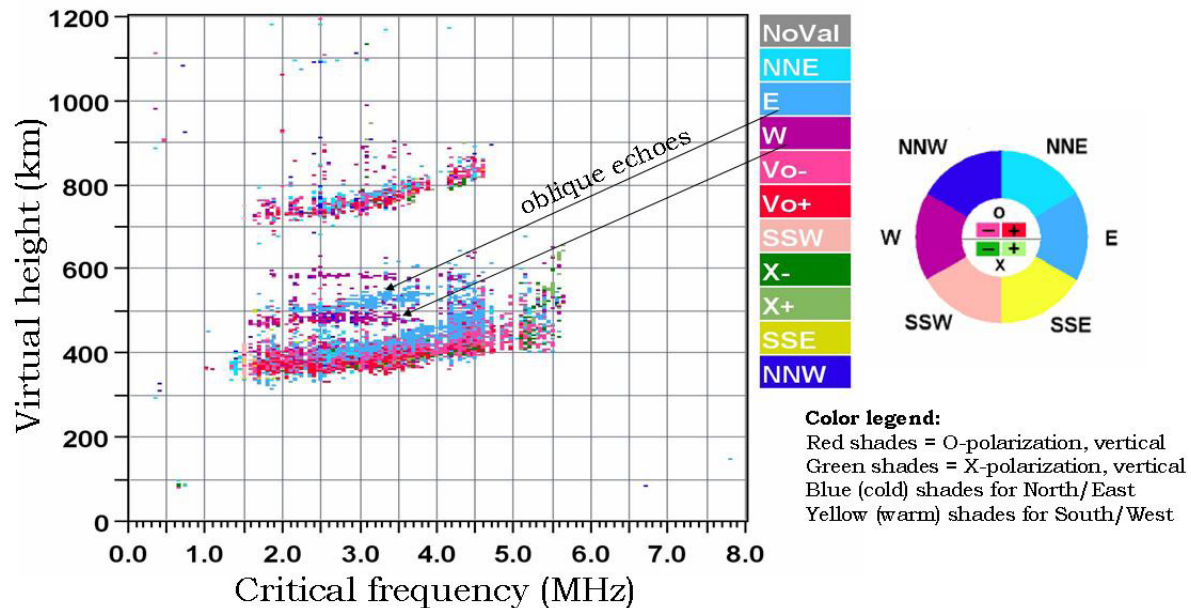


Figure 2.6: Six dimensional ionogram (Digisonde-4D Technical Manual).

2.4.1.1 Ionospheric data derived from Ionograms

The electron density profile, several characteristic features of the ionosphere like the hmF2, F-region peak frequency (foF2) etc., report of Maximum Usable Frequency (MUF), directograms for oblique echoes and ionogram traces are the derived products obtained from the digisonde ionogram. The program used to extract data from the ionograms is the ARTIST which is basically an electron density inversion algorithm. A complete set of scaled data in SAO 4.2 format and SAOXML 5.0 format along with a set of MUF calculated for pre-configured distances is obtained upon using the ARTIST program to read the ionogram files. The program also allows manual processing of the data which can be saved into an SAO file after introducing the corrections. The large scale plasma irregularities drifting across the location of the digisonde can also be viewed using the directogram provided by the digisonde. The directogram provides the altitude of the plasma structure, Doppler direction and amplitude of the echoes using the ionogram.

2.4.1.2 Derived products from Drift measurements

Several data products including the skymap can be obtained from the digisonde in the drift mode. Doppler skymap is a pictorial representation of drift measurements. The line of sight velocity of the reflecting plasma can be estimated using a skymap where the large number of echoes from the ionosphere are resolved on the basis of their time of arrival and Doppler shift. The information about the scattering sources for multiple

frequencies/ranges is extracted from the drift data by using the *DFT2Sky* software. The output file is in the *SKY* format. The positive/negative Doppler is marked as +/0 or using the blue/red color in the skymap. The bulk velocity of the plasma is calculated by applying the least square fit to skymap sources data in the *SKY* file and stored in the *DVL* file. The *DVL* file consists of the V_z , V_{north} and V_{east} components using which it is possible to describe plasma movement as 3D bulk pattern. The local tilt of the ionosphere can also be estimated by calculating the offset of the “gravity center” of skymap sources from the nadir. *TILT* software is used to calculate zenith and azimuth angles and store them in *.TLL* file.

In addition, the digisonde can also be used as a passive RF sensing instrument. In this measurement mode, the digisonde simply receives radio signals in its sensible limit and use them to infer the characteristics of the ionosphere through which the signals have travelled.

2.4.1.3 Electron density Inversion Algorithm

The ARTIST [*Huang and Reinisch, 1996*] is the computer algorithm used widely for calculating the electron density profile using an Ionosonde. It uses the True height inversion program (*NhPC* algorithm) to scale an ionogram trace and derive the plasma frequency profile [*Huang and Reinisch, 1996*]. The electron density distribution of each ionospheric layer is expressed in the inversion algorithm as,

$$h = h_m + \sqrt{g} \sum_{i=0}^I A_i T_i(g) \quad (2.29)$$

where,

$$g = \frac{\ln(f/f_m)}{\ln(f_s/f_m)},$$

h is the altitude,

h_m the peak height of the layer,

f is the plasma frequency at the height h ,

f_s and f_m are the plasma frequencies at the starting height and at the peak of the layer,

T_i are shifted Chebyshev polynomials, and

i equals 4 for F_1 and F_2 layers and 2 for E layer.

The $N(h)$ profile of each ionospheric layer is expressed in the ARTIST program in terms of shifted Chebyshev polynomials which is a logarithmic argument containing the plasma starting frequency and the critical frequency of each layer. As evident from eq. (2.29), a complete set of information which includes the critical frequency data, scaled $h'f$, an estimate of electron distribution in the valley region of the ionosphere, starting heights h_sE , h_sF1 and h_sF2 should be known to construct the electron density profile

of the E-region and the F-region. The ARTIST program begins by scaling (manual or auto) an ionogram trace to obtain $h'f$ from which the plasma frequency profile required in the Chebyshev polynomials can be computed. A valley model derived from the ISR observations at Arecibo is used to construct the electron density distribution in the valley region/E to F transition region. Also, an analytical expression is used in the true height profile instead of direct extrapolation of the $h'(f)$ trace in order to account for the missing of $h'(f)$ data. A set of coefficients derived using the peak height at each layer is used to specify the electron density distribution. Using the above information and approximating the bottom-side profile with α -Chapman functions, the scale height corresponding to the peak height of the ionosphere is estimated. The scale height obtained in this way is used along with the α -Chapman functions to construct the top-side electron density profile (above the F-region peak).

Thus, the information about the ionospheric parameters like ionospheric scale height, size of the valley between E , F_1 and F_2 layers and ionization below the F layer, peak height parameters are obtained using the ARTIST program. These ionospheric parameters are known to be controlled by various factors like the solar zenith angle, chemical and transport processes in the ionosphere.

The Earth's magnetic field has a great influence on the structure and physical features of the ionosphere. The study of magnetic field variations is of vital importance in understanding the electron density changes in the ionosphere. High resolution magnetic field data obtained using magnetometers has been used in the present thesis (Chapter 5) to assess the changes in the ionospheric parameters over the Indian region, induced by stormtime magnetic field variations. A detailed description of the working principle of the magnetometers is presented in the next section.

2.5 Magnetometer

The Earth's magnetic field is one of the most important factors that can be used to determine the properties of plasma in the ionosphere. As described in the previous chapter, several interesting phenomena including the creation of electric field, currents and the aurora, arise in the ionosphere due to the presence of the magnetic field. The magnetic field measured on the surface of the Earth exhibits high variability with respect to local time and location due to its close association with the magnetic activity on the Sun, and the Earth's ionosphere. Therefore, a systematic study of the geomagnetic field variations can throw considerable light into the processes happening in the Solar Wind-Magnetosphere-Ionosphere (SWMI) system during quiet as well as disturbed times. Infact, the very existence of the ionospheric system was first proposed by Stewart in 1890 while studying the variations in the geomagnetic field. It is now known that the regular diurnal variations of the geomagnetic field are caused by currents flowing overhead in the ionosphere [Onwumechili, 1998]. In the present thesis, high resolution

magnetic field data obtained from ground based magnetometers has been used to study the variations in the geomagnetic field and its effect on the ionospheric system during the active phase of the sun. A brief description of the working principle of the different types of magnetometers is presented in the following.

2.5.1 Proton precession magnetometer (PPM)

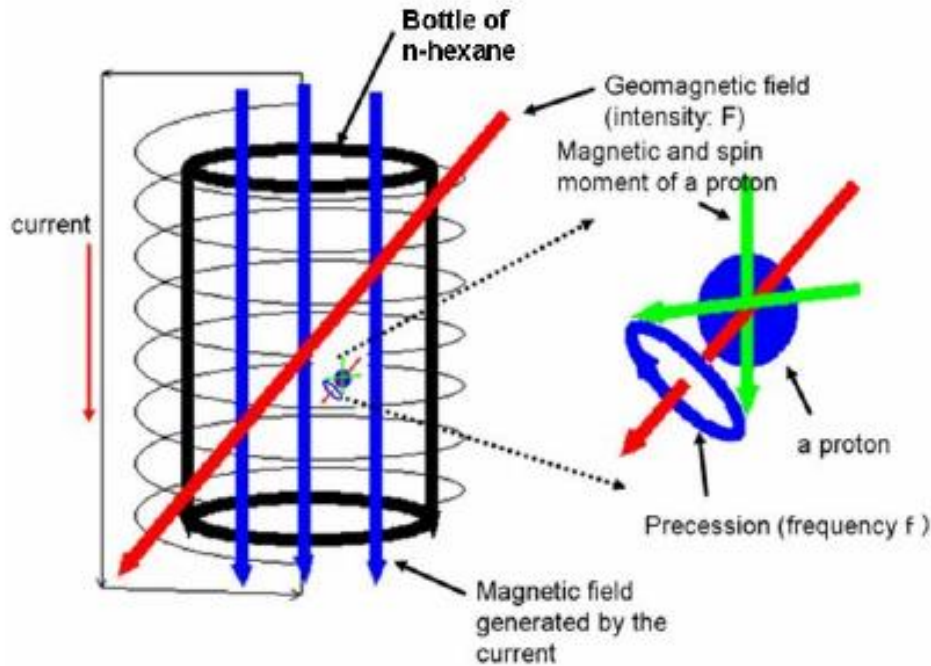


Figure 2.7: Working principle of Proton Precession Magnetometer (PPM)

As the name indicates, the Proton Precession Magnetometer (PPM) uses a proton rich material (n-Hexane, distilled water) whose precession frequencies are measured to estimate the total magnetic field at a point. In the PPM, a bottle of distilled water or hydrocarbon such as kerosene is used as the sensor as they are a rich source of protons. It is known that, the inherent magnetic moment (μ) and an angular momentum (J) of a proton are related by,

$$\mu = \gamma J \quad (2.30)$$

where γ is a ratio of magnetic moment to angular momentum and is known as gyromagnetic ratio.

At room temperature, the proton magnetic moments will remain randomly organized through collisions. A coherent signal can be obtained only if the magnetic moments of the protons in the sensor are all oriented in a particular direction. For this purpose, the sensor is placed inside a solenoid as shown in Figure 2.7. When a current is passed

Table 2.4: Specifications of PPM at Trivandrum (from Technical report).

Accuracy of measurement of the value of H	:	± 1.6 nT
Accuracy of measurement of the relative variation	:	± 0.8 nT
Sampling interval	:	1 minute (normal)
	:	12 seconds (optional)

through the solenoid, a magnetic field is generated. Since the proton possesses a magnetic moment, it experiences a torque in the presence of an external magnetic field.

The magnetic torque experienced by the proton is given by,

$$\text{Torque, } \Gamma = \mu \times B = \gamma J \times B$$

The angular momentum of the proton then precesses about the magnetic field with a particular frequency known as the Larmor frequency given by,

$$\text{Larmor frequency, } \omega = \gamma B \quad (2.31)$$

When placed in an external magnetic field, the magnetic moments of the protons thus precess in phase with the applied magnetic field. If we remove the external magnetic field at any instant, the precession of magnetic moments still continue for a brief period under the influence of geomagnetic field. An alternating current of small magnitude will be induced in the solenoid during the process. The magnetic moments then get quickly disarranged due to thermal collisions. The magnitude of the voltage induced in the solenoid will be directly proportional to the total magnetic field at the location. In this way, the total scalar geo-magnetic field at a particular location can be obtained by using a PPM. The specifications of one such PPM installed at the dip equatorial station, Trivandrum is given in Table 2.4. The PPM can be specifically used to measure the magnetic field at a dip equatorial station, since the total magnetic field therein is equal to the horizontal component of magnetic field. However, in order to measure the components of the field in the X, Y, Z directions, a Flux Gate magnetometer (FGM) can be used.

2.5.2 Flux gate magnetometer (FGM)

The FGM measures the vector component of magnetic field at a particular location using the property of non linear magnetization of soft magnetic materials. The sensing element, a ferromagnetic core, is wound with coaxial excitation and pick up coil as shown in Figure 2.8 in a single axis FGM.

An alternating current is passed through the coaxial excitation coil in order to magnetize the ferromagnetic material. The core is driven through an alternating cycle of magnetic saturation due to the alternating current. This means that the magnetic polarity of the core flips back and forth when an alternating current is passed through

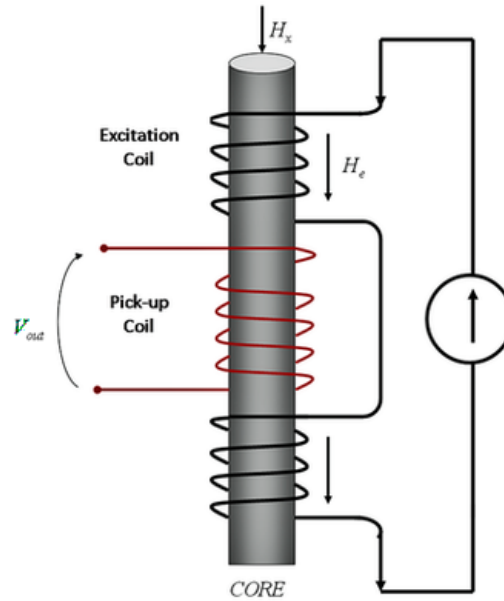


Figure 2.8: Basic circuit of a Flux Gate Magnetometer (FGM). courtesy : [http : //www.measurement.dees.unict.it/rtd_fluxgate.html](http://www.measurement.dees.unict.it/rtd_fluxgate.html).

it. The magnetic saturation occurs in each half cycle in a symmetric way. The core is easily saturable during one half of the alternating cycle while it is not in the other because the existing background geomagnetic field aids/opposes the saturation of the core when the component of induced magnetic field is parallel/antiparallel to it. As a result magnetic saturation occurs quickly in one half of the cycle while it is delayed in the other half. Due to this constantly changing field, an electrical current is induced in the secondary coil. The current in the detector is integrated to obtain an output analog voltage. However, the induced output current differs from the input current due to the influence of the geomagnetic field. The output voltage V , estimated from the measured current will be proportional to the axial component b of the total magnetic field F . If the angle between the sensing axis of the flux gate element and the direction of the total magnetic field F is given by θ , then, we have,

$$b \propto F \cos \theta \quad (2.32)$$

The magnetic flux density along the three axis, is linearly proportional to the analog voltages V_x , V_y and V_z . Hence,

$$V \propto F \cos \theta \quad (2.33)$$

The total scalar value of magnetic field can be calculated from the individual X, Y and Z vector components as

$$B = (V_x^2 + V_y^2 + V_z^2)^{1/2} \quad (2.34)$$

Table 2.5: Specifications of Bartington Mag-03 Three axis FGMc at Trivandrum (Operation manual for Mag-03 Three-Axis Magnetic Field Sensors).

Supply voltage	:	$\pm 12V$ to $\pm 17V$
Analog output	:	$\pm 10V$ ($\pm 12V$ supply)
Output impedance	:	$< 10 \Omega$
Linearity error	:	$< 0.0015 \%$
Bandwidth	:	0 to 3 kHz
standard version	:	7-10 pTrms/ \sqrt{Hz} at 1Hz
low noise version	:	< 6 pTrms/ \sqrt{Hz} at 1Hz
Supply current	:	+35 mA, -6 mA
basic and standard versions	:	(+1.4 mA per 100 T for each axis)
low noise version	:	+26 mA, -6 mA
	:	(+1.4 mA per 100 T for each axis)

A Bartington Mag-03 MSL70 FGM with three orthogonally placed fluxgate sensing elements is used at Trivandrum. The specifications of the FGM installed at Trivandrum is shown in Table 2.5. The Spectomag-6 system software which is similar to an oscilloscope (time domain) and a spectrum analyzer (frequency domain) is used for data acquisition.

2.6 Summary

The experimental techniques used for collection of data for this doctoral study has been described in detail in the present chapter. The next four chapters describe the important results obtained by analyzing the data collected from the instruments described in the present chapter.

Chapter 3

Quiet time variation of the Total Electron Content (TEC)

3.1 Introduction

As described in Chapter 1, the Earth's ionosphere can be broadly classified into the equatorial, low, mid and high latitude ionosphere. These regions, though distinct, remain connected with each other and therefore perturbations in dynamics and chemical properties at any region affects the other regions as well. Normally, what makes the ionosphere over these three regions disparate is the variations in plasma production and their distribution, which are controlled by local production and transport. In addition, dramatic variations in the behaviour of the ionosphere over these regions occur during some specific events like geomagnetic storms. To have a proper understanding of the response of the ionosphere over these regions to geomagnetic storms, it is essential to know the quiet time behaviour of the ionosphere thereat. In this chapter we study the quiet time behaviour of the ionosphere over Bharti, Hanle and Trivandrum which represents the high, mid and the dip equatorial regions in the Indian longitude, respectively.

It is known that solar Extreme Ultraviolet (EUV) radiations and X-rays ionize the neutral constituents of the atmosphere and give rise to electron density in the ionosphere through photoproduction [*Rishbeth and Garriott, 1969*]. The solar zenith angle, which controls the abundance of solar EUV at any location, is known to exhibit a prominent diurnal variation. It is therefore expected that the electron density in the ionosphere, should exhibit a diurnal variation owing to its dependence on the solar zenith angle variation [*Chapman, 1931a, b*]. On the contrary, observations of the electron density variations at these regions show considerable deviations from the zenith angle dependence [*Rishbeth and Garriott, 1969*]. Even when the solar zenith angle in a day does not vary appreciably at the polar region, the electron density exhibits a prominent diurnal variation [*Knetch, 1959*].

The quiet time behaviour of the ionosphere at the mid, low and equatorial regions is controlled by the electric fields, currents and winds generated by solar heating [*Kelley,*

1989]. Phenomena like the Equatorial Electrojet (EEJ), Equatorial Ionization anomaly (EIA) etc arise due to the horizontal configuration of magnetic field over the magnetic equator [Kelley, 1989]. These processes are known to alter the structure of not only the equatorial ionosphere, but the low latitude ionosphere as well [Rastogi, 1959; Anderson, 1973a; Walker, 1981; Tulasiram *et al.*, 2009]. Likewise, the behaviour of the ionosphere over the midlatitudes is also greatly affected by the presence of an inclined magnetic field [Rishbeth, 1972]. The inclined magnetic field over the mid latitudes assists the day-time/nighttime, poleward/equatorward winds to push the ionization downward/upward along the magnetic field [Rishbeth and Garriott, 1969]. As a result the peak height of the F-region (hmF2) reduces during daytime and increases during nighttime. These changes in the hmF2 affects the electron density distribution at mid latitude regions [Rishbeth, 1998; King *et al.*, 1967].

The ionosphere over the polar region is, however, known to differ significantly from its counterpart over low and mid latitude regions, both in terms of the plasma concentration and the physical processes prevalent therein [Kelley, 1989]. One of the reasons which makes the polar ionosphere different is an almost vertical configuration of the geomagnetic field lines which allows the interaction of the polar ionosphere with the magnetosphere and the solar wind. It, in turn, gives rise to a variety of phenomena observed exclusively over the high latitudes. At high latitudes, the energetic plasma of solar wind and magnetospheric origin enters into the atmosphere along magnetic field lines and acts as an important source of ionization [Gussenhoven *et al.*, 1984; Burch, 1968; Fang *et al.*, 2008]. The arrival of these particles into the polar atmosphere gives rise to phenomena like aurora, airglow, joule heating of the atmosphere etc [Newell *et al.*, 2009; Titheridge, 1976; Moen *et al.*, 2013]. The polar ionosphere also gets altered by factors like the ionospheric convection, and the rate of ionization of the auroral zone [Kelley, 1989]. These effects are known to prevail for several hours over the high latitudes depending on the magnetic activity. Therefore, in addition to photoionization, the structure of the polar ionosphere is modulated by the solar wind and the magnetosphere as well, resulting in the deviation from the Chapman theory of photoionization at high latitudes.

Any deviations of the ionospheric electron density distribution from the solar zenith angle dependence are termed as anomalies. Climatological studies of the Total Electron Content (TEC) and F-region peak density (NmF2) have shown annual, semi-annual and winter anomalies [Farmer *et al.*, 1990; Baron *et al.*, 1983] in the equatorial and low latitude ionosphere. Berkner and Wells [1938] were the first to report the presence of ionospheric anomalies. The origin of these ionospheric anomalies has remained a subject of keen interest among space scientists since the time of its discovery. Several investigations using ground based and satellite based observations have been conducted to understand the driving mechanisms of the anomalous behaviour of the ionosphere

[*Rishbeth and Setty*, 1961; *King et al.*, 1967; *Duncan*, 1969; *Torr and Torr*, 1973; *Millward et al.*, 1996; *Balan et al.*, 1997b; *Rishbeth*, 1998; *Mendillo et al.*, 2005; *Rishbeth and Müller-Wodarg*, 2006; *Pavlov et al.*, 2010]. The observed anomalies are normally linked to the variations in the thermospheric composition, geomagnetic field configuration and the Sun-Earth distance [*Cai et al.*, 2007; *Xu et al.*, 2014; *Zeng et al.*, 2008; *Rishbeth and Müller-Wodarg*, 2006; *Mendillo et al.*, 2005].

The annual asymmetry, in which the global average of TEC or NmF2 in December (winter) is greater than those in June (summer), is thought to arise from the additional $\sim 7\%$ solar insolation reaching the atmosphere during December as compared to June. However, this does not completely account for the observed differences in NmF2 and TEC between the two seasons [*Rishbeth and Müller-Wodarg*, 2006]. Similarly, the semi-annual anomaly, in which the TEC/NmF2 is found to be higher during the equinoxes (March/ September) as compared to the solstices (December/June), is known to be caused by variations in the thermospheric neutral composition [*Rishbeth and Setty*, 1961]. Existence of a higher TEC or NmF2 in the winter months as compared to the summer months even when the solar zenith angle dependence of electron density requires the TEC and NmF2 to be minimum in winter, is another type of anomaly in the Earth's ionosphere which is quite intriguing. This phenomena, called the winter or seasonal anomaly, is believed to be caused by the seasonal changes in the thermospheric neutral composition [*Rishbeth and Setty*, 1961; *Rishbeth*, 2000].

In addition, hemispherical differences in these anomalies are also known to exist. Observations from ionosondes, and satellites amply reflect anomaly in NmF2 and TEC at the two hemispheres. Measurements of TEC derived from Ocean Topography Experiment (TOPEX) have shown that the winter anomaly is more pronounced in the northern hemisphere during the solar maximum period than during the solar minimum period in the southern hemisphere. The offset of the southern geographic pole from the geomagnetic pole combined with the solar zenith angle variation is believed to cause the observed variations in TEC [*Millward et al.*, 1996]. Other contributions from the variations in the solar wind [*Lal*, 1992, 1998], and joule heating produced by geomagnetic activity [*Walterscheid*, 1982] to the variations in electron density have also been examined.

Our knowledge of the high, mid and low latitude ionosphere has been based on ground and satellite based measurements mostly from certain regions in the northern hemisphere. Over the southern region, images of the Antarctic ionosphere have been generated using ground based GPS receivers and validated using *insitu* measurements from Challenging Minisatellite Payload (CHAMP), Defence Meteorological Satellite Program (DMSP) satellites and Super Dual Auroral Radar Network (SuperDARN) [*Yin et al.*, 2009]. However most of the studies discuss the response of the polar ionosphere to geomagnetic storms [*Mitchell et al.*, 2005; *Shreedevi et al.*, 2016; *Foster*, 1993; *Ma*

et al., 2002, and references therein]. A comprehensive understanding of the quiet time behaviour of the southern polar ionosphere has not been achieved so far due to the lack of long term continuous measurements over the southern polar region. Coordinated studies of the quiet time behaviour of the ionosphere over the mid and low latitude regions especially from the Indian sector are also very few in number. Such studies are important mainly because a precise understanding of the spatial and temporal variations of electron density in the ionosphere is very important for satellite navigation and operational forecasts.

The present chapter aims to show how the TEC over a southern polar region (Bharti) varies with respect to the local time of a day, month, season and solar activity, and compares with observations at a mid latitude station (Hanle), and at the dip equator (Trivandrum) . Given the fact that the polar ionosphere is highly complex and most of the observations, which have been used to model the polar ionosphere, have come from the northern polar regions, it would be interesting to study how the measurements over southern polar region compares with the existing model outputs. Hence, in this chapter, observations from Bharti have been compared with predictions from the IRI 2012 model. A comparison of the TEC derived from the IRI 2012 model with the TEC derived from GPS measurements at Trivandrum and Hanle is also presented.

3.2 Database

A detailed study of the regularities and anomalies in the distribution of TEC over the Indian longitude is done using the GPS TEC measurements from three stations that represent the high, mid and equatorial regions. The geographic and geomagnetic coordinates of these stations are listed in Table 3.1.

Table 3.1: Geographic and Geomagnetic Coordinates of the stations from where TEC measurements are being made.

Station	Geo. Lat.	Geo. Lon.	Mag. Lat.	Mag. Lon.	Local Time (LT)
Bharti	69.40° S	76.18° E	76.69° S	126.93° E	UT+5 (h)
Hanle	32.8° N	78.9° E	23.92° N	153.79° E	UT+5.5 (h)
Trivandrum	8.5°N	77° E	0.02° S	149.82° E	UT+5.5 (h)

The quiet time variation of TEC over the southern polar hemisphere is studied using continuous measurements of TEC from the Indian Antarctic station, Bharti. The GPS receiver installed at Bharti has been monitoring the ionospheric TEC since 2013. Likewise, the TEC measurements from the mid latitude station, Hanle and the equatorial

station, Trivandrum are available since 2014. The GPS receivers installed at these stations provide the ionospheric Slant TEC at one minute intervals. The STEC is the total number of electrons in a column of unit cross sectional area along the satellite ray path. It is calculated by using the difference between the carrier phases (L1 and L2) of the two frequencies. The STEC values, thus obtained, are converted into Vertical TEC using the technique described by *Smith et al.* [2008]. The satellite ray paths with elevation angles greater than 35° are chosen in the calculation of VTEC at Bharti while at Hanle and Trivandrum, the STEC obtained for satellite ray paths with elevation angles greater than 45° are only converted to VTEC.

The GPS derived TEC obtained from Bharti, Hanle and Trivandrum have also been compared with the TEC predicted by the International Reference Ionosphere (IRI) model, which is one of the widely accepted empirical models for the ionosphere [*Bilitza, 2001; Bilitza and Reinisch, 2008*]. IRI-2012 being the latest version of the IRI model includes many new models for better representation of the high latitude ionosphere [*Bilitza, 2015*]. A stormtime model for the auroral E region, auroral boundary descriptions, an improved electron temperature model and new models for the electron and ion densities in the region below the F-peak are some of the newly added features. The thermosphere model was also upgraded to include the United States Naval Research Laboratory Mass Spectrometer and Incoherent Scatter Radar (NRLMSIS-00) model from the previous Mass Spectrometer Incoherent Scatter radar (MSIS-86) model. For better representation of the auroral and polar latitudes, the Corrected Geomagnetic Coordinates (CGM) was included in the IRI model. The version of IRI-2012 is accessible online at http://omniweb.gsfc.nasa.gov/vitmo/iri2012_vitmo.html.

In the following, the quiet time variation of TEC over the southern polar station, Bharti has been described first followed by the TEC variations over the mid latitude station Hanle and the dip equatorial station, Trivandrum.

3.3 Variations in the TEC at the polar station, Bharti

Since the plasma density over a polar station undergoes large changes as it traverses through regions dominated by photoionization, particle precipitation and transport processes [*Knudsen, 1974*], there can be variations in the TEC at any high latitude station as the position of the station changes with the Magnetic Local Time (MLT). The position of the polar cusp station, Bharti with respect to the auroral oval and the quiet time convection pattern is shown in Figure 3.1. During magnetically quiet times, Bharti station lies in the polar cusp region during magnetic noon, inside the polar cap at night, and in the auroral region twice a day.

During magnetically disturbed periods, both the polar cusp and the auroral oval expands and Bharti station can either be in the cusp region or inside the polar cap. Therefore, large fluctuations in the TEC over Bharti over a diurnal period as well as

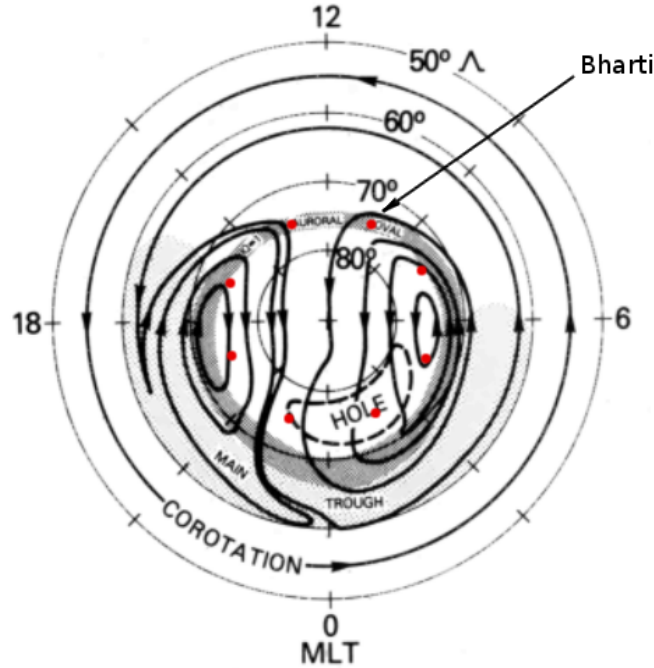


Figure 3.1: The approximate location of Bharti station (shown using red dots) with respect to the plasma convection, the quiet time auroral oval, the main trough and the polar hole [Heppner and Maynard, 1987b; Feldstein and Starkov, 1967; Brinton et al., 1978]. The Local time (LT) = Magnetic Local Time (MLT) + 3 hours at Bharti.

between a solar quiet and geomagnetically disturbed period is expected. In the following sections, the behaviour of the ionospheric TEC over Bharti, during quiet periods are investigated. GPS TEC data from Bharti over a period of 4 years starting from February 2013 to December 2016 has been analyzed to facilitate this study. The diurnal, seasonal variation of TEC and its dependence on the solar activity are described in the following subsections.

3.3.1 Diurnal variations

In order to study the quiet time variations in TEC at Bharti, in Figure 3.2 is shown the diurnal variation of TEC on 19 June 2015 ($A_p=3$), and on 13 December 2015 ($A_p=7$), chosen to represent the typical magnetically quiet winter/summer days, respectively. The TEC variation exhibits a diurnal pattern with a distinct maxima and minima. The maximum value of TEC on 13 December 2015 (summer) is 30 TECu ($1\text{TECu}=10^{-16}$ el/ m^{-2}) and on 19 June 2015 (winter) is about 15 TECu. In comparison, it is seen that on a typical summer day at Bharti, the TEC starts to increase much earlier than during a winter day and is seen to attain its maximum value at about 1200 LT which is the local noon time. However, on 19 June 2015 which is the winter day, the peak appears at 1500 LT instead, which happens to be the magnetic local noon time at Bharti. This difference in time of appearance of peak in TEC only goes to show that the reasons for

the peak in plasma density at Bharti during the summer and winter months may be different.

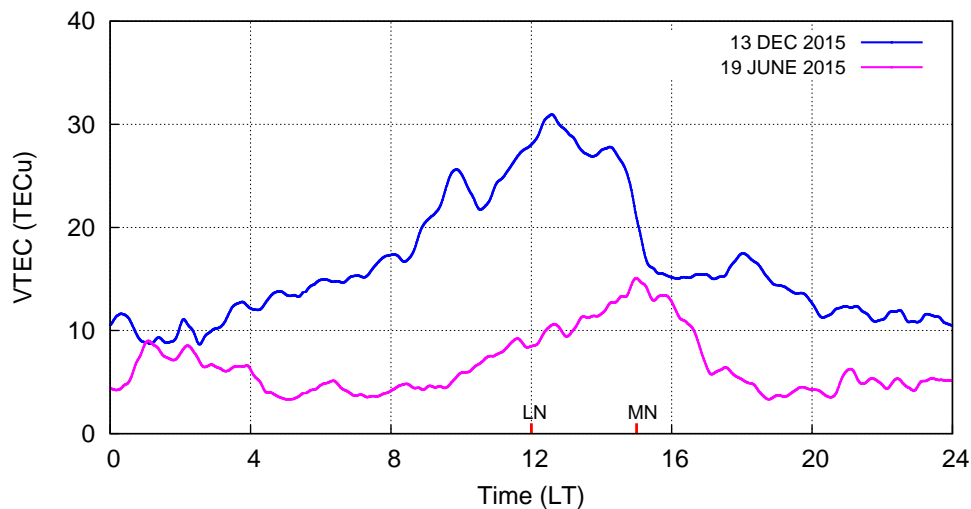


Figure 3.2: Diurnal variation of TEC at Bharti on a typical quiet day in Summer (13 Dec 2015) and in Winter (19 June 2015) respectively. The local noon (LN) and magnetic local noon (MN) at Bharti are marked in red. At Bharti, $LT = MLT + 3$ hours.

The plasma density at any place is dependent upon its local production which is solar zenith angle dependent. The solar zenith angle at Bharti during different months of a year varies as shown in Figure 3.3. It can be noted from Figure 3.3 that in the month of December, the solar zenith angle peaks at 1200 LT and remains below 100° for almost the entire period of the day. It means that although sun never goes overhead at Bharti, it receives sunlight throughout the day. A peak in TEC at 1200 LT therefore must be due to the photoionization due to solar EUV radiation. On the other hand, in the month of June also, the solar zenith angle peaks at 1200 LT, but, remains above 100° during most of the time of the day. This means that there wont be any local production of plasma due to photoionization as the station does not receive sunlight for most of the time during winter months. It is however, interesting to note that there still exists a diurnal variation in TEC during the winter months, with peak at 1500 LT which is the time when Bharti lies in the magnetic noon or cusp region as shown in Figure 3.1. Earlier studies have also shown the relationship between electron density and magnetic noon [Eccles, 1973]. Solar wind particles with energies less than 1 keV enter the high latitude ionosphere at the cusp latitudes [Heikkila and Winningham, 1971]. As the station enters the polar cusp, these soft particles ionize the neutral constituents in the F region. Hence, the cusp particles cause the observed peak in TEC to be at about 1500 LT on a typical winter day. Particles which have higher energies penetrate into the lower altitudes and affect the E and D layers of the ionosphere.

Ionospheric plasma at high latitudes is known to convect across the polar cap from the dayside of the earth to the midnight auroral zone and then drift towards the dawn

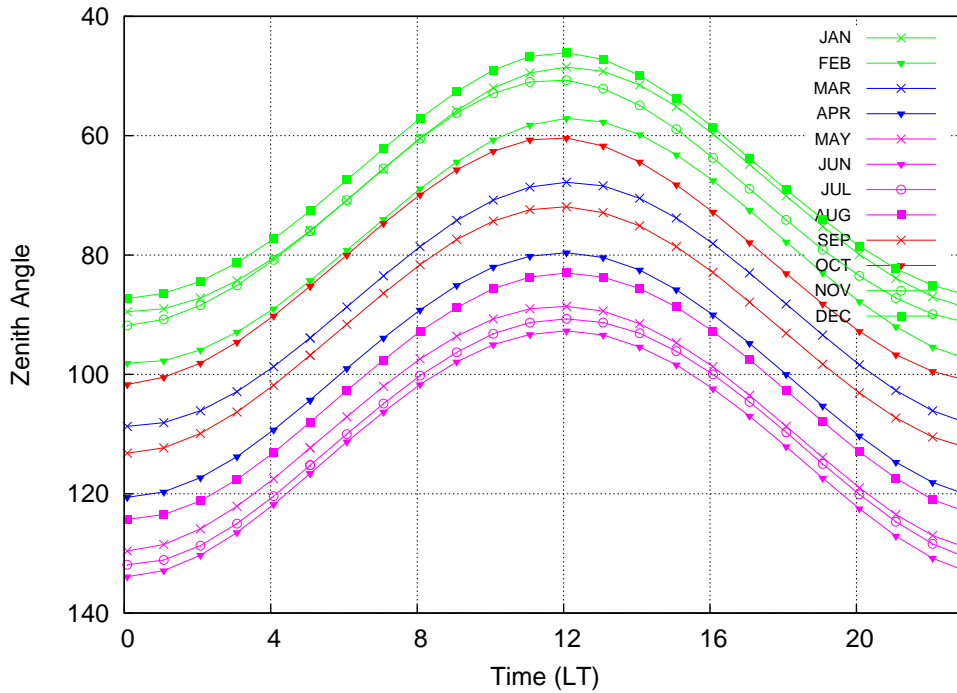


Figure 3.3: Solar zenith angle variation at Bharti: The green, red, blue and magenta colors represent the solar zenith angle variation in the Summer, September equinox, March equinox and Winter months, respectively

and dusk regions [Knudsen, 1974]. As the plasma is transported across the polar cap and into the auroral zones, it undergoes several changes determined by the chemical and transport process which alter the plasma density in the polar ionosphere. When the station leaves the polar cusp and moves into the polar cap at the nightside, the TEC minimizes because the loss processes dominate in the polar cap where solar EUV radiation is not present. The minima in TEC occurs at around local midnight on long summer days and appears earlier at 1900 LT during the long winter nights. During these times the station is located in the polar cap. After reaching the minimum at 1900 LT during winter, the TEC is seen to increase gradually and interestingly, there is an enhancement in the TEC centered around the magnetic midnight during winter. Similar enhancements have been reported earlier by *Xu et al.* [2014] at Longyearben which lies in the same geomagnetic latitude as Bharti and by *Ratovsky et al.* [2013] at Norilsk.

It is known that photoionised plasma from the dayside region can enter into the cusp and be transported across the polar cap [Moen *et al.*, 2008; Beaujardiere *et al.*, 1985]. The transpolar cap transport of plasma can contribute to the appearance of the secondary maximum in the TEC observed in the winter nights over Bharti as the station lies in the region also affected by plasma convection (as seen in Figure 3.1). The effects of plasma convection becomes important in the winter polar ionosphere especially during the solar maximum period. Plasma produced by photoionization and particle precipitation at the auroral and subauroral regions and transported into the polar cap by magnetospheric

convection can also contribute to the formation of the secondary peak in TEC during winter months [Weber *et al.*, 1984].

From the above discussion, it is clear that the diurnal variation of TEC over Bharti is dependent on the local time/magnetic local time as the variation in TEC is controlled by the movement of the station into regions dominated by photoionization, particle precipitation and plasma convection. The time dependent behaviour of the F-region electron density in the Arctic and Antarctic ionosphere was shown earlier also by many [Duncan, 1962; Beaujardiere *et al.*, 1985]. Since the TEC of the ionosphere over Bharti is controlled by the variation of the solar zenith angle and the magnetic local time, the relative importance of the solar local time and the magnetic local time in controlling the TEC variations at Bharti can be understood by studying the seasonal variations in the TEC thereat. The seasonal variation of TEC at Bharti is described in the following section.

3.3.2 Seasonal variations

The seasonal variation of the TEC at Bharti during the local seasons of the southern hemisphere which are September equinox (September, October), Summer (November, December, January, February), March equinox (March, April) and Winter (May, June, July, August) are presented in Figure 3.4. The data during the winter period (May-July) of 2014 was not available and hence, the TEC data from the winter month of August 2014 is used to represent the winter period here. From Figure 3.4, it can be seen that the magnitude of TEC during the winter months is about half of that during the summer months. The absence of solar EUV radiation can reduce the magnitude of TEC during winter months to almost half of that observed during the summer months at Bharti. The time of occurrence of the peak in TEC is also seen to shift with seasons. During the September equinox and the summer period, the TEC is seen to attain its maxima at around 1200 LT which is the local noon time at Bharti. The peak in TEC is seen to shift to 1500 LT which is close to the magnetic noon time at Bharti station during the March equinox and the winter months. It is the combined effects of both the cusp particles and the solar EUV radiation that gives rise to the observed increase in TEC at Bharti, during the September equinox which is the period of transition to summer, and March equinox which is the period of transition to winter months.

As seen in Figure 3.4, except in the year 2016, the maximum value of TEC appears during the equinoctial period. Such a semi-annual variation of TEC at Bharti is quite interesting as we expect the TEC to have its maximum value during the summer months owing to increased photoproduction [Rishbeth and Garriott, 1969]. Even though the magnitude of TEC is highest during the March equinox, it is only after 1100 LT that the value of TEC rises above the summer value indicating that it is a daytime feature. Otherwise as seen from Figure 3.4, the TEC values during the local morning sector and

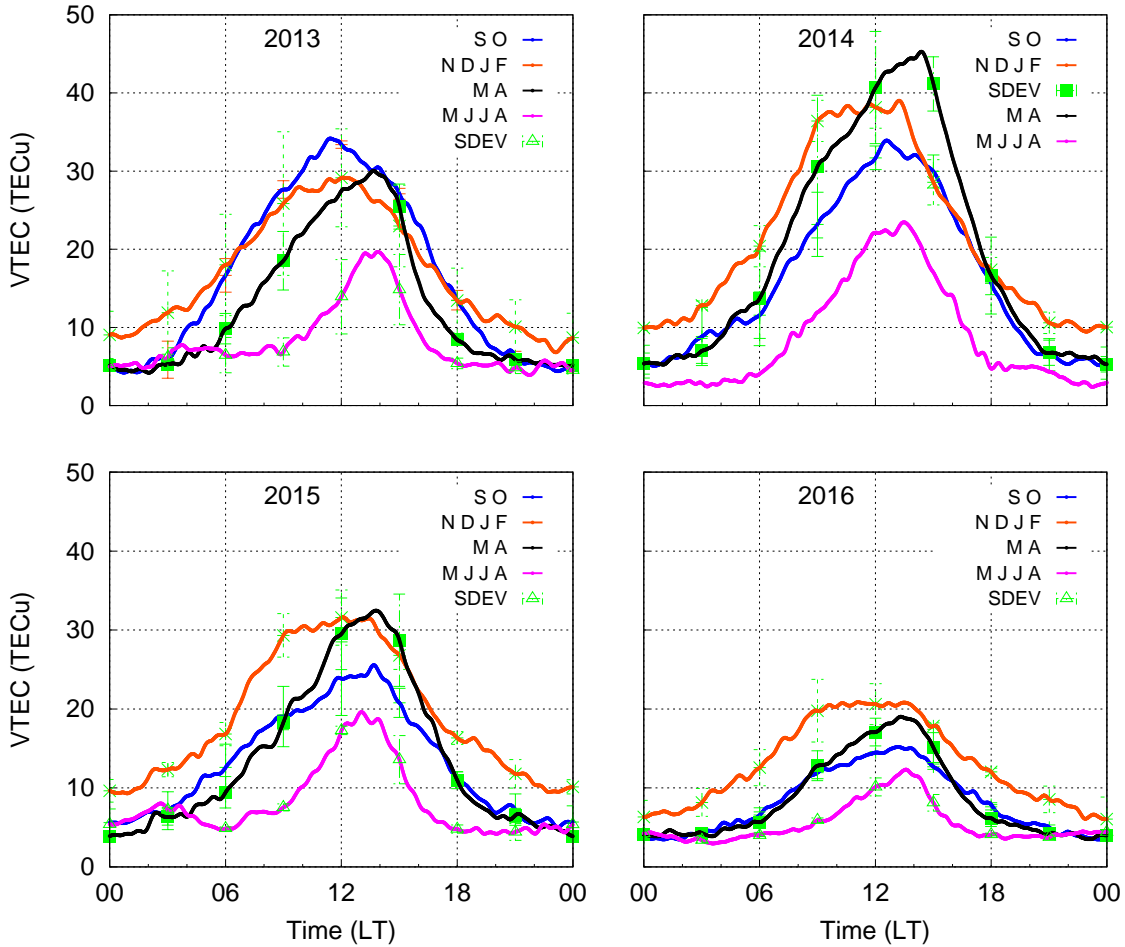


Figure 3.4: Seasonal variation of TEC at Bharti during the years 2013-2016. The winter period in 2014 is represented by the month of August as there was no data during the other winter months. S O, N D J F, M A and M J J A shown in the legend stands for September equinox, Summer months, March equinox and Winter months in the southern hemisphere, respectively

the evening sector remains higher in summer than during the March equinox. Earlier studies have shown that anomalies in electron density of the ionosphere can arise due to the changes in the neutral composition of the upper atmosphere [Rishbeth and Setty, 1961]. At Zhongshan, which is another southern hemispheric Antarctic station that lies close to Bharti, the O/N_2 ratio was shown to be higher during winter, least in summer and intermediate during the equinoxes by Xu *et al.* [2014]. It is known that the loss rate of the ionization in the ionosphere is directly proportional to the density of molecular gases and the production rate is proportional to the density of atomic oxygen [Rishbeth, 1998]. A lower O/N_2 ratio, therefore, may indicate that the molecular species are higher resulting in the loss of ionization. Even though the O/N_2 ratio is higher (which indicates more atomic species) in winter at Bharti, TEC is less compared to equinoxes. This is because photoionization remains absent for most of the period during the winter months. Similarly, the O/N_2 ratio is minimum during summer which implies

that the recombination rates are high due to the presence of molecular species resulting in a reduction of the TEC. The presence of a semi-annual anomaly and winter anomaly in NmF2 at Zhongshan has been reported by *Xu et al.* [2014]. As described earlier, the winter anomaly stands for the abnormal increase in TEC during the winter months as compared to the summer months. Even though Bharti and Zhongshan share the same geomagnetic latitude, the present study reveals the absence of winter anomaly in TEC over Bharti. Our observations agree well with those reported by *Liu et al.* [2009a] who using the mean TEC from Jet Propulsion Laboratory (JPL) GPS data have shown that the winter anomaly does not exist over the southern hemisphere. Observations of electron density from the CHAMP satellite has also showed the absence of winter anomaly above 50°S over the southern hemisphere [*Liu et al.*, 2007].

Although, March equinox seems to be the most favoured period for TEC enhancement at Bharti, the TEC is seen to peak during the September equinox in the year 2013. An equinoctial asymmetry in the magnitude of O/N₂ ratio is known to exist in the southern hemisphere. This may lead to asymmetries in the ionospheric electron densities during the equinoxes [*Zhao et al.*, 2007]. Similarly, in the year 2015, the magnitude of TEC is highest during summer months. These aspects could also be linked to the variations in the solar activity as discussed in the next section.

3.3.3 Solar activity dependence

While discussing the seasonal variations in TEC at Bharti, it was seen that the equinoctial maximum in TEC is seen in all the years except in 2016. In the year 2016, the TEC is seen to have its maximum value in the summer months. Also, the value of TEC was higher in the September equinox as compared to March equinox which is the period where the TEC usually peaks at Bharti. These variations in the magnitude of TEC may be due to the variations in the solar activity. In order to understand the solar activity dependence of TEC at Bharti, the 10.7-cm radio flux (F10.7) which is a proxy for solar activity variation is shown along with the monthly mean of TEC over Bharti for the period 2013-2016 in Figure 3.5. The F10.7 is known to exhibit good correlation with the sunspot number and can be considered to be a very good indicator of solar activity [*Balan et al.*, 1993]. The F10.7 cm flux is shown on the Y axis and the mean VTEC is shown on the Y2 axis. The mean TEC is calculated for the quietest days of the month. The good correlation of the F10.7 and the TEC at Bharti is a notable feature from Figure 3.5 also. The F10.7 which is higher in the year 2014 is seen to decrease over the period from 2014 to 2016. The mean TEC can also be seen to decrease as such over the period 2014 to 2016 and exhibits similar trend in variation as the F10.7. This suggests that the variation of TEC at Bharti depends on the solar activity.

The F10.7 is seen to vary smoothly during the equinoctial period of year 2016 without large differences in magnitude between the summer and equinoctial months. This may

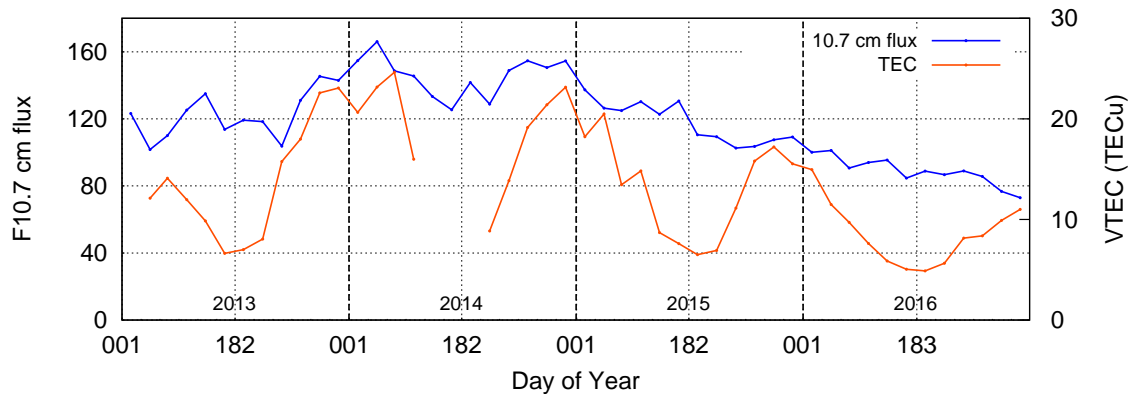


Figure 3.5: Variation of the F10.7 cm radio flux and TEC during the period 2013-2016 at Bharti. The F10.7 cm flux is shown on the Y axis and the mean TEC is shown on the Y2 axis.

be why the TEC at Bharti remained lower during the equinoctial period of 2016 (shown in Figure 3.4). A similar trend can be seen in the year 2013 also wherein the F10.7 starts to increase during the September to December months resulting in the higher value of TEC during the September equinox (Figure 3.4). This suggests that the mean TEC increases faster with increasing solar EUV fluxes at high latitudes. Similar relationship between the variation of TEC at high latitudes and the F10.7 was also shown by *Liu et al.* [2009a].

3.4 Variations in the TEC at the mid latitude station, Hanle

The mid latitude ionosphere is known to exhibit anomalous behaviour in the electron density [*Rishbeth and Garriott, 1969*]. The temporal, seasonal and solar activity dependence of electron density over mid latitude regions have been studied and modeled extensively [*Millward et al., 1996; Rishbeth and Mendillo, 2001, and references therein*]. Nevertheless, there has been differences in conclusions regarding the seasonal and solar activity dependence of electron density over the mid latitude regions [*Rishbeth and Mendillo, 2001; Zhao et al., 2007; Xu et al., 2014; Rajesh et al., 2016, and references therein*]. This is partly because most of the observations are limited to certain areas in the northern hemisphere while the mid latitude ionosphere is also influenced by changes happening in the polar as well as low latitude regions. Studying the electron density variations over the Indian region, which extends from the dip equator to anomaly crest region and to the mid latitudes in the northern hemisphere can give a clear understanding of the processes that contribute to the variation of TEC over a mid latitude station in the Indian region. Moreover, there have been very few reports of TEC measurements from a mid latitude stations in the Indian region so far. In this regard, the diurnal, seasonal

and annual variation of the TEC over the northern hemispheric mid latitude station Hanle (32.8°N , 78.9°E) has been studied for the first time. Hanle, which lies outside the focus of the Solar quiet (Sq) current system, represents a typical mid latitude station. The diurnal variation of TEC at Hanle is described in the following section.

3.4.1 Diurnal variations

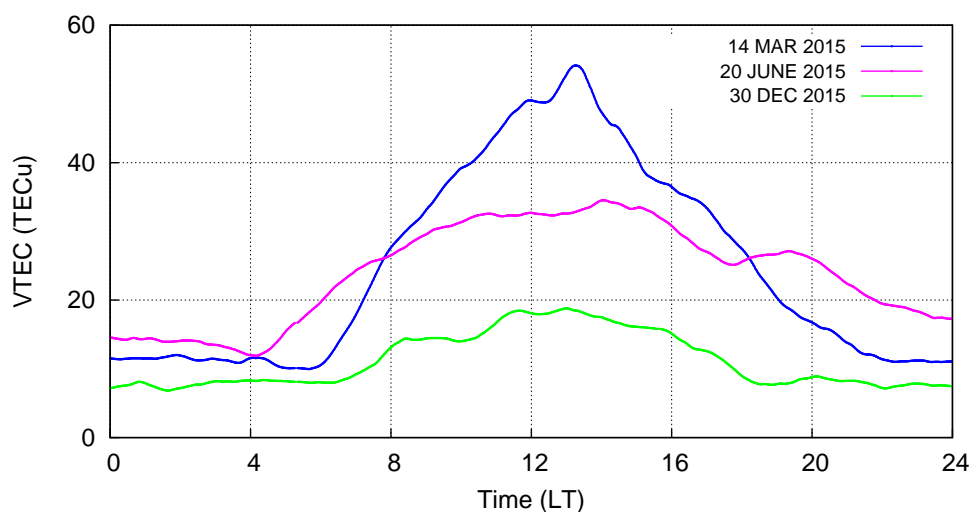


Figure 3.6: Diurnal variation of TEC at Hanle on a typical quiet day in the Summer, Winter and Equinoctial period, respectively

The diurnal variation of TEC over Hanle for three quiet days i.e., 14 March 2015 ($A_p=5$), 20 June 2015 ($A_p=1$) and 30 Dec 2015 ($A_p=2$) is shown in Figure 3.6. These three days are chosen to represent the variation of TEC on a typical quiet day during the equinox, summer and winter period, respectively. Evidently, the TEC over Hanle increases steadily after sunrise. The increase in TEC starts around ~ 0400 LT on a typical summer day while it starts at around ~ 0600 LT during the equinoctial period. The build up of TEC starts at a much later time (~ 0700 LT) in the winter months. This is expected as the sun rises much later in winter as compared to the other months over a mid latitude station. The TEC reaches a maximum value at around local noontime when the sun is overhead. The TEC decays gradually to a minimum value in the predawn hours owing to the absence of solar radiation at nighttime which inhibits photo production. The evolution of TEC with respect to time is obviously synchronized with the position of the sun with respect to the location. However, the nighttime enhancement evident in TEC on 20 June 2015 (shown in Figure 3.6) is interesting. Such an enhancement in TEC at mid latitude regions is known to be caused by the action of thermospheric winds. It is well known that during summer, the strong equatorward winds at nighttime push the ionization up along the inclined magnetic field lines at the midlatitudes [King *et al.*, 1967; Rishbeth, 1998]. This leads to an elevated ionosphere because of which the loss coefficient reduces resulting in the sustenance of ionization at night.

3.4.2 Seasonal variations

The mean seasonal variation of TEC recorded at the mid latitude station, Hanle for the years 2014-2016 is shown in Figure 3.7. The local seasons of the northern hemisphere are March equinox (March, April), September equinox (September, October), Summer (May, June, July, August) and Winter (November, December, January, February). The variation of TEC during these seasons are represented in Figure 3.7 using blue, black, red and magenta colors, respectively. The standard deviation is represented using green color. The TEC data during the September equinox of 2016 was unavailable and hence not shown in Figure 3.7.

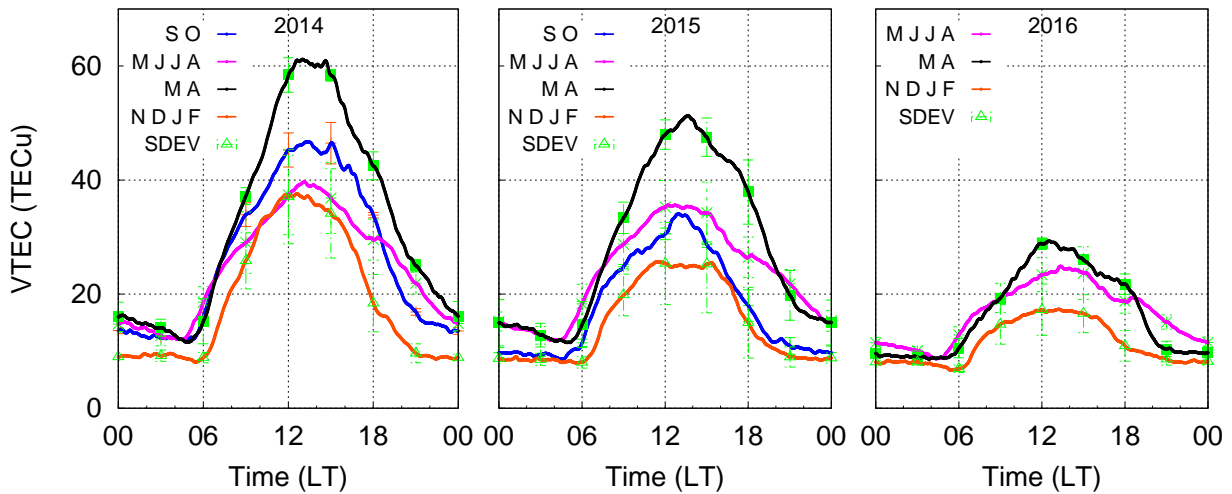


Figure 3.7: Seasonal variation of TEC at Hanle during the years 2014-2016. S O, N D J F, M A and M J J A shown in the legend stands for September equinox, Summer months, March equinox and Winter months in the northern hemisphere, respectively

The first important observation from Figure 3.7 is the presence of higher values of TEC during the equinoctial period as compared to the solstices during the years 2014-2016. This implies the presence of the semi-annual anomaly at Hanle. Secondly, the winter anomaly (in which the TEC is seen to exhibit higher values in winter as compared to summer) is not seen at Hanle during the three years. Instead, the minimum TEC at Hanle is recorded during the winter months while the TEC in summer months have intermediate values. A large number of observational and modeling studies in the past have shown the semi-annual anomaly and the winter anomaly to be caused by changes in the upper atmospheric chemical composition [Rishbeth and Setty, 1961; King et al., 1967; Rishbeth, 1972; Balan et al., 1997b; Rishbeth, 2000; Zhao et al., 2007, and references therein]. As described by these studies, the semi-annual variation in TEC arises due to the asymmetry in atmospheric mixing induced by asymmetric heating of the atmosphere over both the hemispheres [Fuller-Rowell, 1998; Rishbeth, 1998, 2000]. During equinoxes, there is uniform heating of the atmosphere over both the hemispheres which leads to a state of diffusive equilibrium as the atmospheric mixing is balanced by

the daytime poleward winds and the nighttime equatorward winds [Rishbeth, 2000]. In other words, the O/N_2 ratio will be higher during equinoxes as compared to the solstices due to the absence of trans-hemispheric winds. A higher O/N_2 ratio means lower loss rates and hence the magnitude of TEC will be highest during the equinoxes. The semi-annual anomaly in TEC over Hanle is present during the period 0800-1800 LT as seen from Figure 3.7 indicating that it is a daytime feature produced by solar heating of the atmosphere. Another mechanism thought to contribute to the semi-annual variation of electron density over the middle and low latitudes is the semi-annual variation inherent in coupling of the interplanetary and terrestrial magnetic fields [Lal, 1998; Russell and McPherron, 1973].

It can be seen from Figure 3.7 that the value of TEC at Hanle is lesser in the summer months than that observed during the equinoctial period, inspite of Hanle receiving maximum insolation during the summer months. During solstices, the summer hemisphere receives maximum solar radiation and the prevailing neutral winds blow from the summer to winter hemisphere. This leads to upwelling in the summer hemisphere thereby raising the molecular rich air to higher altitudes which inturn enhances loss by recombination [Rishbeth, 2000]. This causes a reduction in the TEC in at a northern midlatitude station like Hanle during summer. Similarly, during the winter months, the prevailing neutral winds blow from the summer to winter hemisphere and causes downwelling in the winter hemisphere [Rishbeth, 1972]. The downwelling air brings in atomic rich species leading to a reduction in the O/N_2 ratio and a subsequent increase in the TEC. However, this is not the case at Hanle during the winter solstice. Infact, the TEC is lowest during the winter months at Hanle as shown in Figure 3.7. This could be because Hanle may not be the location where downwelling takes place. Usually, the convergence of the equatorward winds induced by auroral heating and the poleward winds generated by solar heating would take place at a midlatitude station located in a longitude sector close to the geomagnetic poles leading to an increase in TEC thereat. Since Hanle lies at a longitude sector far away from the northern geomagnetic pole, the downwelling of trans-equatorial winds may take place at a higher latitude during winter solstices. In addition, the large values of solar zenith angle at Hanle during the winter period causes limited photoproduction. A combination of these factors could cause the TEC values to be lower during winter solstice at Hanle as observed in Figure 3.7. The absence of winter anomaly can also arise if the solar activity is high enough during the summer period to cause higher TEC in summer than in winter. This aspect has been discussed while discussing the solar activity dependence of TEC at Hanle in the subsequent sections.

Another characteristic feature is the equinoctial asymmetry in TEC at Hanle. This can be seen in Figure 3.7 as the presence of higher TEC during March equinox as compared to that during the September equinox. The equinoctial asymmetry in TEC

may be due to the asymmetries in the thermosphere arising due to neutral winds and chemical processes [Balan *et al.*, 2000]. Using measurements from the MU radar at Shigaraki (35°N, 136° E) for a solar maximum period, it was shown by Balan *et al.* [2000] that the neutral winds during the March and September equinox are asymmetric. Their results showed that at F_2 layer heights, the daytime poleward wind is upto 50% weaker and the nighttime equatorward wind is upto 40% stronger during March equinox as compared to the September equinox. As the poleward winds act to lower the ionosphere whereas the equatorward winds raise the ionosphere over the mid latitudes, weaker poleward winds during the March equinox results in a elevated ionosphere. This inturn leads to higher TEC during the March equinox and could be the main reason for the observed equinoctial asymmetry.

3.4.3 Solar activity dependence

It is well known that the solar activity has a profound control over the production of plasma in the ionosphere. In order to understand the solar activity dependence of TEC at Hanle, the monthly mean TEC over Hanle for the period 2014-2016 is compared with the F10.7 as shown in Figure 3.8. The F10.7 cm flux is shown on the Y axis and the mean VTEC is shown on the Y2 axis. The mean TEC is calculated for the quietest days of the month.

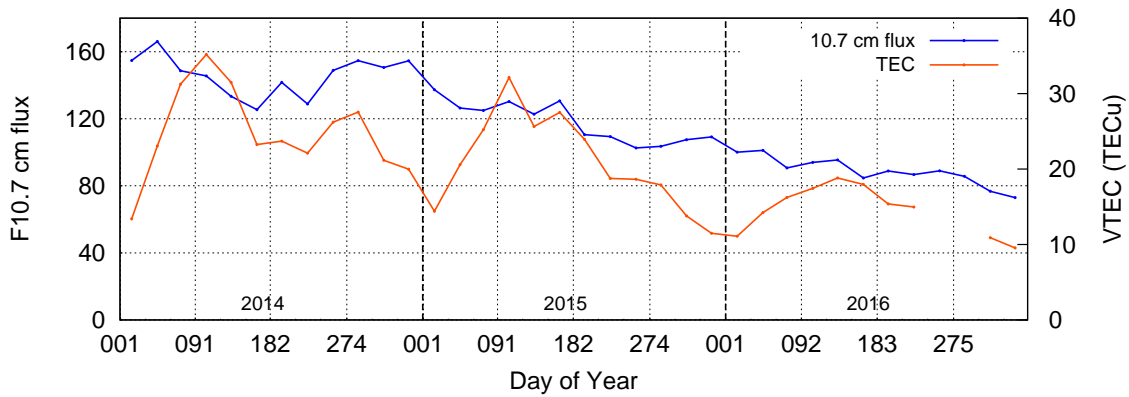


Figure 3.8: Variation of the F10.7 cm flux and mean TEC at Hanle during the period 2014–2016. The F10.7 cm flux is shown on the Y axis and the mean VTEC is shown on the Y2 axis.

A general reduction in the mean TEC is clearly seen in Figure 3.8 over the years starting from 2014. This can be attributed to be due to the decrease in F10.7 in 2015 and 2016 as compared to 2014. The F10.7 is on average greater during the summer months as compared to the winter months during all the three years as seen in Figure 3.8. A greater solar flux during the summer months implies increased photoproduction and hence higher TEC [Ramarao *et al.*, 1985]. This could contribute to the absence of the winter anomaly over Hanle. Earlier studies have shown that the TEC of the ionosphere increases with

the increasing EUV fluxes [Liu *et al.*, 2009a]. As expected, the present results also show that the TEC increases with increasing solar activity and is in agreement with earlier studies.

3.5 Variations in the TEC at the dip equatorial station, Trivandrum

The equatorial ionosphere exhibits unique features due to the horizontal configuration of magnetic field therein which forms the base for a variety of fascinating phenomena like the EEJ and the EIA. These processes play a significant role in altering the distribution of plasma density over the equatorial and low latitude region. These processes are known to exhibit solar cycle, seasonal and day to day variations which also affects the daily variations in the electron density [Kelley, 1989]. Though a number of studies have been conducted in this region, GPS TEC measurements recorded at Trivandrum were studied in order to understand the diurnal, seasonal and annual variation of TEC over the dip equatorial station Trivandrum during the period 2014-2016. The diurnal and seasonal variations of the TEC at Trivandrum are described in the sections that follow.

3.5.1 Diurnal variations

The diurnal variation of TEC over Trivandrum on three quiet days, 14 March 2015 ($A_p=5$), 20 June 2015 ($A_p=1$) and 30 December 2015 ($A_p=2$) are presented in Figure 3.9. These days represent typical equinoctial, summer and winter period, respectively. The TEC on all the three days is seen to increase immediately after sunrise. As described in the previous sections, photoproduction begins immediately after sunrise resulting in the build up of TEC over a particular location. The TEC is seen to increase gradually and attain a broad maximum at around 1600 LT on 14 March 2015. Normally, the peak in TEC is expected to occur around local noon considering its dependence on the solar zenith angle. But, at a dip equatorial station like Trivandrum, the occurrence of the peak gets delayed because of the fountain effect [Hanson and Moffett, 1966] which in turn depends on the strength of the EEJ [Onwumechili, 1998]. Since the strength of the EEJ maximizes around the local noon, the vertical pumping of plasma from the dip equatorial station via magnetic field lines to off equatorial regions continues and is maximum around local noon [Stolle *et al.*, 2008]. This process leads to the removal of plasma from the dip equator which can be seen as the noon time dip in TEC on 14 March 2015 in Figure 3.9. As the EEJ strength starts to decrease, the fountain effect weakens leading to the build up the TEC over the dip equatorial station. Consequently, the maximum value of TEC over a dip equatorial station appears with a delay.

Later, the TEC decays quickly and is observed to reach a minimum value in the predawn hours (0500-0600 LT) during the summer and winter period. A secondary

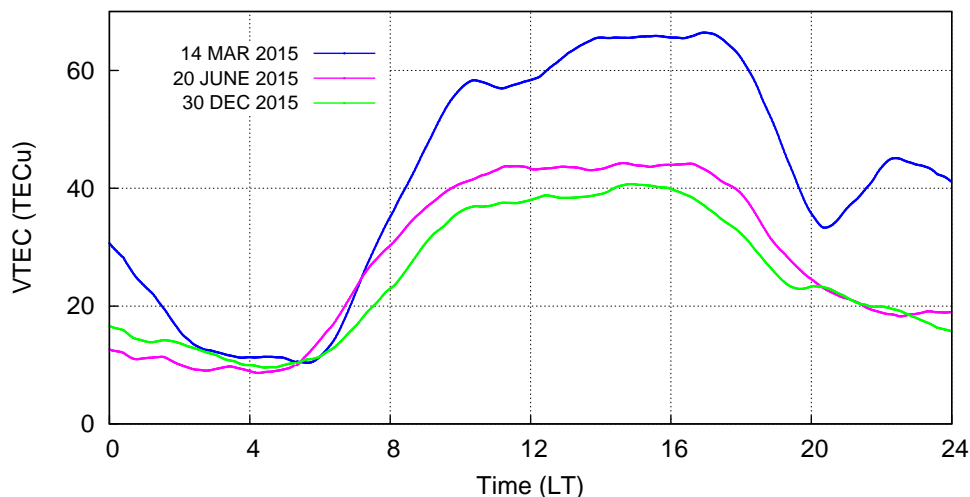


Figure 3.9: Diurnal variation of TEC at Trivandrum on a typical quiet day in the Summer, Winter and Equinoctial period, respectively

peak in the TEC is observed during the nighttime on 14 March 2015, which is the equinoctial period. The nighttime enhancement in TEC observed at Trivandrum during the equinoctial period is caused by the reverse fountain effect [Balan and Bailey, 1995]. This feature is not prominent during the solstices owing to weak evening time F region vertical drifts in the solar minimum period [Fejer *et al.*, 1979] and thus a weak fountain effect. Similar variations in the TEC at the equator has been shown by previous studies [Ramarao *et al.*, 2006; Bhuyan and Borah, 2007]. Owing to the large variabilities in the EEJ and the EIA, the TEC over an equatorial station is expected to exhibit significant, seasonal and solar activity dependencies. The seasonal and solar activity dependencies of the TEC over the dip equatorial station Trivandrum is discussed in the following.

3.5.2 Seasonal variations

The variation of TEC during different seasons over the dip equatorial station Trivandrum is presented in Figure 3.10. The mean TEC calculated for the four local seasons of the year namely, March equinox (March, April), Summer (May, June, July, August), September equinox (September, October) and Winter (November, December, January, February) is used to study the seasonal variation of TEC. The blue, red, black and magenta curves in Figure 3.10 represent the Spring, Summer, Autumn and Winter seasons respectively and the standard deviation is shown using green.

As seen in Figure 3.10, the TEC over Trivandrum attains its highest value during the equinoctial period and therefore exhibits the semi-annual anomaly. A combination of factors are known to cause semi-annual anomaly in TEC at Trivandrum. Firstly, the equatorial region receives maximum solar EUV flux during the equinoctial period. As the position of the sun is overhead at the equator during the equinoxes, the solar zenith angle also remains low causing maximum ion production over an equatorial station. Secondly,

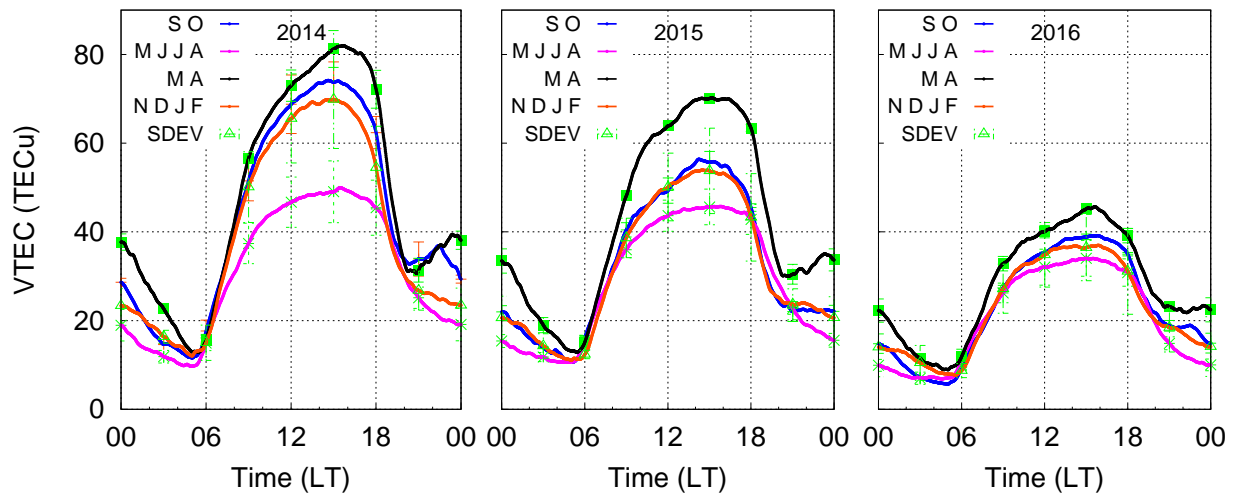


Figure 3.10: Seasonal variation of TEC at Trivandrum during the years 2014-2016. S O, N D J F, M A and M J J A shown in the legend stands for September equinox, Summer months, March equinox and Winter months in the northern hemisphere, respectively

because of the absence of prevailing meridional wind circulation, the thermospheric composition is also fairly uniform during the equinoxes [Rishbeth, 2000]. This implies that a diffusive equilibrium prevails as the upwelling caused by the poleward winds during daytime is balanced by the downwelling caused by the equatorward winds during nighttime. Consequently, as compared to the solstices, the thermosphere has a higher O/N_2 ratio during equinoxes. A higher O/N_2 ratio means lower recombination and by that means an increase in the TEC. In addition, the EEJ strength and the resulting F region vertical drifts in the equatorial ionosphere are strongest during the March equinox [Onwumehili, 1998]. This leads to raising of the F region to altitudes where the effect of recombination will be minimal and results in the sustenance of ionization during the equinoctial months. These factors lead to the equinoctial maxima/semi-annual anomaly in TEC over the equatorial station, Trivandrum. Several studies in the past have shown the presence of the semi-annual anomaly in the TEC at dip equatorial stations [Ramarao et al., 2006; Bhuyan and Borah, 2007, and references therein]

Another important feature evident in Figure 3.10 is the presence of higher TEC during winter months as compared to the summer months at Trivandrum. This could be because the thermosphere at F_2 layer altitudes is more molecular during summer period [Rishbeth and Garriott, 1969]. Hence, the availability of more molecular species during the summer period leads to a reduction in the electron density as the removal of electrons at F_2 layer heights takes place mainly through the dissociative recombination of molecular nitrogen. Therefore in summer period, the TEC is be lowest as shown in Figure 3.10.

3.5.3 Solar activity dependence

In order to understand the solar activity dependence of TEC at Trivandrum, a comparison of the monthly mean TEC over Trivandrum for the period 2014-2016 is made with the F10.7 which is a good indicator of solar activity as shown in Figure 3.11. In general, a reduction in the magnitude of TEC can be observed starting from the years 2014 to 2016 in line with the F10.7 variation. The mean TEC which follows a similar trend as F10.7 can be seen to increase/decrease as the F10.7 increases/decreases.

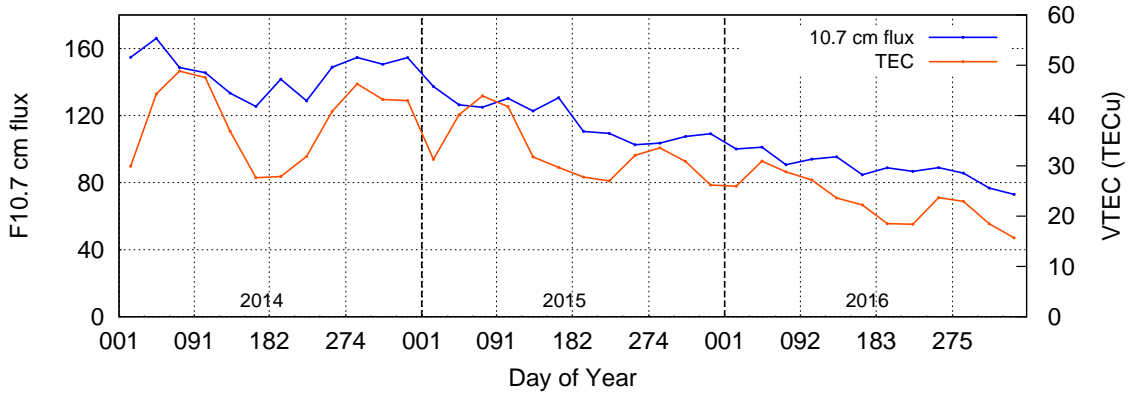


Figure 3.11: Variation of the F10.7 cm flux and mean TEC at Trivandrum during the period 2014-2016. The F10.7 cm flux is shown on the Y axis and the mean TEC is shown on the Y2 axis.

An increase in the F10.7 implies an increase in the solar EUV flux. This, in turn, leads to an increase in photoionization and by that means to an increase in the TEC of the ionosphere. Previous studies have also shown the level of ionization at Trivandrum to be higher during high solar activity periods and vice versa [Ramarao *et al.*, 2006; Kavita *et al.*, 2012]. Our results are also in agreement with the fact that the magnitude of TEC at Trivandrum shows dependence on the solar activity.

3.6 Latitudinal variations in the TEC

While the TEC over the low and equatorial latitudes is modulated by the processes like the EIA, the TEC over the high latitudes and the mid latitudes is greatly affected by non-local processes. Since the polar ionosphere is electro-dynamically and neutral-dynamically coupled to the mid, low and equatorial ionosphere, measurements of the TEC starting from the poles to the equator have been necessary to form a complete understanding of the global distribution of TEC. A comparison study of the TEC variations over Bharti, Trivandrum and Hanle during the year 2015 is presented in the following to have a general understanding of the latitudinal distribution of TEC over these stations that have almost the same local times.

In panels (a), (b), (c) and (d) of Figure 3.12, is shown the variation of the TEC over

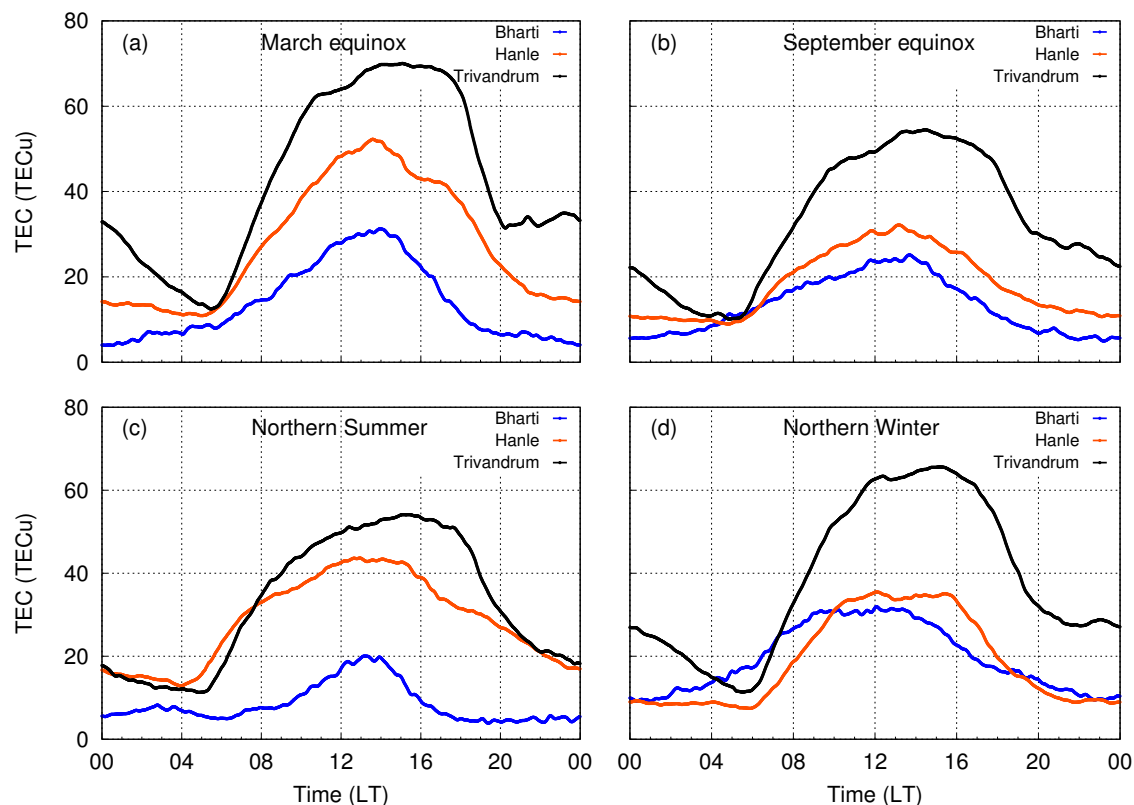


Figure 3.12: Panels (a)-(d) represents the variation of TEC at Bharti, Hanle and Trivandrum during the March equinox, September equinox, Northern summer and Northern winter months of the year 2015, respectively.

Bharti, Hanle and Trivandrum during the March equinox, September equinox, northern summer solstice and northern winter solstice of the year 2015 respectively. It is found that, the daytime electron density is highest over the dip equatorial station, Trivandrum during all months of the year as compared to the mid latitude station Hanle or the polar station Bharti. This is because, the production of ionization will be maximum at the equator as it receives the maximum insolation during equinoxes. Also, the horizontal magnetic field over the magnetic equator, when combined with the perpendicular electric field (which is strongest during the equinoxes), uplifts the ionosphere to higher altitudes during daytime [Onwumechili, 1998]. This leads to a reduction in the loss rates and by that means an enhancement in TEC at the equator during the equinoctial period. Meanwhile, due to the latitudinal gradient in photoproduction, the TEC over Hanle and Bharti remains lower as compared to Trivandrum. In comparison, during the equinoctial period, the maximum difference in TEC occurs during the noontime, while the magnitude of TEC is almost the same at pre-dawn hours at all the three stations as seen in Figure 3.12.

A somewhat similar situation exists during the other months also. In spite of the fact that maximum insolation is received at the northern midlatitude station, Hanle during the summer months, the maximum TEC is observed at Trivandrum as shown in panel

(c) of Figure 3.12. The action of the trans-hemispheric winds is believed to reduce the daytime electron density at the mid latitude station Hanle. The daytime poleward winds push the ionization down along the inclined magnetic field to lower altitudes where the recombination is high [Rishbeth, 1998; King et al., 1967]. This leads to a reduction in the TEC at Hanle. The situation is however quiet different at Bharti. As the southern polar region is in the winter hemisphere during the northern summer, there is complete absence of solar illumination at Bharti. As a result, the TEC recorded at Bharti will be lowest during the northern summer solstice.

However, as shown in panel (c) of Figure 3.12, during the northern winter solstice also (southern summer), the TEC is found to be maximum at Trivandrum. The TEC is low at Hanle during the northern winter owing to limited photoproduction caused by large value of the solar zenith angle thereat. Although, Bharti station receives maximum daylight during this period, the TEC is lower than that at Trivandrum and Hanle except for a short duration in the morning time. A general reduction in TEC is always observed at a high latitude station due to the presence of permanent composition disturbance zone induced by particle precipitation and ionospheric convection [Prölss, 1995] as well as the latitudinal gradient in solar insolation.

It is clear from the discussions of the quiet time variations in the TEC at Bharti, Hanle and Trivandrum that the inclined and horizontal magnetic field configurations at the mid and equatorial regions, respectively gives rise to fundamental differences in the electrodynamics and the neutral dynamics in the mid and equatorial ionosphere as compared to the high latitude ionosphere. While the quiet time behaviour of the mid and equatorial ionosphere is mostly controlled by the electric fields and winds generated by solar heating, the morphology of the quiet time polar ionosphere is significantly affected by the magnetospheric processes [Kelley, 1989].

3.7 Comparison with the IRI 2012 model

The IRI model is the most widely accepted empirical model used to represent the ionosphere. The model includes observations from a wide range of ground based and satellite based measurements and is being continuously improvised by experts [Bilitza, 2015]. Several studies on the comparison of the IRI derived TEC and GPS derived TEC have been performed in the past to test the ability of the IRI model to predict variations in TEC over different geographical regions as well as under varying solar activity conditions [Batista et al., 1994; Abdu et al., 1996; Bhuyan and Borah, 2007; Venkatesh et al., 2014]. Such studies showed that the TEC derived from the IRI model agrees with the GPS derived TEC over the northern mid latitudes [McNamara, 1984, 1985]. However only a few studies have been conducted to evaluate the performance of the IRI model in predicting the behaviour of the high latitude ionosphere [Themens et al., 2014; Moen et al., 2013; Maltseva et al., 2013]. Most of such studies are based on the

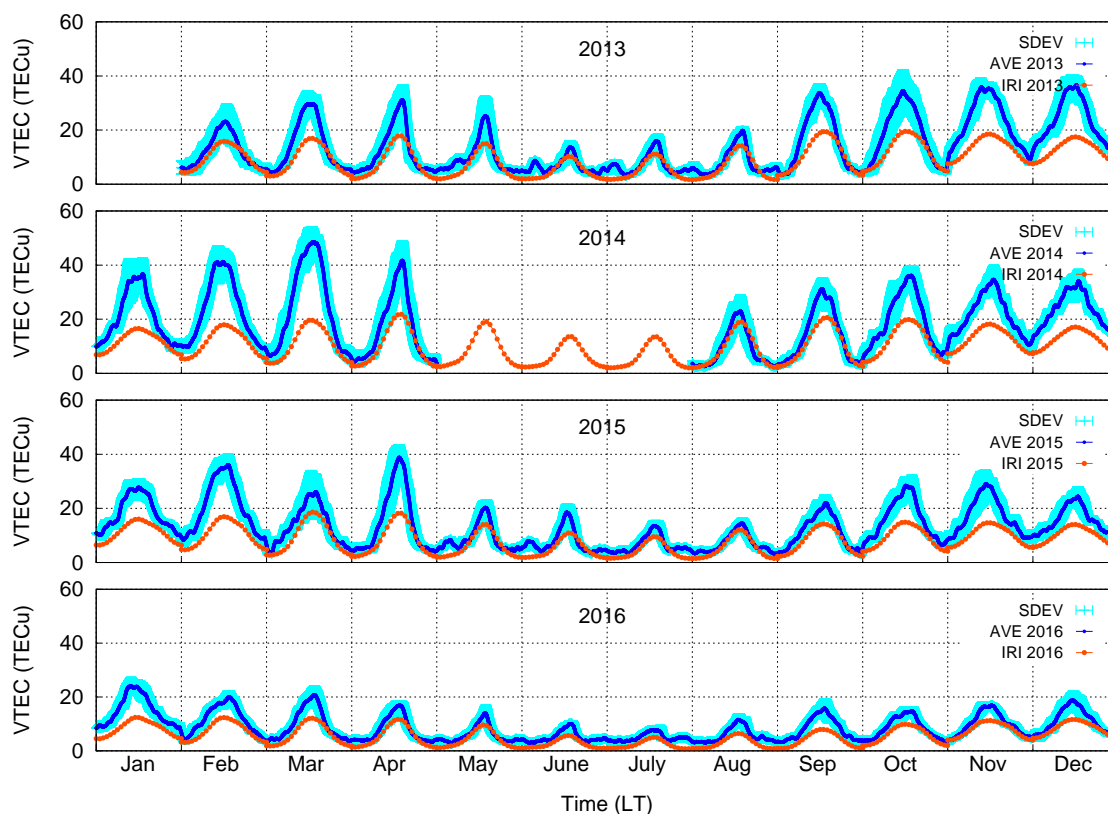


Figure 3.13: Variations in the TEC at Bharti during the years 2014-2016, derived from GPS and IRI model. The quiet time mean and standard deviation of the GPS TEC is represented using black and green color, respectively. The IRI derived TEC is represented by orange color.

northern polar ionosphere only. Even so, the comparison of the IRI 2007 derived hmF2 and NmF2 with the hmF2 and NmF2, derived using the ionosonde measurements from stations located in the northern polar cap showed large differences [Themens *et al.*, 2014]. The IRI 2012 model which is the latest version incorporates new features for better representation of the high-latitude ionosphere [Bilitza, 2015]. The evaluation of the IRI 2012 model in representing the southern polar ionosphere has not been done so far. Since only limited data are available from the high-latitude ionosphere where processes like particle precipitation and magnetospheric convection play a major role in controlling the variability of the plasma density, it would be interesting to examine how well the IRI 2012 model represents the southern high latitude ionosphere. In this context, we present a comparison of the TEC measured from the southern polar station, Bharti with the TEC predicted by the IRI 2012 model.

The variation in the TEC at Bharti obtained from GPS measurements and IRI 2012 model over a period of 4 years starting from February 2013 to December 2016 is presented in Figure 3.13. There is a data gap in the GPS TEC shown in Figure 3.13 during the period May 2014-July 2014 due to unavailability of TEC data during that period. The quiet time mean calculated for the 5 quietest days of a month is represented using the

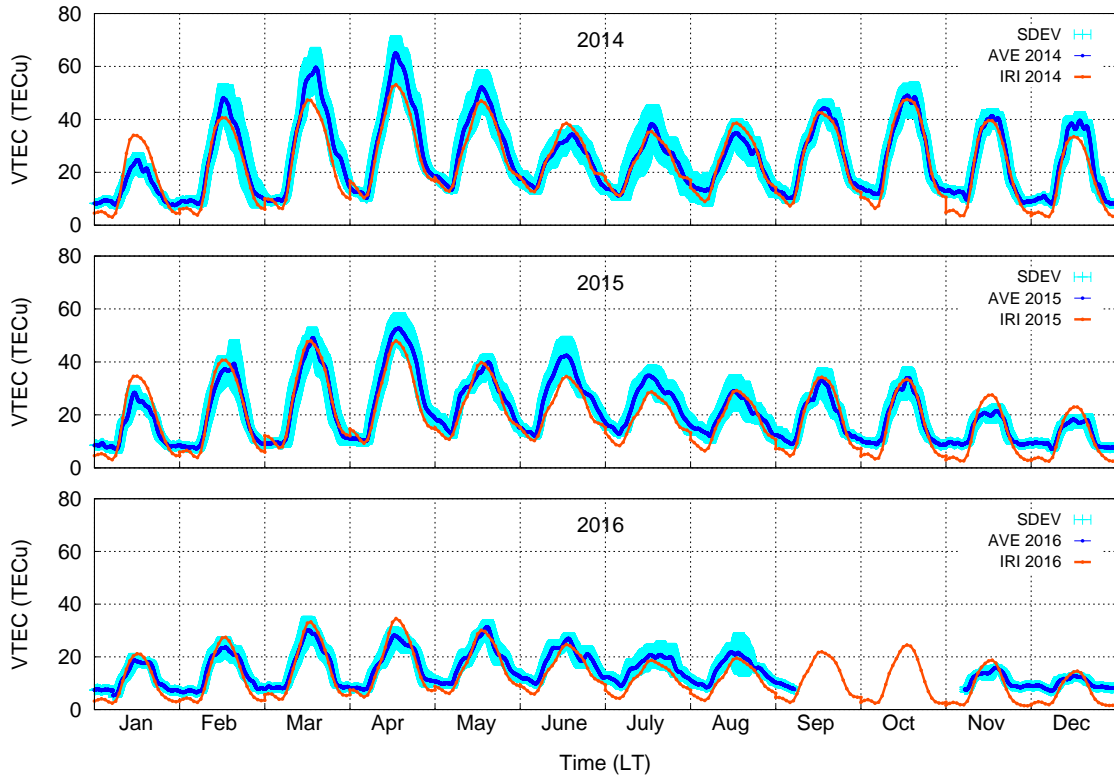


Figure 3.14: Variations in the TEC at Hanle during the years 2014-2016, derived from GPS and IRI model. The quiet time mean and standard deviation of the GPS TEC is represented using black and green color, respectively. The IRI derived TEC is represented by orange color.

black curve in Figure 3.13. The standard deviation is represented using the cyan color. The variation of TEC predicted by the IRI 2012 model is shown by the orange curve along with the GPS derived TEC in Figure 3.13. During the summer and equinoctial months of the year 2014, there is a threefold difference in magnitude between the TEC predicted by the IRI 2012 model and the measured GPS TEC. Large differences in the magnitude of the model predicted TEC and the observed TEC is seen particularly during the summer months of 2013, 2015 and 2016 also. On the other hand, the IRI model predicted TEC for winter months, matches well with the GPS TEC observations even though the nighttime enhancement in TEC is not seen in the IRI 2012 model derived TEC. The absence of the nighttime enhancement in the TEC predicted by the IRI 2012 model points to the fact that the cross polar cap transport processes have not been well accounted for in the model. In an earlier study, *Moen et al.* [2008] have shown that the IRI 2001 model does not represent the cross polar cap transport of the F_2 region plasma and hence cannot be applicable to the polar cap regions in the northern hemisphere. Another notable point is that the TEC obtained from the model also has its maximum during the equinoxes rather than the summer months suggesting the presence of a semi-annual anomaly in the variation of TEC at Bharti. This suggests that the

neutral composition changes are well represented in the IRI 2012 model.

While the northern hemispheric mid latitude TEC is shown to be represented well by the IRI model, differences in the IRI derived TEC and GPS derived TEC for the northern hemispheric equatorial latitudes have been shown to exist [Bhuyan and Borah, 2007; Lühr and Xiong, 2010; Venkatesh et al., 2014; Olwendo et al., 2013]. In order to study how the IRI 2012 model represents the TEC over the mid latitude station, Hanle and the equatorial station, Trivandrum, a comparison of the same is presented here. The variation of TEC over the northern midlatitude station, Hanle during the years 2014-2016 as obtained from GPS measurements as well as IRI 2012 model is shown in Figure 3.14. The mean TEC calculated for the 5 quietest days of the month is shown using the blue curve in Figure 3.14. The standard deviation is represented using cyan color. The IRI derived TEC is represented by the orange curve in Figure 3.14. It is seen from Figure 3.14 that the IRI derived TEC is well in agreement with the GPS derived TEC at Hanle. The only exception is the underestimation of the TEC by the IRI model during the nighttime period in the winter months of all the years. The daytime TEC in the winter months of the year 2015 and January 2014 also shows deviations from the GPS TEC.

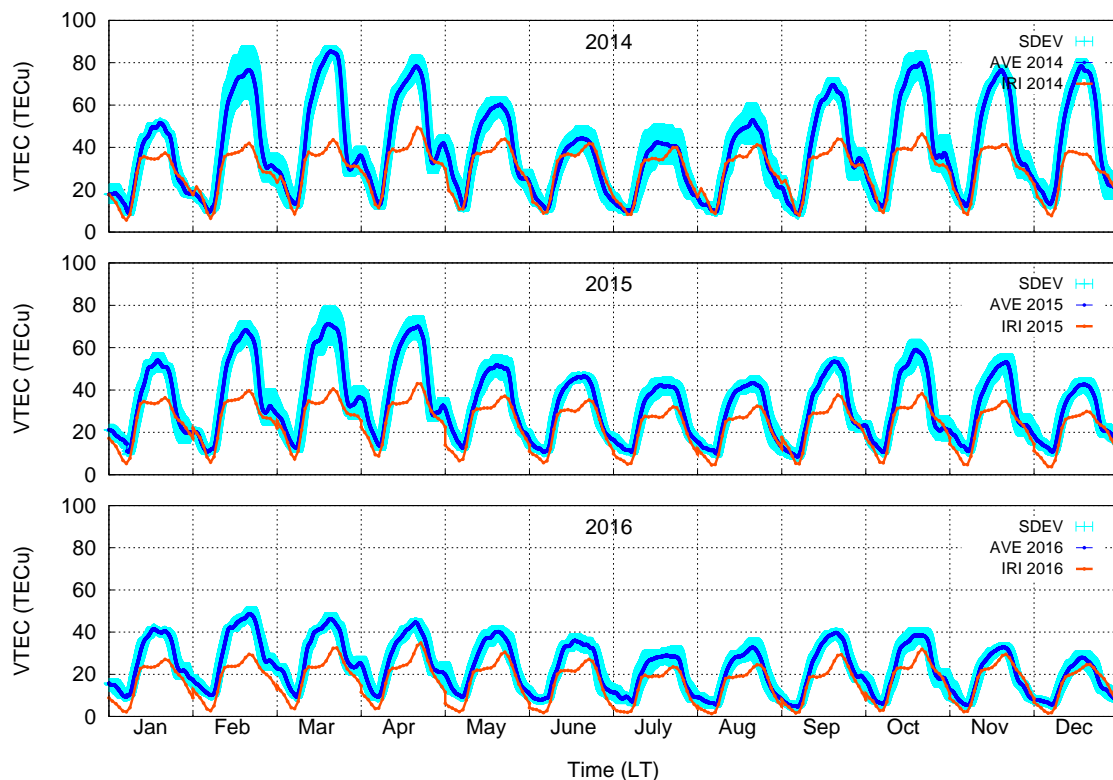


Figure 3.15: Variations in the TEC at Trivandrum during the years 2014-2016, derived from GPS and IRI model. The quiet time mean and standard deviation of the GPS TEC is represented using black and green color, respectively. The IRI derived TEC is represented by orange color.

Similarly, the variation of TEC at Trivandrum obtained from GPS measurements and the IRI 2012 model during the years 2014–2016 is presented in Figure 3.15. It can be seen that the IRI model largely underestimates the TEC at Trivandrum. The difference is highest during the equinoctial period of the year 2014, which is a period of high solar activity. The nighttime variations are also seen to be underestimated in the years of 2015 and 2016. Comparison studies of the IRI 2007 derived TEC and GPS derived TEC during the year 2004–2005 over the dip equatorial station, Chumpon, Thailand also showed similar variations with TEC being grossly underestimated during the daytime as well as nighttime [Kenpankho *et al.*, 2011]. Venkatesh *et al.* [2014] showed that the discrepancies in estimation of TEC over the low and equatorial regions, by the IRI 2012 model, still remains like in the previous versions. The discrepancies in the IRI derived TEC particularly during the high solar activity conditions could arise due to the differences in the estimation of the density of the F layer peak and related parameters [Venkatesh *et al.*, 2014].

3.8 Conclusions

The morphological features of the variation of TEC over the southern polar station, Bharti, the mid latitude station, Hanle, and the equatorial station, Trivandrum has been studied in this chapter. In general, the TEC variation at all these stations exhibit the semi annual variation with maximum TEC during the equinoctial period. However, the presence of the winter anomaly is recorded only at Trivandrum. The absence of winter anomaly at Hanle arises from the fact that it is located farther away from the auroral zone and hence may not be at the region where downwelling of composition disturbances (leading to an increase in O/N_2 and hence an increase in TEC) takes place. The TEC at Bharti does not show winter anomaly because during the local winter period, the station does not receive any sunlight at all due to which there is no photoproduction. Even so, it is found that the TEC at Bharti follows a diurnal pattern with the noontime peak appearing close to magnetic noon during the winter months and local noon during the summer months. This is because, in addition to photoproduction, the ionosphere over Bharti is most of the times under the influence of external sources like the magnetosphere and the solar wind owing to the vertical configuration of magnetic field lines thereat. Hence, particle precipitation acts as a source of ionization in the absence of photoproduction. A secondary peak in TEC is found at Bharti especially in the winter period due to ionospheric convection. This feature is evident at Bharti only when it is located inside the polar cap, i.e., at around magnetic midnight. This also shows that the dynamic nature of the location of Bharti with respect to the position of polar cap plays an important role in the control of plasma density therein. The morphological comparison between the TEC derived from the IRI 2012 model and the GPS TEC shows only a qualitative agreement. The daytime TEC during the winter

months obtained from GPS measurements as well as IRI 2012 model agrees well except for the fact that the nighttime peak is absent in the model output. This indicates the fact that cross polar cap transport processes have not been well accounted for in the model. A comparison of IRI 2012 model derived TEC and GPS TEC at Trivandrum also shows a wide departure. Except during summer (May to August), the IRI overly underestimates the TEC at Trivandrum. The model, however, represents the TEC at Hanle quite well. These comparisons show that while the mid, and low latitude ionospheric regions are well represented by IRI 2012 model, appreciable differences are seen at the dip-equatorial and the polar regions.

Chapter 4

Impact of space weather events on the southern polar ionosphere

4.1 Introduction

In the last chapter, morphological features of the variation of Total Electron Content (TEC) during magnetically quiet times over the polar cusp station, Bharti was studied. It was shown that the dynamic nature of the location of Bharti with respect to the polar cap plays an important role in control of plasma density at the polar station. The quiet time TEC of the ionosphere over Bharti was found to exhibit diurnal, seasonal and solar cycle dependence. However, during magnetically disturbed times, as the high latitude regions receive excess amount of energy from the magnetosphere, the ionosphere over this region can vary dramatically. The origin of geomagnetic storms and their impact on geospace has remained a subject of investigation for decades [Gonzalez *et al.*, 1994; Prölss, 1995; Foster, 2008; Elphinstone *et al.*, 1996; Buonsanto, 1999]. A great deal of information has also been collected using ground and satellite based observations and a general understanding of the sequence of events affecting the high latitude ionosphere during magnetically disturbed times has been achieved. Most of these studies describe the quiet and disturbed time behaviour of the northern high latitudes only. Observations from the southern hemisphere remain limited because of the geographical restrictions and limitations. In this chapter we study the impact of space weather events on the southern polar ionosphere and present a morphology of the variation of TEC at Bharti during geomagnetic storms.

The polar ionosphere is strongly influenced by the changes in the solar wind and the magnetosphere as they are closely linked through magnetic field lines. It is known that during the periods of southward Interplanetary Magnetic Field (IMF), the Earth's magnetic field, which is northward in direction, weakens. To maintain pressure balance with the solar wind, the Earth's magnetopause moves inward and comes closer to the Earth [Sibeck *et al.*, 1991]. The geomagnetic field lines, passing through the dayside magnetopause, merge with the southward IMF. The solar wind flow carries the open field

lines and the associated magnetosheath plasma in the antisunward direction. Merging of the field lines at the magnetopause enables the entry of the magnetosheath plasma into the magnetosphere and vice-versa [Cowley, 2000; Liu and Fujimoto, 2011]. A net transfer of mass, energy and momentum takes place from one region to the other. These open field lines close again through reconnection processes in the nightside region. This cycle gets completed once they return to the dayside region following nightside reconnection [Dungey, 1961]. Thus, magnetic flux and currents in the magnetosphere and ionosphere gets redistributed as a geomagnetic storm progresses [Kivelson and Russell, 1995; Milan et al., 2017]. The rate of reconnection at the magnetopause, the location of reconnection and the precipitation of the solarwind and magnetospheric plasma play important roles in deciding the electrodynamics of the polar ionosphere [Kivelson and Russell, 1995; Cowley, 2000; Milan et al., 2017].

Energy input into the polar ionosphere in the form of particle precipitation, enhanced electric fields and currents, maximizes during the main phase of the storm and decreases during the recovery phase [Schunk and Nagy, 2000]. The enhanced magnetospheric electric fields when combined with the vertical magnetic field at the polar regions cause large-scale horizontal motions ($E \times B$ drifts). This leads to the expansion of the convection cell into the lower latitudes. Storm Enhanced Densities (SEDs) are formed at the equatorward edge of the convection cell [Foster, 2008]. These are convected in the sunward direction at the low latitude boundary of the convection cell and in the antisunward direction across the polar cap [Knudsen, 1974] from where they may drift into the morning and evening sector [Senior and Blanc, 1987; Robinson et al., 1985; Rodger et al., 1986] following a typical two cell pattern [Greenwald et al., 1995]. As the storm progresses, the ring current develops and the Region-2 Field Aligned Currents (R2 FACs) flow into the subauroral ionosphere. In order to facilitate the closure of R2 FACs flowing through the subauroral ionosphere and the Region-1 Field Aligned Currents (R1 FACs) flowing in the poleward boundary of the auroral latitudes, a poleward directed Subauroral Polarisation streams (SAPS) electric field is setup [Foster, 2008]. These SAPS play an important role in the distribution of plasma in high latitude ionospheric regions [Foster et al., 2005; Foster, 2008]

The stormtime undershielding electric field which is eastward in direction during daytime penetrates into the low latitudes and uplifts the F-region plasma to very high altitudes [Maruyama et al., 2004]. The uplifted plasma flows along the magnetic field lines and fills the plasmaspheric flux tubes at higher latitudes resulting in enhanced density of plasma at the Plasmaspheric Boundary Layer (PBL) [Foster, 2008]. The SAPS electric field acts to transport the high density plasma from the PBL to the noontime cusp region in the polar ionosphere [Foster and Burch, 2002]. At higher altitudes, SAPS electric field acts to transport the SED plumes to the dayside magnetopause [Foster et al., 2004; Foster, 2008]. Stormtime high resolution GPS TEC maps often show a

polar TOI extending across the polar cap and into the nightside auroral region [Foster *et al.*, 2005]. It is the SED plume which is carried by the SAPS electric field into the noontime cusp [Foster *et al.*, 2005] that appears as the polar TOI in GPS TEC maps of the polar ionosphere.

The TOI may break into discrete patches as it traverses through the polar cap [Sojka *et al.*, 1993]. This could arise from the temporal changes in IMF B_y component [Sojka *et al.*, 1993] or the expansion and contraction of the convection cell into and out of a region of solar ionization at the lower latitudes [Anderson *et al.*, 1988]. Another theory by [Lockwood and Cowley, 1992] suggests that patch structure can be formed by flux transfer events or pulsed reconnection which controls the expansion and contraction of polar convection. The precipitation of soft particles in the sub-polar regions could also be a source for patch ionization [Walker *et al.*, 1999]. Experimental evidence for precipitation-produced plasma enhancements with characteristics of polar patches was presented by [Walker *et al.*, 1999] who showed that soft precipitation played an important role in the direct formation of structured plasma at high altitude [Pryse *et al.*, 2004]. Density gradients associated with the polar cap patches result in rapid fluctuations of radio wave phase and amplitude and give rise to scintillations [Moen *et al.*, 2013].

The high latitude ionosphere is also affected by magnetic substorms [Elphinstone *et al.*, 1996]. The ionospheric convection and the dynamics of the polar cap during the growth and expansion phase of substorms agrees well with the Expanding/Contracting Polar Cap (EPCP) paradigm [Cowley and Lockwood, 1992; Lockwood and Cowley, 1992; Clausen *et al.*, 2013]. Magnetopause erosion [Aubry *et al.*, 1970; Holzer and Slavin, 1978; Meng, 1970; Fairfield, 1971; Russell, 1980], development of R1 FACs and R2 FACs [Iijima and Potemra, 1976; Schield *et al.*, 1969; Siscoe, 1982], dynamics of the polar cap [Burch and Heelis, 1980; Meng, 1980] and formation and evolution of ionospheric plasma structures, like the SED and the TOI [Foster *et al.*, 2005] have been extensively studied for decades. Still, their influence on redistribution of plasma at high-latitude ionospheric region is still far from clear. This is mainly because the variability of space weather events depends among other factors, on the state of the Magnetosphere-Ionosphere-Thermosphere (M-I-T) system. This is where the importance of the St.Patrick's day storms of 2013 and 2015 comes into picture. These events are unique because they occurred around the same local time sector but had different intensities which helped us to delineate the relative influence of various factors which controls the space weather.

The St.Patrick's day storm of 2015, the largest storm of the 24th solar cycle with Dst index reaching a minimum value of -238 nT, has gathered immense interest among researchers, and has been a subject of several investigations [Le *et al.*, 2016; Astafyeva *et al.*, 2015; Cherniak *et al.*, 2015; Tulasiram *et al.*, 2015; Joshi *et al.*, 2016; Nava *et al.*, 2016; Ramsingh *et al.*, 2015]. The storm which had a huge impact on the Earth's M-I system was triggered as a Coronal Mass Ejection (CME) which originated from

the sunspot AR2297 hit the Earth's magnetosphere on 17 March 2015 at ~ 0445 UT. Differences in the magnetic field geometry, changes in the O/N₂ ratio and IMF B_y component gave rise to hemispheric asymmetries in the ionospheric response during this event [Astafyeva *et al.*, 2015]. Strong magnetopause erosion led to significant changes in the magnetosphere [Le *et al.*, 2016]. The ionospheric irregularities generated during this storm exhibited a high correlation with the auroral hemispheric power and electrojet indices [Cherniak *et al.*, 2015]. The response of the ionosphere over the low and mid latitude region to the convection electric fields during the St.Patrick's day storm of 2015 has also been studied [Tulasiram *et al.*, 2015; Joshi *et al.*, 2016; Nava *et al.*, 2016; Ramsingh *et al.*, 2015]. It was rated as a G4 scale storm as per the NOAA's geomagnetic storm scale and falls under the category of a severe storm.

In the same solar cycle, another intense geomagnetic storm rated as G2 class on the NOAA's geomagnetic storm scale (Dst ~ -130 nT) had occurred on the same day i.e., 17 March but in the year 2013. This storm was triggered at 0600 UT as a CME which originated from the sunspot AR1692 hit the magnetosphere. Large enhancements in magnetic field associated with substorm injections were observed using Van Allen probes [Foster *et al.*, 2013]. Erosion of the plasmasphere, which took place under the action of the SAPS electric field, gave rise to the formation of the TOI in the polar ionosphere [Foster *et al.*, 2014].

Table 4.1: Geophysical conditions during the St.Patrick's day storms of 2013 and 2015.

Parameter	17 March 2013	17 March 2015
F10.7 index	118	126
Commencement time	0600 UT	0445 UT
Onset of main phase	0600 UT	0600 UT
Minimum Dst	-130 nT	-223 nT
Duration of main phase	14 hours	17 hours
Peak AE	2700 nT	2200 nT

Fortunately, the St.Patrick's day storms 2013 and 2015, occurred in the same season, when similar conditions existed on the Sun and the Earth (listed in Table 4.1) i.e., when the state of the Ionosphere-Thermosphere (I-T) system were almost similar. Coincidentally, both the storms had the same onset times too. Hence a study of the response of the southern polar ionosphere to the St.Patrick's day storms of 2013 and 2015 will provide better insight into the role of Magnetosphere-Ionosphere-Thermosphere (MIT) coupling in altering the plasma distribution over the polar ionosphere. Though the response of the polar ionosphere over the northern hemisphere to both these storms has been studied extensively, the southern hemispheric polar region has remained relatively unexplored due to limited number of observations from in this region. Fortunately our GPS receiver system at Bharti worked faultlessly on both these days. In this chapter,

the evolution of ionospheric storms over the southern polar station, Bharti has been studied in detail. In addition, a morphological study of the variations in TEC during 24 storm events that occurred during 2013-2015 has been performed to address the role of MIT coupling in the redistribution of plasma over the southern polar station, Bharti during space weather events.

In the following, we first describe the impact of St.Patrick's day storms of varying intensity on the ionosphere over Bharti. Later we will continue the discussion on the space weather impact in a morphological sense by analysing 24 storms based on their intensity and onset time.

4.2 Database

The response of the southern polar ionosphere to the storm events have been studied primarily using GPS observed TEC the Indian Antarctic research station, Bharti (69.4°S, 76.2°E geographic, 76.69°S, 126.93°E geomagnetic). Slant TEC data recorded at 1-minute intervals by the GPS TEC receiver, are converted to Vertical TEC values using a mapping function described by *Smith et al.* [2008]. Satellite ray paths at elevation angles greater than 35° are used to calculate the VTEC at Bharti. The phase and amplitude scintillation of the L1 signals are also recorded by the GPS receiver. Standard deviation of the detrended carrier phase averaged over intervals of 1, 3, 10, 30, and 60 seconds gives the phase scintillation (σ_ϕ) indices. Only those signals coming from satellites with an elevation greater than 30° and with a time of lock greater than 4 minutes are used for studying scintillations. The scintillation indices are projected to the vertical in order to account for the geometrical effects on the measurements made at different elevation angles using the technique described by *Spogli et al.* [2009] .

The solar wind and geomagnetic conditions during the St.Patrick's day storms were obtained from satellite based measurements and ground based magnetometers. The solar wind, interplanetary and geomagnetic parameters used to study the evolution of geomagnetic storm are obtained from the CDAWeb (<http://cdaweb.gsfc.nasa.gov>). The changes in the Auroral Electrojet (AEJ) are reflected in the H and Z-component of magnetic field measured using the ground magnetometer installed at Bharti.

Measurements from the polar orbiting DMSP F16 satellite were also examined as it follows a sun-synchronous dawn-dusk orbit at an altitude of 850 km, and therefore, is able to provide insight into the response of the topside polar ionosphere to geomagnetic storms. *In situ* measurements of plasma density and cross-track velocity components by the Ion Drift Meter (IDM) and Retarding Potential Analyser (RPA) onboard DMSP satellites have been used to study the signatures of particle precipitation, SAPS and the polar TOI. Observations by the Special Sensor Ultraviolet Spectral Imager (SSUSI) instrument onboard DMSP F16 have also been used in this study. The SSUSI instrument onboard DMSP satellite consists of two instruments, namely (i) a system of three Nadir-

looking Photometers (NPS) which operate in the visible portion of the electromagnetic spectrum, and (ii) a Scanning Imaging Spectrograph (SIS) with a cross track line scan mirror. The NPS consists of three photometers with filters designed to monitor the airglow at 427.8nm and 630nm and the terrestrial albedo near 630nm. The SIS produces simultaneous monochromatic images at five “colors” in the spectral range 115nm to 180nm. SSUSI therefore gives the Far Ultraviolet (FUV) auroral and airglow emissions in five channels (1216 Å, 1304 Å, 1356 Å, Lyman-Birge-Hopfield Short (LBHS), and Lyman-Birge-Hopfield Long (LBHL)) [Paxton *et al.*, 1992a, b]. We used the emissions derived from the N_2 LBHS channel (N_2 emissions in the 1400 –1500 Å range) in the present study. The DMSP IDM and the DMSP SSUSI measurements are obtained from the NOAA data center (<http://www.ngdc.noaa.gov/stp/satellite/dmsp/>) and the JHU/APL website (<http://ssusi.jhuapl.edu/>) respectively.

4.3 The impact of St.Patrick’s day storms of 2013 and 2015 on the ionosphere over Bharti

As discussed in the earlier section, the St.Patrick’s day storms of 2013 and 2015 that occurred in the current solar cycle provided an unique opportunity to understand how two distinct events of different intensities and nearly identical commencement times, occurring when the background conditions on the Sun and the Earth are almost similar (listed in Table 4.1), affects the polar ionosphere. In the sections that follow, the evolution of the St.Patrick’s day storm of 2013 and 2015 and the ionospheric conditions that prevailed as a result of the storms has been described.

4.3.1 Geomagnetic conditions

The solarwind and geomagnetic conditions during 16-18 March 2013 and 16-18 March 2015 are shown in panels in panels (a)-(g) and (h)-(n) of Figure 4.1 respectively. The IMF B_z turned northward at 0600 UT on 17 March 2013 concurrent to which the solar wind speed, density and pressure are also seen to have increased as shown in panels (a) -(d) of Figure 4.1. A larger increase in the solar wind density and pressure is seen to have occurred on the 17 March 2015 case as well (panels (h) - (k)) when compared to the geomagnetic storm of 17 March 2013. The sudden increase in Symmetric Geomagnetic Disturbance (Sym-H) index at 0600 UT marks the SSC in correspondence to which the auroral indices have also enhanced. The geomagnetic storm on 17 March 2015 also commenced with the northward turning of IMF B_z at 0445 UT.

The IMF B_z turned southward immediately after SSC on 17 March 2013. It oscillated between southward and northward directions with a period of ~ 1.5 hours till 1400 UT after which it remained southward for ~ 0600 hours and then gradually turned northward. On 17 March 2015, on the other hand, the IMF B_z became northward after the SSC

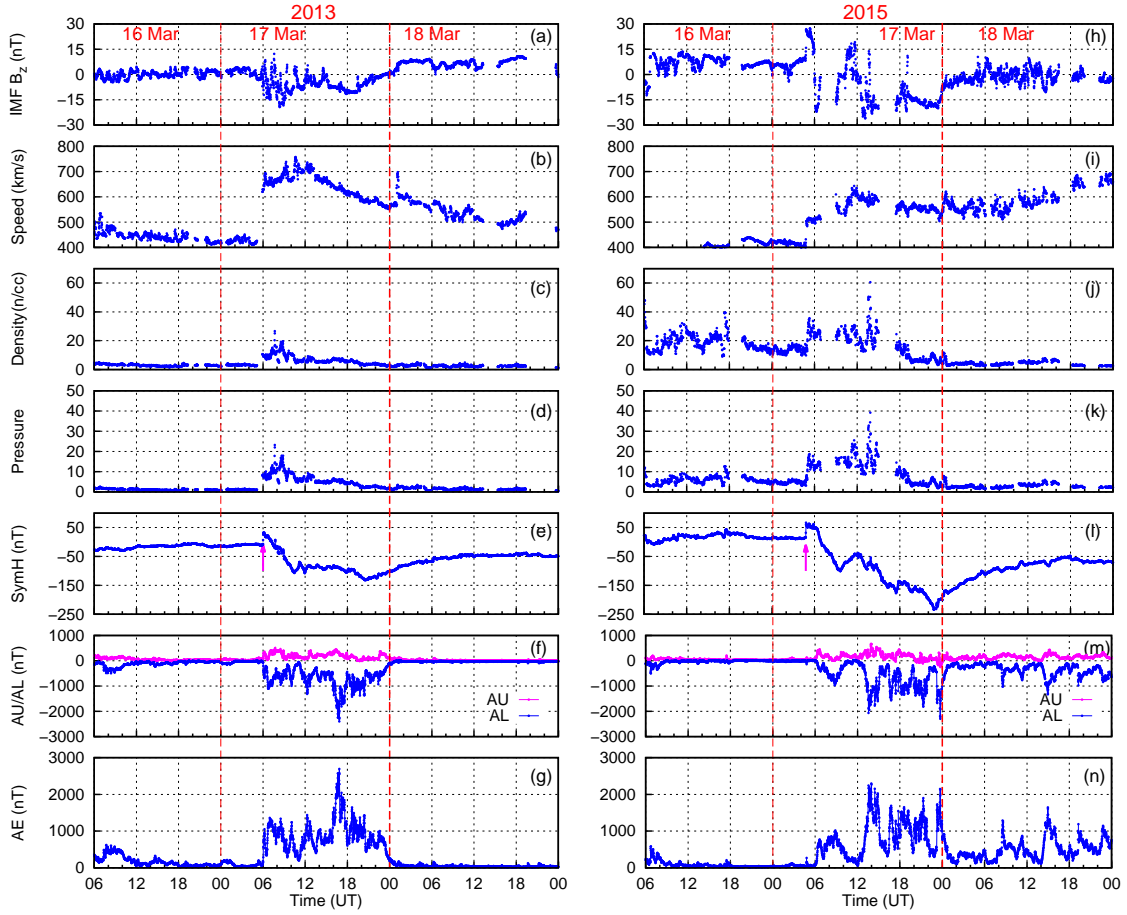


Figure 4.1: Panels (a)-(g) and (h)-(n) show the geomagnetic conditions during 16-18 March 2013 and 16-18 March 2015, respectively.

for a short duration. The IMF B_z however remained mostly southward till ~ 1000 UT after the onset of the main phase of the storm on 17 March 2015. After being northward till 1200 UT, it again turned southward and remained so for ~ 1200 hours. As we note, the IMF B_z remained primarily in the southward direction on 17 March 2015 whereas on 17 March 2013 it was mostly fluctuating in nature. The maximum excursion of IMF B_z during the space weather event of 17 March 2013 was -15 nT while it was ~ -25 nT during the geomagnetic storm of 17 March 2015.

The Sym-H index is seen to descend to ~ -90 nT by ~ 1000 UT in both the cases. A tendency to recover was seen with the Sym-H index turning positive for a short while after 1000 UT. However, the Sym-H index dropped further and reached a second minimum of ~ -130 nT at 2000 UT on 17 March 2013 while it descended to ~ -223 nT on 17 March 2015. A second step like increase in the solar wind speed followed by enhancement in the solar wind pressure and density going upto ~ 50 n/cc and ~ 35 nPa is observed on 17 March 2015 at around 1200 UT. This sudden increase in the solarwind speed, pressure and density could have driven of the Sym-H index to the second minima of -223 nT. A slow recovery followed in both the cases.

Even though the SSC during the St.Patrick's day storm of 2015 took place an hour before the SSC on 17 March 2013, the onset of the main phase of both the storms was at 0600 UT. The nature of variation of Sym-H index was also quite similar in both the cases till it reached the first minimum. The main phase of the geomagnetic storm that occurred on 17 March 2013 lasted for ~ 14 hours while of that occurred on 17 March 2015 lasted for ~ 17 hours. During the entire duration of the main phase, the Auroral Electrojet (AE) index remained high indicating intense heating taking place at the polar latitudes. The AE index remained high for a longer duration, even during the recovery phase in the case of the geomagnetic storm triggered on 17 March 2015. The Auroral Lower (AL) index which is an indicator of the auroral electrojet activity implies that a number of substorms were triggered during the main phase of these storms. How the southern polar ionosphere was impacted by the aforementioned similarities and differences in the solarwind and geomagnetic conditions during the St.Patrick's day storms of 2013 and 2015 are discussed in the subsequent sections.

4.3.2 Response of the polar ionosphere on 17 March 2013 and 17 March 2015

The ionospheric electron densities undergo large changes when subjected to the inflow of large energy from the magnetosphere during geomagnetic storms [Prölss, 1995]. The storm induced changes immediately get reflected in almost all the ionospheric parameters in the polar ionosphere. To examine how the ionosphere over the polar region in the southern hemisphere responded to the St.Patrick's day storms of 2013 and 2015, we study the diurnal variation of TEC and the phase scintillation index (σ_ϕ) over the Indian Antarctic station, Bharti.

The diurnal variation of VTEC over the southern polar station, Bharti, on 17 March 2013 is shown in panel (a) of Figure 4.2. The blue curve in this panel represents the variation in TEC on the day of the storm over Bharti. The red curve represents the monthly mean variation of TEC over Bharti calculated for 5 quietest days of the month and the cyan shade shows the standard deviation. The Magnetic Local Time (MLT) is also shown in x-axis of the Figure 4.2 for reference. The TEC over Bharti is seen to enhance at two distinct time zones on 17 March 2013. The first peak in TEC is observed around 0930 UT (which corresponds to magnetic local noon) with a magnitude of ~ 10 TECu. The second peak in TEC appeared around 2000 UT (magnetic midnight) with a magnitude of ~ 10 TECu. In panel (b) of Figure 4.2 is shown the variation of the phase scintillation index (σ_ϕ) on 17 March 2013. It can be seen that appearance of phase scintillations over Bharti coincided with the surge in the TEC.

Similarly, the temporal variation of the TEC and the phase scintillations (σ_ϕ) over Bharti during the St.Patrick's day storm of 2015 are shown in panels (a) and (b) of Figure 4.3. A striking feature in panel (a) of Figure 4.3 is the large enhancement of

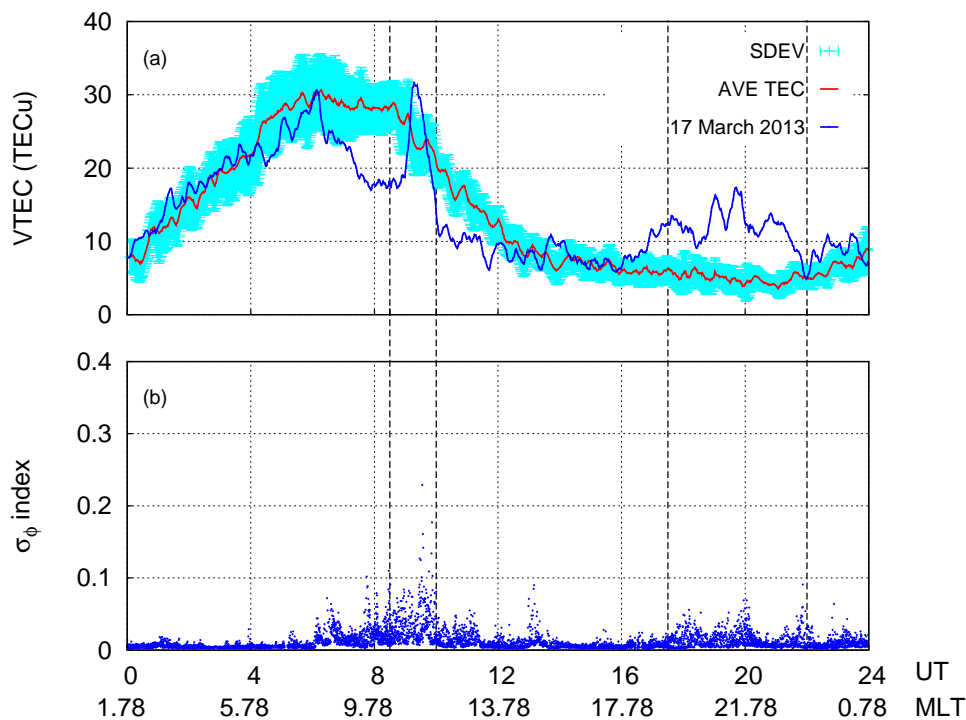


Figure 4.2: Panels (a) and (b) represent the diurnal variation of TEC and σ_ϕ index, respectively at Bharti on 17 March 2013. The blue curve in panel (a) represents the variation in TEC on the day of the storm and the red curve represents the monthly mean. The cyan shade shows the standard deviation. Regions of high TEC and σ_ϕ index are highlighted using black vertical lines.

~ 20 TECu observed around 1900 UT over Bharti. This is the time when the station locates itself around the magnetic midnight. A comparatively smaller enhancement in TEC is also seen around 0900 UT (close to magnetic local noon). An increase in phase scintillations over Bharti especially during nighttime is clearly seen in panel (b) of Figure 4.3. The large enhancement in the phase scintillations (σ_ϕ index) is seen to coexist with higher values of the TEC. The magnitude of phase scintillations is much larger in the midnight sector than in the morning time enhancement and also as compared to the enhancement during the 17 March 2013 storm.

4.3.3 Salient points of the observations on the two days:

1. The main phase of the geomagnetic storm on 17 March 2013 began at 0600 UT during which the IMF B_z was mostly fluctuating in nature.
2. The large enhancement in the AE index during this event showed that intense heating was taking place over the high latitudes.
3. On 17 March 2013, enhancements in the TEC were observed at Bharti around local magnetic noon (1000 UT) and magnetic midnight (2200 UT) in concurrence

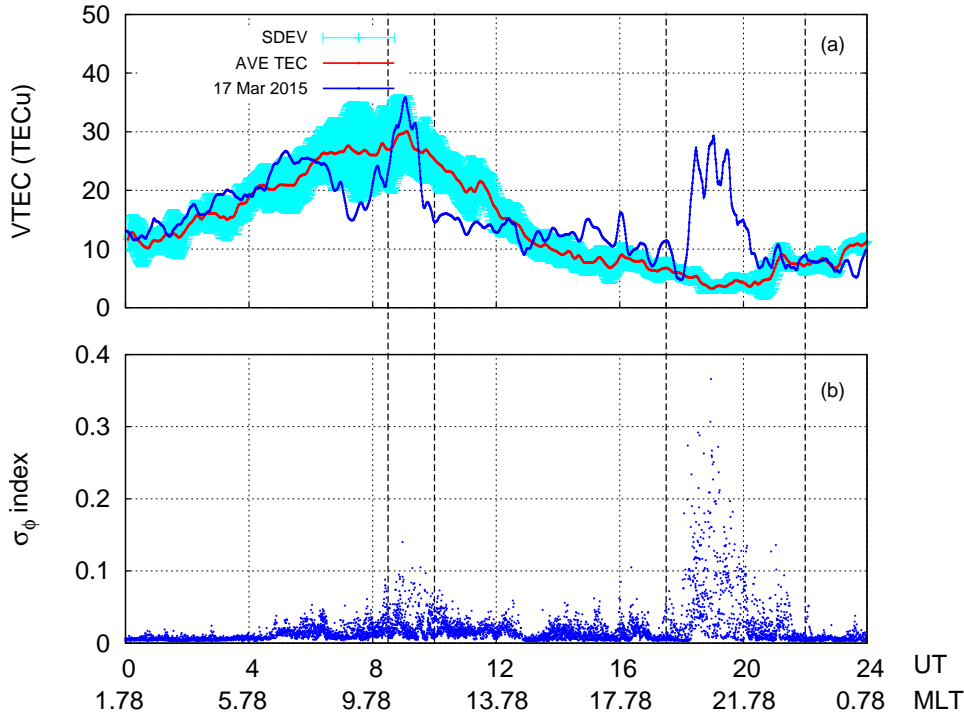


Figure 4.3: Panels (a) and (b) represent the diurnal variation of TEC and σ_ϕ index, respectively at Bharti on 17 March 2015. The blue curve in panel (a) represents the variation in TEC on the day of the storm and the red curve represents the monthly mean. The cyan shade shows the standard deviation. Regions of high TEC and σ_ϕ index are highlighted using black vertical lines.

with the appearance of phase scintillations.

4. The main phase of the storm on 17 March 2015 began at 0600 UT. The IMF B_z was primarily in the southward direction during the main phase of the storm.
5. There were two peaks in the TEC measured at Bharti station. The first peak appeared around the local magnetic noon (1000 UT). The second rise (of about 30 TECu) occurred near local magnetic midnight (2200 UT).

Even though both the storms occurred when almost similar conditions prevailed in the Earth's I-T system, the magnitude of increase of the TEC at magnetic midnight on 17 March 2015 was much higher (~ 20 TECu) compared to the increase (~ 10 TECu) on 17 March 2013. These differences in magnitude could be a result of the variabilities in the electrodynamics of the auroral and polar ionosphere due to the varied solar wind and magnetospheric conditions that existed during these events. Here, we attempt to explain these variabilities and their impact on the southern polar ionosphere.

4.3.4 Plausible reasons for the differences in the enhancement of the TEC on the two days

The first increase in the TEC was observed around 0930 UT during both the storms. As described in the previous chapter, this is the time when Bharti station lies in the vicinity of the cusp region. Thermalised solar wind can enter into the high latitude ionosphere through the magnetospheric cusps [Heikkila and Winningham, 1971] and ionize the neutral species present in the F-layer. Enhanced precipitation of low energy electrons (few eV) into the ionosphere during stormtime can give rise to an increase in plasma density. Since Bharti station lies in the vicinity of the cusp region at 1000 UT (local magnetic noon), the observed enhancement in TEC at around 0930 UT may be attributed to be due to the soft particle precipitation into the cusp/cleft region.

The second increase in TEC appeared around 2000 UT (local magnetic midnight) during both the storms. This is the time when the station lies completely in darkness and so contribution from the solar photoionization towards enhancement of the nighttime TEC is completely absent. Hence, the observed surge in TEC ($\sim 30\text{TECu}$) could be due to other possible mechanisms. To understand possible reasons for the observed increase in TEC and the difference in their magnitudes during the two storms, the conditions that existed in the polar ionosphere during both the events need to be examined. Information about the changes in the auroral ionosphere and the topside ionospheric parameters can be obtained from the DMSP satellites. As the formation of the aurora is a direct evidence for the interaction of the solar wind, magnetosphere and the ionosphere [Elphinstone *et al.*, 1996], the intensity of the emissions provides a measure of the energy input into the ionosphere. Hence, auroral images obtained from the SSUSI instrument onboard DMSP satellite can be used to understand the response of the auroral ionosphere to stormtime energy input.

4.3.4.1 DMSP–SSUSI Observations on 17 March 2013

In panels (a) to (i) of Figure 4.4 are shown the selected auroral images of the southern polar ionosphere obtained during 17 March 2013 from the SSUSI instrument onboard DMSP F16 satellite. As one can see in Figure 4.4, at 0439 UT, i.e., before the commencement of the storm, the brightness of the aurora was very weak, commensurate with geomagnetically quiet periods. The auroral oval was located around 70° MLAT at 0805 UT (panel (c)). It is seen that later at 0947 UT, the polar cap expanded and the equatorward boundary of the auroral oval shifted further to 60° MLAT. The brightness of the aurora increased significantly during this time. The polar cap area began to increase as reconnection at the magnetopause begins to create open magnetic flux tubes [Kivelson and Russell, 1995]. This is also a signature of the reconnection of field lines lying closer to the Earth and hence results in an equatorward displacement the auroral

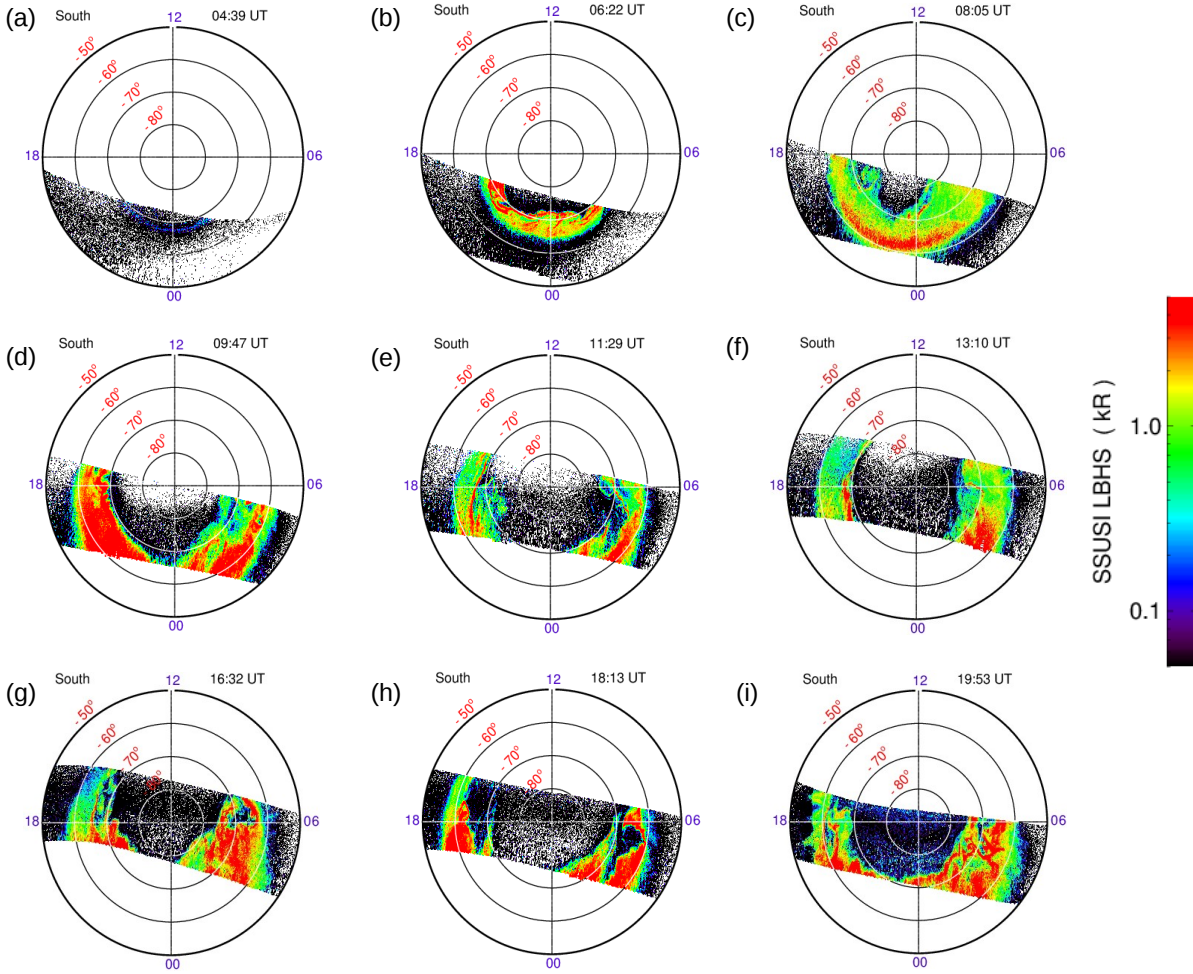


Figure 4.4: Observations from SSUSI instrument onboard DMSP F16: Panels (a) to (i) show the auroral emissions in the southern hemisphere derived from the N_2 LBHS channel at different times on 17 March 2013.

oval [Elphinstone *et al.*, 1996]. Observations at 1129 UT and 1310 UT show that the auroral oval has contracted and the emissions have reduced which means that the energy input into the auroral ionosphere has diminished. This is a consequence of the IMF B_z being mostly northward during the period 1000-1400 UT.

The presence of substorm activity during the main phase of the 2013 storm can be inferred from the ground based magnetic field indices like the AL index and the H-component of magnetic field. Substorm activity is known to be an important source for nightside auroral precipitation [Foster *et al.*, 2013] and acts as a driving mechanism for neutral and electrodynamic processes in the polar ionosphere. As described earlier in Figure 4.1, large deviations in the AL indices were observed on 17 March 2013 after ~ 1600 UT. Further, large deviations in the H-component of magnetic field which is a signature of substorm activity [Huang *et al.*, 2003] was also observed during nighttime at Bharti. The temporal variation of the H and Z component of magnetic field at Bharti is presented in panels (a) and (b) of Figure 4.5. It can be seen that there were

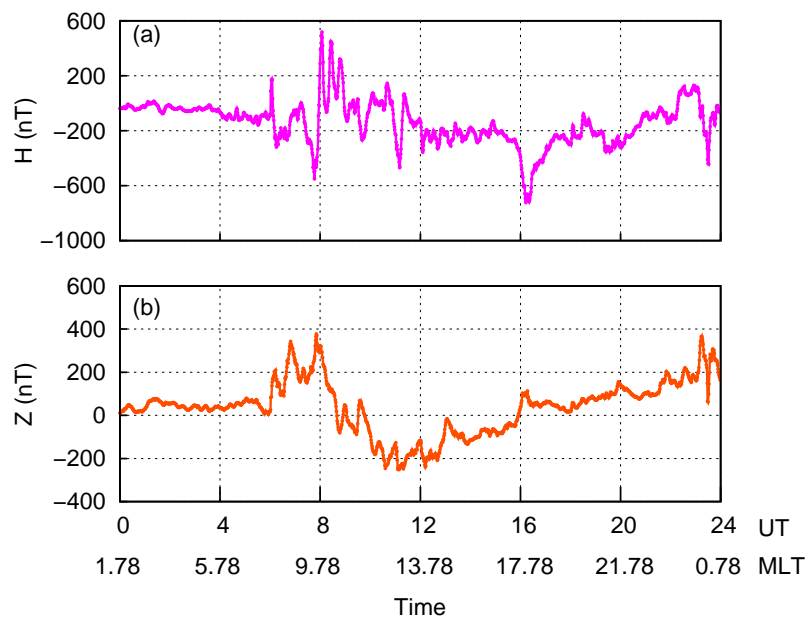


Figure 4.5: Panels (a) and (b) represent the temporal variation of the H and Z component of the magnetic field, respectively at Bharti on 17 March 2013.

large depressions in the H component of magnetic field at Bharti during nighttime. The negative deviations in the H component of magnetic field gives a measure of the strength of the auroral Westward Electrojet (WEJ) and the Z component of magnetic field indicates the location of the current. The poleward expansion of the auroral oval and brightening of the aurora at 1632 UT (as seen in Figure 4.4) and at later times confirm that substorm injections were taking place. Evidences for the occurrence of a substorm polarisation event on 17 March 2013 were presented in an earlier study by *Foster et al.* [2013]. They showed using the Van Allen Probes that large enhancements were present in the magnetic field and electron fluxes on 17 March 2013 during the substorm dipolarisation event.

4.3.4.2 DMSP–SSUSI Observations on 17 March 2015

The SSUSI images of the southern hemisphere obtained during the 17 March 2015 storm are shown in panels (a) to (i) of Figure 4.6. During this storm also, prior to onset, at 0353 UT, only a weak auroral glow was present. The auroral image at 0719 UT shows the expansion of the polar cap in response to the stormtime magnetospheric convection. During the main phase of the storm, intense N_2 emissions were present as evident from the auroral image at 0901 UT. The equatorward boundary of the oval reached 60° MLAT. But the next image at 1043 UT shows reduced emissions and a contracted auroral oval. The auroral images from 1405 UT to 1907 UT (panels (f) to (i) of Figure 4.6), display certain common features, like the intensification of the emissions mainly in the dawnside of the auroral oval. This could be because of the enhanced precipitation of electron fluxes aided by the strong FACs which are upward in the dawn

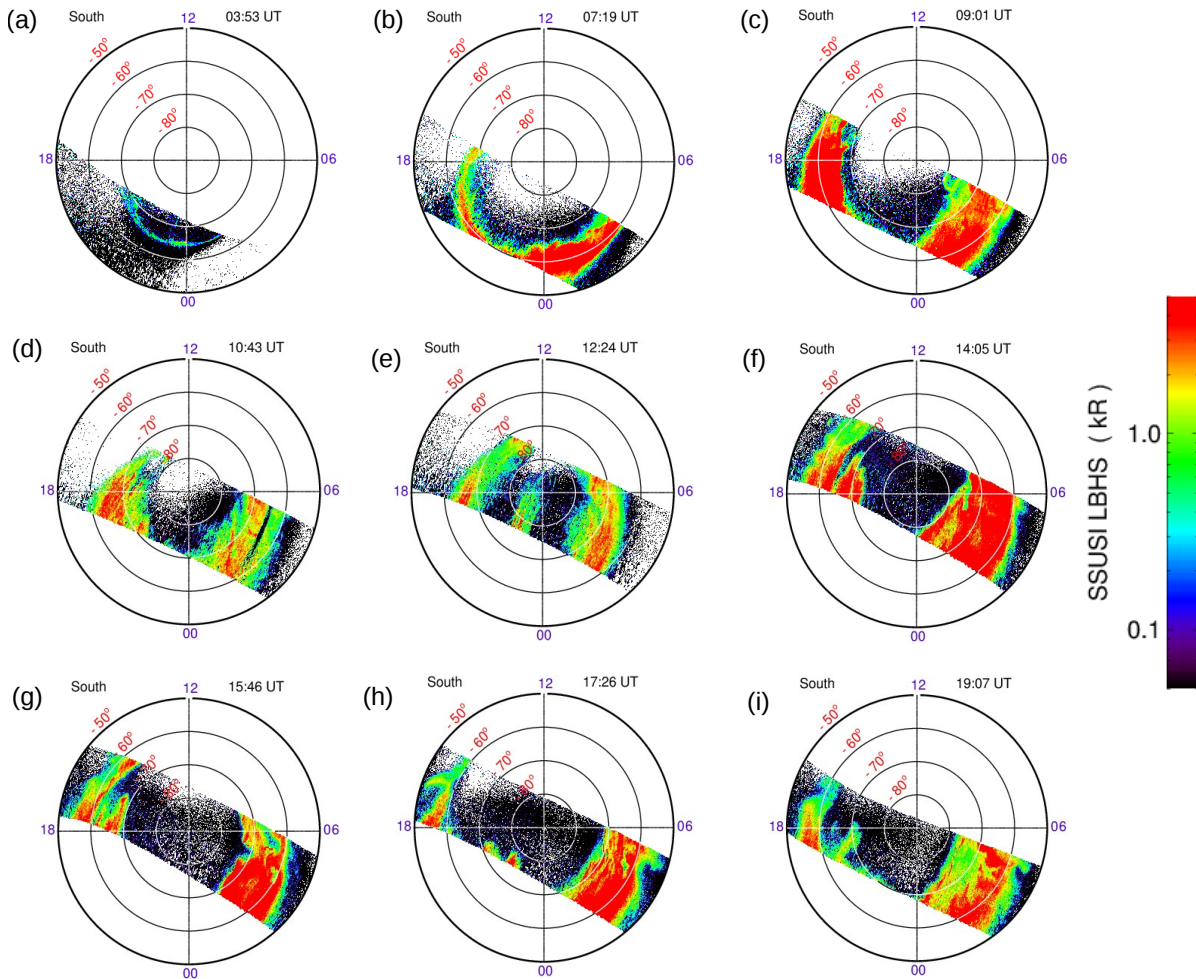


Figure 4.6: Observations from SSUSI instrument onboard DMSP F16: Panels (a) to (i) show the auroral emissions in the southern hemisphere derived from the N_2 LBHS channel at different times on 17 March 2015.

cell [Valladares *et al.*, 1994]. In the image at 1405 UT, we find large poleward expansion of the auroral oval which is the signature of strong substorm activity. The AL index at around 1400 UT (in panel(m) of Figure 4.1) also shows the intensification of the WEJ current. The signature of substorm activity was observed in the ground magnetic field at Bharti. The variation of H and Z component of magnetic field at Bharti during 17 March 2015 is shown in panels (a) and (b) of Figure 4.7. Large depressions in the value of the H-component of magnetic field at Bharti during the nighttime are clearly seen in Figure 4.7. The Z component of magnetic field is seen to enhance at times when the H component decreases. The electrojet current is seen to have intensified at ~ 1400 UT and 1800 UT (1600 to 2000 MLT in the dusk to night sector) apart from the smaller depressions that are evident in the nightside sector. Such large enhancements in the currents at the auroral zone during substorm events leads to the expansion of the auroral oval [Elphinstone *et al.*, 1996].

As described above, there was significant activity in the auroral ionosphere during

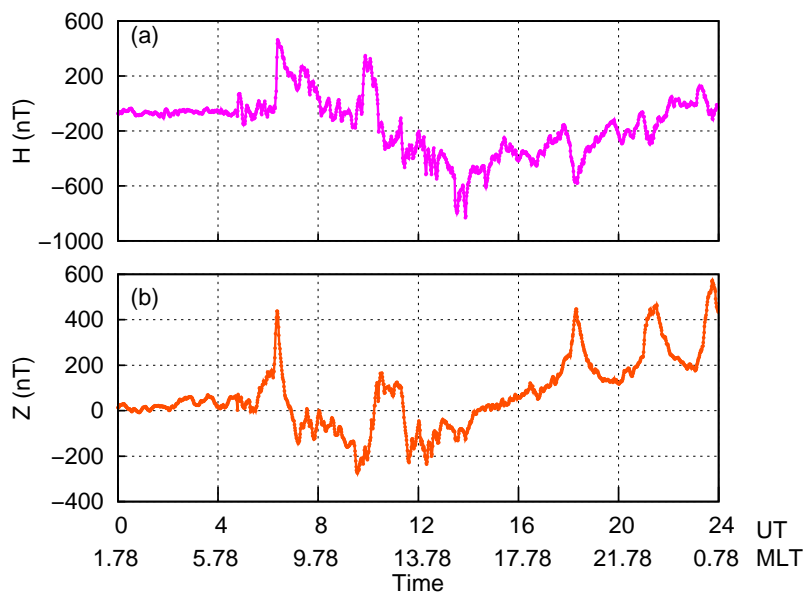


Figure 4.7: Panels (a) and (b) represent the temporal variation of the H and Z component of the magnetic field, respectively at Bharti on 17 March 2015.

the St. Patrick's day storms of 2013 and 2015. In the case of the St. Patrick's day storm of 2015, the ionospheric effects were dramatic. The polar cap remained expanded and the auroral oval was seen to extend upto 50° MLAT on 17 March 2015. This is a signature of magnetic reconnection at regions closer to the Earth. Strong auroral emissions and complex flows were observed during most of the duration of the storm which indicates significant energisation of the southern polar ionosphere on 17 March 2015. The auroral emissions on 17 March 2013 were much weaker as compared to the 2015 case which may be mainly due to the fluctuating nature of the IMF B_z .

The changes in the size and location of the auroral oval indicates the changes happening in the magnetosphere due to its interaction with the solar wind and the IMF. It was seen that in both the cases, as the main phase progressed, in response to the enhanced convection electric field, the oval expanded towards lower latitudes. This allows the build up of solar photoionized plasma along the equatorward edge of the convection cell and leads to the formation of the SEDs [Foster, 2008]. The R1 FACs that flow into the poleward edge of the auroral ionosphere in the morning sector strengthen during stormtime [Clausen *et al.*, 2013]. The R2 FACs flow into the equatorward edge of the evening auroral ionosphere and are driven by large pressure gradients in the ring current region [Harel *et al.*, 1981]. SAPS electric field develop in these regions to achieve current continuity by closing the R1 FACs and the R2 FACs [Yeh *et al.*, 1991]. The SAPS electric field acting in the subauroral regions drives large sunward plasma flows and can modify the topside ionospheric electron densities significantly [Foster, 2008].

4.3.4.3 DMSP ion drift measurements on 17 March 2013, and 17 March 2015

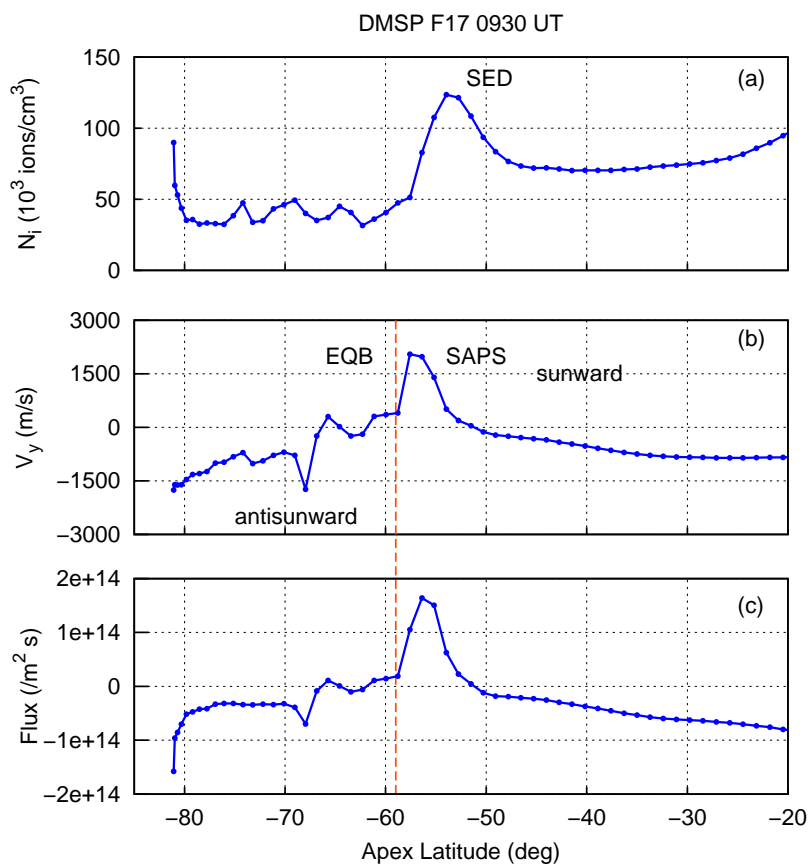


Figure 4.8: DMSP F-17 observations on 17 March 2013: Panels (a) and (b) represent the ion density and cross track velocity measured at an altitude of 840 km at 0930 UT. The ion flux calculated as a product of density and cross-track velocity is shown in panel (c). The equatorward boundary (EQB) of the auroral oval is indicated by the red line.

In order to understand the changes in the plasma density of the top side ionosphere during the St. Patrick's day storm of 2013 and 2015, DMSP IDM measurements from the southern hemisphere were examined. In panels (a) and (b) of Figure 4.8, the ion density and cross track velocity measured with the DMSP F17 satellite at ~ 0930 UT on 17 March 2013 are shown. The ion flux calculated as the product of the density and the cross track velocity is shown in panel (c). The equatorward boundary of the auroral oval obtained from the DMSP particle flux measurements is also shown using the red line in panels (b) and (c). Large enhancements in sunward plasma velocity at subauroral latitudes colocated with regions of SEDs can be seen in Figure 4.8. This is a signature of SAPS electric field [Foster and Burch, 2002]. Associated with the SAPS electric field, an enhancement in the sunward ion flux ($\sim 2 \times 10^{14} \text{ m}^{-2} \text{ s}^{-1}$) is observed over the sub auroral latitudes.

Similar measurements of the ion density, cross-track velocity and the ion flux observed by the DMSP F16 satellite at 0830 UT on 17 March 2015 are presented in panels (a), (b) and (c) of Figure 4.9. The equatorward boundary of the auroral oval is at ~ 61 MLAT as indicated by particle flux measurements and is marked in panels (b) and (c) using the red line. Sunward flow velocities of upto 1300m/s are also observed at the subauroral latitudes. The presence of large sunward ion flux ($\sim 1.6 \times 10^{14} \text{ m}^{-2} \text{ s}^{-1}$) at the sub-auroral regions imply the presence of SAPS E field. Another notable feature is the Polar Cap Enhancements (PCE) that were not apparent during the St.Patrick's day storm of 2013.

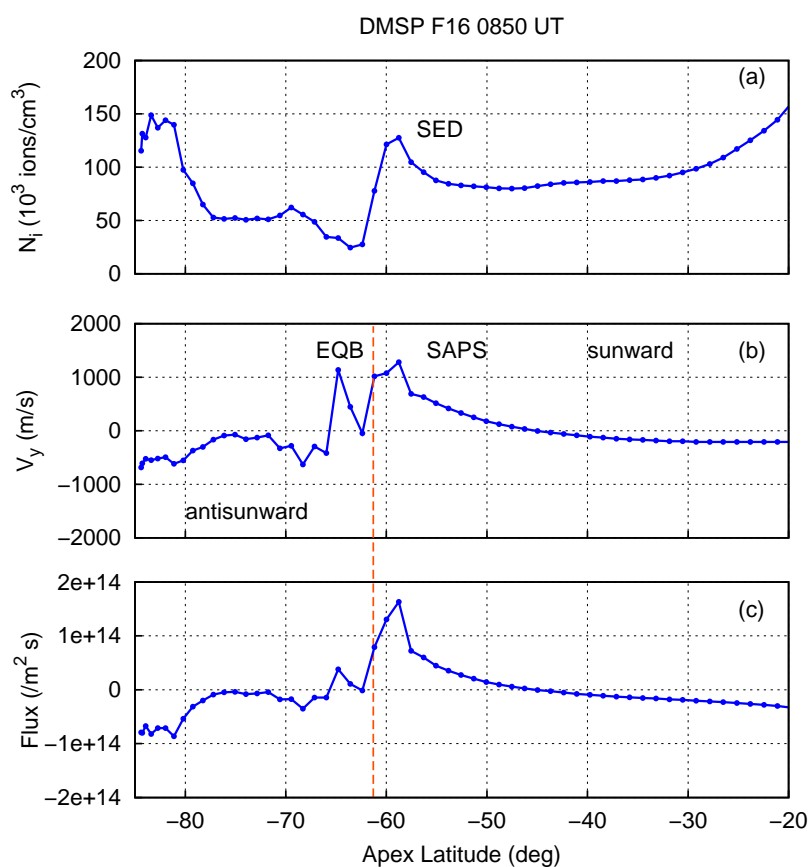


Figure 4.9: DMSP F-16 observations on 17 March 2015: Panels (a) and (b) represent the ion density and cross track velocity measured at an altitude of 840 km at 0850 UT. The ion flux calculated as a product of density and cross-track velocity is shown in panel (c). The equatorward boundary (EQB) of the auroral oval is indicated by the red line.

Under the action of the SAPS electric field, the ionospheric/plasmaspheric plasma drifts in the sunward direction towards the noontime cusp. The SED plumes transported towards the polar cusp forms a tongue of high density plasma extending across the polar cap and into the nightside region [Foster *et al.*, 2005]. The TOI may break into polar cap patches while convecting through the polar cap [Sojka *et al.*, 1993] and is a source of ionospheric irregularities. As the GPS signal traverses through regions of irregularities, they undergo phase fluctuations. Intense phase scintillations were observed when the

station was located in the vicinity of the polar cusp and in the polar cap region. Increased particle precipitation in the cusp region and strong ionospheric convection during the St. Patrick's day storms could give rise to irregularities in the polar ionosphere [Aarons, 1997]. Moen *et al.* [2013] have also shown scintillations to be observed in the cusp inflow region of the ionosphere around magnetic local noon. The generation of the TOI and polar patches gave rise to intense irregularities in the polar cap ionosphere [Cherniak *et al.*, 2015] during the St. Patrick's storm of 2015. The evolution of the TOI during a storm in fact depends on the strength of ionospheric convection which in turn depends on the SWMI coupling.

As mentioned earlier, the expansion/contraction of the auroral oval and brightening of the aurora were the distinct features observed during both these storms. Over the southern hemisphere on 17 March 2015, the appearance of the most extended aurora (equatorward boundary at $\sim 55^\circ$ MLAT) in association with intense particle precipitation and strong electrojet currents corresponds to dayside magnetopause erosion [Le *et al.*, 2016]. The changes in the solar wind conditions and the orientation of IMF B_z controls the magnetopause standoff distance [Shue *et al.*, 1998; Sibeck *et al.*, 1991] which is a signature of magnetopause erosion [Holzer and Slavin, 1978; Le *et al.*, 2016].

4.3.4.4 Variations in magnetopause on 17 March 2013 and 17 March 2015

The magnetopause standoff distances during 16-18 March 2013 and 16-18 March 2015 calculated to the first order by using the pressure balance equation described by Roelof and Sibeck [1993] is presented in panels (a) and (b) of Figure 4.10 along with the IMF B_z . At about 0600 UT on 17 March 2013, the magnetopause is seen to have moved earthward ($\sim 8 R_E$) in response to the southward turning of IMF B_z . As the IMF B_z turns southward, magnetic reconnection drives the erosion of magnetic flux and the magnetopause moves earthward in order to maintain the balance between the solar wind and the magnetospheric pressure [Aubry *et al.*, 1970]. At the point of minimum B_z , i.e., around 1000 UT on 17 March 2013, the magnetopause moved further closer to $\sim 7 R_E$. During the 17 March 2015 storm also, the magnetopause was pushed to $\sim 7 R_E$ in response to the southward turning of IMF B_z and remained around $\sim 7-8 R_E$ for ~ 6 hours after the onset of the main phase of the storm. A second southward turning pushed the boundary further earthward to $\sim 6 R_E$ at about 1200 UT.

It is clear that during the geomagnetic storm of 17 March 2015, the magnetopause erosion sustained for a much longer time (~ 13 hours) than during the storm on 17 March 2013, wherein the magnetopause was seen to trace back to its original position within ~ 3 hours after the onset of the main phase. Le *et al.* [2016] have also shown that dayside reconnection led to strong magnetopause erosion on 17 March 2015. In contrast, as the IMF kept on changing its polarity (panel (a) of Figure 4.10) on 17 March 2013, the dayside reconnection would have decreased leading to the reverting of

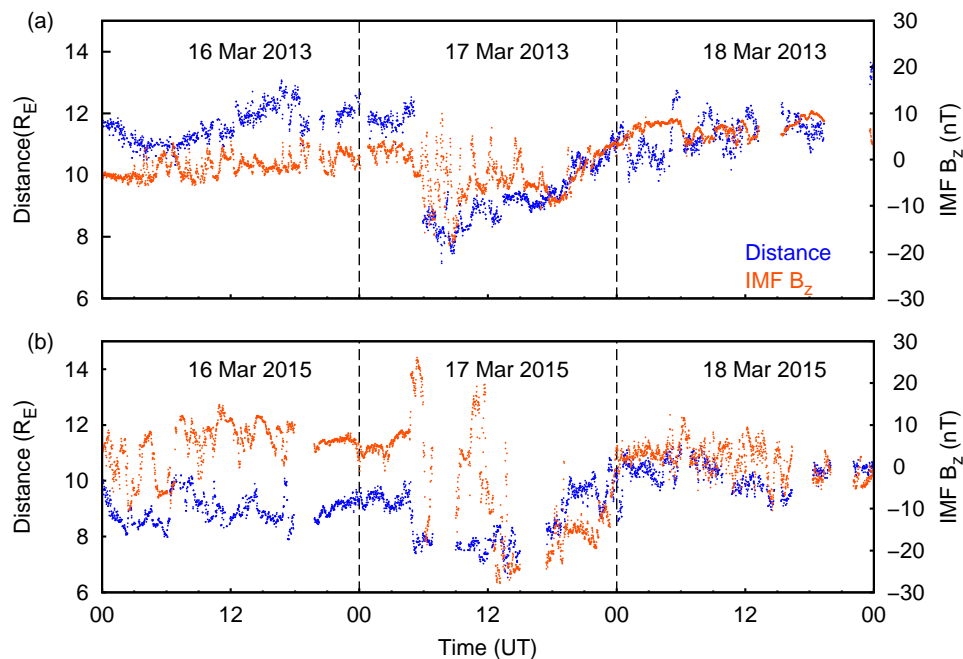


Figure 4.10: Panels (a) and (b) represents the temporal variations in the magnetopause stand off distance along with the IMF B_z during 16-18 March 2013 and 16-18 March 2015. The blue and red dots represent the magnetopause standoff distance and the IMF B_z respectively. The black vertical lines indicate change of day.

the magnetopause distance within ~ 3 hours from the onset of the main phase. The FACs and particle precipitation weakens under such conditions. These differences in the duration and extent of magnetopause erosion, are perhaps causing the observed changes in the dynamics of the polar cap and auroral oval during the St.Patrick's day storms of 2013 and 2015 discussed in the previous section. In this context, the large enhancement in TEC (~ 20 TECu) observed during the St.Patrick's day storm of 2015 could be a result of the continuous enhancement of the polar TOI due to steady convection and particle precipitation. The same for the St.Patrick's day storm of 2013 was weak and short-lived due to the fast fluctuating nature of the IMF B_z .

4.3.5 Summary of Discussion

The response of the southern polar ionosphere to the St.Patrick's day storms of 2013 and 2015 is studied using measurements from ground based GPS TEC receiver, magnetometer and DMSP satellites. These storms occurred around the same local time and the enhancements in TEC over Bharti also appeared at identical times. We find that TEC response at cusp latitudes is largely a function of the disturbance onset time. The increase in TEC during local magnetic noon can be attributed to enhanced precipitation of particles into the polar cusp. Enhanced ionospheric convection and associated formation of polar cap patches give rise to intense phase scintillations in the polar cusp and the polar cap ionosphere. Particle precipitation and ionospheric flows

were excited due to prolonged magnetopause erosion and the occurrence of multiple substorms. The continuous enhancement of the polar TOI under the action of steady convection gave rise to a large enhancement in TEC in the polar cap region on 17 March 2015. This was not the case during the St. Patrick's day storm of 2013 mainly because magnetopause erosion is sustained for a much shorter period due to fluctuating IMF B_z . This study highlights the fact that the behaviour of the polar ionosphere is strongly influenced by the magnetospheric dynamics and the duration of magnetopause erosion is an important parameter which controls the dynamics of the magnetosphere and the spatio-temporal evolution of the various stormtime processes in the polar ionosphere.

4.4 Morphology of the TEC over Bharti during geomagnetic disturbances

As discussed in the previous sections, the response of the polar ionosphere to space weather events can be dramatic because a large amount of energy gets dissipated into the polar ionosphere during geomagnetic storms [Prölss *et al.*, 1988]. Almost all the ionospheric parameters get affected by the energy dissipated into the polar ionosphere during magnetically disturbed times [Buonsanto, 1999]. In order to have a comprehensive understanding of the response of the southern polar ionosphere to geomagnetic storms, a morphological study of variation of TEC during 24 geomagnetic storm events, which occurred during the period 2013-2015, has been studied. In total there were 15 moderate storm cases, 7 intense storms and 2 severe storms during 2013-2015 as listed in Table 4.2. The storms are categorized into moderate, intense and severe based on the classification provided by Gonzalez *et al.* [1994].

Accordingly, events with $Dst \leq -100$ nT were classified as moderate storms while events with Dst between -100 nT and -200 nT as intense storms and events with $Dst \leq -200$ nT were considered as super storms. The onset time of the main phase, response of the TEC on the day of the magnetic storm and on the next day are highlighted in Table 4.2 using different colors. The positive/negative responses of TEC indicated in Table 4.2 imply the increase/decrease in TEC over Bharti while the "No change" in TEC response means that the variation in TEC more or less followed the quiet day pattern. The salient features to note from Table 4.2 are as follows.

1. A negative ionospheric storm prevailed invariably over Bharti on the day after the onset of the storm irrespective of the onset time or the intensity of the storm.
2. The response of the TEC over Bharti, however, varied on the day of the storm. A positive ionospheric storm appeared if the storm had its onset in the morning sector. There were no changes in the TEC over Bharti when the storm had its onset in the evening sector. The response of the ionosphere to storms having

Table 4.2: TEC response at Bharti to the 24 geomagnetic storm events that occurred during 2013-2015.

Intensity	Date	Dst (nT)	Main Phase Onset time (UT)	TEC response	
				Day 1	Day 2
Severe	17/03/2015	-234	0600	Positive	Negative
	22/06/2015	-208	0600	Positive	Negative
Intense	20/12/2015	-170	0030	Negative	Negative
	17/03/2013	-130	0600	Positive	Negative
	28/06/2013	-110	1000	No change	Negative
	31/12/2015	-117	1100	Positive	Negative
	27/02/2014	-101	1700	Positive	Negative
	18/02/2014	-125	1800	Positive	Negative
	06/12/2015	-105	1930	No change	Negative
Moderate	10/04/2015	-88	0000	Negative	Negative
	02/08/2013	-90	0200	Negative	Negative
	27/08/2014	-90	0330	Negative	Negative
	11/04/2014	-80	0600	Positive	Negative
	03/11/2015	-59	0730	No change	Negative
	15/08/2015	-94	0830	Positive	Negative
	08/10/2014	-50	0930	Positive	Negative
	14/10/2014	-52	1230	Positive	Negative
	06/07/2013	-88	1500	No change	Negative
	27/08/2013	-63	1600	No change	Negative
	30/04/2013	-67	1630	No change	Negative
	16/02/2015	-70	2000	No change	Negative
	08/10/2013	-77	2030	No change	Negative
	09/07/2013	-57	2100	No change	Negative
07/12/2013	-72	2230	No change	Negative	

onset times in the early morning sector was also a reduction in TEC that prevailed throughout the day at Bharti.

4.4.1 Storm onset time : How does it impact TEC variations at Bharti

In Table 4.2, we have categorized all the 24 events in terms of their onset time and have considered three moderate storm event cases for detailed description. The response of the polar ionosphere to intense storms (that occurred during 17 March 2013 and 17 March 2015) has already been discussed in detail in the earlier sections. Both the storms had their onset in the morning sector and a positive ionospheric storm was seen to appear over Bharti. Here, we discuss three moderate storms that occurred during 02 Oct 2013, 11 April 2014 and 10 April 2015 which has been chosen to represent disparate storm onset times. The main phase of the 02 Oct 2013 storm began in the local morning time, the main phase of the storm on 11 April 2014 began around noon time and the main

phase of the 10 Apr 2015 storm started in the nighttime.

4.4.1.1 Onset of storm in the morning sector

In Figure 4.11, is shown the variation of Sym-H, AE index and TEC on 01-03 Oct 2013. The SSC of the geomagnetic storm on 02 October 2013 was at ~ 0130 UT (shown in top panel of Figure 4.11). The main phase of the storm can be seen to began immediately after the SSC. The Sym-H index reached a minimum value of ~ -90 nT on 02 Oct 2013 indicating that the storm was of moderate intensity. The main phase of the storm continued for next four hours after which a slow recovery phase began. The AE index was high during the entire main phase of the storm as can be seen from middle panel of Figure 4.11. The variation of TEC over the polar cusp station Bharti during the period 01-03 October 2013 is shown using pink color in the bottom panel of Figure 4.11. The quiet time monthly mean is also shown using black in bottom of Figure 4.11 along with the standard deviation shown in green. We find that the depletion of TEC started immediately after the SSC at 0130 UT on 02 Oct 2013. The magnitude of TEC is seen to reduce to half of its quiet time value during the day. A negative ionospheric storm is seen to persist on 03 Oct 2013, during the recovery phase also.

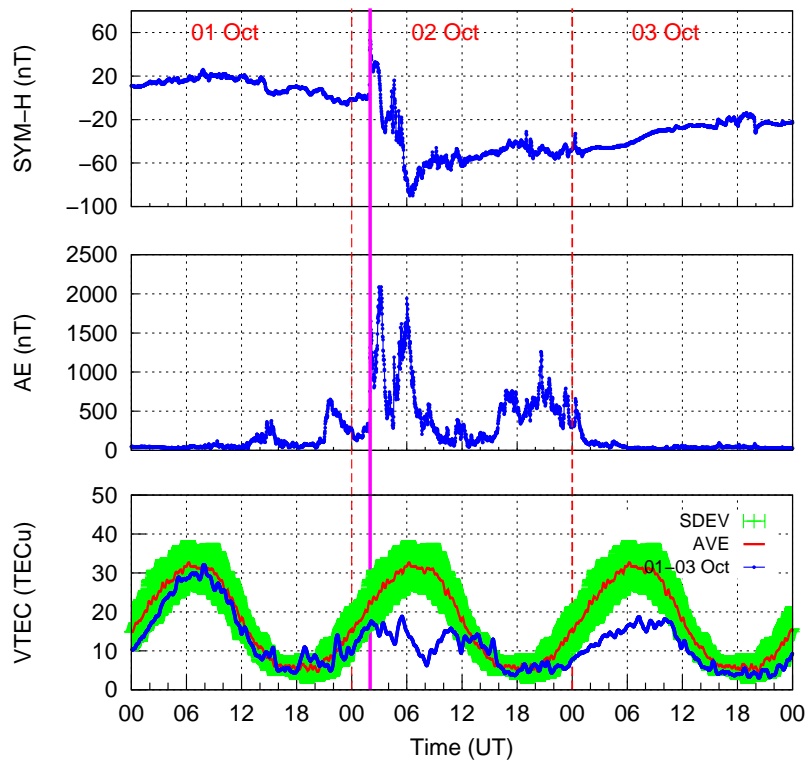


Figure 4.11: Temporal variation of Sym-H, AE index and TEC on 01–03 Oct 2013. The VTEC (blue curve) is shown along with the monthly mean (red curve) and the standard deviation (green shade) in bottom panel.

4.4.1.2 Onset of storm in the afternoon sector

The variation of Sym-H index, AE index and VTEC during 11-13 April 2014 is shown in Figure 4.12. A moderate geomagnetic storm (Sym-H \sim -80 nT) was triggered at 0600 UT (1100 LT) in the morning time of 11 April 2014. The main phase of the storm continued for \sim 12 hours during which time intense heating continued at the high latitudes as indicated by the high values of AE index. The variation of VTEC is represented by the blue curve in bottom panel of Figure 4.12. The monthly mean is shown using the red color and standard deviation is shown in green. The TEC is seen to increase for a few hours at nighttime (positive ionospheric storm) on 11 April 2014 after which it follows the quiet time pattern. A reduction in the magnitude of TEC indicating a negative ionospheric storm is observed, but on the next two days of the geomagnetic storm only.

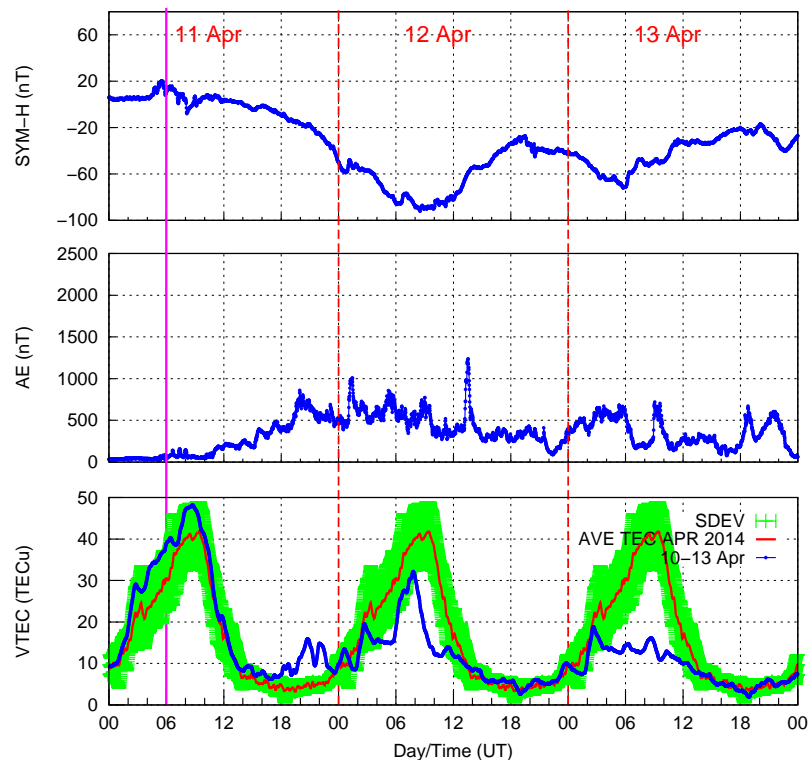


Figure 4.12: Temporal variation of Sym-H, AE index and TEC on 11-13 April 2014. The VTEC (blue curve) is shown along with the monthly mean (red curve) and the standard deviation (green shade) in bottom panel.

4.4.1.3 Onset of the storm in the nighttime sector

In Figure 4.13 we present an example case wherein the main phase of the storm commenced in the nighttime sector. The variation of Sym-H index, AE index and VTEC during 09-11 April 2015 are shown in of Figure 4.13. As can be seen from Figure 4.13, the main phase of the storm lasted for \sim 12 hours with a minimum Sym-H value of \sim -90

nT. The AE index remained high starting from the onset of main phase. The VTEC represented by the blue curve is shown along with the monthly mean (red curve) and the standard deviation (green shade) in bottom panel of Figure 4.13. We may note that from the storm onset at 2200 UT till \sim 0500 UT (seven hours), the magnitude of the TEC at Bharti followed its monthly average curve. We must mention that both during the intense as well as moderate storms (from the cases we studied) that were triggered in the period 1800-2400 UT, it was observed that there was no appreciable change in the TEC over Bharti immediately after the onset of the storm in all the cases. But, a negative ionospheric storm was seen to persist from the morning of the very next day of the storm.

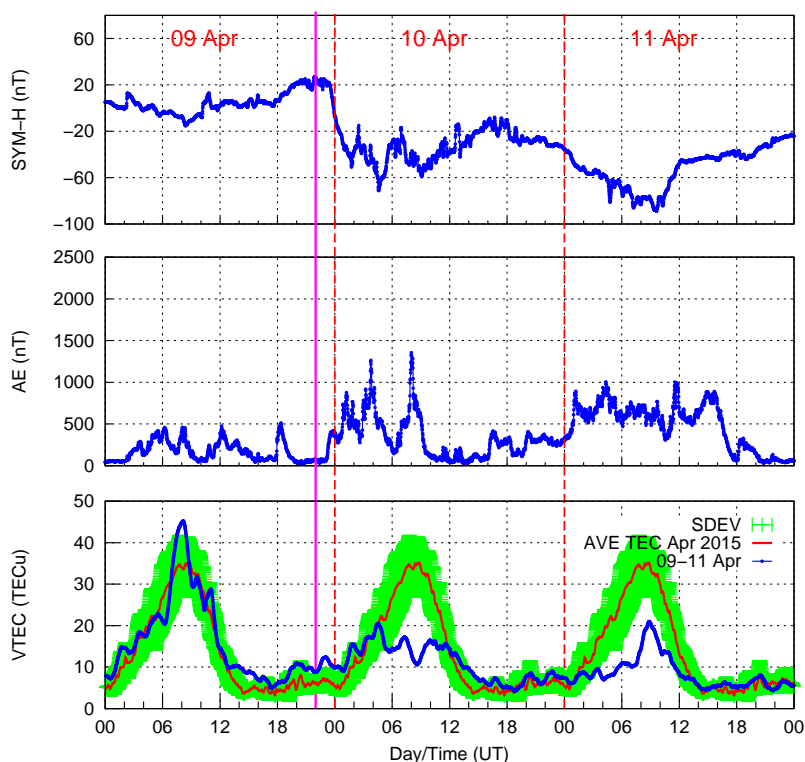


Figure 4.13: Temporal variation of Sym-H, AE index and TEC during 09–11 April 2015. The VTEC (blue curve) is shown along with the monthly mean (red curve) and the standard deviation (green shade) in bottom panel.

4.4.2 Storm impact : Positive and Negative Ionospheric storms

As seen in Table 4.2, a negative ionospheric storm (depletion in TEC) prevailed at Bharti invariably on the second day of the storm during all the geomagnetic storm events. It is known that at the midlatitudes, negative ionospheric storms usually commence in the early morning period [Prölss, 1976, 1993a]. But, at a cusp latitude station like Bharti, we find that the negative ionospheric storm persists throughout the time when the station is located in the vicinity of the auroral oval. As mentioned earlier, during magnetically quiet times, Bharti station comes in the vicinity of the auroral oval twice

in a day i.e., during the local morning time and the evening time. During disturbed times, the station may lie either inside the auroral oval or in the polar cap nevertheless affected by the magnetic disturbance. We discuss the possible reasons for the occurrence of a negative/positive ionospheric storm at Bharti in the following sections.

4.4.2.1 Negative ionospheric storms

Negative ionospheric storms are triggered mainly due to changes in the composition of the neutral atmosphere during stormtime [Prölss, 1995, and references therein]. In the high latitudes, joule heating of the atmosphere takes place due to the inflow of additional energy from the magnetosphere during magnetically disturbed times [Kelley, 1989]. As a consequence, vertical and equatorward meridional winds develop in the regions where joule heating takes place [Buonsanto, 1999]. The storm induced winds carry molecular species to higher altitudes leading to a reduction in the O/N_2 ratio [Fuller-Rowell *et al.*, 1997]. A reduction in O/N_2 ratio leads to enhanced recombination rates which in turn leads to a negative ionospheric storm [Prölss, 1995]. At a high latitude station like Bharti, which lies in the vicinity of the auroral oval during the daytime, the joule heating related effects are expected to be more pronounced during storms. The composition disturbances generated as a result of joule heating could lead to the observed negative ionospheric storm at Bharti.

Negative ionospheric storm effects develop on the first day of the storm at Bharti when they are triggered during the local morning time. The build up of TEC on a typical quiet day starts from the morning and maximizes at local noon during summer and magnetic noon in the winter. This does not happen during disturbed days as the depletion of plasma starts with the onset of the main phase in the morning time itself. Joule heating of the polar ionosphere begins with the onset of the main phase during which the storm induced winds uplift the molecular species to F region altitudes leading to recombination of the ionospheric plasma. The composition disturbances that originate due to joule heating are also carried into the dayside region as the Earth rotates. This could also result in the prevalence of a negative ionospheric storms at Bharti throughout the day of the storm. Meanwhile, magnetospheric convection also strengthens during stormtime and causes the horizontal motion of plasma [Kelley, 1989] which in turn causes heating and triggers other related processes that lead to an increase in the loss of ionization [St-Maurice and Torr, 1978]. The expansion of the disturbance zone depends on the duration and intensity of the main phase of the storm. These factors also play an important role in deciding the duration of the negative ionospheric storm over the high latitudes.

4.4.2.2 Positive ionospheric storms

Two of the severe storms of the 24th solar cycle occurred in the year 2015. Both the storms had their main phases beginning at 0600 UT. We do not describe these events in detail here as they have been subjects of other communications. The gist of observations on these two storm cases are as follows: a positive ionospheric storm was seen to occur on the first day of the storm in both the cases while a strong negative ionospheric storm prevailed on the second day of the storm. This feature was also found in most of the cases of the intense storms whose main phases commenced in the time interval 0600-1700 UT and in the case of moderate storms whose main phases began in the interval 0600-1500 UT. This corresponds to the time interval 1100-2200 LT which is the local afternoon to evening time at Bharti.

The precipitation of soft magnetosheath plasma into the polar cusp ionosphere can ionize the neutral species in the F region [Heikkila and Winningham, 1971]. During magnetic storms, particle precipitation into the cusp/cleft regions gets enhanced which could lead to the observed increase in TEC as the station enters in the cusp region. In addition, the convection of photoionized plasma from the lower latitudes into the cusp region under the action of convection electric field can also be a source of positive ionospheric storm [Foster, 2008]. Hence, if the station is located near the cusp region or in the magnetic noon sector during the initial phases of the geomagnetic storm, we can expect an increase in TEC. This feature was present in almost all the storm cases having their onset during the time interval 0600-1700 UT. Another notable feature during most of the intense and severe storm cases examined was the increase in TEC around the magnetic midnight. This could be due to the extension of the TOI into the midnight auroral zone as a result of enhanced ionospheric convection [Foster et al., 2014].

4.4.3 Salient features of the stormtime variation of TEC at Bharti

The morphology of variation of TEC during during geomagnetic storms over the polar ionospheric station Bharti has been studied using measurements of the TEC of the ionosphere by a dual frequency GPS receiver. The important features derived from the GPS TEC measurements are as follows:

1. The storm-time response of the TEC at the polar cusp station Bharti depends on the onset time of the geomagnetic storm.
2. A positive ionospheric storm is observed in most of the cases if the storm has its commencement in the afternoon sector.
3. Negative ionospheric storms persist throughout the day of the storm only if they commence during the morning sector.

4. The negative storm effects are observed invariably on the second day of the storm irrespective of their onset times.
5. Joule heating related effects cause the occurrence of a negative ionospheric storm over Bharti while enhanced particle precipitation and ionospheric convection give rise to positive ionospheric storms.

4.5 Conclusions

The response of the southern polar ionosphere to the geomagnetic storms that occurred on the St.Patrick's day of 2013 and 2015 has been studied using measurements from a ground based GPS receiver, magnetometer and DMSP satellites. The TEC of the ionosphere and magnetic field measurements were made at Bharti (69.4°S, 76.2°E geographic, 76.69°S, 126.93°E geomagnetic), an Indian station in Antarctica. During the main phase of both the storms, Bharti registered enhancements in the TEC and the phase scintillation near local magnetic noon and near magnetic midnight. The magnitude of the mid-night increase in the TEC on 17 March 2015 was however way high compared to the same on 17 May 2013 despite of the two years being at the same level of solar activity. The intensity of the two storms was different though ($Dst \sim -238$ nT in 2015, and ~ -130 nT in 2013). The increase in TEC at magnetic noon during both the storms can be attributed to intense particle precipitation. The larger enhancement in TEC near the magnetic midnight during the storm of 2015 could be caused by the enhancement of the TOI by steady convection resulting from long-lived magnetopause erosion. The same was weaker during the St.Patrick's day storm of 2013 due to the fast fluctuating nature of IMF B_z . We show that the differences in the duration of magnetopause erosion led to the varied response of the southern polar ionosphere during the St.Patrick's day storms of 2013 and 2015. Similar and distinct responses of the southern polar ionosphere to the changes in the magnetospheric system during the St.Patrick's day storms reflect the strong coupling between the solar wind, magnetosphere and the polar ionosphere. The morphological study of variation of TEC during 24 geomagnetic storms at Bharti revealed that the storm-time response of the TEC at the polar cusp station Bharti depends on the onset time of the geomagnetic storm.

Chapter 5

High-mid-low latitude coupling

5.1 Introduction

The role of Magnetosphere-Ionosphere (MI) coupling in modulating the structure of the polar ionosphere was discussed in the previous chapter. It was shown that the coupling between the magnetosphere and polar ionosphere decides the extent to which the geomagnetic disturbance affects the high latitude plasma density, magnetic field as well as the processes like aurora, ionospheric convection etc. As described in Chapter 1, during severe magnetic storms, magnetic reconnection between the Interplanetary Magnetic Field (IMF) and the geomagnetic field causes the transfer of the solar wind energy into the terrestrial atmosphere [Kelley, 1989]. When this happens, the equatorial, low, mid and high latitude ionospheric electric fields and currents undergo large departures from their quiet time behaviour. As a consequence, several processes with different features, scale sizes and time scales appear in the Earth's Ionosphere-Thermosphere (IT) system depending on the intensity of the geomagnetic disturbance [Prölss, 1995; Elphinstone et al., 1996; Mendillo, 2006; Foster, 2008; Yin et al., 2009]. Their effects manifest as ionospheric storms which is signified by increase or decrease in electron density [Buonsanto, 1999]. In this chapter, we study the role of electrodynamical and neutral dynamical coupling of the high, mid and low latitude ionosphere in the evolution of ionospheric storms.

We know that geomagnetic storms are triggered at the Earth when strong convection electric fields are generated as a result of the solar wind-magnetosphere coupling [Gonzalez et al., 1994]. These dawn-to-dusk electric fields get transmitted to the polar ionosphere along the highly conducting magnetic field lines which extends to the magnetosphere and beyond [Heppner, 1972; Lyons, 1992]. From the polar ionosphere, the electric fields penetrate into the low and equatorial latitudes [Kikuchi et al., 1996; Kikuchi and Hashimoto, 2016]. The shielding electric fields in the inner magnetosphere generally takes more than 30 minutes to build up during which enhanced magnetospheric convection causes the plasma sheet to move earthward, and creates a partial ring current [Southwood, 1977]. Once set up, this electric field shields the low and equatorial latitudes

from the prompt penetration electric field (PPEF) [Kelley *et al.*, 1979; Fejer *et al.*, 1979; Spiro *et al.*, 1988]. However, when the IMF recovers to the northward configuration, the PPEF weakens and the shielding electric field itself penetrates to the low and equatorial latitudes in what is known as the over-shielding condition. Huang *et al.* [2005] have shown that during a geomagnetic storm, if the IMF turns southward, the normal daytime eastward electric field at the dip equator gets enhanced and remains enhanced till the IMF remains southward. Alternatively, when the IMF turns northward, the westward field enhances and remains enhanced till the IMF orientation remains northward. The westward polarity of the zonal electric field during daytime leads to a current which is opposite to the eastward flowing electrojet current and is known as the Counter Electrojet (CEJ).

In addition to electric fields and currents, energy in the form of enhanced particle precipitation also arrives at the high latitude Ionosphere-Thermosphere (IT) system during magnetic storms. Impact of the energetic particles on the atmospheric gases gives rise to enhanced conductivities which combined with strong electric fields give rise to substantial electric currents and strong joule heating of the atmosphere [Rees *et al.*, 1983; Smith, 1998b; Sojka *et al.*, 1998]. Accordingly, the impulsive input of energy into the polar regions generate strong vertical and horizontal winds and even Travelling Atmospheric Disturbances (TADs) [Field *et al.*, 1992; Fuller-Rowell *et al.*, 1996; Smith, 1998a; Richmond and Lu, 2000]. The upwelling air in the polar thermosphere during geomagnetic storms brings molecular species (like N₂, O₂) to higher altitudes and generates composition disturbances. Consequently, the loss rates at F-region altitudes increase and gives rise to a corresponding decrease in the electron density at high latitudes [Buonsanto, 1999]. These disturbances, that are carried by the storm induced equatorward flow to the mid and low latitudes diverges at a latitude where the storm induced winds are balanced by the background winds. The downwelling happens therein and brings down atomic rich species to lower altitudes in the ionosphere. As a result, the loss rates at these altitudes decrease which inturn leads to an increase in the electron density at mid latitudes [Buonsanto, 1999]. At the mid latitudes, positive ionospheric storms may also occur under the action of the TADs. The TADs uplift the plasma along the magnetic field lines as they propagate towards the equator and moves it from a region of increased recombination to a region of reduced recombination, directly affecting the ambient plasma density [Prölss, 1995]. These processes constitute the negative/positive ionospheric storm effects over the high and mid latitudes [Richmond and Lu, 2000]. The effect of composition disturbances is seen to be more significant at night and morning hours than in the afternoon and evening hours [Fuller-Rowell *et al.*, 1994] while that caused by TADs are more prominent during daytime as compared to nighttime [Prölss, 1995].

The response of the global wind system to the high latitude energy input has another

effect on the equatorial region. In response to intense joule heating of the high latitude ionosphere during magnetic storms, a delayed impact, known as the Disturbance Dynamo (DD), is induced by the neutral dynamical coupling of the high-to-low latitude region. A detailed description of the disturbance dynamo process [Blanc and Richmond, 1980; Richmond and Roble, 1997], whose effects appear slowly in a day or two after the SSC [Blanc and Richmond, 1980; Fejer, 1997; Sastri, 1988] can be found in Chapter 1 of this thesis. In the equatorial region, as the plasma properties are strongly controlled by ionospheric electrodynamics, the stormtime electric fields, combined with the already existing ionospheric dynamo induced electric field, give rise to a variety of interesting phenomena from raising/lowering of the F layer [Sastri et al., 1995; Fejer and Scherliess, 1995; Maynard et al., 1998] to facilitating the development/inhibition of the Equatorial Ionization Anomaly (EIA), and a number of other well documented plasma processes [Kelley, 1989]. For e.g., the PPEF which is eastward during daytime is in the right direction to enhance the daytime eastward dynamo electric field and consequently the vertical drifts. As a result, the EIA is seen to extend further latitudinally at the low and equatorial regions during geomagnetic storms [Mannucci et al., 2005; Balan et al., 2010]. On the contrary, the disturbance dynamo electric field (DDEF), driven by the storm time neutral winds is westward during daytime and eastward during night time [Blanc and Richmond, 1980]. Hence, the DDEF reduces the upward drift of the plasma during daytime resulting in the weakening of the fountain effect. The DDEF which is eastward at nighttime in turn triggers a strong EIA during the nighttime [Fuller-Rowell et al., 2002; Tsurutani et al., 2004]. The electron density over the equator may therefore get enhanced/depleted under the action of the PPEF or DDEF. The degree of enhancement/depletion depends on the altitude of the ionospheric F-layer, the loss rates therein, and is often coupled with the effects of the composition disturbances associated with the positive storms [Richmond and Lu, 2000].

The mechanisms leading to the generation of PPEF and DDEF have been studied in detail using a number of theoretical as well as experimental studies [Vasyliunas, 1970; Gonzales et al., 1983; Kikuchi et al., 1996; Blanc and Richmond, 1980; Fejer and Scherliess, 1995; Fejer, 1997; Sastri, 1988]. A large number of studies have also documented the role of neutral winds and composition disturbances in generating positive/negative ionospheric storms over the high, mid, low and equatorial latitudes [Immel et al., 2001; Prölss, 1976; Rishbeth et al., 1987; Roble et al., 1977; Burns et al., 1995] during geomagnetic disturbances. Regardless, a comprehensive knowledge of the stormtime redistribution of plasma has been difficult to achieve because each space weather event is different from the others in one or the other way depending upon conditions in the overlying magnetosphere and the coexisting neutral thermosphere. A proper understanding of the stormtime coupling of the high, mid and low latitude ionosphere and the dynamics of redistribution of plasma during geomagnetic storms can

be achieved only with the help of simultaneous space and ground based observations from the equatorial, low, mid and polar regions. In the present chapter, we study the latitudinal evolution of ionospheric storms using multi instrument measurements from stations extending from pole to equator along the Indian longitude (76-77°E) meridian with an objective to address the following aspects:

- The role of the electrodynamic coupling of the high-mid-low latitude ionosphere in redistribution of plasma over the Indian sector.
- The role of disturbance dynamo process in altering the ionospheric system over the Indian sector.
- The relative contribution of the disturbance electric fields (PPEF and DDEF) in causing positive/negative ionospheric storms.

5.2 Database

Different aspects of the effects of geomagnetic disturbances on the high, mid, low and equatorial ionosphere have been studied in this chapter using measurements from ground based instruments like the magnetometers, ionosonde and Global Positioning System (GPS) Total Electron Content (TEC) receivers located at various stations in the Indian region and in the southern polar region. The location of the stations and the instruments thereat are listed in Table 5.1.

Table 5.1: Details on the locations of different stations and instruments thereat, used in the present study.

Station	Geographic Latitude	Geographic Longitude	Geo-Magnetic Latitude	Geo-Magnetic Longitude	Instrument
Trivandrum	08.47° N	76.92° E	00.05° S	149.74° E	GPS Digisonde
Tirunelveli	08.77° N	77.82° E	00.18° N	150.65 ° E	Magnetometer
Agati	10.51° N	72.11° E	02.41° N	145.20° E	GPS
Bangalore	12.95° N	77.68° E	04.33° N	150.87° E	GPS
Hyderabad	17.45° N	78.47° E	08.72° N	152.01° E	GPS
Alibag	18.64° N	72.91° E	10.38° N	146.78° E	Magnetometer
Mumbai	19.09° N	72.85° E	10.83° N	146.77° E	GPS
Bhopal	23.28° N	77.34° E	14.59° N	151.44° E	GPS
Gaya	24.74° N	84.94° E	15.49° N	158.74° E	GPS
Guwahati	26.12° N	91.59° E	16.51° N	165.06° E	GPS
Delhi	28.56° N	77.22° E	19.84° N	151.83° E	GPS
Shimla	31.08° N	77.06° E	22.35° N	151.93° E	GPS
Bharti	-69.40° S	76.18° E	-76.68° S	126.93° E	GPS

The TEC measured from GPS receivers have been used to infer the spatial and temporal distribution of the electron density in the ionosphere during geomagnetic storms. To understand the response of the high-mid latitude ionosphere, the GPS data from the high latitude station, Bharti and midlatitude station, Hanle are used. To study the response of the equatorial and low-latitude (near the EIA crest) ionosphere, the GPS TEC data from Trivandrum and Ahmedabad, respectively, have been used. The Vertical TEC (VTEC) data is obtained by converting the Slant TEC (STEC) data using a mapping function [Smith *et al.*, 2008]. The 5 min averaged VTEC calculated for all GPS satellites visible above an elevation of 45° is used to obtain the diurnal variation of TEC at Hanle and Trivandrum, while, at Bharti, the VTEC is calculated using GPS signals from all visible satellites above elevation of 35° . The average quiet time behavior is obtained by averaging the TEC variation for the magnetically quietest days of the month. The standard deviation is given at the 1σ levels.

Apart from this, the radio beacon observations from Ahmedabad (23.04°N , 72.54°E geographic, dip latitude 17°N) are used to understand the response of the EIA. These data are obtained from the GNU Radio Beacon Receiver (GRBR), which tracks the 150 and 400 MHz transmissions from low-Earth orbiting satellites to get the latitude variation of ionospheric TEC. An ensemble average method developed by Smitha *et al.* [2014] is used to estimate the latitudinal variation absolute TEC using radio beacon-based differential phase measurements.

The variations in the E-region electric field responsible for the currents that cause magnetic perturbations at the equator and the resultant F-region dynamics, can be inferred using magnetometer measurements. The standard procedure of subtracting the Alibag (non-equatorial low latitude station in the same longitude sector) magnetic perturbations from the Tirunelveli (dip equatorial station) ones was followed to obtain ΔH [Anderson *et al.*, 2002; Huang *et al.*, 2005]. Being a measure of the relative strength of the equatorial electrojet (EEJ), ΔH is considered to be a proxy of the zonal electric field as a function of time [Rastogi and Klobuchar, 1990; Anderson *et al.*, 2002]. The associated variations in the F-region peak height (hmF2) at the magnetic equator and the F-region peak frequency (foF2) have been studied using measurements from the digisonde located at the dip equatorial station, Trivandrum. The ionograms obtained from the digisonde at every 15 minute intervals were manually scaled using the DIGION algorithm [Titheridge, 1995] embedded in the SAO Explorer software package. The empirical model described by Bilitza [1990] is used in the DIGION algorithm to estimate the F-region peak altitude (hmF2).

The evolution of the geomagnetic storm is represented using the basic interplanetary and geomagnetic parameters, i.e., the solar wind speed, Z component of IMF (IMF B_z), dawn-to-dusk component (Y component) of the Interplanetary Electric Field (IEF), Polar Cap (PC), Symmetric Disturbance (Sym-H) index, and the Auroral Electrojet

(AE) index. The high-resolution Sym-H (1 min) data are used to represent the magnetospheric ring current variations [Iyemori and Rao, 2008]. The PC index is a proxy of the ionospheric electric field in the near-pole region [Troshichev et al., 2000]. These data are obtained from the CDAWeb (<http://cdaweb.gsfc.nasa.gov>). The IEF_y is calculated based on the solar wind velocity and IMF measurements by the Advanced Composition Explorer (ACE) satellite located at the first libration point (L1 point) of the Sun-Earth system. The ACE data provided in the CDAWeb are time shifted up to the nose of the bow shock. The IEF_y time series is further shifted by the propagation lag up to the ionosphere in order to have a meaningful comparison of the data. The propagation lag from the bow shock to ionosphere is composed of the propagation time from the bow shock to the magnetopause, and the Alfvén transit time along magnetic field lines from the subsolar magnetopause to the ionosphere. The formalism for the calculation of propagation lag is adopted from [Chakrabarty et al., 2005].

The changes in thermospheric composition during the stormtime are inferred from the global maps of O/N₂ ratio obtained from the Global Ultraviolet Imager (GUVI) instrument onboard Thermosphere-Ionosphere-Mesosphere Energetic Dynamics (TIMED) satellite. The details about the GUVI instrument and the data products are described by Paxton [1999] and Christensen [2003].

The Global Ionosphere Thermosphere Model (GITM) has been used in the present study to simulate the variations in the electron density and the neutral winds on 17 March 2013 and 29 June 2013. The GITM model uses the non hydrostatic assumption and a stretchable latitude and altitude-based grid to solve the high-latitude physics as well as the dynamo equation self-consistently. The vertical winds, electric fields, pressure and gravity, are computed by explicitly solving the vertical momentum equation and the ion-momentum equations. The GITM takes initial inputs from the International Reference Ionosphere (IRI) model and the MSIS-86 model for charged particle densities and the neutral atmosphere, respectively, only to calculate these quantities on its own later. The magnetic field in GITM can be specified using the International Geomagnetic Reference Field (IGRF) model or the APEX coordinate system. More details on the GITM model and its usefulness in studying the low latitude ionospheric electrodynamics can be found in Ridley et al. [2006] and Vichare et al. [2012].

5.3 Role of electrodynamic coupling: How the low latitude ionospheric system responded to the intense geomagnetic storm of 17 March 2013

It is known that the stormtime PPEF modifies the already existing Sq electric field and gives rise to electron density perturbations at the low and equatorial ionosphere. The direct penetration of undershielding/overshielding electric field into the low and

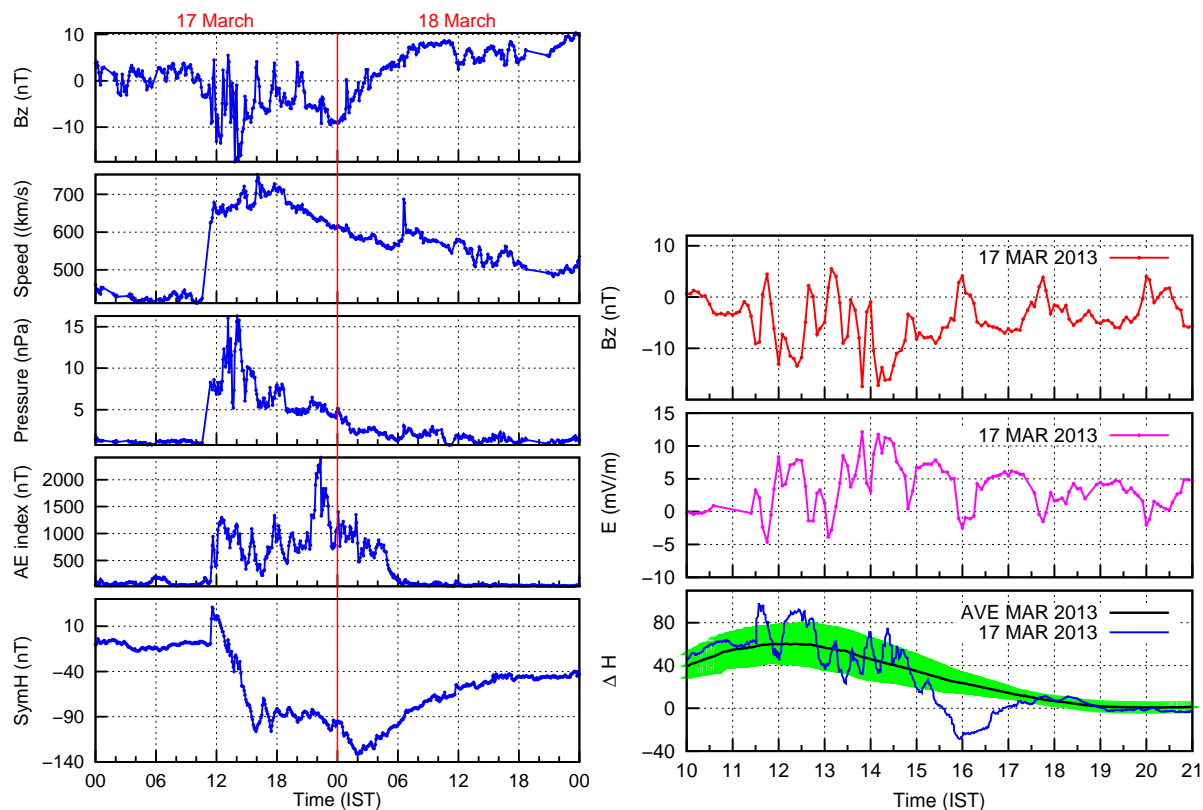


Figure 5.1: Left panel : Geomagnetic conditions during 17-18 March 2013 obtained from the OMNIWeb database. The time along X axis is in IST (UT+5.5 hrs). Right panel : IMF B_z (top), and IEF (middle) on 17 March 2013 between 10:00 and 21:00 IST. The bottom right panel shows how the ΔH varied with respect to time on 17 March 2013 (blue curve) as compared to its monthly mean variation (black curve) and standard deviation (shaded green area).

equatorial latitudes is facilitated by the electrodynamic coupling of the high to low latitude ionosphere. In order to understand the role of electrodynamic coupling in altering plasma distribution over the Indian longitude, a case study of the St.Patrick's day storm of 17 March 2013 was performed. On this day, the IMF B_z exhibited large fluctuations which resulted in the undershielding condition. Large deviations were observed in the plasma density distribution over the Indian sector during this period. In the following, the response of the ionosphere over the Indian region has been discussed in detail.

5.3.1 Geomagnetic conditions on 17 March 2013

The geomagnetic storm on 17 March 2013, which is also known as the St.Patrick's day storm, happened to have its onset coinciding with the local noon time sector for the Indian longitude. In response to the CME-driven shock that arrived at the magnetosphere, the IMF B_z on 17 March 2013 turned southward at around 11:00 IST

triggering an intense ($Dst \sim -130\text{nT}$) geomagnetic storm. Figure 5.1 (left panel) displays the IMF B_z component, solar wind speed, pressure, AE index and Sym-H index on 17 March 2013 as obtained from the OMNIWeb database. There was a sudden increase in the solar wind speed and pressure simultaneous to the southward turning of IMF B_z at 11:00 IST. The AE index also increased simultaneously in response to the IMF B_z . A persistent increase in AE index, reaching a magnitude as high as 2000 nT, indicates that strong heating was taking place in the high latitude ionosphere. The Sym-H index also exhibited a steep increase at 11:00 IST, indicating the Sudden storm commencement (SSC) as a result of the high speed, high density stream of solar wind particles ramming across the magnetosphere. It then dropped to a first minimum of -100 nT at around 15:00 IST followed by a second minimum of -134 nT at around 01:30 LT on the following day i.e., 18 March 2013.

An interesting point to note in Figure 5.1 (left panel) is the several sharp fluctuations in the IMF B_z on 17 March 2013 between 11:00 and 20:00 IST. For the sake of convenience, a zoomed portion of the IMF B_z is also shown in the top right panel of the Figure 5.1. The bottom right panel of Figure 5.1 shows temporal variations in the ΔH between 10:00 and 21:00 IST (the period when the IMF B_z had several sharp fluctuations in its polarity from southward to northward). The IEF_y recorded by the ACE satellite at L1 point and time shifted to ionosphere, is shown in the middle right panel of the Figure 5.1. As one can note, corresponding to each southward excursion in the IMF B_z , there was an increase in the eastward component of IEF, and correspondingly the ΔH (bottom panel) also exhibited strengthening of the eastward zonal field. Between 11:00 and 14:00 IST, almost one to one correspondence can be noted in the IMF B_z excursion and ΔH fluctuations at the dip-equator. However, after 15:00 IST as the IMF B_z turned predominantly northward, though fluctuations in the IEF_y followed fluctuations in the IMF B_z , ΔH took a negative turn, giving the signature of a CEJ like situation at the dip-equator. The ΔH dipped down to -40 nT by 16:00 IST only to recover by 18:00 IST. In the following, we study how this affects the distribution of plasma at the dip-equator and the low latitude ionospheric region.

5.3.2 F-region over the dip equator

To examine how the ionosphere over the equatorial region responded to the geomagnetic event of 17 March 2013, in Figure 5.2 we show variations in the foF2 (in left panel) and hmF2 (in right panel) with respect to time between 10:00 and 20:00 IST at Trivandrum, a dip equatorial station. The temporal variations in hmF2 shows the electrodynamic conditions prevailing at the dip-equator following the onset of the storm. In line with the gross variations in ΔH , the hmF2 at Trivandrum modulated sinusoidally along its monthly mean value between 11:00 and 15:00 IST. After 15:00 IST, however, it slid down from 380 km at 15:00 IST to about 320 km by 16:30 IST.

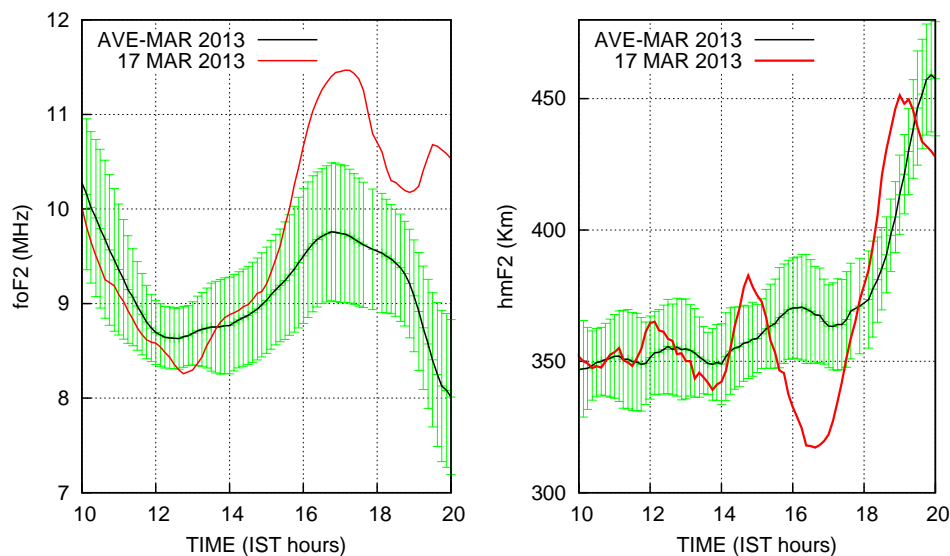


Figure 5.2: Digisonde measurements: Temporal variations in foF2 and hmF2 on 17 March 2013 are represented in red. The monthly mean and the standard deviation are represented using the black curve and the green shade respectively.

The downward excursion of the hmF2 shows the presence of a westward electric field at the dip-equator. It is well known that a westward electric field at the dip-equator leads to a downward $E \times B$ drift. It indeed was the case at Trivandrum on 17 March as ΔH , as shown in the lower panel of Figure 5.2, which shows a sharp negative excursion attaining its minimum value of -40 nT by 16:00 IST. During the period 15:00 - 18:00 IST, when the hmF2 descended down to 320 km and later returned back to its monthly average, the hmF2 experienced an appreciable increase (from approx. 7 MHz to 11.5 MHz i.e., from 6.1×10^5 to $16.5 \times 10^5 \text{ cm}^{-3}$).

5.3.3 Redistribution of plasma in the ionosphere over the Indian region

To study how the ionosphere over the entire equatorial and low latitude region responded to the fast fluctuations in the IMF B_z during the geomagnetic storm of 17 March 2013, we present in Figure 5.3, the estimates of the total electron content (TEC) of the ionosphere as measured by the dual frequency GPS receivers installed at different stations in the Indian mainland starting from Trivandrum, an equatorial station, to Shimla which being at 31.08°N geographic latitude falls in the mid-latitude region. The red curve represents temporal variations in the TEC observed on 17 March 2013, the storm day while the black color curve represents the monthly average of the month. We have considered the TEC observed at each station on 10 quiet days of March 2013 to generate the monthly average. The shaded area in the color green represents the standard deviation in the mean.

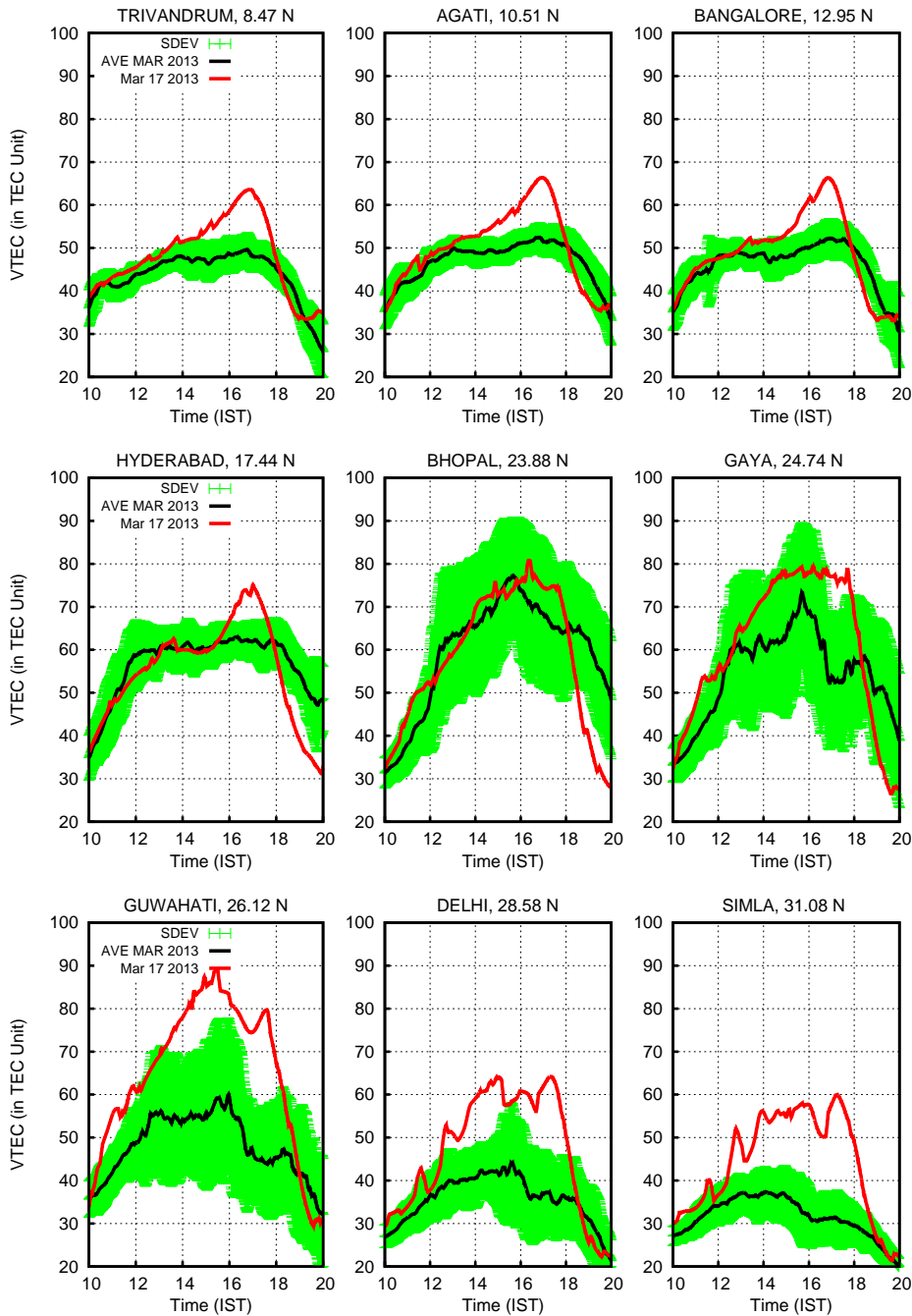


Figure 5.3: Diurnal variation of the TEC at different locations in the Indian region on 17 March 2013 is represented using the red curve. The monthly mean calculated for 10 quietest days of March 2013 and their standard deviation are shown using the black curve and the green shade respectively.

We may note in Figure 5.3 that the daytime maximum average TEC of about 78 TECu was seen at Bhopal (23.28°N Geographic, 12.8°N dip-latitude) around 16:00 IST. It made Bhopal a location for the peak of the anomaly crest. We also note that on 17 March there was an appreciable increase in the TEC around 16:00 IST at Trivandrum (8.47°N), and Agati (10.51°N), which are dip-equatorial stations. On average there

was about 15 TECu increase, compared to the monthly mean of these stations. The increase in the TEC, albeit of reduced magnitude, was seen at Bangalore (12.95°N) and Hyderabad (17.44°N) as well. These stations are low latitude stations which are at the ascending phase of the EIA, equatorward of the anomaly peak. Bhopal (23.28°N) and Gaya (24.74°N) which are near the equatorial anomaly crest, on the other hand showed no appreciable changes in the TEC on 17 March compared to the monthly mean thereat as their magnitude were within the standard deviation.

Also worth noting in Figure 5.3 is a substantial increase in the TEC on 17 March at all stations poleward / southward of the the anomaly crest. While at Guwahati (26.12°N), which is at the descending phase of the EIA, the increase in the TEC on 17 March was about 30 TECu, at Delhi (28.58°N), and Shimla (31.08°N) there was a two fold increase in the magnitude of TEC as compared to the monthly mean. This is interesting because there was a positive storm impact at the dip-latitude and low latitude stations as well as at stations southward/poleward of the anomaly crest, but there was no increase in the TEC at the anomaly zone.

Another interesting point to note in Figure 5.3 is a very sharp decrease in the magnitude of the TEC at all the stations after it reaches its peak value. At the anomaly regions (Hyderabad, Bhopal, and Gaya), the magnitude of the TEC after 17:00 IST became even less compared to its monthly mean. Further, while the positive storm effect (increase in the TEC) at the dip-equator/low latitude stations was seen to be centered between 14:00 and 18:00 IST, the same at stations poleward of the anomaly crest started after 12:00 IST only and lasted till 18:00 IST. We will discuss these aspects in detail in the following section.

5.3.4 Synthesis of observations

The observations presented in the previous section bring out the following points:

1. Southward turning of IMF B_z triggered an intense geomagnetic storm of a magnitude ~ -130 nT on 17 March 2013 at around 11:00 IST.
2. There were several sharp fluctuations in the IMF B_z between 11:00 and 20:00 IST. These fluctuations led to a CEJ like condition at the dip-equator during 15:00 - 17:00 IST.
3. The AE index shot up to about 1500 nT in response to the geomagnetic storm signaling intense thermospheric heating at the polar region.
4. In response to the CEJ during 15:00 - 17:00 IST, there was a decrease in the peak height of the F-region at Trivandrum. The hmF2 descended by about 60 km in ~ 1.5 hours between 15:00 and 17:30 IST.

5. The peak density of the F-region during this period increased from approximately 6.1×10^5 to $16.5 \times 10^5 \text{ cm}^{-3}$.
6. There was a positive storm effect (increase in the TEC) at the dip-equator, at low latitude, and southward/ poleward of the anomaly crest during 15:00 and 17:00 IST. The TEC of the ionosphere at the anomaly crest zone (Bhopal, and Gaya) however remained unchanged (compared to its monthly average).
7. While the positive ionospheric storm at the dip-equator/low latitude stations was seen between 14:00 and 18:00 IST, the same at stations poleward of the anomaly crest started earlier by 12:00 IST and lasted till 18:00 IST.
8. There was a very sharp decrease in the magnitude of the TEC at all the stations after it reached its peak value. At the anomaly regions (Hyderabad, Bhopal, and Gaya), it became even less than the monthly mean after $\sim 17:00$ IST .

The CEJ like condition at Trivandrum on 17 March 2013 can be linked to the fast-fluctuating IMF B_z . As discussed by *Rastogi and Patel* [1976] and *Kikuchi et al.* [2003], large and quick changes in the IMF B_z from southward to northward lead to a dusk to dawn electric field which is westward in the dayside. This westward field opposes the daytime Sq produced electric field in the equatorial region and creates a situation alike the CEJ at the dip-equator. It is fairly known that the polarity of the zonal electric field has a profound control over the movement of the F-region plasma at the dip equator in the Earth's ionosphere. The eastward electric field moves the plasma up and leads to the equatorial fountain effect [*Anderson, 1973b; Hanson and Moffett, 1966*]. The westward field, on the other hand, pushes the F-region plasma down in altitude, triggering a reverse-fountain. If the plasma gets pushed down too low in altitude because of a stronger westward field, it leads to a depletion in the plasma density (negative ionospheric storm) at the F-region as a result of increased recombination with the neutrals [*Ambili et al., 2014*]. However, if the plasma does not slide down too low in altitude, the loss of electrons by recombination gets inhibited. At the same time since the plasma is not moved up, its diffusion along the field lines also gets inhibited. The resultant is a net increase in the plasma density (positive ionospheric storm) at the dip-equator as depicted in the left panel of Figure 5.3. In the following, we will study how the ionosphere over the Indian low latitude region responds to a typical non-storm induced CEJ event.

5.3.5 The Indian low latitude ionospheric region during a typical CEJ event

In a previous study, *Choudhary et al.* [2012] examined the impact of a daytime westward electric field at the dip-equator (CEJ like condition) on the distribution of plasma in the Indian low latitude region. In response to an annular eclipse, which had

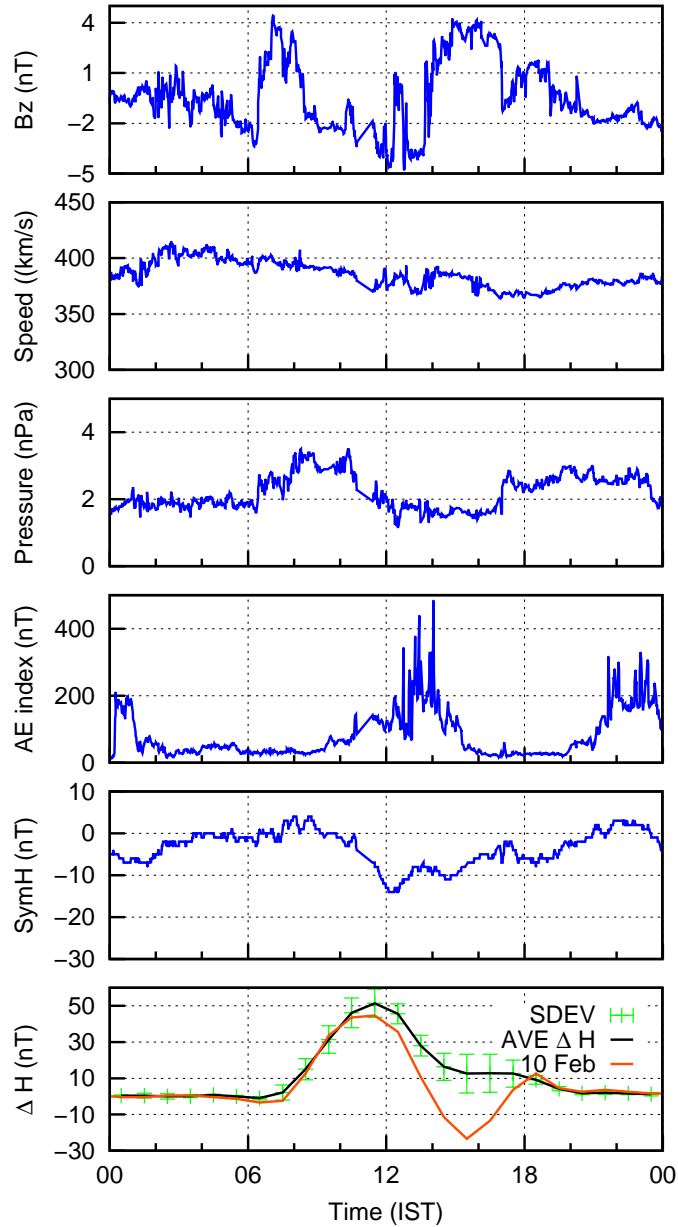


Figure 5.4: Variation of IMF B_z , Solar wind speed, pressure, AH index, Sym H index and ΔH on 10 February 2013 is shown in top to bottom panels, respectively. In the bottom panel, the temporal variation of ΔH on 10 February 2013 represented using the blue curve along with the monthly mean of ΔH calculated for the 10 quietest days in February 2013 is shown. The monthly mean and the standard deviation are shown using the black and green color respectively.

approximately 80.3 % obscuration of sun during 13:10 to 13:18 IST, the ΔH at the dip-equator dipped down to ~ -25 nT by 14:00 IST. A CEJ like condition at the dip-equator, so emerged, led to a negative ionospheric storm in the entire Indian low latitude region. But since the event studied was an annular solar eclipse, the negative storm impact was an outcome of a combination of multiple effects which included the CEJ as well as the reduced photoproduction due to inhibited EUV flux during obscured Sun. In the

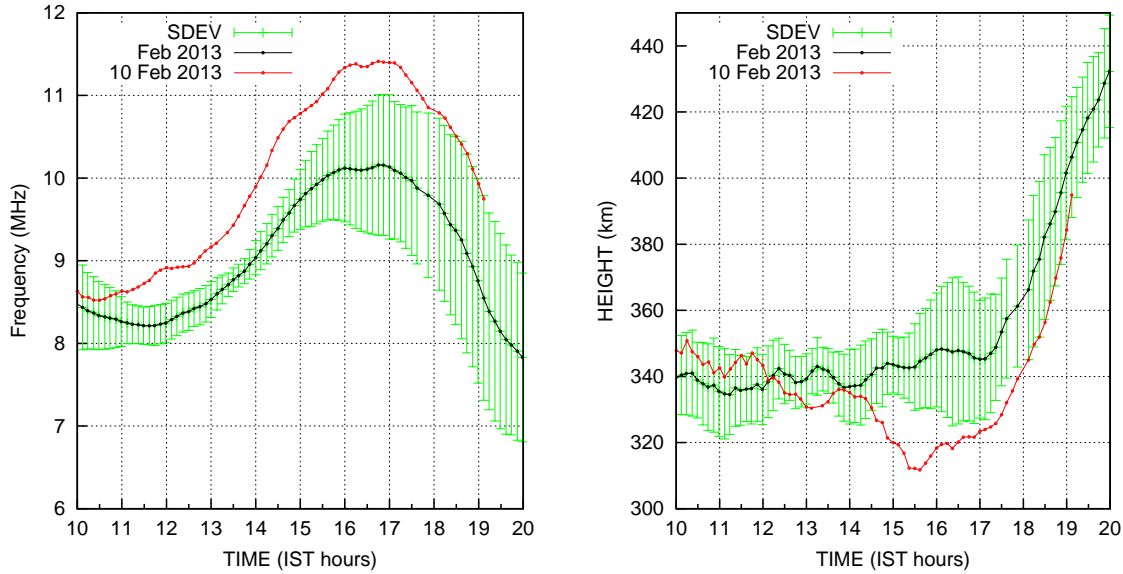


Figure 5.5: Temporal variations in the peak height of the F-region (hmF2) and peak density of F-region (foF2) (red curve) on 10 February 2013 to the its monthly mean variations (black curve) and standard deviation (green lines) is shown in the right and left panels respectively.

following we present a CEJ event which occurred on 10 February 2013, a geomagnetically controlled day ($K_p=1.0$, minimum $Dst = \sim -15$ nT). Since reasons for the onset of a CEJ on 10 February is beyond the scope of the presentation, we only discuss how the zonal electric field (ΔH) responded to the CEJ event and how it impacted the distribution of plasma at the dip-equator and over the Indian low and mid-latitude regions.

The five panels of Figure 5.4 presents IMF B_z , solar wind speed, pressure, AE index and Sym-H index on 10 February 2013 respectively. The bottom panel of Figure 5.4 compares temporal variations in ΔH on 10 February 2013 with the quiet day average of ΔH for February 2013 (black curve) and its standard deviation (shaded area in green color). We note in Figure 5.4 that 10 February 2013 was a quiet day with minimum Dst of about -15 nT. While IMF B_z kept on changing its polarity from negative to positive, the AE index magnitude remained low indicating a quiet time condition. However, on that day there was a sharp decrease in the magnitude of ΔH between 12:00 and 18:00 IST. Around 15:00 IST, ΔH dipped down to about -25 nT. We have chosen the 10 February 2013 event for comparison as the local time of CEJ onset coincides with that on 17 March 2013. Even the the magnitude of minimum ΔH during the two events were of the same order. It shows that the intensity of zonal westward electric field on both the days were comparable. It also suggests that there should be a similar response in the ionospheric parameters (hmF2 and foF2) on the two days. It indeed was so as reflected by the on-site Digisonde at Trivandrum. In the following we present observations from Digisonde at Trivandrum to study how the F-region of the ionosphere responded to such

a sharp mid-afternoon decrease in ΔH .

The right panel of Figure 5.5, which compares temporal variations in the hmF2 on 10 February 2013 to its monthly mean variations (black curve) and standard deviation (green lines), clearly shows that F-region responded quickly to the negative excursion in ΔH at around 12:00 IST. The hmF2 started descending sharply and came down to an altitude ~ 310 km by 15:30 IST (compared to the monthly average of about 340 km). Alike in the case of 17 March 2013, during this event also the hmF2 descended, by about 30 km, during the period when ΔH dropped from 10 nT to -25 nT.

We may note from the left panel of Figure 5.5, which compares the foF2 on 10 February 2013 to its monthly mean, that the peak density of F-region kept on increasing between 12:00 and 16:00 IST, though during this period, the hmF2 descended from 350 km to 310 km similar to the case on 17 March 2013. Putting the observations on 17 March 2013 and 10 February 2013 in perspective, we note that though hmF2 had a decrease on both 10 February and 17 March, but since it remained above 300 km, there was no loss in plasma density either due to recombination or transport. In the meantime since photo-production of ions was still continuing, there was a net increase in foF2. The combined effect of these two processes resulted in a net increase in the peak plasma density of the F-region at the dip-equator.

Since there was a net increase in foF2 on 10 February 2013 during the CEJ, it would be interesting to know how the ionosphere over the Indian low and mid-latitude region responded to the increased peak electron density in the F-region. We once again used measurements of the TEC from the dual frequency GPS receivers at different stations in India for this purpose. Along the line as shown in Figure 5.3 for 17 March 2013, in Figure 5.6 we compare the TEC observed on 10 February 2013 at Trivandrum, Agati, Hyderabad, Mumbai, Bhopal, and Gaya to their monthly averages and standard deviation. Since the receiver at Bangalore was not operational on 10 February 2013, we do not show the data over Bangalore. Alike Figure 5.3, the black color curves in the Figure 5.6 represent the monthly average while the green shaded area represents the standard deviation. The red colored curve represents TEC measurements on 10 February 2013.

We note a distinct negative storm impact of the CEJ on 10 February 2013 in the Indian low latitude ionospheric region. There was an appreciable loss of plasma after 14:00 IST at the low latitude stations, Hyderabad, Mumbai and Bhopal compared to their monthly mean. But we do not see a negative storm effect over the equatorial regions. From the variation of hmF2 and foF2 over the dip equatorial station Trivandrum, shown in Figure 5.5, it can be seen that the F layer remained at altitudes (~ 300 km) where the loss processes like diffusion and recombination play a minimal role in affecting the plasma density. Meanwhile, since photoproduction continued to take place because being daytime, the net impact was an enhancement in TEC over the dip equatorial station

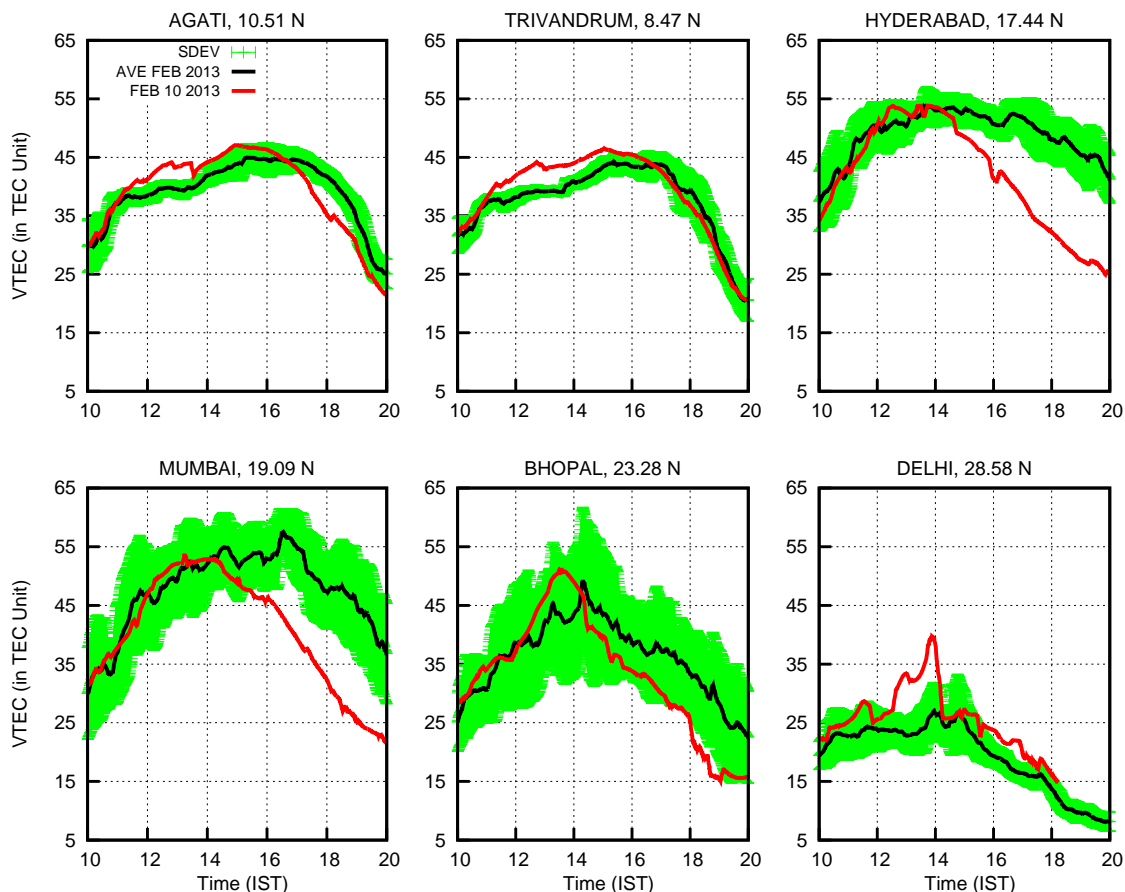


Figure 5.6: Same as Figure 4, but for 10 February 2013.

[Shreedevi *et al.*, 2016; Tsurutani *et al.*, 2008]. At the same time, since the plasma from the dip-equator was not pushed along the magnetic field to the low latitude region, a net decrease in the TEC was observed in the anomaly region.

On 17 March 2013, on the other hand, we note that there was a positive ionospheric storm impact at the equatorial/low latitude stations as well as at the stations away from the anomaly crest (Figure 5.3) though the magnitude of the westward electric field remained of the same order (~ -35 nT) as on 10 February 2013. The stations close to the anomaly crest (Bhopal and Gaya) show no appreciable changes in the plasma density on 17 March compared to their monthly mean. Ideally, since the equatorial fountain on 17 March 2013 was inhibited, it should have led to a decrease in the TEC at these stations as seen on 10 February 2013 (Figure 5.6). It only goes to add that there was a positive storm impact at the EIA crest region as well on 17 March 2013.

5.3.6 Polar ionosphere on 17 March 2013

Despite of 17 March 2013 being a CEJ day, since a positive storm impact was seen in the entire equatorial and low latitude ionospheric regions, it only goes to suggest that the reasons for an increase in the TEC at these locations would be non-local. In order to check if it had any connection with the geomagnetic conditions prevailing over the

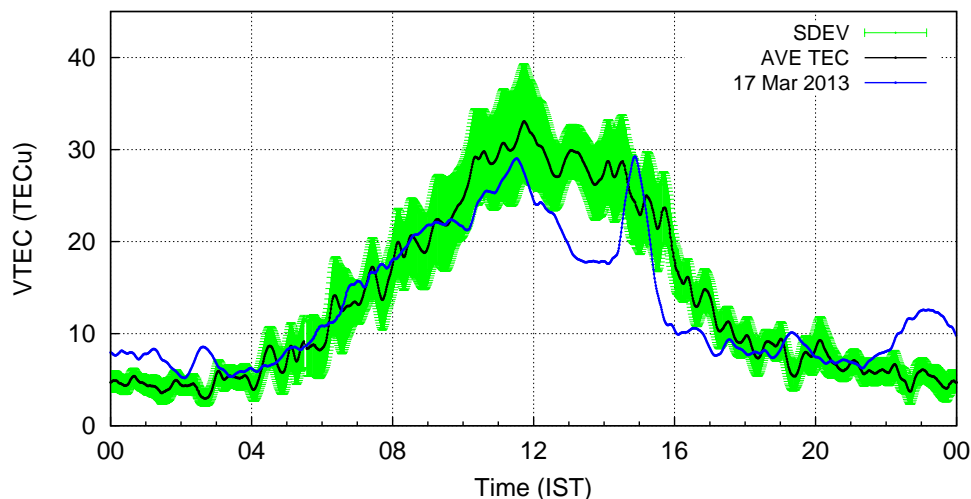


Figure 5.7: Temporal variation of the TEC on 17 March 2013 at Bharti is represented using the red curve along with the monthly mean calculated for the 10 quietest days of March 2013 and their standard deviation shown using the black curve and the green shade respectively.

polar region, where the impact of a geomagnetic storm was directly felt, in Figure 5.7 we present variations in the TEC recorded at Bharti, a polar station located in Antarctica.

In Figure 5.7, the red and black curves represent temporal variations in the TEC on 17 March 2013 and monthly mean TEC at Bharti respectively, and the green hatched area shows the standard deviation from the monthly mean values. We may note that the TEC on 17 March responded in unison with the sudden onset of the storm at 11:00 IST. As Bharti is located at 76.18°E longitude, the local time at Bharti is the same as at the Indian mainland. We may note that the TEC at Bharti on 17 March started to decrease immediately after 11:00 IST and barring a steep rise with an equally sharp decrease in the TEC at around 14:00 IST, it remained low till about 17:00 IST. The large enhancement in TEC seen at Bharti around 14:00 IST shows the immediate response of the high latitude ionosphere to geomagnetic activity. Earlier investigations have reported such increase in the TEC in the afternoon to dusk sector following SSC at the high latitudes [Mendillo and Klobuchar, 1975; Buonsanto, 1999]. Mechanisms like soft precipitation [Schodel, 1974] and plasma transport due to convection [Foster, 1993] were proposed to explain the observed increase in TEC over the high latitudes.

A reduction in the TEC at the polar latitudes could be either due to the neutral composition changes arising due to storm induced thermospheric heating or transport of plasma to the lower latitudes. It is known that the large amount of energy that gets deposited into the polar latitudes during a geomagnetic storm leads to joule heating of the neutral atmosphere which, in turn, alters the neutral winds and hence the thermospheric dynamics [Sastri et al., 2000; Maruyama et al., 2005]. Upwelling of molecular species due to expansion of the neutral atmosphere at high latitudes is aided by these storm-induced

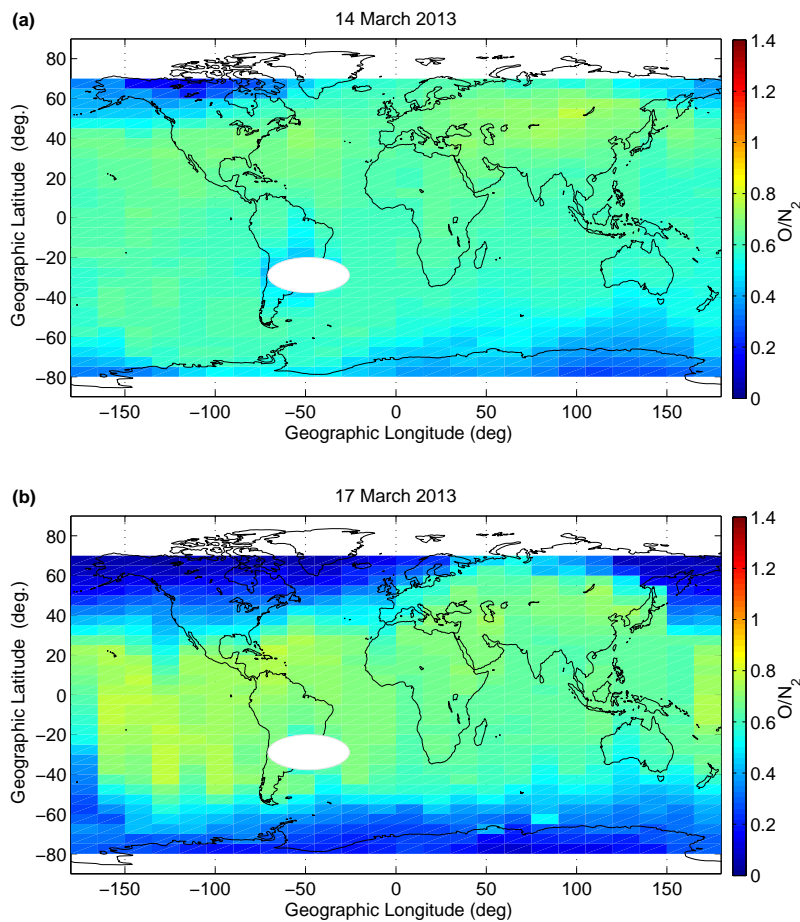


Figure 5.8: Top and bottom panels show the O/N_2 maps obtained on 14 March 2013 and 17 March 2013 from the GUVI/TIMED satellite measurements, respectively

neutral winds and enhanced upward vertical winds which transports the compositional disturbances to mid and low latitudes [Immel *et al.*, 2001]. The equatorward meridional wind driven by joule heating along with the prevailing trans-equatorial winds decide the latitudinal extent of the plasma redistribution during geomagnetic storms [Prölss, 1976]. At the high latitudes, there will be decrease in the O/N_2 ratio resulting from upwelling of molecular rich species (e.g., O_2 and N_2) which results in a depletion in the TEC because of increased recombination.

To examine the whether the negative storm effect over the high latitude and the positive storm effect over the mid and low latitude ionosphere on 17 March 2013 was caused by compositional disturbances, we present O/N_2 maps obtained from the GUVI instrument onboard the TIMED Satellite. In Figure 5.8, the top/bottom panel shows O/N_2 ratio on 14/17 March 2013. The O/N_2 ratio for 14 March 2013, which is a quiet day, is shown for comparison purposes. We may note that on 17 March 2013, around the location of Bharti (69.4°S , 76.1°E), the O/N_2 ratio shows a decrease whereas in the conjugate region in the northern hemisphere, the O/N_2 ratio is of greater magnitude. A comparison of the O/N_2 values on 17 March 2013 with those on the quiet day of

14 March 2013 shows not a greater change in the northern hemisphere. Hence, the positive ionospheric storm observed over the stations located poleward of the EIA crest (Guwahati, Delhi and Shimla) in the northern hemisphere could be due to some other factor.

5.3.7 Plausible reasons for a positive ionospheric storm in the Indian sector on 17 March 2013

We discussed in the previous sections the occurrence of a positive ionospheric storm over the entire low latitude ionospheric region in the Indian sector on 17 March 2013. Appreciable increase in the magnitude of the TEC was seen at the equatorial stations (Trivandrum, Agati, and Bangalore) as well as at the stations poleward of the anomaly crest (Guwahati, Delhi, and Shimla). At the anomaly crest stations (Bhopal, and Gaya), though there were no noticeable changes in the magnitude of the TEC, we still interpret it as positive ionospheric storm. This is because following a CEJ, there should have been a decrease in the TEC on 17 March 2013 at these stations, as it was on 10 February 2013, during a non-storm induced CEJ event. No decrease in the TEC at these stations therefore was considered as a signature of a positive ionospheric storm.

The polar region (Bharti, Antarctica, Figure 5.7), on the other hand, presented a different picture. Following the SSC at 11:00 IST, the TEC at Bharti started decreasing and apart from the sudden increase at 14:00 IST, it remained consistently low till 1700 IST as compared to the monthly mean on 17 March 2013. Observations of net decrease in the TEC at the auroral region in response to sudden commencement of a storm however is not new and there are several reports in this regard [*Mendillo, 2006*]. It is known that the joule heating of thermosphere in auroral region, in response to a geomagnetic storm, leads to rapid expansion of neutral atmosphere, which, in turn, modifies the global circulation pattern and produces enhanced equatorward wind [*Fuller-Rowell et al., 2002; Buonsanto, 1999*]. The existence of intense joule heating of the auroral thermosphere on 17 March 2013 can be inferred from consistently high values of AE index (Figure 5.1) after 11:00 IST. However since measurements of the neutral winds induced by joule heating are unavailable, to study thermospheric wind conditions on 17 March 2013 we use simulation results from the GITM model. In Figure 5.9 we show results of the simulation runs depicting global distribution of the meridional wind (top panel) and electron density (bottom panel) at 15:30 IST on 17 March 2013. The location of Bharti is marked by a white filled circle in both panels of Figure 5.9.

We may note in Figure 5.9 that around the location of Bharti, there was an enhanced meridional wind having velocity around 500 m/s which maybe due to intense joule heating of the thermosphere on 17 March 2013. Corresponding to the enhanced wind, the electron density was also very low in the region around Bharti, while it was quite high in the region around 40° geographic latitude in both the hemispheres. Our observations

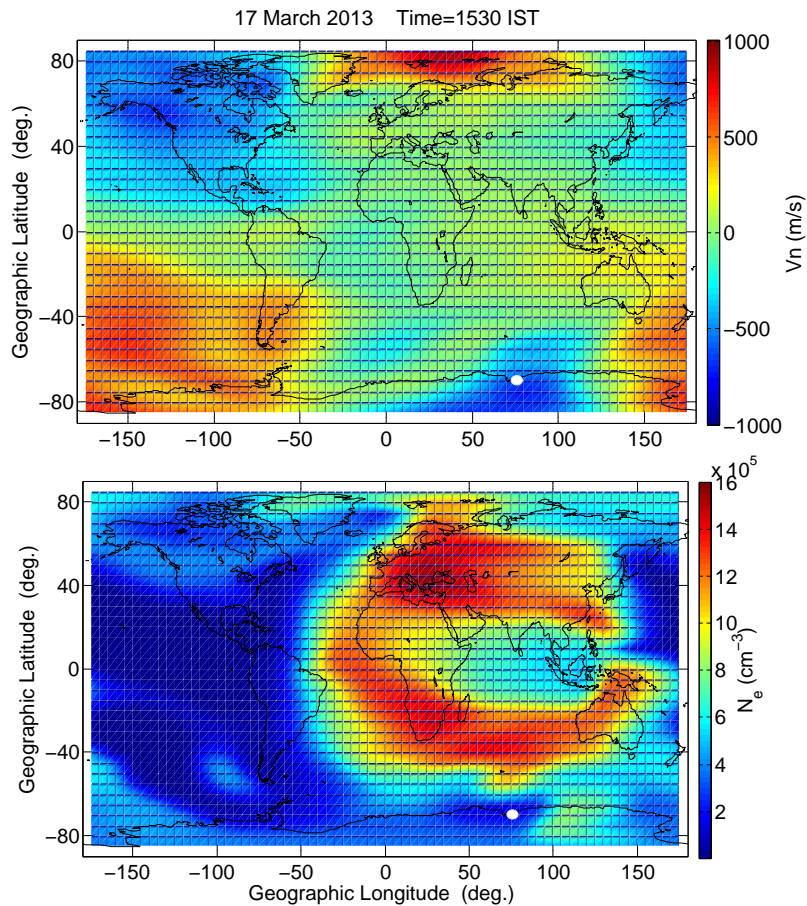


Figure 5.9: Top panel shows the meridional thermospheric wind at 350 km while the bottom panel shows the distribution of electron density at 350km on 17 March 2013 at 1530 IST.

of the TEC at Bharti, and over the Indian low latitude stations on 17 March support the simulations results shown in Figure 5.9. We may recall that there was a decrease in the TEC at Bharti during the period when the low latitude stations had positive ionospheric impact. These evidences suggest that enhanced meridional wind at the auroral regions, and the positive storm at the low latitudes are correlated.

Enhanced meridional winds are known to cause positive ionospheric storm at the low latitude regions. In a study, *Lu et al.* [2008] have shown that the joule heating induced pressure gradients at the auroral region gives rise to a strong equatorward meridional wind in the thermosphere. The neutral wind surges propagates in the form of gravity waves with a velocity as high as 700 m/s. Initially these surges uplift the ionospheric plasma to higher altitudes which in turn inhibits the recombination of plasma resulting in an increase in the plasma density at low latitude regions (a positive ionospheric storm). In the later phase, the rarefaction associated with the gravity waves push the ionospheric plasma down in altitude and the subsequent increase in plasma recombination leads to a sharp decrease in the ion density (negative ionospheric storm).

We may note in Figure 5.9 a few marked differences in the increase of plasma density

near the dip equator and at regions poleward of the anomaly crest vis-a-vis decrease in the TEC at Bharti (Figure 5.9). Compared to Bharti, where the TEC started decreasing immediately following the SSC at 11:00 IST, the enhancement in the TEC at stations poleward of the anomaly crest started at 12:00 IST, while the same at stations close to the dip-equator was only after 14:00 IST. In other words, there was \sim one hour of difference between the onset of negative ionospheric storm at auroral region, and positive ionospheric storm at mid-latitude, and \sim two hours of time difference between the onset of a positive storm at mid-latitude and equatorial regions. We may also note a sharp decrease in the TEC at all the stations after 17:00 IST. At locations close to the crest of equatorial anomaly, the decrease in the TEC was so sharp that its magnitude became much less compared to the monthly mean. One hour of difference in the onset time of the TEC decrease at Bharti, an auroral station, and stations poleward of anomaly crest can be inferred to be caused by to the propagation of the wind surge with velocity close to 800 m/s (assuming auroral zone to be near 60°N in the Northern Hemisphere). This estimated velocity is of the same order as suggested by *Lu et al.* [2008]. The increase in the TEC can be associated with the uplift of F-region at these locations by the surging gravity waves. At the same time, the sharp decrease in the TEC after 17:00 IST can be associated with the rarefaction phase of gravity waves which pushed the plasma down in altitude leading to enhanced recombination.

At the equatorial and low latitude stations, the positive storm impact may not be linked to the storm induced gravity waves. This is because the on-site digisonde at Trivandrum presents a different picture. Between 14:00 and 16:00 IST, when the TEC as well as foF2 at the dip-equator increases, the F-region peak height slides down in altitude rather than been pushed up, as proposed by [*Lu et al.*, 2008]. Since the F-region remained above 300 km and was not pushed low enough in altitude, the recombination of plasma could not happen. At the same time, the photoproduction of ions was continuing due to sunlit conditions. The combined effect, therefore was a net increase in the TEC. The increase in the TEC at the mid latitudes was for a longer duration (of about 6 hours between 12:00 and 18:00 IST), compared to the equatorial region where the impact remained limited to a period between 14:00 and 17:00 IST.

In the light of these observations, we surmise that the joule heating at the polar region created a latitudinal pressure gradient in thermosphere and led to a meridional surge in TADs which moved at a velocity close to 800 m/s. Initially these TADs raised the F-region plasma near anomaly crest region to higher altitudes and nullified the loss of plasma by recombination and hence an increase in the TEC (positive storm impact). Near the equatorial region, on the other hand, the CEJ induced westward field pushed the plasma down in altitude to annul the equatorial fountain and hence the no loss of plasma due to transport. At the same time, since the plasma was not pushed too low in altitude, its effective loss via recombination was also low. A combination of these two

factors gave rise to the positive storm effects at the equatorial region.

5.3.8 Salient features

In the present study, it is shown that the fast fluctuations in the IMF B_z on 17 March 2013 gave rise to a CEJ-like condition at the dip equator and resulted in a positive storm in the entire ionosphere over the Indian sector. There was an appreciable increase in the TEC in the entire Indian ionospheric region starting from Trivandrum, a station located at the dip equator, to Shimla which is far poleward of the anomaly crest in response to the intense geomagnetic storm ($Dst \sim -130$ nT) that occurred on 17 March 2013. The reasons for the increase in the TEC at near equatorial region and in the equatorial anomaly zone are however different. In the equatorial region, the increase in the TEC was due to the westward field (CEJ), resulting from the overshielding condition. The westward electric field pushed the daytime F-region over the dip equator down in altitude region where recombination and diffusion played minimal roles. Since the photo-production of plasma is taking place at a much higher rate than loss due to diffusion and recombination, there is an enhancement in the electron density at equatorial/ low-latitude region. In the anomaly zone, on the other hand, the increase in the TEC was due to the action of TADs. Storm induced joule heating at the auroral regions gave rise to TADs propagating equatorward at velocity as high as 800 m/s. These TADs raised the daytime F-region plasma up in the anomaly zone leading to the subsidence in their recombination. Meanwhile, since the production of plasma due to photo-ionization was also continuing, a positive storm impact resulted in the anomaly region and beyond. This is the first ever evidence of a simultaneous occurrence of a positive ionospheric storm at the equatorial, low and mid-latitude regions, though reasons of the increase in TEC at different latitudes were different.

5.4 Role of neutral dynamical coupling: How the low latitude ionosphere responded to the intense geomagnetic storm of 28 June 2013

It was shown in the previous study that the PPEF plays an important role in the redistribution of the plasma over the equatorial and low latitude ionospheric region during magnetic storms. In the studies of the low-latitude ionospheric response to geomagnetic storms, the PPEF is usually inferred using IMF B_z or IEF $_y$ data, and has clear signatures in the ground magnetic field data [*Simi et al.*, 2012]. In contrast, the identification of DDEF is mostly based on inferences from the ionospheric observations and modeling. The major challenge in identifying the DDEF from ionospheric observations lies in delineating the effects of DDEF from those due to composition changes. Over low latitudes, the DD effects are seen prominently in the zonal and vertical drifts

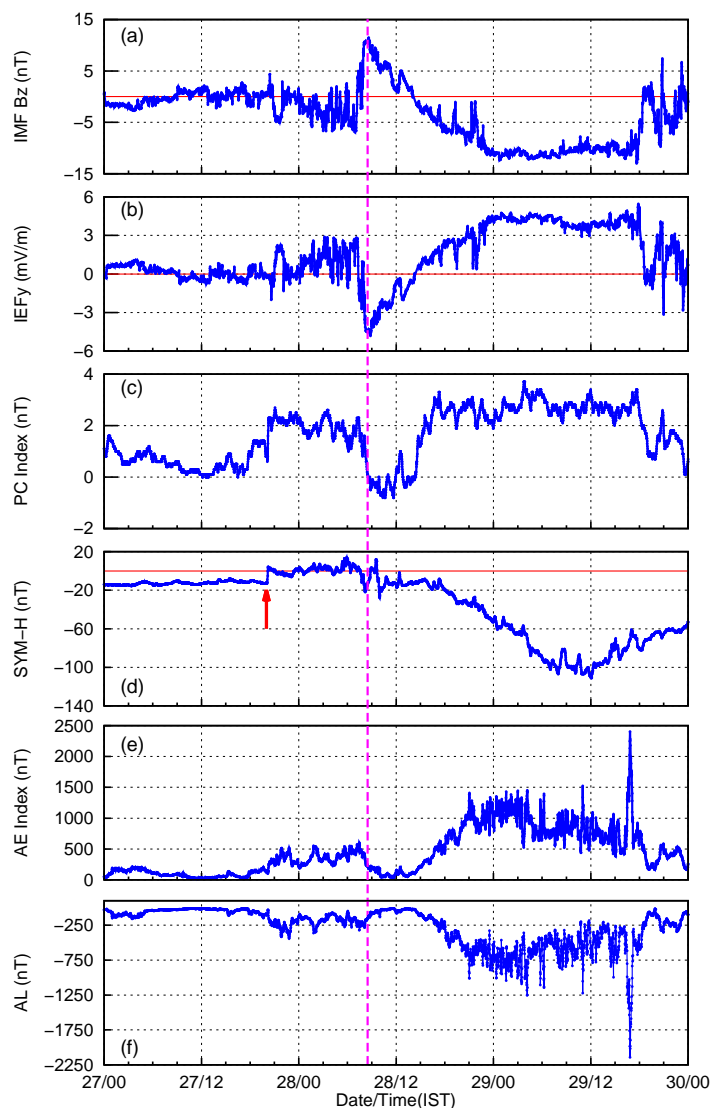


Figure 5.10: Geomagnetic conditions during 27-29 June 2013.

during afternoon and nighttime [Fejer and Emmert, 2003]. Little is known about the response of the ionospheric system to the prevalence of DDEF from morning hours itself. Many times, it is seen that although DD currents develop in the daytime, the resulting dynamo electric fields are shorted out by the large E-region conductivities [Huang, 2013]. However, model simulations have shown that DD tends to reduce the daytime upward drifts [Maruyama *et al.*, 2005]. In the following, a case study of the geomagnetic storm that occurred on 28 June 2013 has been presented with an objective to understand the effects of DDEF on the equatorial and low latitude ionospheric system.

5.4.1 Geomagnetic conditions between 27-29 June 2013

The geomagnetic storm commenced with the southward turning of IMF B_z on 28 June 2013. The variation of IMF B_z , IEF $_y$, PC index, Sym-H, AE and AL indices during 27-29 June, 2013 is shown in panels (a)-(f) of Figure 5.10. The IEF $_y$ initially reversed its polarity at around 08:00 IST on 28 June. It remained eastward while fluctuating

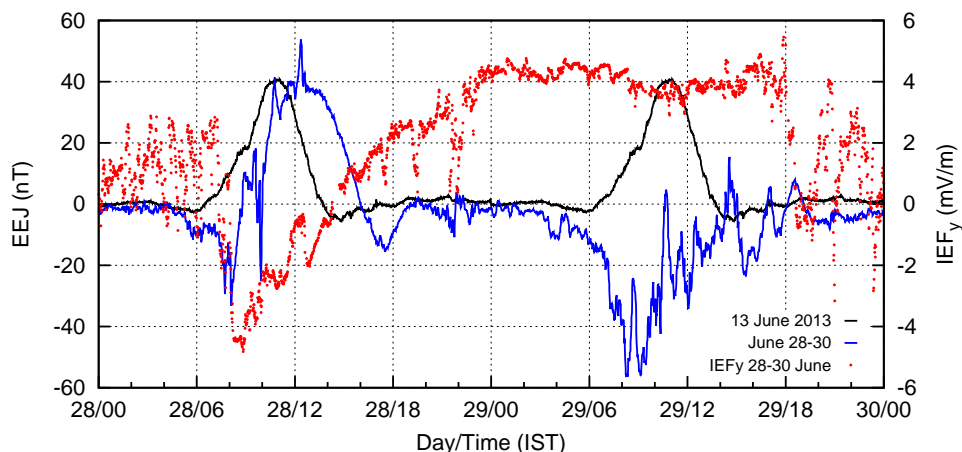


Figure 5.11: EEJ variation during 28-29 June 2013 (blue line) along with variation in IEF_y (red dots). The black line represents the typical quiet day variation of EEJ on 13 June 2013 which is a quiet day. The variation of EEJ on the quiet day is shown with both 28 and 29 June to facilitate comparison.

upto ~ 3 mV and then became suddenly westward again. Later in ~ 5 hours, the IMF B_z and IEF_y slowly changed their polarities to southward and eastward respectively. The ionospheric storm actually started with the second southward turning of IMF B_z on 28 June. The pink vertical line marks this time. The PC showed corresponding enhancements in association with the southward turning of the IMF B_z . Panel (d) of Figure 5.10 shows the variation in the Sym-H values. Sym-H increased abruptly with the southward turning of the IMF B_z revealing the SSC on 27th June. However, the main phase of a geomagnetic storm ensued much later, after the second southward turning of the IMF B_z at $\sim 11:55$ IST on 28 June. Significant substorm activities were also found to occur after this, as evident from the AL variation. The auroral electrojet (AE) index variation shown in panel (e) of Figure 5.10 indicates an enhanced joule heating of the polar thermosphere few hours after the southward turning of IMF B_z on 28 June.

The changes in the IMF B_z / IEF_y are also known to get reflected in the ground magnetometer observations as enhanced EEJ (CEJ) conditions. The EEJ strength during the period 28-29 June, along with the quiet day mean and standard deviation is shown in Figure 5.11. In order to facilitate comparison, the variation in IEF_y is also shown. It can be seen that the EEJ responds promptly to the changes in the IEF_y as evident from the concurrent enhancements in the EEJ current corresponding to enhancements in eastward electric field during daytime on June 28. However, on 29 June, the EEJ is completely suppressed, and does not show any correspondence with IEF_y , confirming the presence of a westward electric field during daytime. How these conditions affected the ionosphere over the Indian region on 28 and 29 June 2013 are described in the following sections.

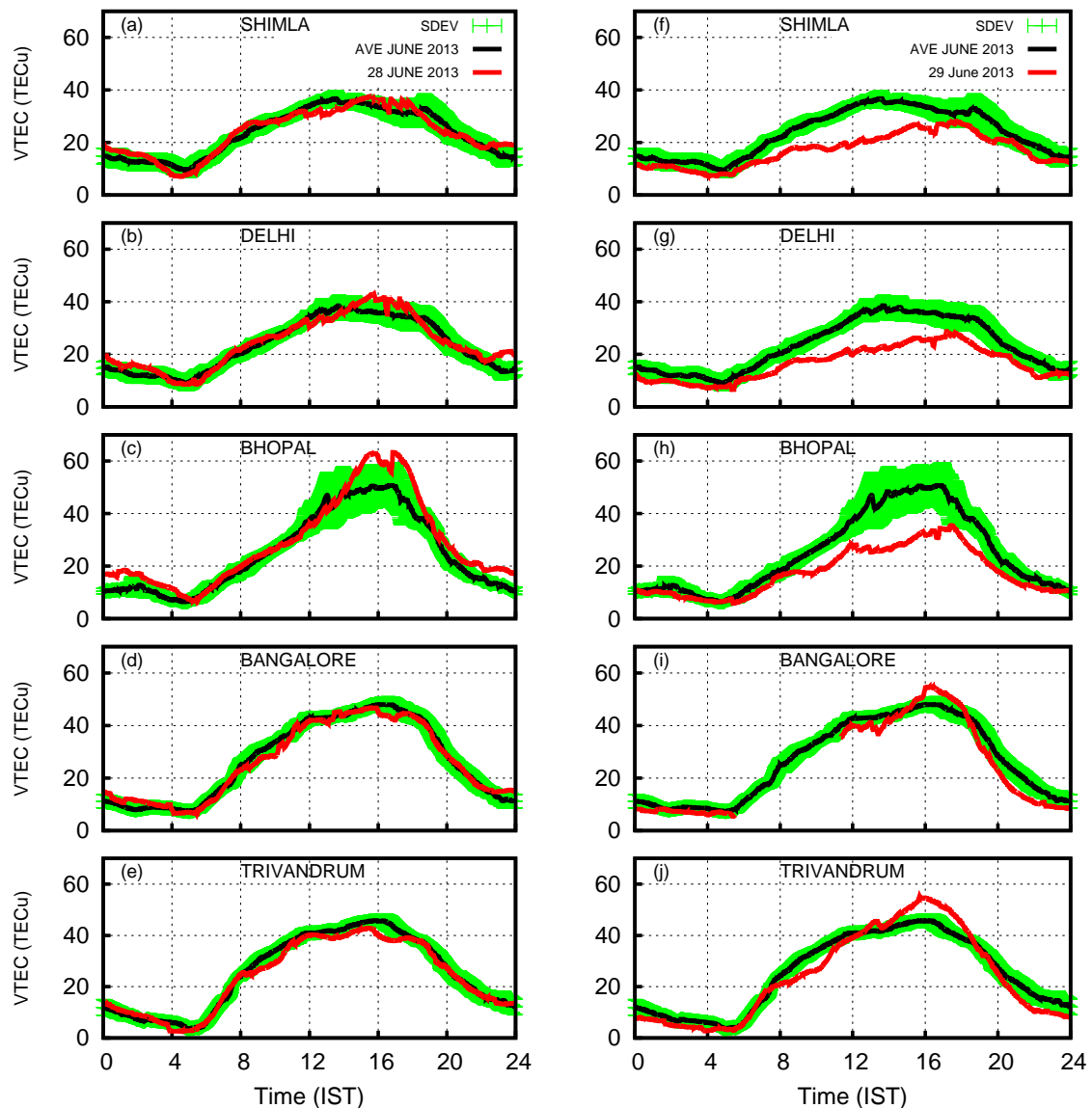


Figure 5.12: Panels (a)-(e) and (f)-(j) shows the TEC variations at the several GPS stations in the Indian sector during 28 and 29 June 2013, respectively. The TEC variation on 28 and 29 June 2013 is shown in red. The black line represents the quiet day mean variation of TEC and the standard deviation shown in green.

5.4.2 Ionospheric Response on 28 and 29 June 2013

In order to see the response of the ionosphere over the mid- low- and equatorial latitudes, the TEC data from a network of stations over the northern hemisphere along the Indian longitude sector are used. Figure 5.12(a)-(j) shows the TEC variation over Shimla, Delhi, Bhopal, Bangalore and Trivandrum on 28 and 29 June 2013. It can be seen that on 28 June, there was hardly any change in the TEC over Shimla and Delhi from the quiet day mean behaviour in response to the eastward turning of IEF_y . The TEC over Bhopal (anomaly crest region) shows only a marginal increase in the afternoon hours, which also is close to the standard deviation for the quiet period. The TEC over

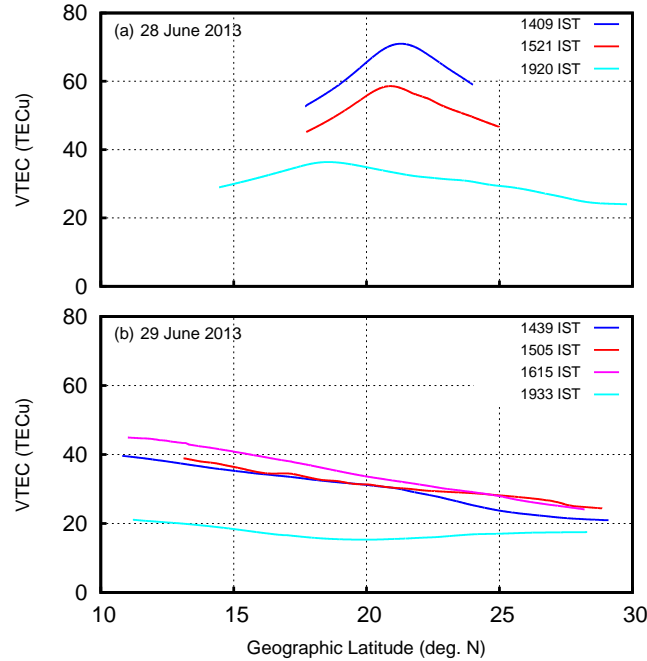


Figure 5.13: Panels (a) and (b) represent the latitudinal variation in TEC on 28 and 29 June 2013 as observed by radio beacon, respectively. The start time of the satellite pass over the location is given in the legend.

Trivandrum does not register any significant change on this day. However, on 29 June 2013, the TEC over Shimla, Delhi and Bhopal remained substantially low from morning till evening as evident from panels (f)-(j) of Figure 5.12. There is no data from Bangalore during the morning hours, but a marginal increase in TEC was observed in the afternoon hours on 29 June. The TEC over Trivandrum on this day increased as compared to the quiet time during afternoon hours.

To see the degree to which the EIA is affected by the storm time electric fields, the latitude variation of TEC as obtained from the LEOS beacon based observations is shown in Figure 5.13. Figure 5.13(a)-(b) shows the latitude variation of TEC obtained using several beacon passes on June 28 and 29. The start time of the satellite pass over the location is given in the legend. On both these days, unfortunately we do not have any satellite passes in the morning sector. The presence of an EIA crest on 28 June can be seen clearly from the satellite passes that commenced at 14:09 IST and 15:21 IST, respectively. Hence, it is clear that the electron density at Trivandrum (dip equator) did respond to the PPEF on 28 June 2013 (although not reflected in the TEC over Trivandrum as seen in panel (e) of Figure 5.12(e)). On 29 June (seen in panel (b) of Figure 5.13), the EIA is completely suppressed as evident from the TEC variations at 14:39 IST, 15:05 IST and 16:15 IST. Compared to the previous day, on 29th the EIA is not developed at all. The latitudinal variation of TEC shows a maximum over equator decreasing northward. This is a direct evidence for the presence of westward DD electric field. The possible reasons for the apparently different degree of responses on 28 and 29

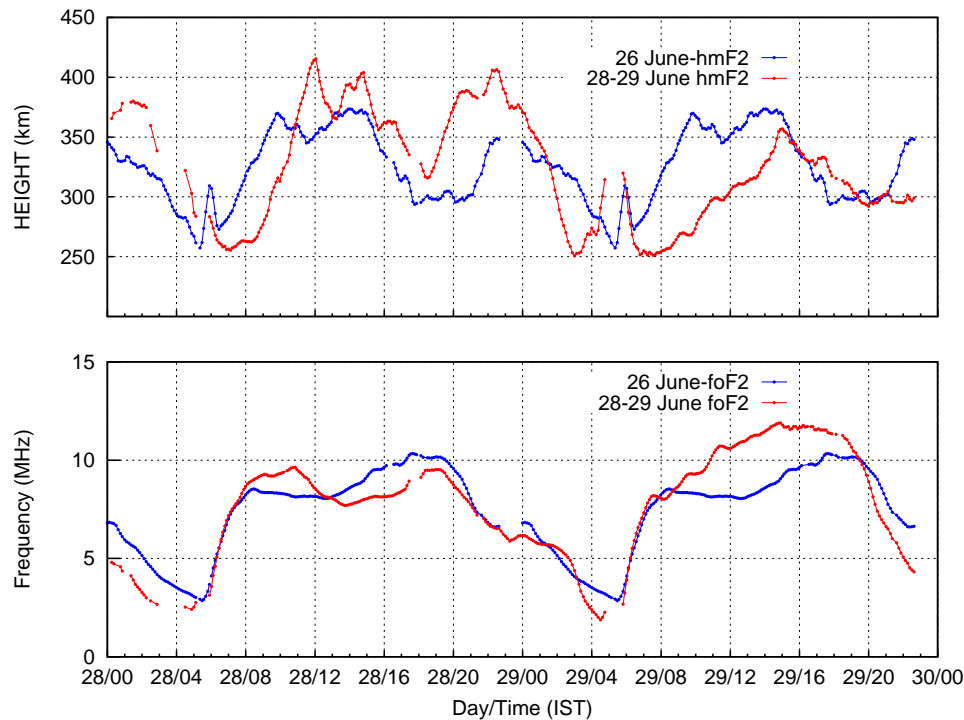


Figure 5.14: Digisonde measurements from Trivandrum: Top and bottom panels represent variation of hmF2 and foF2, respectively during 28-29 June 2013. The red line represents the diurnal variation during the period 28-29 June 2013. The blue line represents the variations on a quiet day (26 June 2013) and is shown here to facilitate comparison of the disturbed day variation with that of the quiet day.

June 2013 as seen in TEC and ionosonde data are discussed in the following sections.

5.4.3 Digisonde observations on 28 and 29 June 2013

Further evidences for the changes in the low latitude plasma distribution under the storm time electric fields can be found in the temporal variation of equatorial foF2 and hmF2, as observed by the digisonde. The temporal variation of hmF2 and foF2 during 28-29 June 2013 are shown in Figure 5.14. The diurnal variation of hmF2 and foF2 on a quiet day closest to the storm period is represented using the blue line. There is a reduction in foF2 and a corresponding overall increase in hmF2 during daytime on 28 June, indicating enhanced vertical drifts (compared to the quiet time value), resulting in an enhanced fountain. Hence, the presence of the enhanced fountain due to PPEF can be confirmed. In contrast, there is an increase in foF2 and a corresponding overall decrease in hmF2 during daytime on 29 June, indicating westward and downward drifts and a decreased fountain effect.

On the night of 29 June, there is a marginal increase in hmF2 over Trivandrum from 18:00-20:00 hours and foF2 remained high compared to the quiet time value. This may indicate the presence of an enhanced eastward electric field that led to the corresponding

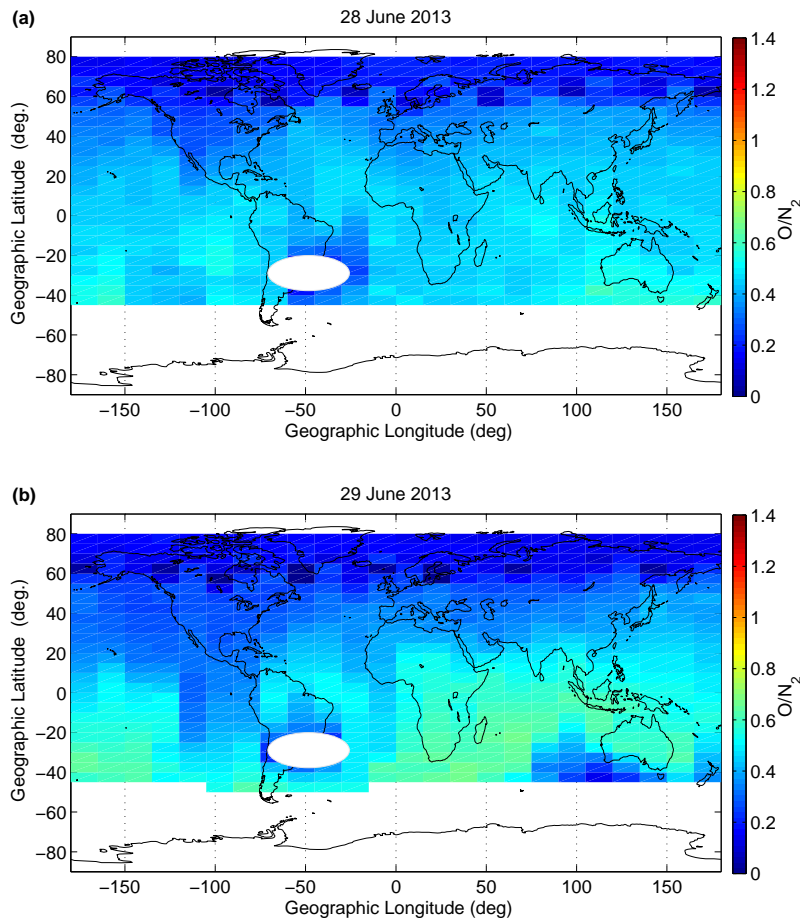


Figure 5.15: Panels (a) and (b) show the O/N_2 maps obtained from TIMED/GUVI satellite measurements on 28 and 29 June 2013, respectively. The measurements were made at 1400LT.

increase in electron density (because the recombination rates are lower at higher altitudes). However, we do not see any indication for the presence of a DD eastward electric field in TEC (Figure 5.12). By 20:00 IST, the DD effect almost ceases. This corroborates with the model simulations by *Huang* [2013], wherein they show that in the night time, during the summer months, the equatorward and westward neutral disturbances in the northern hemisphere can penetrate into the southern hemisphere. In such cases the DD electric field effects in the northern hemisphere become small and most of the DD currents become poleward in the southern hemisphere [*Huang*, 2013]. By $\sim 18:00$ IST on 29 June, the IMF B_z also starts to turn northward, indicating the beginning of recovery to normal state. The signature of a clear Pre Reversal Enhancement (PRE) is absent both during quiet and disturbed day, and this corroborates with the typical drift variation during the summer months of during moderate solar activity [*Scherliess and Fejer*, 1999].

5.4.4 The role of composition disturbances

The DD effects which tend to reduce the electron density during daytime may offset the effect of composition disturbances (which may cause a positive ionospheric storm) over mid latitudes. It is hence necessary to understand the thermospheric composition changes during the stormtime to delineate the effects of composition changes, if any, from the DD effects. The O/N_2 maps obtained from the GUVI observations have been used for this purpose. Panels (a) and (b) of Figure 5.15 shows the GUVI maps of the O/N_2 ratio, for 28 and 29 June 2013, respectively. Both the maps are shown for the same time of the day, i.e., 14:00 IST when the EIA is supposed to be significant. There is a substantial increase in O/N_2 ratio in the southern low-mid latitudes on 29 June 2013. Compared to this, the degree of enhancement in O/N_2 is much less over northern mid and low latitudes. This indicates that the effect of composition disturbances was less over the northern mid and low latitudes on 29 June, compared to the southern hemisphere. The O/N_2 ratio on 29 June 2013, however shows a moderate increase in the northern hemisphere low-mid latitudes, which favors a positive storm over low-mid latitudes. In spite of this, the TEC data showed the presence of a negative storm associated with the daytime westward electric field. Hence it is apparent that the effect of the composition disturbance, if any, is offsetted by the presence of the DD electric field. The O/N_2 change is most prominent in the southern (winter) hemisphere compared to summer hemisphere, which is expected [Huang, 2013].

5.4.5 Possible reasons for the ionospheric storm during 28-29 June 2013

Although signatures of the PPEF was found in the ground magnetic field as well as in the behaviour of hmF2 and foF2 over the dip equator (Trivandrum) on 28 June 2013, the TEC over the Indian equatorial and low latitude regions displayed more or less the quiet time pattern. Such events were reported previously as well [Tsurutani *et al.*, 2008; Lei *et al.*, 2015; Shreedevi *et al.*, 2016], wherein the TEC over the equator does not reflect the enhanced fountain effect during daytime. This behaviour is probably because of the enhancement/replenishment of ionization in the equatorial ionosphere [Tsurutani *et al.*, 2008; Lei *et al.*, 2015]. This can also happen when the TEC is dominated by the electron density of the topside ionosphere. However, the TEC variation over Bhopal on 28 June indicates that, at the crest location also, the TEC does not show a clear enhancement. If replenishment of ionization was the mechanism for the TEC at Trivandrum to remain unchanged despite an active fountain effect, then the TEC at Bhopal would have been much higher. This is because photoproduction would lead to such an increase at Bhopal too which is unlike the case on 28 June.

The TEC over both equatorial and low latitude regions can remain unchanged only

during two scenarios: (1) when the TEC is dominated by the density of the topside ionosphere and, (2) when the signature of the PPEF is not clearly seen in the summer crest which is more influenced by the trans-hemispheric winds. However, if the TEC over the crest region was dominated by the topside electron density (unlike in the case of a typical quiet day), we would have expected significant increase in TEC compared to a typical quiet day. This is because (1) chemical recombination rates are low in the topside ionosphere and hence if there is considerable accumulation of plasma at those altitudes it should manifest in TEC, and (2) because the effective scale height of the plasma at the topside ionosphere is also higher, the TEC should show an increase compared to a quiet day as TEC is more weighted to the F-region peak [Lei *et al.*, 2015]. Hence, we conjecture that the trans-hemispheric winds play an important role in deciding the TEC variation on this day.

It is understood from the Formosat-3/Constellation Observing System for Meteorology, Ionosphere, and Climate (COSMIC) observations that the winter EIA crest forms earlier than the summer crest, due to summer-to-winter neutral wind effect. The summer crest starts to develop after the fountain effect becomes dominant, i.e., around 12:00 IST, and the winter EIA crest becomes stronger than the southern crest around 15:00 IST [Lin *et al.*, 2007]. In the observations that we present here, the effect of PPEF is not discernable from TEC even at 14:00 – 15:00 IST i.e., even when the fountain effect maximizes. This indicates either the presence of strong meridional winds to the winter hemisphere, or the enhanced contribution of topside electron density in TEC, which we may not be able to demarcate. The summer EIA crest is indeed present in the afternoon hours as evident from the radio beacon observations. This corroborates with the earlier results by Lin *et al.* [2007].

On the next day, i.e., 29 June 2013, there is a reduction in the TEC over low latitude stations due to the suppression of fountain effect, because of the existing westward DD electric field. In the presence of a DD electric field, the resultant suppression of fountain would cause an enhancement in TEC over the dip equatorial region (compared to the normal day, wherein the plasma from the equator would be transported to low latitudes due to the fountain). This means, the effect of DD would be manifested as a positive ionospheric storm over Trivandrum, which is a dip equatorial station. Consequently, due to the suppression of the fountain, the plasma density over low latitude regions, would be lower (compared to the normal day, wherein the plasma from the equator would be transported to low latitudes due to the equatorial fountain). As mentioned earlier, several observations showed that over the low latitudes, the DD electric field effects are seen prominently in the afternoon and nighttime zonal and vertical drifts [Fejer and Emmert, 2003], and not during the morning-noon hours. The development of EIA may also take place during weak CEJ conditions as the typical response time of the EIA to zonal electric field is 1-2 hours [Stolle *et al.*, 2008]. Sastri [1988] have even shown that

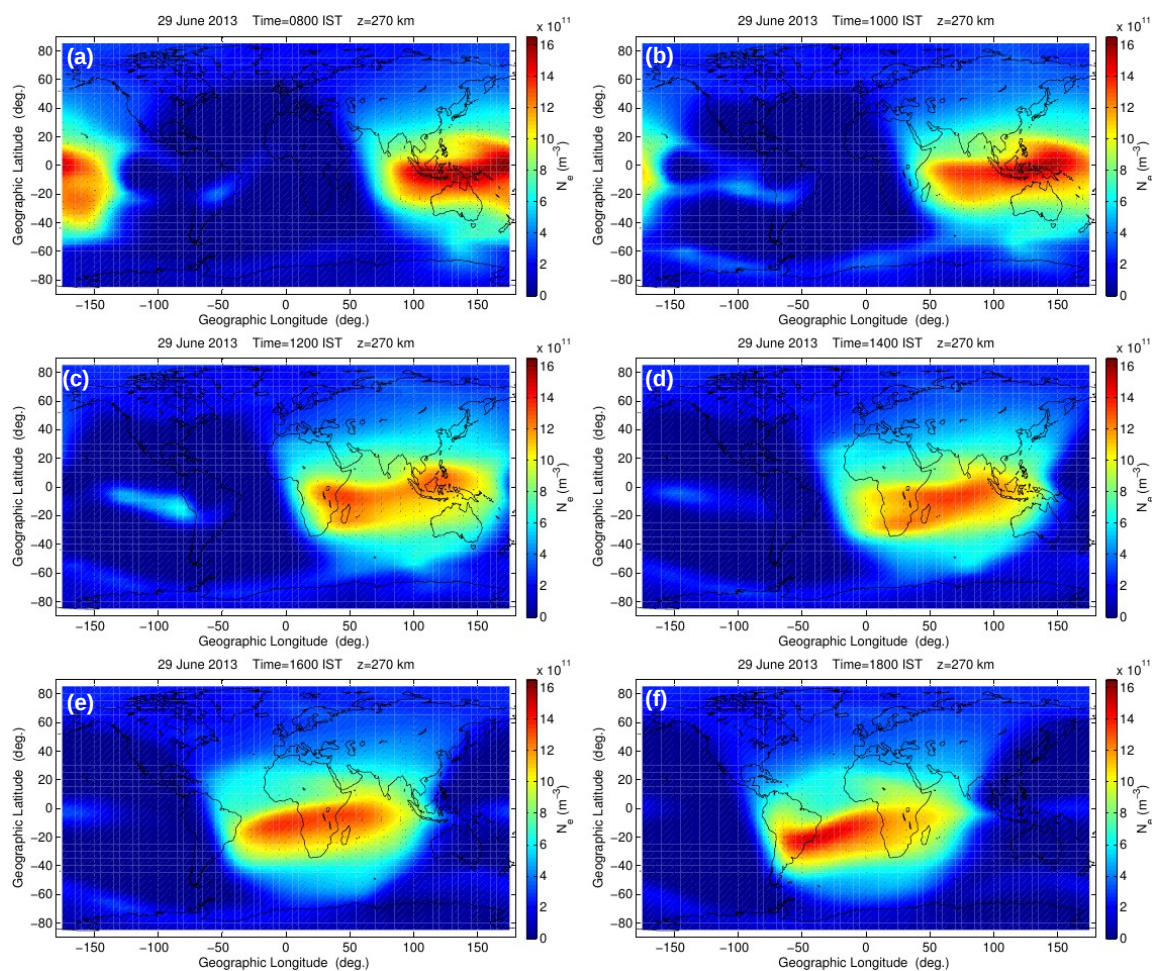


Figure 5.16: Simulated electron density distribution of the ionosphere on 29 June 2013 using the GITM model. Panels (a)–(f) represent the electron density maps at 08:00 IST, 10:00 IST, 12:00 IST, 14:00 IST, 16:00 IST and 18:00 IST, respectively.

some geomagnetic storms do not generate detectable patterns of equatorial DD electric fields for the entire day. In contrast, the case presented here shows a clear presence of DD electric field effect during entire daytime, continuing at a lesser extent over night time and ceasing by 20:00 IST. In this case, the DD electric field has become active from the main phase of the storm and continues for the whole day while the recovery phase is in progress.

Simulations by *Balan et al.* [2013] have shown that the zonal electric fields during daytime recovery phases can be zero or westward, and hence the fountain can cease and the latitude variation of N_{max} and TEC can peak over the equator, especially when the zero or westward electric field in the morning hours. If the electric field becomes westward only in the afternoon hours (after the development of EIA), it may not be able to completely alter the latitudinal structure, but only can cause positive ionospheric storm over equator. To obtain further evidence for this, we have performed simulations using GITM using the space weather conditions that prevailed for this event. Simulated

electron density distribution of the ionosphere at 08:00 IST, 10:00 IST, 12:00 IST, 14:00 IST, 16:00 IST and 18:00 IST on 29 June 2013 is presented in panels (a) to (f) of Figure 5.16. A notable feature in Figure 5.16 is the suppression of the EIA over the Indian low-mid latitudes on 29 June 2013 (also evident in Figure 5.12). The enhancement in electron density seen in the daytime winter hemisphere (southern hemisphere) could be a result of the summer-to-winter hemispheric transport of plasma. As mentioned earlier, during quiet times, the summer-to-winter neutral wind effect causes piling up of the electron density at the winter hemisphere, even before the equatorial fountain sets up, and this feature gets diminished after 17:00 LT [Lin *et al.*, 2007].

In the GITM simulations, the pile-up of electron density in the winter hemisphere due to trans-hemispheric wind is clearly seen for the entire day. The feature appears even before the commencement of the fountain process. As mentioned earlier, a lag of ~ 2 hours is expected for a change in the electric field to be manifested in the EIA crest densities [Rush and Richmond, 1973; Stolle *et al.*, 2008] and hence we can conclusively say that the pile up of electron density observed in the winter hemisphere is related to trans-equatorial winds, and not related to fountain. This is further evident from the fact that northern crest is not at all developed for the entire day. Previous studies have shown that the summer EIA crest due to fountain effect forms near 1200 LT and becomes stronger (than the southern winter crest) near 15:00 LT [Lin *et al.*, 2007]. In contrast, the simulation results for the disturbed day show suppression of northern EIA crest during 10:00 -18:00 IST, which indicates the absence of a fountain process. With the support of the evidences from the model and observations, it is clear that the presence of the westward electric field (DDEF) from the morning time on 29 June 2013 has inhibited the fountain effect. This is in contrast to the observations by Fejer and Emmert [2003] and Huang [2013] that over low latitudes, the DD effects are only seen significantly in the equatorial plasma drifts during afternoon and nighttime.

In a study of the climatology of zonal plasma drifts over Jicamarca by Fejer *et al.* [2005], the DD electric field was shown to act with a time delay of about 3-15 hours after a period of increased magnetic activity. The intensity of the geomagnetic activity was defined in terms of the Kp indices (quiettime conditions defined by an average Kp 3.0 over the preceding 9 hours). They suggested that the DD electric field largely accounted for the disturbed time zonal plasma drifts. The short term DD effects were attributed to TADs which can reach equatorial latitudes a few hours after enhancement in the high latitude disturbance current. The study of DD effects on the nocturnal equatorial F-region over Indian longitudes also showed short term DD effects with a time delay of 4 hours or even less [Kakad *et al.*, 2011]. However, they have not studied the DD effects on the daytime F-region. The case study presented here gives clear evidence for the complete alteration of the latitudinal pattern of TEC in the presence of the westward zonal electric field. In this event, the stormtime response is dominated by

the electrodynamical forcing and hence the composition changes or chemistry plays a secondary role highlighting the relative importance of ionospheric electrodynamics over chemistry (composition changes).

5.4.6 Salient features

The impact of a geomagnetic storm that occurred during 28-29 June 2013 on the ionosphere over the northern midlatitude station Shimla, low latitude stations Bhopal and Ahmedabad and the magnetic equatorial station, Trivandrum was studied to demonstrate the influence of DDEF on the plasma distribution over the Indian region. The northern hemispheric low-mid latitudes showed a clear response to the DDEF that was active since the morning hours of 29 June 2013. It is found that, as a result of the westward DDEF, the EIA was completely suppressed and the TEC distribution peaked over the equator. This is an interesting event which shows that daytime zonal electric fields can become westward during the late main phase to recovery phase of a storm, and because this happens from the morning hours, the fountain can completely cease and the latitude variation of TEC can be completely altered. The evidences for DD electric fields over the low latitude region are sparse, especially during daytime. Apart from this, it is always difficult to delineate the DD effects from the compositional disturbances based on ionospheric observations (like GPS based diurnal variation of TEC) alone, and this investigation makes a definite progress on this account, because of the availability of other simultaneous data like latitudinal variation of TEC from beacon satellites along with magnetic field and ionospheric observations from equatorial stations. This study also provides a clear example of the effect of stormtime neutral dynamical forcing on the low latitude plasma density distribution.

5.5 Relative contribution of stormtime electric fields and composition disturbances in redistribution of plasma

The influence of stormtime electric fields and composition disturbances on the ionosphere over the Indian region was studied in detail in the previous sections. However, the relative roles played by the composition changes and the disturbance electric fields have been difficult to demarcate. The long-duration positive ionospheric storm triggered on 18-21 February 2014 provided an opportunity to assess the relative contribution of disturbance electric fields and composition changes in modulating the response of the ionosphere over the Indian region during geomagnetic disturbances. The Z component of the IMF remained southward persistently for a long duration (~ 22 hours) during this event. The ionosphere over the Indian region as well as the southern polar region showed large deviations from their quiet time behaviour during the time. In the following section,

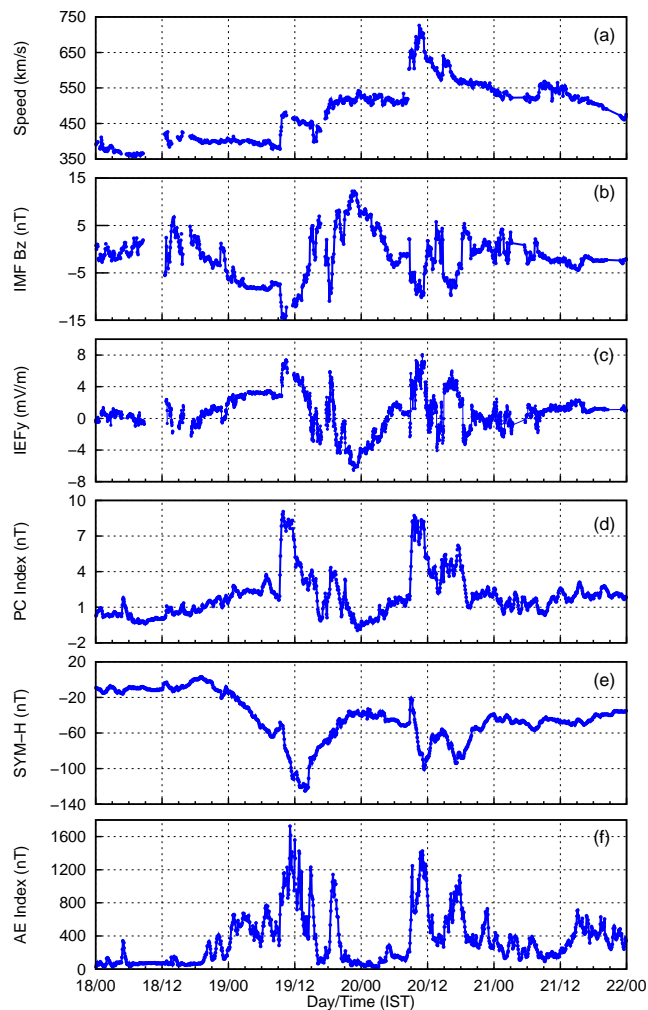


Figure 5.17: Geomagnetic conditions during February 18-21, 2014.

the latitudinal evolution of ionospheric storm ionospheric along the Indian longitude ($76-77^\circ$ E meridian) during 18-21 February 2014 has been described.

5.5.1 Geomagnetic conditions during 18-21 February 2014

The southward turning of IMF B_z at around 12:00 IST on 18 February 2014 marked the beginning of a geomagnetic storm ($Dst \sim -130$ nT) whose main phase lasted for ~ 24 hours. Panels (a)-(f) of Figure 5.17 shows the variation of solar wind speed, IMF B_z , IEF $_y$, PC index, Sym-H index, and AE index during 18-21 February, 2014. The Indian Standard Time (IST) (IST = Universal time (UT) + 5.5 hours) is shown on the x-axis. The geomagnetic storm triggered on 18 February is a highly structured one with two geomagnetic storms developing in quick succession. The Sym-H index shown in panel (e) Figure 5.17 indicates commencement of the storm on 18 February. On 18 February, the solar wind speed increased by about 30 km/s at $\sim 12:00$ IST and continued to remain so for the next 22 hours. Although there is a data gap in panels (a), (b), (c) of Figure 5.17, it can be seen that the IMF B_z turned southward following the first increase in solar

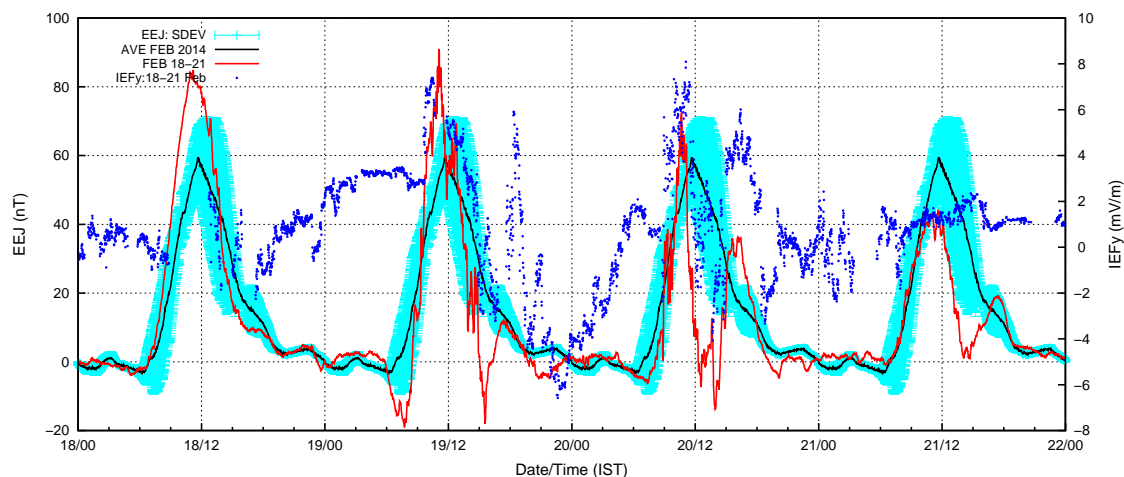


Figure 5.18: Variation of IEF_y and the EEJ along with the quiet time mean and standard deviation for the period 18-21 February 2014. The blue dots represents the IEF_y component. The black line represents the quiet day mean of EEJ along with the standard deviation in green. The red line represents the variation of EEJ during the period 18-21 February 2014.

wind speed and persisted for a long duration (~ 22 hours). This kind of a long duration southward IMF condition could be due to a magnetic cloud event. The IEF_y turned eastward in correspondence to the southward turning of IMF B_z on 18 February. The recovery phase which started at ~ 1500 IST on 19 February was interrupted by a two stage geomagnetic storm that was triggered on 20 February with SSC at ~ 0900 IST. The main phase of the second geomagnetic storm lasted only for ~ 0300 hours and ended at ~ 1200 IST on 20 February. On 19 and 20 February the solar wind speed increased abruptly above the quiet time value by about 50 km/s and 220 km/s respectively. With this sudden increase in solar wind speed, IMF B_z turned further southward. The y component of interplanetary electric field (IEF_y), which remained mostly eastward till the second step-like increase in the solar wind speed, turns further eastward after which it flipped directions for shorter durations. There is a significant eastward turning of IEF_y , followed by several fluctuations on 20 February. The polar cap index also indicates an enhancement in the polar cap potential on 19 February. This increase in the PC index is almost coincident with the eastward turning of IEF_y . The Sym-H also responded to these changes, nevertheless the minimum was observed on 19 February. The IEF_y regained its normal quiet time behaviour by the night of 21 February.

As mentioned earlier, the changes in the IEF_y directly affect the ground magnetic field, whose variations can be studied to understand the ionospheric behaviour. Figure 5.18 shows the EEJ strength for the period 18-21 February, 2014 along with the quiet day mean and standard deviation. In order to facilitate comparison, the variation in IEF_y is also shown. It can be seen that the EEJ responds promptly to the changes in the IEF_y during day time. For instance, on February 19, the enhancement in EEJ

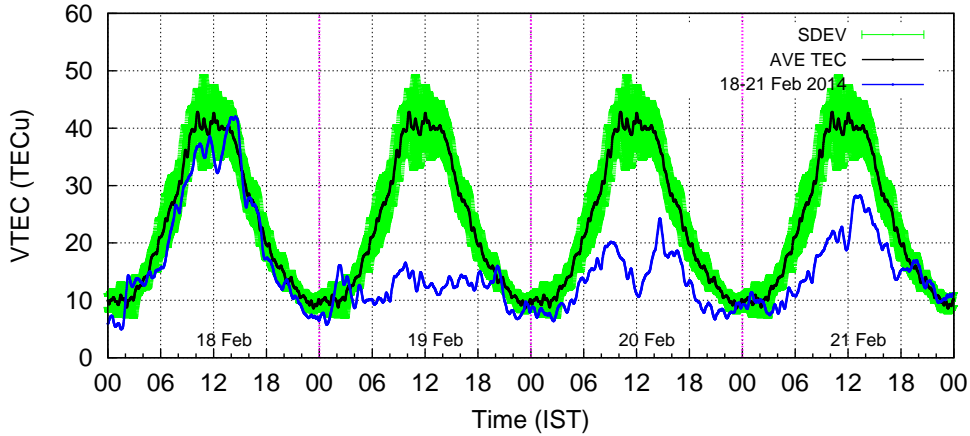


Figure 5.19: Temporal variation of TEC over Bharti during the period 18-21 February 2014 is represented by the blue line. The black curve represents the quiet day mean variation of TEC and the standard deviation is shown in green.

strength coincides with the increase in IEF_y which is of eastward polarity and later becomes a CEJ when the IEF_y turned westward. Similarly, on 20 February, the strength of EEJ decreased sharply in response to the westward turning of IEF_y . If we compare the variations of EEJ and IEF_y , it can be seen that for each eastward (westward) fluctuation of IEF_y , the EEJ strength exhibits a corresponding increase (decrease). The EEJ can promptly respond to the undershielding electric field, as a prompt enhancement, and change polarity (become CEJ condition) due to the overshielding condition i.e., due to the Region-2 Field Aligned Currents (R2 FACs) generated deep inside the magnetosphere [Kikuchi *et al.*, 2008]. The evidence for this has been shown by Simi *et al.* [2012], wherein they showed that under the influence of the strong eastward prompt penetration electric field, the EEJ was enhanced.

5.5.2 Latitudinal variation of TEC

The TEC variation over Bharti during 18-21 February 2014 is shown in Figure 5.19. The average diurnal variation obtained using 4 quietest days of the month is represented by the black curve, along with the standard deviation shown using the green color. It can be seen that on 18 February the TEC shows a minor surge at around 1200 IST, just after the increase in the solar wind speed and the southward turning of the IMF B_z . However, these TEC changes lasted only for $\sim 2-3$ hours, after which, it became almost identical to the quiet time values. On the next day i.e., on 19 February, there is a very prominent reduction in TEC with a maximum deviation of ~ 25 TECu from the quiet day mean. On 20 February also, there is considerable reduction in TEC till noon/early afternoon hours i.e., by ~ 20 TECu from the quiet day average. In the late afternoon to night hours, the TEC deviation from the quiet time value is less compared to the earlier hours. A notable departure from the quiet time mean, more prominent in the morning

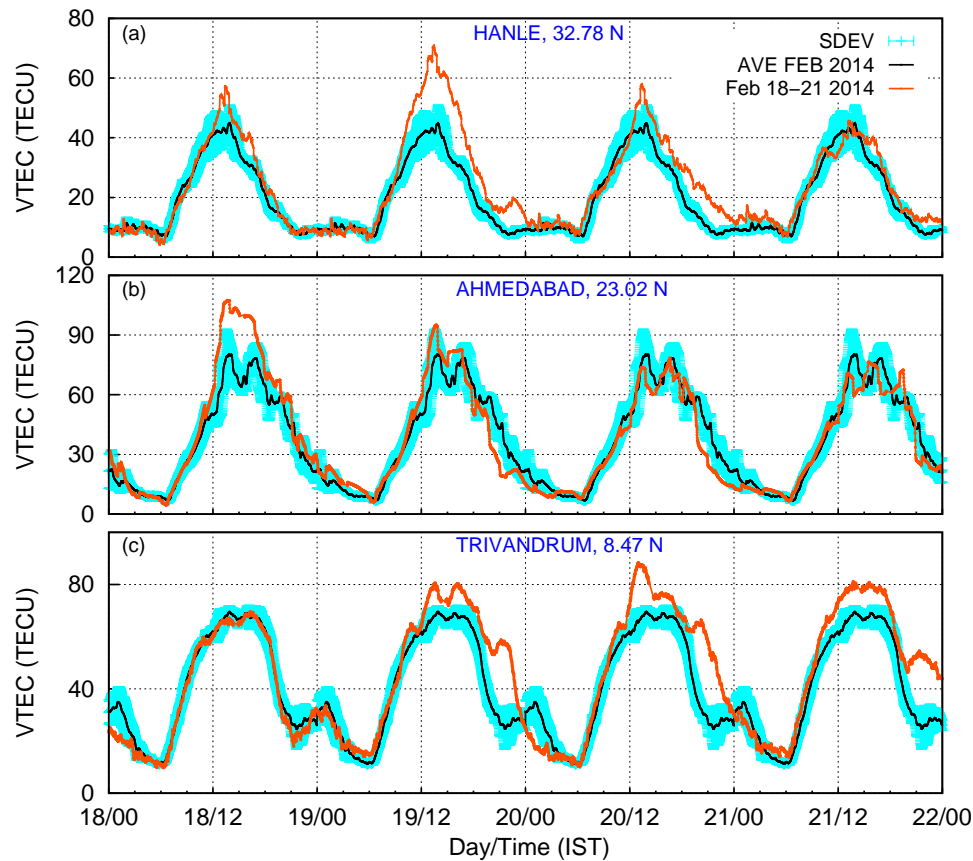


Figure 5.20: Same as figure 2, but for the northern mid latitude station Hanle, anomaly crest station Ahmedabad and the dip equatorial station Trivandrum.

to noon hours and to a lesser extent in the afternoon to evening hours is seen on 21 February also. Interestingly, the degree of TEC reduction gradually decreased from 19 February to 21 February.

In panel (a) of Figure 5.20 is shown the TEC variation over the northern hemisphere mid-latitude station, Hanle during 18-21 February 2014. Since Hanle lies outside the focus of the Sq current system, it represents typical northern mid latitude and hence it is expected that the effect of compositional disturbances will be seen more effectively at Hanle. It can be seen that, on 18 February, the deviation from the quiet day mean is very marginal. However, on 19 February, the TEC over Hanle is seen to increase starting from ~ 0900 IST up to midnight with an increase in magnitude by ~ 25 TECu during the daytime and ~ 10 TECu at night as compared to the quiet day mean. On 20 February also, TEC enhancement by about ~ 15 TECu is seen, which is prominent in the afternoon hours. The diurnal variation almost agrees with the quiet time values on 21 February.

The temporal variation of the TEC over Ahmedabad which lies in the vicinity of the EIA crest is shown in panel (b) of Figure 5.20. There is a large increase in TEC over Ahmedabad starting from 1200 IST to 1700 IST of February 18, which indicates the presence of a stronger EIA crest during this time probably as a consequence of the

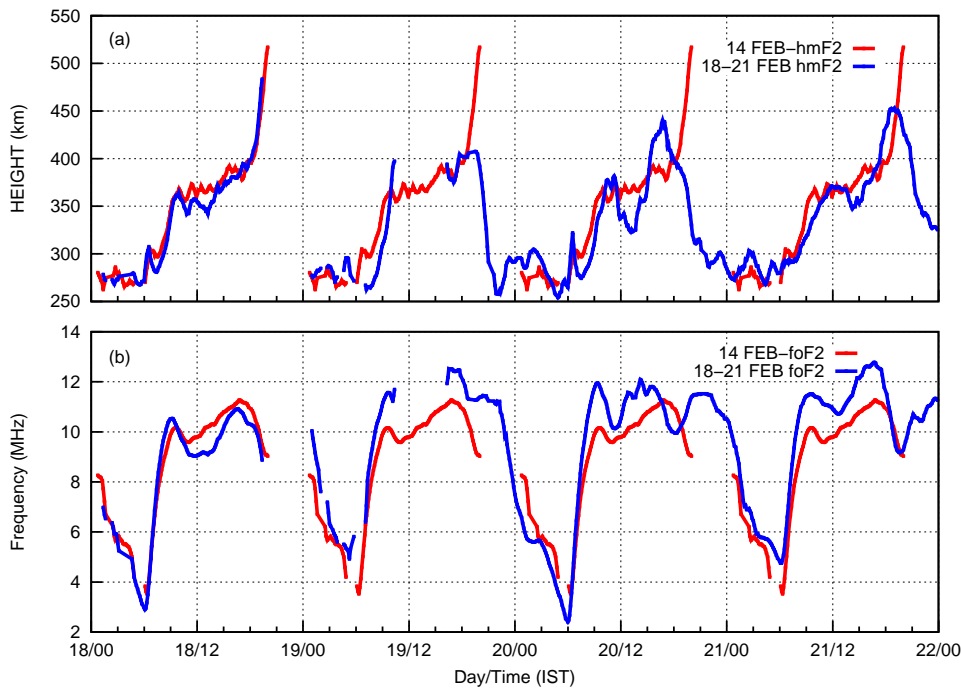


Figure 5.21: Digisonde measurements: The temporal variation of hmF2 and foF2 are shown in panels (a) and (b) respectively. The red line represents the variation on a quiet day and the blue line represents the diurnal variation during the period 18-21 February 2014. Data gap in both hmF2 and foF2 is due to the presence of spread F except during the period from 10:00 IST to 16:00 IST on 19 February.

eastward prompt penetration in the morning hours. On 19 and 20 February, the TEC seems to follow the quiet time trend from morning to afternoon hours whereas a steep decrease in TEC is seen during the afternoon to evening hours. The TEC is seen to display its normal quiet time behaviour on 21 February.

In panel (c) of Figure 5.20 is shown the TEC variation at the dip equatorial station, Trivandrum, plotted in a similar manner as described above. It can be seen that, on 18 February, the deviation from the quiet day mean is very marginal. However, on 19 February, there is an enhancement in TEC from noon to pre-midnight time, and afterwards there is a small decrease in TEC. The TEC enhancement is seen from noon to pre-midnight hours on 20 February also. However, the night time values are more or less close to the quiet day mean. The enhancement in TEC is seen during daytime on 21 February as well. This increase in TEC is seen to persist until midnight. It may be noted that, this feature is present in the mean quiet day variation as well, but to a lesser extent.

5.5.3 Digisonde measurements over the dip equator

The temporal variation of hmF2 and foF2 are shown in panels (a) and (b) of Figure 5.21. Blue line represents the variation of hmF2 and foF2 for the period 18-21

February. The diurnal variation of hmF2 and foF2 on a quiet day closest to the storm period is represented using the red line. The hmF2 and foF2 during the disturbed period from 18-21 February is plotted against the quiet day in order to facilitate comparison with quiet time behaviour of hmF2 and foF2. A gap in both hmF2 and foF2 on the quiet day represented by the red line is because of the presence of spread F. On 19 February, which is a disturbed day represented by the blue line, the data gap during the period from 1000-1600 IST is due to the absence of data. Both hmF2 and foF2 does not deviate much from the quiet day values on 18 February. As seen from panel (a) of Figure 5.21, hmF2 exhibits an abrupt decrease during ~ 1930 IST to ~ 2130 IST on 19 February in contrast to the quiet day pattern. A similar behaviour is also evident on 20 and 21 of February though not as prominent as on 19 February.

5.5.4 What led to the evolution of ionospheric storm during 18-21 February 2014?

During geomagnetic storms, the high latitude ionosphere responds first to the convection electric fields, the resulting changes in the neutral dynamics become important afterwards and for longer timescales. There is an increase in the TEC at Bharti around ~ 1300 IST on 18 February, which is rather intriguing. A probable cause is the enhanced production in the F region of the ionosphere by soft precipitation, which can increase the magnitude of nighttime TEC to daytime values [Schodel, 1974]. TEC over the high latitudes can also be altered by other processes like the transport of dayside F layer plasma across the polar cap to night side by convection [Buonsanto, 1995; Mendillo and Klobuchar, 1975; Foster, 1993] and electrodynamic drifts [Kelley, 1989].

On 18 February, the TEC over Trivandrum does not show any considerable change whereas there is an enhancement in TEC during the period 1300-1700 IST over the crest location Ahmedabad. The enhancement in EIA on this day is in response to the PPEF. Although the IEF_y data has a gap during the period 0900-1200 IST on 18 February (panel (c) of Figure 5.17), the enhancement in electric field is evident from the increase in the EEJ as compared to the quiet time value (Figure 5.18). The other observations supporting this are (1) the noon-time dip in foF2 over Trivandrum that is more prominent compared to the typical quiet day (panel (b) of Figure 5.20) and (2) an enhancement in TEC over Ahmedabad (crest location) in the afternoon hours. It must be noted that there is a characteristic time delay associated with the changes in the electric field to manifest in the EIA crest density [Raghavarao et al., 1978; Sastri, 1990]. Usually a lag of ~ 2 h is expected for a change in the electric field to be manifested in the EIA crest densities [Rush and Richmond, 1973; Raghavarao et al., 1978; Simi et al., 2012]. Even though there is ample evidence for an enhanced fountain effect, there is no significant decrease in TEC over Trivandrum. The TEC over Trivandrum does not show any noticeable reduction because as the electric field penetrates into the dayside equatorial

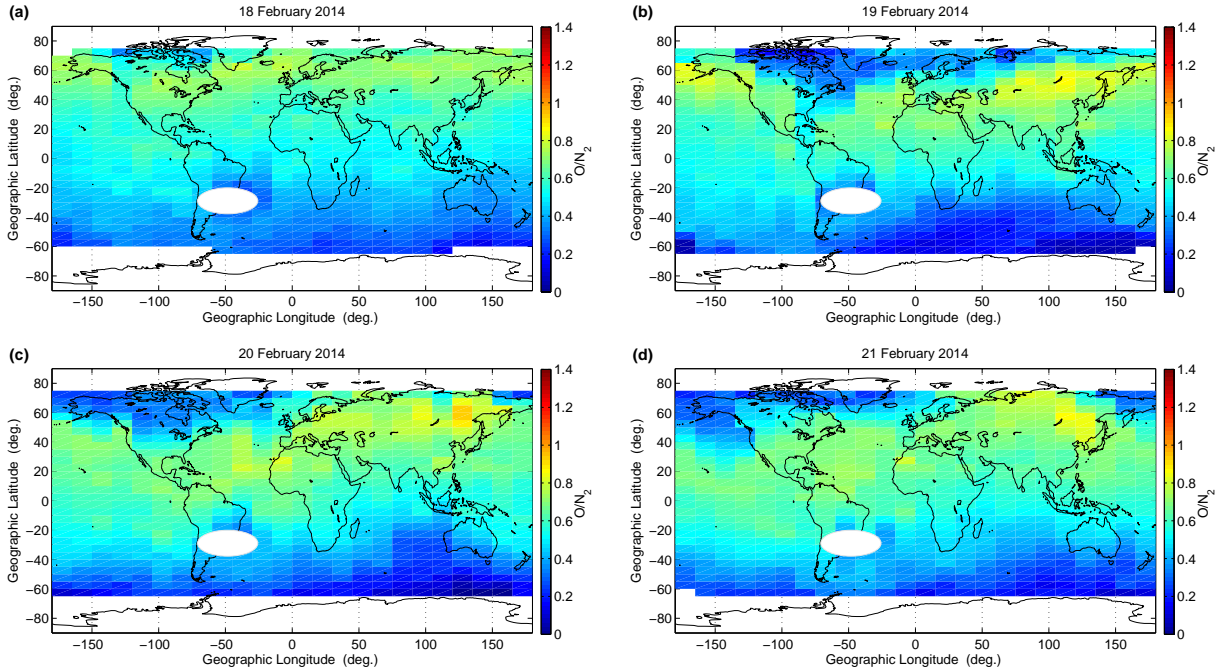


Figure 5.22: O/N_2 maps obtained from TIMED/GUVI satellite measurements to show the composition changes in the thermosphere during the period 18-21 February 2014.

ionosphere, the plasma is uplifted to higher altitudes where the recombination rates are considerably low. At the same time photoionization continues to take place at lower altitudes replenishing the uplifted plasma over equator. Therefore, at the dip equatorial latitudes, an overall decrease (due to enhanced fountain) may not be apparent [Tsurutani *et al.*, 2008]. Similar observations have been reported by Lei *et al.* [2015] wherein they showed that the TEC over Jicamarca did not show a significant decrease even though there was an increased upward drift. This is because the plasma from the bottomside ionosphere is transported to higher altitudes owing to increased upward vertical drifts. Since chemical recombination rates are low in the topside ionosphere, accumulation of plasma takes place at those altitudes. Meanwhile, the plasma that was transported from the bottomside ionosphere will be compensated by daytime photoionization. The effective scale height of the plasma at the topside ionosphere was also found to increase owing to increase in upward drift. As a result, not much decrease in plasma was seen over the equator. Our observations are consistent with these results. Also, our observation of the enhanced noon-time dip in foF2 over the equator on 18 February is consistent with the CHAMP observations reported by Mannucci *et al.* [2005].

On 19 February, a negative ionospheric storm (decrease in TEC) was observed at the high latitude station Bharti. The AE indices shown in panel (f) of Figure 5.17 indicates an enhanced joule heating in the polar thermosphere during the storm period. Expansion of the polar thermosphere due to enhanced joule heating could lead to the upwelling of molecular species to higher altitudes resulting in an increase in loss rates of plasma at F-region [Richmond and Lu, 2000]. The O/N_2 ratio during the period 18-21 February

2014 is presented in Figure 5.22. Two features are well evident from these maps. (1) There is a substantial reduction in O/N_2 ratio in the southern high latitudes, with the maximum decrease being seen on 19 February. (2) There is an increase in O/N_2 over northern mid-latitudes on 19 and 20 February, compared to 18 February, whereas the O/N_2 values over mid-latitudes almost recovers to the pre-storm values on 21 February. These observations indicates that composition disturbances prevailed during the storm period at the high latitude regions in both the hemispheres and were more prominent in the southern hemisphere on 19 February. Hence, the large decrease in TEC observed over Bharti is primarily due to the composition changes related to the upwelling of the air rich in molecular species from the lower altitudes.

As a consequence of the upwelling over the high latitudes and the storm induced equatorward winds there is a downwelling where the equatorward meridional wind converges over the mid-low latitudes [Richmond and Lu, 2000]. In addition, transport along magnetic field lines due to enhanced equatorward meridional wind also aids the enhancement in plasma density over the mid latitudes [Balan *et al.*, 2010]. TADs are also known to uplift the ionization to higher altitudes causing positive ionospheric storm effects at mid latitudes [Prölss, 1978]. These factors could be responsible for the enhanced plasma densities seen over the mid-latitude location, Hanle on 19 February. The enhanced O/N_2 ratio over the northern mid-latitude region (Figure 5.22) provides evidence for this positive storm feature induced by the neutral dynamics. On 20 February also, this situation prevails over the northern mid-latitude region, but to a lesser extent. This is also confirmed from the fact that the enhancement in O/N_2 values are less compared to that of the previous day. On 21 February, the O/N_2 values are almost identical to the pre-disturbance values corroborating with the fact that the TEC values also recovered to the quiet time value. Lu *et al.* [2008] showed using Thermosphere-Ionosphere- Electrodynamics General Circulation Model (TIE-GCM) simulations, with realistic time-dependent ionospheric convection and auroral precipitation as inputs, that the primary cause of the positive storm response over the near mid-latitude region was the enhanced meridional neutral wind. The present observations are consistent with these results. It may be noted that usually such enhancements associated with neutral equatorward circulation and composition changes, generally occur only during the early phase of the storm [Balan *et al.*, 2012]. The dominance and long duration of this positive ionospheric storm is unusual and interesting, because in this case, the positive storm condition prevails during most of the main phase of the storm.

Over the equatorial location, we see that the TEC responds to both the PPEF and the DDEF during the entire duration of the storm. The effect of the circulation changes and/or composition changes would be minimum over equator [Buonsanto, 1999, references therein]. On 19 February, there is an enhancement in TEC over both Trivandrum (starting at ~ 1000 IST) and Ahmedabad (starting at ~ 1200 IST). The enhancement in

TEC over Ahmedabad is because of the fountain effect that was triggered in response to the eastward turning of IEF_y at ~ 0930 IST. The EEJ strength is seen to increase initially at ~ 0930 IST but decline immediately leading to a CEJ condition. The weakening of the eastward electric field can be due to two reasons namely (1) the over shielding condition, which is an instantaneous response to the sudden northward turning of the IMF B_z . This situation can cause the CEJ over equator [Kikuchi *et al.*, 2000b; Simi *et al.*, 2012] and (2) the westward DDEF during daytime. In response to the CEJ, there is an increase in TEC over Trivandrum which is due to the decreased fountain effect. Over Ahmedabad, there is a decrease in TEC, which is due to lowering of the F layer to altitudes where recombination is higher. The nighttime increase of TEC over Trivandrum further confirms the presence of the DDEF which has an eastward polarity during nighttime. This is evident from panel (a) of Figure 5.21 which clearly shows the rise in hmF2 after 21:00 IST. The F layer was uplifted to altitudes where loss rates are lesser, thereby leading to an enhancement in TEC. On 20 February also, the combined effects of the IEF_y fluctuations and the daytime westward DDEF are expected to cause variations in the EEJ and TEC. On 21 February, any significant fluctuations in IEF_y are not seen. However, the EEJ strength shows the presence of a westward electric field during daytime from which the presence of DDEF is evident. The usual post-sunset increase of hmF2 at Trivandrum indicative of the PRE of vertical plasma drift (eastward electric field) is severely inhibited and is, in fact replaced by a marked decrease of hmF2 with varying amplitudes on all the three days 19, 20 and 21 February. This confirms the presence of a westward electric field during the period. When the PRE takes place, the prevailing ionospheric dynamo electric field is in the eastward direction and the DDEF which is in the westward direction would weaken the PRE as observed in the present case. However, later at nighttime, the DDEF is in the eastward direction which effectively reduces the prevailing downward drift of ionospheric plasma which can result in an enhancement in TEC.

Balan *et al.* [2011] reported that positive ionospheric storms develop at the equatorial latitudes (within about 15° magnetic latitudes) during daytime recovery phases, and they conjectured that this could be caused by (1) zero or westward electric fields due to disturbance dynamo and/or prompt penetration, (2) plasma convergence due to the mechanical effects of storm-time equatorward neutral winds and waves, (3) increase of atomic oxygen density and decrease of molecular nitrogen density due to the downwelling of equatorward winds, and photoionization. In the present case, the recovery phase of the first storm started at 1500 IST and continued till 2200 IST on 19 February. Over Ahmedabad which is a low latitude station, the daytime disturbance dynamo effects (through reduced fountain effect) and composition disturbances compete with each other. As a result of this, the TEC changes (governed primarily by equatorial electrodynamic) are not significant compared to the mid-latitudes. However, over dip equatorial region, TEC

gets enhanced (compared to a quiet day) due to the disturbance dynamo owing to lesser meridional plasma transport away from this region and inefficiency of the compositional disturbances to reach equatorial region. Global O/N₂ maps from GUVI/TIMED satellite also show that the composition disturbances are insignificant over the equator. Hence, in the present case the observed positive storm over equator is primarily due to the interplay of DD electric field and changes in the IEF_y.

5.5.5 Salient features

The impact of a geomagnetic storm that occurred during 18-21 February 2014 on the redistribution of plasma in the Indian longitude was studied in the present work. This is the first report of simultaneous GPS TEC observations from Bharti and Hanle. The simultaneous TEC measurements from the southern polar ionosphere to the northern low-mid latitude ionosphere along the 76-77°E meridian made it possible to study the evolution of a long duration positive ionospheric storm discussed here and address the relative contributions of the disturbance electric fields and composition changes in modulating the response of the I-T to geomagnetic disturbances. During the main phase of the geomagnetic storm, an intense negative ionospheric storm prevailed at Bharti which is due to the upwelling of air rich in molecular species owing to changes in global circulation due to enhanced joule heating. A positive ionospheric storm is seen to commence over the mid latitude station Hanle which persists until midnight. This is ascribed to be due to (1) TADs (2) transport of plasma along field lines due to storm induced equatorward meridional wind and (3) the composition disturbances propagating from the high latitudes reaching the mid latitudes. Overall, the impact of the composition bulge over the mid-latitudes is seen to reduce over a period of ~48 hours. The PPEF that dominated over the low latitudes during the initial phase of the storm caused an enhanced fountain effect. As the storm progressed, the combined effects of PPEF and DDEF are seen to cause the observed positive storm effects over the dip equatorial station, Trivandrum. Over the EIA crest region, during the recovery phase of the storm, the effects of the disturbance dynamo compete with the changes caused by the composition disturbances resulting in a condition where no significant changes appear in the TEC. Considering the fact that the ionospheric response to a geomagnetic storm over both the poles would be more or less the same, it is clear that the long duration positive ionospheric storm discussed here showcases the strong coupling between the thermosphere and the ionosphere and the response of the global wind system to the high latitude energy input. There could be hemispherical asymmetry in terms of the degree of the responses, but we would not be able to comment on this.

5.6 Conclusions

The role of electrodynamical and neutral dynamical coupling of the high-mid-low latitude ionosphere in the evolution of ionospheric storms over the Indian sector has been studied in the present chapter. Three case studies were performed in which the response of the ionosphere over the Indian region to three intense geomagnetic storms of almost the same intensity, were analysed. In the first case, i.e., on the St. Patrick's day storm of 2013, the penetration of the westward electric field gave rise to a CEJ like situation at the dip equator. The westward zonal electric field pushed the F-layer at the dip-equator down to the altitudes where recombination and diffusion played minimal roles and gave rise to an enhancement in the electron density. The joule heating of the thermosphere, gave rise to the TADs which pushed the plasma up in the EIA regions. It supplemented the loss of plasma at the anomaly crest region resulting in no change in the TEC therein and a marked increase in the TEC in the mid-latitude ionosphere. As a consequence, a positive ionospheric storm was seen to occur simultaneously at the equatorial, low and mid-latitude regions in the Indian sector. Secondly, a case of the westward DDEF influencing the daytime equatorial and low latitude ionosphere, during the geomagnetic storm of 28-29 June 2013 was presented. The presence of the DDEF from the morning hours itself on 29 June 2013 led to the complete alteration of the latitudinal structure of the electron density with the peak in TEC occurring over the dip equator. This is in contrast to the already existing idea that, the effects of DDEF are seen prominently in the afternoon hours because the EIA takes some time (typically 1-2 hours) to respond to the changing electric field. Also, the effect of composition disturbance was observed to be offsetted by the DDEF during this event highlighting the relative importance of electrodynamical forcing over chemistry. The relative contributions of the composition disturbances and the disturbance electric fields (PPEF and DDEF) in controlling behaviour of the ionosphere over the Indian region was studied by taking the case of the geomagnetic storm of 18-21 February 2014. The positive ionospheric storm observed over Hanle during this event was caused by the composition disturbances propagating from the high to mid latitudes. Considering the fact that the ionospheric response to a geomagnetic storm over both the poles would be more or less the same (degree of responses might differ), the presence of composition disturbances could be inferred from the negative ionospheric storm observed at Bharti. Meanwhile, it was found that the PPEF dominated during the initial phase of the storm at the low latitudes and led to a positive ionospheric storm. However, during the later phase of the storm, both the PPEF and DDEF are found to play an active role in causing positive ionospheric storms over the dip equator, Trivandrum, whereas, the TEC variations over the low latitude station, Ahmedabad are not so significant due to the competing effects of the daytime DDEF and composition disturbances.

Chapter 6

Influence of ionospheric conductivity on the magnetospheric dynamics

6.1 Introduction

The impact of space weather events on the ionosphere over the high, mid, low and equatorial latitudes along the Indian longitude was studied in detail in the previous chapters. It was shown that state of the ionosphere during space weather events is determined by the magnetospheric electric fields, currents and particle precipitation that gets dissipated therein. One of the important outcomes of the Solar Wind-Magnetosphere-Ionosphere (SWMI) coupling is the formation of the Field aligned current systems (FACs). The Region 1 Field aligned currents (R1 FACs) that flows at the high latitudes is generated as a result of the interaction of the solar wind and the Interplanetary Magnetic Field (IMF) with the magnetosphere [Potemra *et al.*, 1980; Potemra, 1984]. Similarly, the formation of pressure gradients in the inner magnetosphere gives rise to the Region 2 Field aligned currents (R2 FACs) that lies equatorward of the R1 FACs in the high latitude region [Iijima and Potemra, 1978; Potemra, 1984]. The presence of the conducting ionosphere enables the closing of the R1 FACs [Wolf, 1970; Fedder and Lyon, 1987] resulting in the occurrence of the magnetospheric convection and the penetration of the convection electric field into the ionosphere [Dungey, 1961; Gonzalez *et al.*, 1989; Lyons, 1992; Cowley, 2000; Clausen *et al.*, 2013]. The presence of the conducting ionosphere also allows the R2 FACs to flow into the ionosphere and by that means control the build up of ring current energy density in the inner magnetosphere [Wolf, 1970; Clausen *et al.*, 2013]. Ionospheric conductivity thus becomes one of the important factors that determines the global state of the magnetosphere [Fedder and Lyon, 1987; Siscoe *et al.*, 2002; Merkin *et al.*, 2003; Ridley *et al.*, 2004; Merkin *et al.*, 2005]. In this chapter, the role of the ionosphere in controlling the magnetospheric dynamics during geomagnetic storms is examined.

Ionospheric conductivities arise as a result of the interaction of the ionospheric plasma with the neutral species in the atmosphere [e.g., Torr and Brinton, 1979]. It is primarily

a measure of the resistance offered by the neutral atmosphere towards the motion of charged particles. As described in Chapter 1, the motion of the charged particles in the ionosphere is greatly influenced by the collisions with the neutrals in the atmosphere. Since the number density of neutrals decrease with altitude, the ion-neutral/electron-neutral collision frequency also exhibits a similar trend. As a result, the Hall conductivity is very low in the region above ~ 150 km because there are very few collisions between ions, electrons and neutrals and the motion of both, ions and electrons are essentially controlled by the magnetic field. However, in the region between 100 to 150 km of the ionosphere, the motion of the ions is controlled by the collisions with the neutral species whereas the electrons are still tied to the magnetic field. Hence, a Pederson current arises due to the retarded ion motion while the electrons drifting in the $E \times B$ direction gives rise to Hall current [Kelley, 1989]. Enhancements in ionospheric conductivities in the high latitude regions also arise due to particle precipitation [e.g., Galand *et al.*, 2001], especially during geomagnetic storms [Cowley, 2000].

Quantifying the ionospheric conductivity on a global scale is a difficult task to achieve as a complete knowledge of the altitudinal and temporal variation of the neutral and plasma densities are essential for this purpose. However, since the conductivity of the ionosphere depends upon the solar zenith angle and the composition of the neutral atmosphere, the Hall and Pederson conductances in the ionosphere can be expressed in terms of the solar zenith angle and the solar EUV flux (F10.7) in the absence of particle precipitation [Moen and Brekke, 1993]. Likewise, the conductance in the auroral zone can be specified using expressions that relate the average energy of the precipitating particles and the average energy flux to the Hall and Pederson conductances [Robinson *et al.*, 1987]. The Hall and Pederson conductances are also expressed in terms of ground based magnetometer measurements [Ahn *et al.*, 1983, 1998]. Based on these, several conductance models of the ionosphere have been developed using which a number of studies that examine the variabilities of the ionospheric conductivity during different geophysical conditions have been performed in the past [Chapman, 1956; Zhang *et al.*, 2004, and references therein].

Understanding how the ionosphere affects the magnetospheric processes has been extremely hard to achieve using observations. This is because it is difficult to obtain satellite measurements from the same region of the magnetosphere for the same solar wind conditions and varying ionospheric conductivities. As a result, it becomes necessary to rely on models for understanding the Magnetosphere-Ionosphere (M-I) coupling processes and the effects one has on the other. A number of studies have been done in the past using global MagnetoHydroDynamic (MHD) codes to determine what effects the ionosphere has on the magnetosphere [e.g., Fedder and Lyon, 1987; Ridley *et al.*, 2004]. One of the first studies by Fedder and Lyon [1987] suggested that the ionospheric conductance plays an important role in regulating the SWMI coupling by influencing

the reconnection rate in the dayside magnetosphere. They showed that the amount of magnetic flux in the open field lines is determined by the length of the reconnection line. They suggested that the conducting ionosphere provides a negative feedback to the SWMI coupling by controlling the strength of the R1 FACs. Later, *Siscoe et al.* [2002] showed that the magnetic field generated by the R1 FACs act to balance the effect of the solar wind dynamic pressure at the magnetopause. For larger values of ionospheric conductance, the strength of the R1 FACs and the associated magnetic field increases, resulting in an increase in the $J \times B$ pressure inside the magnetopause [*Siscoe et al.*, 2002]. Such an increase in pressure inside the magnetopause leads to a shift in the location of the magnetopause. Consequently, the solar wind dynamic pressure decreases and the flanks of the magnetosheath becomes wider leading to the reduction of reconnection potential [*Siscoe et al.*, 2002; *Merkine et al.*, 2003; *Merkin et al.*, 2005]. The decrease in solar wind dynamic pressure was shown to cause saturation of the cross polar cap potential as it limits the current in the R1 FACs [*Siscoe et al.*, 2002; *Connor et al.*, 2014].

Attempts have been made in the past to model the development of the ring current and its dynamics during quiet as well as disturbed times [*Wolf*, 1970; *Senior and Blanc*, 1984; *Garner et al.*, 2004; *Jordanova et al.*, 2006, 2010, 2012]. The source of energetic particles in the ring current comes from the impulsive plasma sheet injections that occur during geomagnetic storms or substorms [*Ebihara and Miyoshi*, 2010; *Yu et al.*, 2014]. The outflow of ions from the ionosphere during disturbed periods is also known to enhance the ring current energy density [*Lotko*, 2007]. Several numerical and theoretical studies provide evidence to the fact that variations in the ring current and flux enhancements in the inner magnetosphere are related to enhancements in the convection electric field [*Yu et al.*, 2014]. The earthward movement of the central plasma sheet under the action of the convection electric field brings the plasma sheet population into the ring current region leading to enhancement in the ring current density [*Kivelson and Russell*, 1995]. However, observations of the magnetotail region from the Wind spacecraft showed that plasma flows in the central plasma sheet are concentrated towards the midnight [*Lotko et al.*, 2014]. The meridional gradient in the ionospheric Hall conductance [*Hardy et al.*, 1987; *Fuller-Rowell and Evans*, 1987] was shown to cause the asymmetries in the plasma sheet flows and rate of reconnection in magnetotail by *Lotko et al.* [2014]. The clockwise rotation and dawn-dusk asymmetry of the ionospheric convection pattern in the polar regions is also known to be caused by the meridional gradients in the ionospheric conductance [*Yasuhara et al.*, 1983]. The Alfvén wave energy flux derived from Fast Auroral Snapshot Explorer (FAST) measurements, electron precipitation energy flux obtained from DMSP satellite measurements also show the dawn-dusk asymmetry [*Chaston et al.*, 2003; *Newell et al.*, 2009, 2010].

Investigation in the past carried out by first principle physics based models as

well as empirical models, have provided a broad understanding of the behaviour of the M-I system. However, an accurate representation of the M-I physics requires self-consistent coupling of the R1 FACs and R2 FACs with the ionosphere. The previous models lack self-consistency as they do not account for the feedback from the inner magnetosphere [e.g., *Li et al.*, 1998; *Zaharia et al.*, 2004; *Liu et al.*, 2009b]. Instead, these models use artificial localized electromagnetic pulses to simulate the induced electric field and magnetotail dipolarization [*Li et al.*, 1998; *Zaharia et al.*, 2004; *Liu et al.*, 2009b; *Sarris et al.*, 2002]. In this study we use the SWMF (Space Weather Modelling Framework) [*Toth et al.*, 2005] which is an unified self-consistent model for the comprehensive investigation of the processes happening in the global magnetosphere, inner magnetosphere and the ionosphere during the geomagnetic storm of 17 March 2013. The inner magnetosphere dynamics in this study is simulated using a new self-consistent model which is two-way coupled to the MHD code and the ionospheric potential solver. Global simulations of the M-I system is performed by varying the ionospheric conductances in this study to examine the dependence of magnetospheric dynamics on the ionospheric conductance. The results from these simulations are compared with the satellite measurements. A description of the SWMF model used for simulating the behaviour of M-I system is provided in the following section.

6.2 Description of the Model

Global simulations of the SWMI interaction during the geomagnetic storm triggered on 17 March, 2013 (also referred to as the St.Patrick's day storm) was performed by coupling several first-principle physics-based models. The models include a global MHD code Block-Adaptive Tree Solar-Wind Roe Upwind Scheme (BATS-R-US) [*Powell et al.*, 1999], a kinetic ring current model RAM-SCB [e.g., *Jordanova et al.*, 2010; *Zaharia et al.*, 2006], and an ionospheric electrodynamics solver [*Ridley et al.*, 2004]. The schematic representation of the coupling framework between these models is shown in Figure 6.1.

The global MHD code (BATS-R-US) is coupled to the ionospheric electrodynamics solver at an altitude of 100km. The FACs computed at $3.5 R_E$ of the BATS-R-US code are mapped to the ionosphere at an altitude of 100km at every 10 seconds. The ionospheric electric potential is computed using the FACs and the ionospheric conductance. A boundary condition of zero potential at 50° MLAT is used as the inner boundary condition in the MHD for estimation of the electric potential. The electric potential computed in this way is mapped to the inner boundary of the MHD code (i.e. $2.5 R_E$) to obtain the $E \times B$ convection velocity.

The ionospheric conductance used in the potential solver includes solar generated conductance which is dependent on the solar zenith angle and the F10.7, nightside conductance caused by star light and galactic sources and auroral conductance that is associated with particle precipitation. The solar generated ionospheric conductance

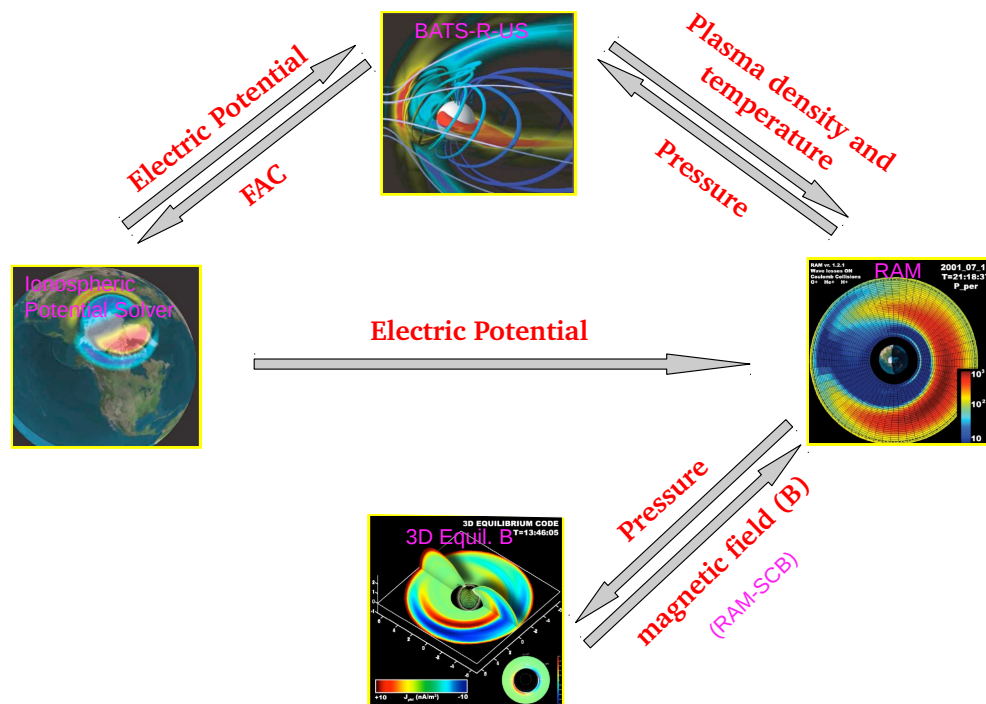


Figure 6.1: The Space Weather Modeling Framework(SWMF) and its coupling between the various physics based models.

is specified as a function of the solar zenith angle and the F10.7 [Moen and Brekke, 1993]. The auroral conductance is specified through an empirical relationship of the Hall and Pederson conductances with the FACs derived using the Assimilative Mapping of Ionospheric Electrodynamics (AMIE) technique [Richmond and Kamide, 1988; Ridley *et al.*, 2004].

The physics of the inner magnetosphere is simulated using the kinetic Ring current Atmosphere interactions Model (RAM) model. The RAM code models the kinetic physics of charged particles inside $6.5 R_E$ in the inner magnetosphere [Jordanova *et al.*, 2012]. The RAM code along with a 3-D Euler-potential based plasma equilibrium code is coupled by Ring current Atmosphere interactions Model-Self Consistent B (RAM-SCB) code. The MHD code and the ionospheric potential solver are also coupled to the RAM-SCB code. The 3-D equilibrium code uses the plasma pressure produced by the RAM ring current distribution to calculate the force balanced magnetic field which is again coupled back to the RAM code. The pressure and density corrections obtained from the RAM-SCB code is used by the BATS-R-US code to modify the global magnetospheric configuration and current systems. In turn, the kinetic model receives density and characteristic temperature at $6.5 R_E$ from the MHD code. This is updated every 5 minutes and is used by the RAM-SCB code as the plasma sheet source boundary condition. The 3-D equilibrium code gets the magnetic field boundary condition from

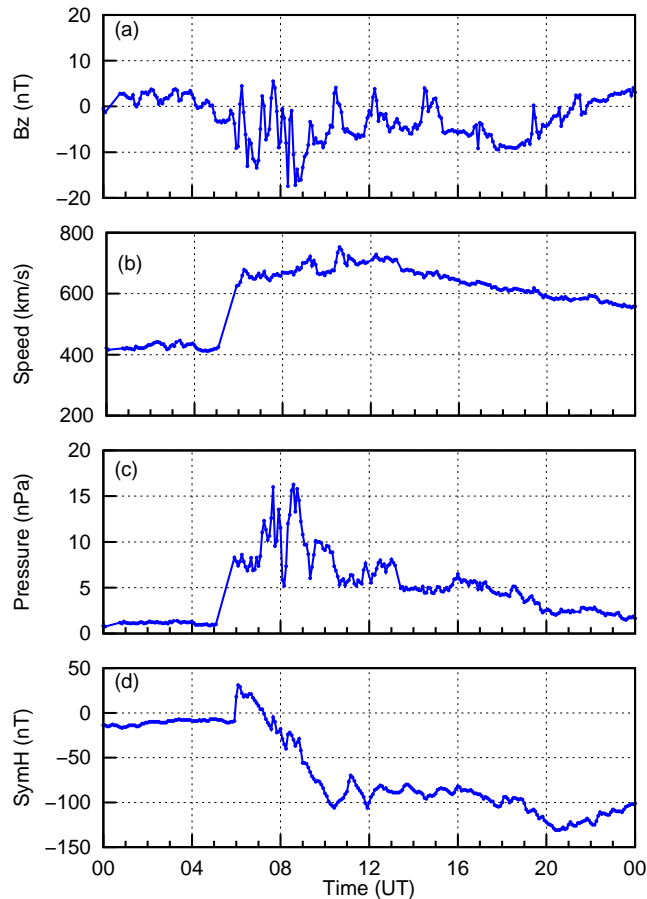


Figure 6.2: Geomagnetic conditions on 17 March 2013: Panels (a), (b), (c) and (d) represents the temporal variation of IMF B_z , Speed, Pressure and Sym-H index respectively on 17 March 2013.

an empirical model T-89 [Tsyganenko, 1989]. The electric field needed in the RAM is derived by mapping the electric potential obtained from the ionospheric potential solver in regular intervals of 10 seconds onto the inner magnetosphere. In this way a self consistent electric field drives the ring current model along with its self-consistent magnetic field.

6.3 Simulation results

The response of the M-I system to the geomagnetic storm that occurred on 17 March 2013 was simulated using the SWMF.

The intense geomagnetic storm, began with the arrival of the CME – driven shock at the magnetosphere following which the solar wind speed and pressure exhibited sudden enhancements as seen in Figure 6.2. It can be seen that the Z-component of the IMF (IMF B_z) turned southward at around 0600 UT on 17 March 2013 and is mostly fluctuating in nature. The sudden enhancement in Sym-H index at 0600 UT marks the SSC. Later at around 0700 UT, the Sym-H index began to decrease steeply

as seen in Figure 6.2, indicating the beginning of the main phase of the geomagnetic storm. At around 1100 UT, the Sym-H index reached its first minimum of -100 nT.

In order to examine how the variations in ionospheric conductivity could affect the magnetospheric behaviour on this day, the global simulations of the behaviour of the M-I system on 17 March 2013 were run with two different types of conductance models. The Type 1 simulation uses a realistic conductance model with contributions from solar EUV radiation (specified using the F10.7 and solar zenith angle), the nightside conductances (specified by the starlight and galactic sources and the polar cap conductance) and the auroral conductance (specified using an empirical relationship between the FACs and the Hall and Pederson conductances). The Type 2 simulation was performed using a constant Hall and Pederson conductance in the ionosphere. This simulation demonstrates how the absence of day-night conductivity gradients in the ionosphere affects the magnetospheric configuration. Among the two conductance models used in the simulating the M-I coupling, the second type in which the ionospheric conductance is assumed to be uniform is physically unrealistic. Even so, a comparison of the results with the realistic case helps in demonstrating the ionospheric control on magnetospheric dynamics.

Each simulation was run for 24 hours. The upstream boundary conditions used to run the BATS-R-US code were obtained from the satellite measurements. The IMF and solar wind conditions measured at the L1 point was shifted to the boundary of the MHD code to obtain the driving conditions for the BATS-R-US code. The simulation results at three selected times representing the quiet time (0500UT), the time around SSC (0700 UT) and the main phase of the storm (0920 UT) are presented here. The response of the M-I system to changes in the ionospheric conductivity simulated using the SWMI has been described in the following section.

6.3.1 Type 1: The realistic conductance model

The distribution of FACs, electric potential, Hall and Pederson conductances in the southern hemisphere on 17 March 2013 simulated using the realistic conductance model is shown in panels (a)-(d) of Figure 6.3. During the quiet time, i.e., at 0500 UT, the FACs display the typical quiet time pattern with strong R1 FACs formed at higher latitudes (75-80° MLAT). The R1 FACs flow into the ionosphere in the dawn sector and flow out in the dusk sector, respectively, as indicated by the blue and red colors in row (a) of Figure 6.3. The R2 FACs are very weak at 0500 UT. This is usually the case as the R2 FACs are generated by the formation of pressure gradients in the ring current region which are weak during quiet times [Potemra, 1979; Le et al., 2004]. However, both the R1 FACs and R2 FACs are seen to intensify during the time of SSC i.e., at 0700 UT.

The distribution of R1 FACs and R2 FACs, which is somewhat symmetric with

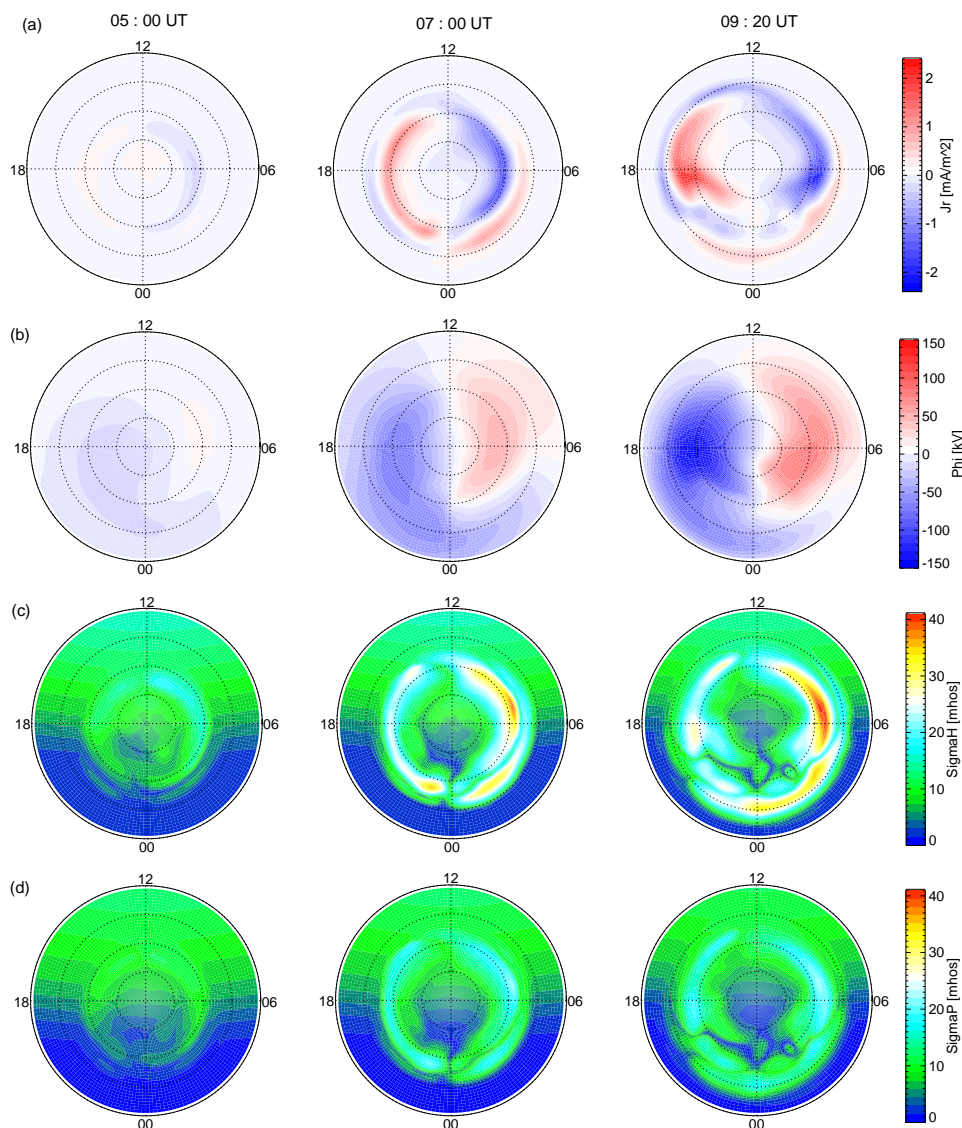


Figure 6.3: Results of Type 1 simulation using the realistic conductance model at 0500 UT (quiet time), 0700 UT (SSC) and 09:20 UT (storm main phase): Rows (a) – (d) represents the field aligned currents (red indicates upward current system and blue indicates downward current system), electric potential, ionospheric Hall conductance and Pederson conductance, respectively.

respect to the noon-midnight meridian is seen to undergo further intensification and equatorward expansion (upto 60° MLAT) during the main phase of the storm (at 0920 UT) on 17 March 2013. A notable feature in the FAC distribution is its westward rotation with the axis of symmetry located at about 21 MLT during the main phase of the storm (at 0920 UT). Such a westward rotation is a result of the development of a partial ring current in the inner magnetosphere. The ring current energy density in the equatorial plane of the magnetosphere during the geomagnetic storm of 17 March 2013 is shown in Figure 6.4. After the SSC, the ring current is seen to slowly evolve in the regions between $4-6 R_E$ in the inner magnetosphere. Usually, the development of

the ring current takes at least ~ 30 minutes from the SSC [Ebihara and Miyoshi, 2010]. The plasma sheet population which is an important source of ring current is known to enhance with the southward turning of the IMF [Kivelson and Russell, 1995]. As the plasma sheet particles enter the dipole region of the earth under the action of the convection electric field, they come under the influence of the gradient and curvature forces induced by the geomagnetic field. Accordingly, the ions drift westward towards the duskside and the electrons drift towards the dawnside in the equatorial plane around the earth leading to the formation of a partial ring current [Ebihara and Miyoshi, 2010]. The misalignment in the plasma pressure in the ring current region allows the R2 FACs to flow into the ionosphere in the dusk sector while a similar current flows upward in the dawn sector. These currents which constitute the R2 FACs also rotate westward as the partial ring current flows westward [Yu *et al.*, 2014]. The formation of a strong ring current in the westward direction during the main phase of the storm is evident from Figure 6.4. When projected onto the ionosphere, this maps to $60\text{-}65^\circ$ MLAT which is where the R2 FACs are also seen to be located.

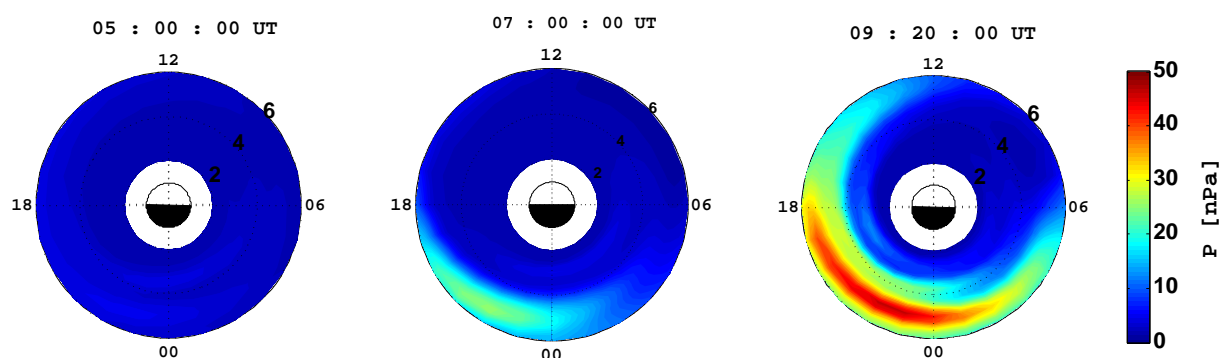


Figure 6.4: Simulated pressure gradients in the inner magnetosphere ($2\text{-}6 R_E$) at 05:00 UT (quiet time), 0700 UT (SSC) and 09:20 UT (storm main phase) using the realistic conductance model.

Simultaneous to the strengthening of FACs, the expansion of the auroral oval and large enhancements in the auroral conductances are also seen to occur on 17 March 2013 (row (c) and (d) of Figure 6.3). These processes are known to begin with the reconnection of the IMF with the geomagnetic field during which a large amount of energy in the form of electric field, currents and energetic particles is transferred into the polar ionosphere [Kivelson and Russell, 1995]. When dayside reconnection happens, closed field lines are converted into open field lines because of which the polar cap area increases resulting in the equatorward movement of the auroral oval [Kivelson and Russell, 1995]. Such an expansion of the polar cap and the auroral oval can be clearly seen during the main phase of the storm at 0920 UT. These processes are also accompanied by large enhancements in the magnitude and area occupied by the electric potential cell as indicated in row (b)

of Figure 6.3. The penetration of the convection electric field to the polar ionosphere along the highly conducting magnetic field lines during stormtime is what leads to such an expansion of the electric potential cell [Lyons, 1992]. Large enhancement in the magnitude of the electric potential and its expansion to much lower latitudes (50° MLAT) during the storm main phase signify continuous energization of the M-I system. The extension of the potential cell into the post midnight sector and the close iso-potential contours at 0920 UT in the subauroral regions (seen in row (b) of Figure 6.3), suggests the presence of strong poleward directed electric fields which can cause enhanced plasma convection in the sunward direction. The presence of strong poleward directed electric fields, during the geomagnetic storm of 17 March 2013, in the subauroral regions of the northern hemisphere has been shown by Yu *et al.* [2015]. Associated with this electric field were also observed large sunward and westward flows in a narrow channel extending into the post midnight sector. These large enhancements in the sunward plasma convection is an important feature of the SAPS. Similar features are also expected to be seen in the southern hemisphere as SAPS exhibit magnetically conjugate features [Foster, 2008]. Another notable feature is the reversal of plasma flow from eastward to westward direction occurring at about $50\text{-}60^\circ$ MLAT in the post midnight region. Such a reversal is a commonly observed during stormtime and is a result of the complex electrodynamic that occur when the auroral eastward electrojet (EEJ) overlaps with the auroral westward electrojet (WEJ) in the midnight harang region [Koskinen and Pulkkinen, 1995; Marghitu *et al.*, 2009].

It is clear from the above discussion that the global simulations of the M-I coupling physics using the realistic conductance model reproduces the typical stormtime features like the intensification of the FACs and electric potential, their expansion to lower latitudes, enhancement in the Hall and Pederson conductances due to auroral particle precipitation etc. The behaviour of the M-I system when the ionospheric conductances are assumed to be uniform is described in the next section.

6.3.2 Type 2: Uniform conductance model

In the second simulation, the ionospheric Hall (0.25 S) and the Pederson conductances (1.0 S) are assumed to be uniform. The resulting FACs and the electric potential as observed in the southern hemisphere on 17 March 2013 at three chosen times that represent the quiet time (0500UT), the time around SSC (0700 UT) and the main phase of the storm (0920 UT) is shown in Figure 6.5. As seen in row (a) of Figure 6.5, before the commencement of the storm, at 0500 UT, there exists only a weak R1 FACs. The R2 FACs are very weak probably due to a weak ring current in the inner magnetosphere. After the commencement of the storm, at 0700 UT, the R1 FACs and R2 FACs are found to strengthen and expand to lower latitudes. The large expansion in the polar cap area seen in the storm main phase (at 0920 UT) in Figure 6.5 suggests that dayside

reconnection must be taking place closer to the earth. As described in the previous section, the conversion of the closed geomagnetic field lines into open field lines during reconnection with the IMF results in the expansion of the polar cap.

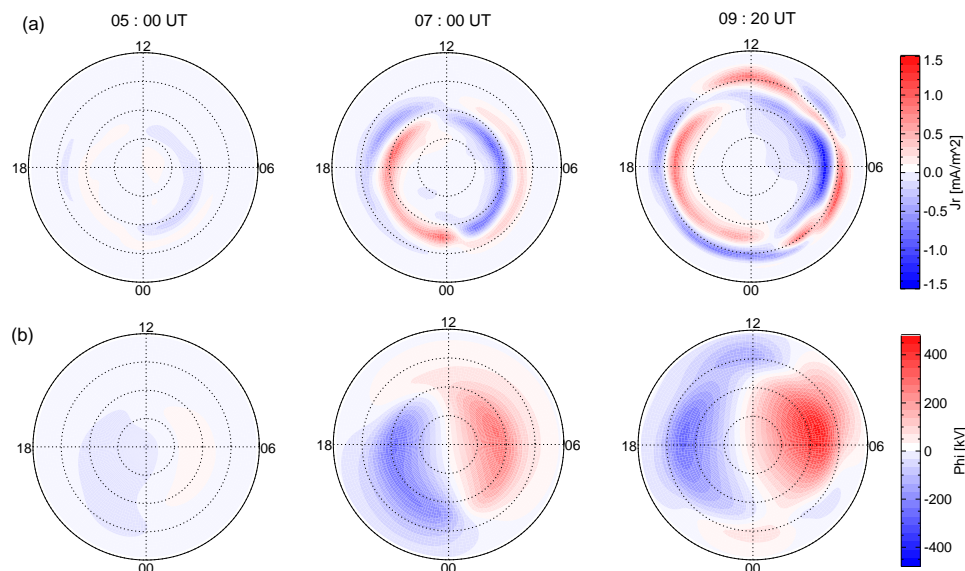


Figure 6.5: Results of Type 2 simulation using the uniform conductance model at 0500 UT (quiet time), 0700 UT (SSC) and 09:20 UT (storm main phase): Rows (a) – (b) represents the field aligned currents (red indicates upward current system and blue indicates downward current system) and the electric potential, respectively.

The electric potential cell shown in row (b) of Figure 6.5, displays the typical two cell pattern. Both the dawn and dusk potential cells appear symmetric across the noon-midnight meridian and have almost equal magnitudes unlike the earlier case wherein the dusk cell is larger than the dawn cell. This feature that arises due to the absence of day-night conductivity gradient in the ionosphere has been a subject of investigation of many studies [Yasuhara *et al.*, 1983, and references therein]. Yasuhara *et al.* [1983] suggested that the difference in magnitude of Hall conductivity in the nightside region as compared to the dayside region leads to the development of a positive/negative potential on the nightside/dayside. In other words, the absence of the gradient in ionospheric Hall conductivities adds symmetry to the potential pattern. They showed that the deflection of the currents in the polar cap and the potential distribution to earlier local times depends on the ratio of the Hall conductivity in the auroral oval to that of the polar cap. Hence, the absence of extended flow reversal into the post midnight region as seen in the potential distribution (row (b) of Figure 6.5) may arise from the fact that ionospheric conductivities are uniform in the present case. Previous simulation studies using both zero Hall conductance and a non zero Hall conductance also show similar results [Ridley *et al.*, 2004; Zhang *et al.*, 2014].

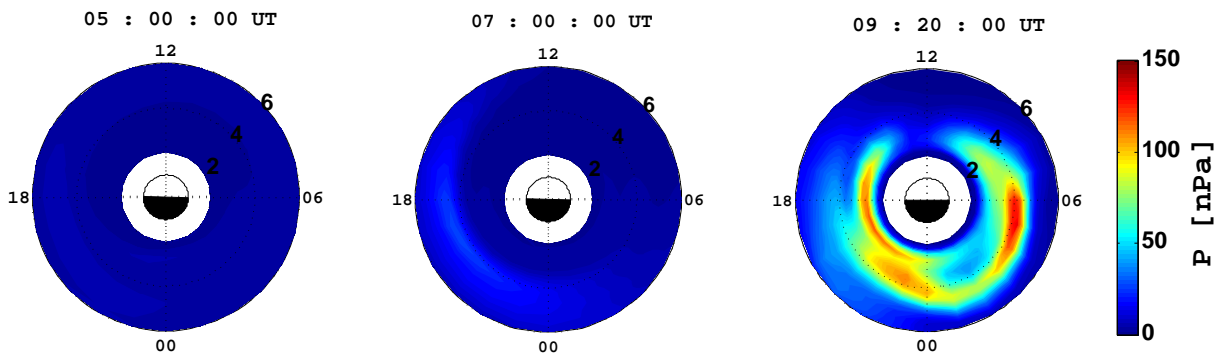


Figure 6.6: Simulated pressure gradients in the inner magnetosphere ($2 - 6 R_E$) at 05:00 UT (quiet time), 0700 UT (SSC) and 09:20 UT (storm main phase) using the uniform conductance model.

The FACs are seen to enhance and expand to the lower latitudes during the main phase of the storm. The FACs maintain symmetry across the noon-midnight meridian nevertheless in the present case unlike the previous case wherein the FACs exhibited westward rotation. This could be a result of the changes in the magnetosphere response owing to the uniform distribution of the ionospheric conductances. In order to examine the magnetospheric behaviour when the ionospheric conductances are uniform, the ring current energy density in the inner magnetosphere is shown in Figure 6.6. As expected, the ring current energy density increases as the storm progresses. The maximum value of energy density at 0920 UT is however threefold higher than that simulated by the realistic conductance model. As described earlier, the R2 FACs that flow into the equatorward edge of the auroral oval achieve closure through the Pederson currents that connect them to the R1 FACs in the poleward edge of the auroral oval [Prölss, 2004]. However, the low value of Pederson conductance (1 S) in the ionosphere in the present case restricts the flow of R2 FACs into the ionosphere. Consequently, a stronger ring current is seen to have formed in the present case. The presence of strong convection electric field could also give rise to such large enhancements in the ring current energy density [Ebihara and Miyoshi, 2010].

The ring current has formed closer to the earth in between $2-4 R_E$ during the main phase of the storm at 0920 UT as seen in Figure 6.6. It is known that longer ion precipitation time constant allows the ions to penetrate deep into the magnetosphere [Senior and Blanc, 1984]. Since the precipitation into the ionosphere is restricted by the low magnitude of the ionospheric conductance, the ions move closer to the earth resulting in the formation of the ring current at regions close to the earth. In addition to this, the ring current distribution appears to be dawn-dusk symmetric unlike the realistic conductance case wherein the ring current energy density is clearly concentrated towards the dusk sector. The symmetric distribution of the ring current in the present

case could be because the plasma sheet flows in the magnetotail are symmetric for a uniform distribution of ionospheric conductance [Lotko *et al.*, 2014; Zhang *et al.*, 2014]. Lotko *et al.* [2014] showed that the meridional gradient in Hall conductance is what causes the plasma sheet flow to be concentrated towards the premidnight sector. As described in Chapter 1, the Hall current flows in a direction opposite to the direction of plasma flow. If there is a gradient in Hall conductance which is usually the case in the night sector in the polar region due to auroral particle precipitation, then there is an accumulation of charges in the midnight region where the auroral EEJ overlaps the auroral WEJ [Yasuhara *et al.*, 1983]. This gives rise to an electric field which is directed equatorward in the poleward edge of the auroral oval and poleward in the equatorward edge of the auroral oval [Marghitu *et al.*, 2009]. The resultant of this secondary electric field when added to the convection electric field in the polar cap is in the sunward direction. The sunward electric field when projected to the nightside magnetosphere causes a duskward drift because of which the plasmasheet flows appear to be concentrated towards the premidnight region [Lotko *et al.*, 2014]. Our results show that the gradient in ionospheric Hall conductivity could give rise to asymmetry in the ring current distribution in the inner magnetosphere.

It is clear from the above discussion that the uniform conductivity of the ionosphere gives rise to a symmetric distribution of electric potential as well as the ring current energy distribution. In addition, the typical stormtime features like the strengthening of the FACs and the electric potential, expansion of the polar cap and equatorward shifting of the auroral oval are seen to be reproduced in the simulations using the uniform conductance model. However, the magnitudes of the FACs and electric potential were very high as compared to that the case of realistic ionospheric conductances.

6.4 How the ionospheric conductivity influences the magnetospheric dynamics?

The two simulations performed using the SWMF highlights the important effects the ionospheric conductivity has on the global state of the magnetosphere. The Type 1 simulation performed using a conductance model which includes contributions from the solar EUV radiation, nightside conductances and auroral particle precipitation, showed typical storm time features such as the strengthening of the FACs and the electric potential, their expansion to the lower latitudes, the westward rotation of the current distribution and the reversal of plasma flow in the midnight region. The Type 2 simulation performed with a uniform Hall and Pederson conductance in the ionosphere also shows typical stormtime features like the strengthening of the FACs and their expansion to lower latitudes. However, there are significant differences in the ionospheric and magnetospheric response between the two simulations which arise due to the difference

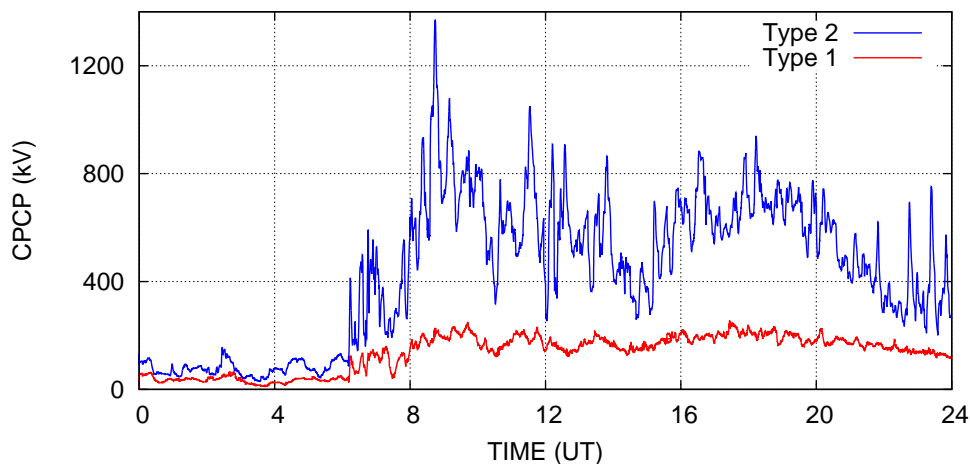


Figure 6.7: Cross Polar Cap Potential (CPCP) in the southern hemisphere on 17 March 2013 obtained using the realistic conductance model (red curve) and the uniform conductance (blue curve).

in ionospheric conductivities.

The FACs generated using the uniform ionospheric conductance run were found to be weaker as compared to the FACs obtained using a realistic conductance model. Since the driving conditions are the same for both the simulations, the change in ionospheric conductance is what must have given rise to such a variation in the strength of FACs. It is the Pederson conductance that plays an important role in regulating the flow of R1 FACs across the polar cap [Liu *et al.*, 2009b]. The Pederson conductance was set to 1.0 S in the uniform conductance model while it amounted to about 20.0 S in the realistic conductance model. The lower value of Pederson conductance in the ionosphere limits the FACs flowing through it and gives rise to a corresponding increase in the potential drop (as given by $J = \sigma_p E$) across the polar cap [Ridley *et al.*, 2004]. This trend is observed in both the simulations with maximum value of electric potential/FACs being 480kV/1.5 $\mu A/m^2$ in the case of the Type 1 simulation and 150 kV/2.5 $\mu A/m^2$ in the case of the Type 2 simulation respectively. A similar relationship between the FACs, Pederson conductance and the Cross Polar Cap Potential (CPCP) in the ionosphere has also been shown by studies in the past [for e.g., Merkin *et al.*, 2005].

The simulation results also demonstrate that a uniform conductance pattern gives rise to a stronger symmetric ring current. The ring current energy density obtained from the Type 2 simulation was noted to be threefold higher than the ring current energy density simulated with realistic ionospheric conductances. The generation of such a strong ring current could be due to the action of enhanced convection electric field [Ebihara and Miyoshi, 2010; Yu *et al.*, 2014]. As described in Chapter 1, the convection electric field generated as a result of the Solar Wind-Magnetosphere coupling drives the reconnected open magnetic field lines across the polar cap from noon to midnight in what is known as magnetospheric convection [Lyons, 1992]. The convection electric

field (in the dawn-to-dusk direction) also maps along the highly conducting reconnected open magnetic field lines to the polar cap ionosphere [Lyons, 1992]. Accordingly, the potential drop generated at the magnetopause would map to the polar cap ionosphere along the magnetic field lines and the plasma contained in the open field lines convect in the direction given by $E = -V \times B$. The cross polar cap potential which is the difference between the maximum and minimum electric potential in the ionosphere is also known to be a good proxy for the strength of the magnetospheric convection [Connor *et al.*, 2014; Siscoe *et al.*, 2002].

The CPCP obtained from both the Type 1 and Type 2 simulations are presented in Figure 6.7. The red and blue curves represent the CPCP simulated using the realistic conductance model and the uniform conductance model, respectively. Clearly, the magnitude of CPCP is very high reaching upto 1400 kV (at ~ 0900 UT) for the uniform conductance run while the CPCP simulated using the realistic conductance model is about 200kV only. From a comparison of the CPCP and FACs obtained from the Type 1 and Type 2 simulations, it can be seen that for lower ionospheric conductances, the FACs are weak while the CPCP is found to be very high and vice versa. This suggests that the magnetospheric convection is stronger in the case of the low, uniform conductances, than observed when the ionospheric conductances assume realistic values. This may be the reason for the formation of a strong ring current as indicated by very high values of ring current energy density (as seen in Figure 6.6) formed in the case of the uniform conductance run.

The strength of the ring current is usually quantified using the Dst index [Gonzalez *et al.*, 1994]. The Dst index estimated using the Dessler-Parker-Sckopke relationship [Dessler and Parker, 1959; Sckopke, 1966] for both the simulations is shown in panel (a) of Figure 6.8. The black and blue curves in panel (a) of Figure 6.8 represents the Dst index simulated using the uniform conductance model and the realistic conductance model, respectively, while the orange curve represents the measured Sym-H index on 17 March 2013. It can be seen that the Dst index simulated using the realistic conductance model is well in agreement with the observed values except for the time of SSC. However, the Dst index obtained from the Type 2 simulation, falls steeply after SSC as shown in panel (a) of Figure 6.8 and attains a minimum of ~ -200 nT. Such a large decrease in the Dst index could be due to the formation of stronger ring currents in the inner magnetosphere due to enhanced magnetospheric convection.

The simulated CPCP which is a proxy for the strength of magnetospheric convection is also shown in panel (b) of Figure 6.8 for comparison. On comparing the variations in the Dst index with the CPCP, it is clear that the fall in the Dst index corresponds to the periods of enhancement in the CPCP indicating that enhanced magnetospheric convection led to the formation of stronger ring current in the case of uniform conductance run. The low value of Pederson conductance also contributes to the formation

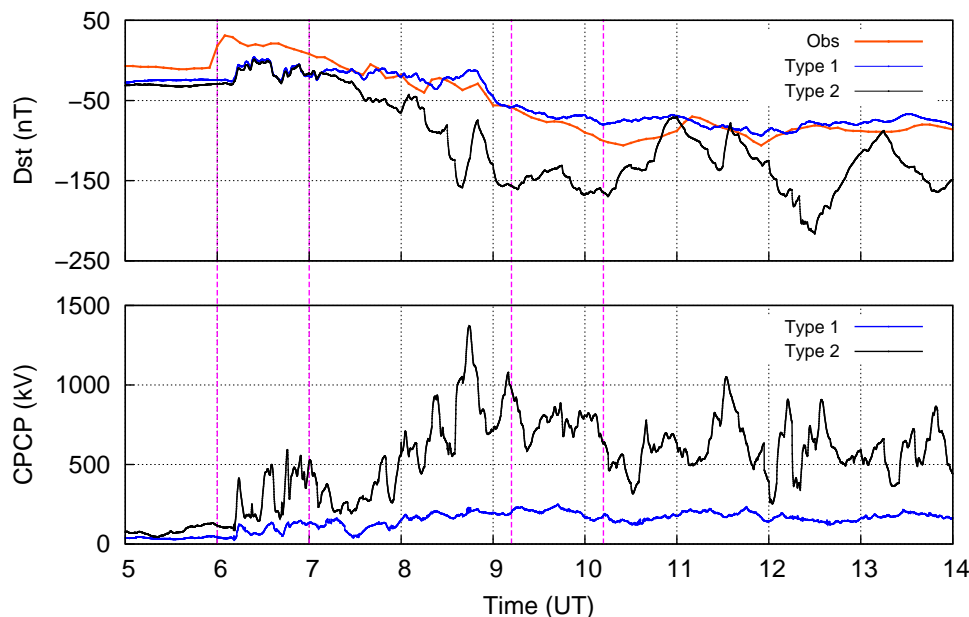


Figure 6.8: Dst index on 17 March 2013 simulated using the uniform conductance model and the realistic conductance model are shown in black and blue colors, respectively, while the observed SYM-H index is shown using orange color.

of a strong ring current by limiting the strength of R2 FACs. Hence, it is clear that a change in ionospheric conductivity significantly affects the magnetospheric convection and ring current energy distribution through its control on the FACs and by that means the global state of the magnetosphere.

A comparison of the z -component of magnetic field obtained from GOES-15 and RBSP-B satellite measurements is made, with the simulation results is presented Figure 6.9, to understand how well the model captures the stormtime magnetic field variations in the magnetosphere. In the top panel is shown the orbits of the GOES-15 and RBSP-B satellites. The middle panel shows the variation of B_z simulated along the track of GOES-15 using the realistic conductance model (blue curve) along with the GOES-15 observations (red curve). The bottom panel shows the variation of B_z simulated along the track of RBSP-B (blue curve) using the realistic conductance model along with the RBSP-B observations (red curve). A comparison of the simulated B_z along the tracks of GOES-15 with the actual observations show deviations around the time of SSC and at later times after 1600 UT also. This suggests that the magnitude dayside magnetic field is underestimated in the model. Hence a less compressed cavity may be formed in the dayside because of which the Dst appears to be underestimated (seen in Figure 6.8) during the time of SSC. The magnetic field measurements in the inner magnetosphere (inside $6.5 R_E$) obtained from the RBSP-B satellites are well in agreement with the simulated values of B_z .

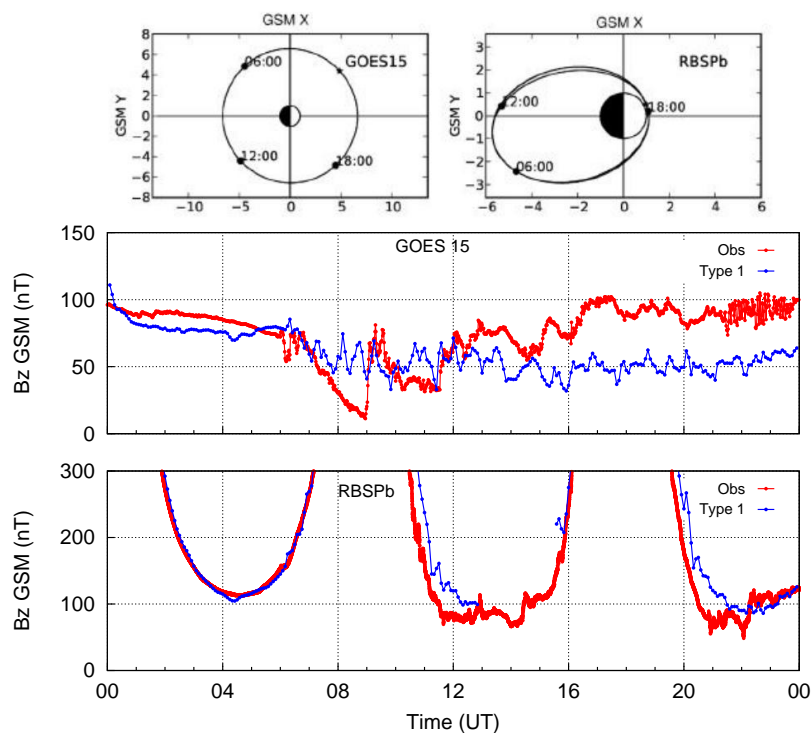


Figure 6.9: Top panel shows the orbits of GOES-15 and RBSP-B satellites on 17 March 2013. The middle panel shows the variation of B_z simulated along the track of GOES-15 using the realistic conductance model (blue curve) along with the GOES-15 observations (red curve). The bottom panel shows the variation of B_z simulated along the track of RBSP-B (blue curve) using the realistic conductance model along with the RBSP-B observations (red curve).

6.5 Conclusion

This study investigated the processes happening in the global magnetosphere, inner magnetosphere and the ionosphere during the geomagnetic storm of 17 March 2013 using the SWMF (Space Weather Modelling Framework) which is an unified self-consistent model. The RAM-SCB code used in this study to simulate the inner magnetospheric dynamics is a new self-consistent model which is two-way coupled to the MHD code and the ionospheric potential solver. Comparison of the ionospheric and magnetospheric dynamics on 17 March 2013, simulated with the two different types of conductance models highlighted the important effects the ionospheric conductivity has on the global state of the magnetosphere. The ionospheric convection pattern was found to be symmetric across the noon midnight meridian when the ionospheric conductivities were assumed to be uniform whereas when the conductances assumed real values, the FACs and electric potential were found to be asymmetric. This suggested that the addition of gradients to the ionospheric conductivity significantly affected the ionospheric convection pattern. The large increase/decrease in the CPCP and reduction/enhancement in the

strength of the R1 FACs for low/high values of Pederson conductivity indicated that the ionospheric conductivity through its control on the magnitude of R1 FACs regulates the energy supplied into the ionosphere and by that means affects the strength of the magnetospheric convection. The results also point to the fact that a non uniform distribution of ionospheric conductivity gives rise to asymmetry in the electric potential and by that means the ring current distribution. The variations in the simulated Dst indices shows good correlation with the pressure variations in the inner magnetosphere and the CPCP which points to the fact that the plasma injected into the inner magnetosphere after reconnection is an important source for the intensification of ring current. The simulated magnetic field is also in agreement with the measurements from the RBSPb satellites which indicates that the model is able to capture well the dynamics of the inner magnetosphere.

Chapter 7

Summary and Future Scope

7.1 Summary

The variabilities of the ionosphere, is in one or the other way, necessarily related to the solar energy that we receive on the Earth. From what is known, the ionosphere behaves erratically when the Sun becomes active because the magnetic disturbances that cause ionospheric storms originate in the Sun. They propagate away into the interplanetary medium in the form of solar wind embedded in the Sun's magnetic field. A small fraction of this solar wind energy enters the Earth's near-space environment in the form of electric fields, currents and particle precipitation. As the polar ionosphere is intimately coupled to the magnetosphere through the vertical magnetic field lines, the excess energy received by the magnetosphere can directly enter the polar regions. Thus, the ionospheric disturbances, initiated at the high latitudes regions, eventually propagate to the mid, low and equatorial latitudes. Large unpredictable deviations in the plasma density distribution driven by changes in the electric field and neutral winds are not a rare sight during geomagnetic storms. However several aspects related to the propagation of the disturbances from the polar regions to the lower latitudes, and the evolution of ionospheric storms are still not clear. The ionospheric irregularities, generated during storms, cause significant problems to satellite based communication and navigation. Hence, the primary objective of this doctoral work was to study the processes responsible for the evolution of ionospheric storms over the Indian longitude.

One of the biggest problem in achieving a comprehensive understanding of the physical processes that cause the redistribution of plasma during geomagnetic storms is the lack of simultaneous measurements from different geographical locations. It becomes even more difficult when intra-event differences or the dependence of the degree of response of the ionosphere on factors like solar cycle, time of year and the time of day are considered. In the present thesis, as an attempt towards developing an understanding on the latitudinal evolution of ionospheric storms, the response of the ionosphere over Antarctic region and the Indian region to space weather events was studied. Studying the ionosphere over the Indian region becomes highly suitable to

achieve this objective as the Indian region extends from the magnetic equator to the anomaly crest and beyond the Sq focus region in the northern hemisphere. The high latitude component was included by having measurements from the Indian research station, Bharti located in Antarctica which also lies along the same longitude as the Indian region. Simultaneous and coordinated measurements of GPS derived TEC from these regions along with a knowledge of variations in the electron density, peak height obtained from the ionosonde and magnetic field variations obtained from magnetometers have helped in understanding the stormtime processes to some extent. The important results obtained from the present doctoral work is organized into seven chapters. A brief summary of the chapters is presented in the following.

The first chapter provides an introduction to the already existing information about the quiet and disturbed time behaviour of the Earth's Magnetosphere-Ionosphere (M-I) system. It describes the current understanding about the high, mid, low and equatorial latitudinal ionospheric system, phenomena, and uniqueness. The relevance and uniqueness of the present doctoral thesis and its scientific objectives is also introduced in the first chapter. The experimental techniques and the specifications of the instruments used to obtain ionospheric data for the present study is described in the second chapter.

The third chapter describes quiet time variations in the Total Electron Content (TEC) over the polar, mid and equatorial ionosphere. A sound knowledge of the quiet time variations in electron density of the ionosphere is essential to describe the degree of deviation in the behaviour of the ionosphere during space weather events. Diurnal, seasonal and solar activity variations in TEC over Bharti, Hanle and Trivandrum which represent the polar, mid and dip equatorial latitude, respectively have been described in detail. In general, the TEC variation at all these stations exhibit a semi annual variation with maximum TEC during the equinoctial period. However, the presence of the winter anomaly is recorded only at Trivandrum. Since Hanle lies in a longitude sector far away from the pole, the downwelling of composition disturbances may take place at higher latitudes because of which there may not be an apparent change in the TEC over Hanle. The TEC at Bharti remains lower than the local summer TEC, leading to the absence of winter anomaly. This is due to the absence of sunlight at Bharti resulting in no photoproduction during the local winter period. Nevertheless, the TEC at Bharti follows a diurnal pattern with the noontime peak appearing close to magnetic noon during the winter months and local noon during the summer months. Nighttime enhancements in TEC due to ionospheric convection when Bharti station is located inside the polar cap are evident especially in the winter period. This also shows that the dynamic nature of the location of Bharti with respect to the position of polar cap plays an important role in the control of plasma density therein. However, a morphological comparison between the TEC derived from the IRI 2012 model and the GPS TEC at Bharti shows only a qualitative agreement. Except for the nighttime enhancements in

TEC at Bharti, the TEC estimated during the winter months from GPS measurements agree well with the TEC derived from the IRI model. This indicates that cross polar cap transport processes have not been well accounted for in the model. A comparison of IRI model derived TEC and GPS TEC at Trivandrum also shows a wide departure. Except during summer (May to August), the IRI overly underestimate the TEC at Trivandrum. The model, however, represents the TEC at Hanle, quite well. These comparisons show that while the mid, and low latitude ionospheric regions are well represented by IRI 2012 model, appreciable differences are seen at the dip-equatorial and the polar regions.

The fourth chapter focusses on the impact of geomagnetic storms on the ionosphere over the southern polar station, Bharti. The St.Patrick's day storms of 2013 and 2015 provided an unique opportunity to understand how two distinct events of different intensities and nearly identical commencement times, occurring when the background conditions on the Sun and the Earth were almost similar, affect the polar ionosphere. During the main phase of both the storms, Bharti registered enhancements in the TEC and the phase scintillation near local magnetic noon and near magnetic midnight. Despite the geophysical conditions being almost similar during the years 2013 and 2015, the enhancement in TEC on 17 March 2015 at Bharti was way higher than that observed at Bharti on 17 March 2013. Since the enhancement during both years were centered around the local magnetic noon which is the time when the station lies in the cusp region, this could be a result of the impact of intense particle precipitation. The larger enhancement in TEC near the magnetic midnight during the storm of 2015 could be caused by the enhancement of the TOI by steady convection resulting from long-lived magnetopause erosion. The same was weaker during the St.Patrick's day storm of 2013 due to the fast fluctuating nature of IMF B_z . The changes in the magnetospheric system due to the coupling between the solar wind, magnetosphere and the polar ionosphere during the St.Patrick's day storms led to the similar and distinct responses of the southern polar ionosphere. We show that the differences in the duration of magnetopause erosion led to the varied response of the southern polar ionosphere during the St.Patrick's day storms of 2013 and 2015. The response of the ionosphere at Bharti was found to depend on the onset time of the geomagnetic storms.

The fifth chapter investigates various aspects of the coupling between the high, mid, low and equatorial latitudes during magnetically disturbed periods. Three case studies were performed to understand the electro-dynamical and neutral dynamical coupling of the high-low latitude ionosphere. Relative contributions of the disturbance electric fields (Prompt Penetration and Disturbance Dynamo) and the compositional disturbances in altering the behaviour of ionosphere over the Indian longitude were studied. In the first case study for the event on 17 March 2013, the penetration of the westward electric field, that originated from the overshielding condition, gave rise to a CEJ like situation at the dip equator. The downward movement of the F-region of the ionosphere under the action

of the westward zonal electric field to altitudes wherein recombination and diffusion are less, led to a positive ionospheric storm. On the other hand, the joule heating of the thermosphere, gave rise to the Travelling Atmospheric Disturbances (TADs) which pushed the plasma up in the equatorial anomaly region. There was no change in the TEC thereat as the electron density enhancement resulting from the upward movement of the F-region under the action of TADs compensated for the plasma loss at due to the CEJ. As a consequence, a positive ionospheric storm was seen to occur simultaneously at the equatorial, low and mid-latitude ionospheric regions in the Indian sector. In the second study, a case of the westward DDEF influencing the daytime equatorial and low latitude ionosphere, during the geomagnetic storm that occurred on 28-29 June 2013 was presented. The presence of the DDEF from the morning hours on 29 June 2013 led to the complete alteration of the latitudinal structure of the electron density with the peak in TEC occurring over the dip equator. The effects of composition disturbance was observed to be offsetted by the DDEF during this event highlighting the relative importance of electrodynamical forcing over chemistry. The relative contributions of the composition disturbances and the disturbance electric fields (PPEF and DDEF) in the controlling the ionosphere over the Indian region was studied by taking a case study of the geomagnetic storm that occurred during 18-21 February 2014. The propagation of composition disturbances generated due to storm induced joule heating from the high to mid latitudes gave rise to the positive ionospheric storm at the mid latitude station, Hanle. The action of daytime eastward PPEF gave rise to positive ionospheric storms at the low latitudes. Both the PPEF and DDEF are found to play an active role in causing positive ionospheric storms over the dip equator, Trivandrum, whereas, the TEC variations over the low latitude station, Ahmedabad are not so significant due to the competing effects of the daytime DDEF and the composition disturbances.

The sixth chapter examines the influence of ionospheric conductivity on the magnetospheric dynamics using the SWMF which is an unified self-consistent model. The RAM-SCB code used in this study to simulate the inner magnetospheric dynamics is a new self-consistent model which is two-way coupled to the MHD code and the ionospheric potential solver. Comparison of the ionospheric and magnetospheric dynamics on 17 March 2013, simulated with the two different types of conductance models highlighted the important effects the ionospheric conductivity has on the global state of the magnetosphere. The ionospheric convection pattern was found to be symmetric across the noon midnight meridian when the ionospheric conductivities are uniform. The introduction of day-night conductivity gradients was shown to add asymmetry to the ionospheric convection pattern. The strength of the magnetospheric convection depends on the ionospheric conductivity which limits the energy supplied into the ionosphere through its control on the magnitude of R1 FACs flowing into the ionosphere. The results also pointed to the fact that a non uniform distribution of ionospheric conductivity gives rise

to asymmetry in the electric potential and by that means the ring current distribution. The variations in the simulated Dst indices show good correlation with the pressure variations in the inner magnetosphere and the CPCP which points to the fact that the plasma injected into the inner magnetosphere after reconnection is an important source for the intensification of ring current. The simulated magnetic field is also in agreement with the measurements from the Radiation Belt Storm Probes (RBSP) satellites which indicates that the model is able to capture well the dynamics of the inner magnetosphere. This work highlights the role of global conductance patterns in modulating the dynamic M-I system.

The seventh chapter summarises the major scientific outcomes of the present doctoral thesis. This chapter also presents the future scope of this study which is presented in the next section.

7.2 Scope for future studies

This doctoral work highlights several aspects of high-mid-low latitude ionospheric coupling through neutral and electrodynamical processes during disturbed times. It also emphasizes the need for a coordinated simultaneous ionospheric measurements from various vantage points in gaining a proper understanding on how the ionosphere over the Indian longitude responds to space weather events. But there is an obvious shortcoming in the present study—it is the location of the station (Bharti) used in the study. While Bharti is located in the southern hemisphere, the Indian region falls in the northern hemisphere, and is impacted more by the northern polar dynamics than the southern one. To link observations at Bharti with the measurements in Indian low latitude regions, we assumed spherical symmetry. But it's not always true and reports on the asymmetry in degree of response between the two poles are galore. At the very least, the response of the ionosphere over Bharti during space weather events can only be considered to be a proxy of the ionospheric response over the northern poles. This work opens up several questions regarding the behaviour of the ionosphere over a polar station that lies in a magnetically conjugate location to Bharti. The fact that Bharti lies close to the southern geomagnetic pole while a conjugate station in the northern hemisphere that shares a same geomagnetic latitude and longitude, lies in a different geographical location could lead to asymmetries in the degree of ionospheric response of the ionosphere thereat. Hence, the simultaneous observations from both the northern and southern hemispheric magnetically conjugate locations are necessary to quantify the differences in the degree of response of the ionosphere over both the poles during space weather events. The asymmetries in the behaviour of the southern and northern polar hemisphere during space weather events as well as quiet times can also be studied using the SWMF. A comparison of the response of the southern and northern hemispheric regions to space weather events would throw considerable light into the asymmetric response of the polar

ionosphere over both the poles and the role of M-I coupling in causing the asymmetries.

Quiet time behaviour of the ionosphere over three stations, representative of equatorial (Trivandrum), mid-latitude (Hanle), and high latitude (Bharti) has been studied. We have seen that except for the mid-latitude, the IRI 2012 model underestimates TEC values at both the equatorial and high-latitude regions. It is however understood that the three sample stations do not represent characteristics of entire Indian low latitude ionospheric region as it is a seat of equatorial anomaly zone as well. A comprehensive understanding of the quiet time behaviour of the ionosphere over the Indian region can be achieved only when ionospheric data from more and more stations are analyzed. An ideal situation would be a coordinated measurements with GPS receiver systems placed in a one degree by one degree grid. Under InSWIM program, 16 stations across India have been identified as the site for GPS receiver stations. A better understanding of Indian low latitude ionospheric region will emerge on the analysis of ionospheric data from these stations.

Dedicated measurements for the study of the ionosphere at regions southward of Trivandrum are also unavailable. The lack of observations from regions south of the dip equatorial station, Trivandrum has to be addressed by conducting regular ship-borne campaigns. As a pilot experiment, GPS receiver system was used in ship-cruise to Bharti from Cape-town during 2016. As a future work, the data collected from the ship-borne campaigns would be analyzed to gain understanding about ionospheric variations south of Trivandrum which has remained unexplored due to geographical reasons. In addition, this data will be used in generating TEC maps of the ionosphere during quiet as well as disturbed times over the Indian region.

Another aspect which requires a thorough study is the coupling between high and low latitude, both during quiet and disturbed periods. In the present doctoral study, the behaviour of the polar ionosphere during 24 geomagnetic storm events during the period 2013-2015 was studied to obtain an understanding about the response of the southern polar ionosphere to space weather events. Similar investigation needs to be performed using observations from several locations in the Indian region as well as the conjugate polar location in the northern hemisphere in order to gain insight into the coupled response of the high, mid, low and equatorial ionosphere during stormtime. The ultimate aim of these studies would be to model ionospheric variabilities in the Indian region with the comprehensive set of data collected from different regions in the Indian sector.